
University College Cork, Ireland
Coláiste na hOllscoile Corcaigh

DOCTORAL THESIS

# Performance and power smoothing of innovative closed-circuit Oscillating Water Column wave energy converter

*Author:*
Pierre BENREGUIG

*Supervisor:*
Dr. Jimmy MURPHY
*Co-Supervisors:*
Dr. Wanan SHENG

*Head of School:*
Prof. Liam MARNANE

*A thesis submitted in fulfilment of the requirements for the degree of Doctor of Philosophy*

in the

Offshore Renewable Energy Technology Group
MaREI Centre
School of Engineering
University College Cork

December 2019

# Contents

# Declaration of Authorship

This is to certify that the work I am submitting is my own and has not been submitted for another degree, either at University College Cork or elsewhere. All external references and sources are clearly acknowledged and identified within the contents. I have read and understood the regulations of University College Cork concerning plagiarism.

Signed:

_____

Date:

_____

# Acknowledgements

I would like to gratefully acknowledge the help from the following people and research groups throughout these years of knowledge, experiences and learning.

To my supervisors, Jimmy Murphy and Wanan Sheng, for their support through this research work. A special thanks to Jimmy Murphy who gave me the opportunity to pursue a PhD in UCC, in the best possible conditions and for his helpful guidance and valuable corrections.

To the MaREI Centre and all the colleagues that have shared with me these three years at work. Thanks to Jimmy, Cora, Grainne and Annette for their support in all the logistics. Thanks to Tom, Niall, Florent and James for the technical support they provided me during the physical experiments. Thanks to Christian for his support on informatics. Thanks to Chris, Nicolas, Damien, Ash, Cian, Sigmund and Deirdre who sat with me in the office and helped me with insights and tips on how to progress in my PhD, all that in a nice relaxed office atmosphere.

To Florent, Nicolas, Cyrille, Celia and Michael, with who I lived during the whole duration of my PhD in the most stable, warm and quite environment.

To Maeve, for all the good times and the support.

To my parents and brother, with who I kept close contact on the phone, for their patience to listen to the ups and downs of a PhD candidate.

Finally I would like to acknowledge that the research leading to these results is part of the Tupperwave project, which has received funding through the OCEANERA-NET European Network (OCN/00028).

# *Abstract*

School of Engineering
University College Cork

Doctor of Philosophy

**Performance and power smoothing of innovative closed-circuit Oscillating Water Column wave energy converter**

by Pierre BENREGUIG

Due to the urgency to limit global warming to 1.5°C, it is necessity to find alternatives to fossil fuel energy to empower human activities. Among the alternative resources of energy, wave energy has a large potential as it could potentially represent 10% of the world electricity demand. Significant progress in this field is however still needed to produce affordable electrical energy. Oscillating-Water-Column (OWC) devices are among the most promising types of wave energy converters because of their relative simplicity. The present work investigates the possibility of improving the performance of this well-established concept by introducing a variation in the working principle. The resulting new Tupperwave concept is equipped with non-return valves and air pressure accumulators to create a smooth unidirectional air flow, harnessed efficiently by a unidirectional turbine. In this thesis, the Tupperwave concept is investigated physically and numerically on a floating structure. In order to assess the relevance of the Tupperwave device against the conventional OWC, wave-to-wire numerical models for both devices are developed, using different thermodynamic approaches and considering the use of the current state-of-the-art turbines for each device. The different power conversion processes of the wave-to-wire models are validated through physical experiments. The wave-to-wire models are then used to identify the benefits of pneumatic power smoothing by the Tupperwave device and assess its electrical power performance. The results demonstrate the potential of the new Tupperwave concept to outperform the conventional OWC concept in terms of electrical power production and quality.

# List of Publications

This thesis is presented as a collection of the following seven papers included in the Appendix in a text-based manuscript format. The author of this thesis (first author in most papers) carried out the research work presented in the seven publications and the rest of co-authors participated to the research work, supervised the work and collaborated in the reviewing process.

## Publications appended in this thesis

- **Paper A:**
  M. Vicente, P. Benreguig, S. Crowley, J. Murphy, "Tupperwave-preliminary numerical modelling of a floating OWC equipped with a unidirectional turbine", in: *Proceedings of the 12th European Wave and Tidal Energy Conference (EWTEC)*. Cork, Ireland, 2017

- **Paper B:**
  P. Benreguig, J. Murphy, W. Sheng, "Model scale testing of the Tupperwave device with comparison to a conventional OWC", in: *Proceedings of the ASME 2018 37th International Conference on Ocean, Offshore and Arctic Engineering*, American Society of Mechanical Engineers (ASME). Madrid, Spain, , 2018.

- **Paper C:**
  P. Benreguig, V. Pakrashi, J. Murphy, "Assessment of primary energy conversion of a closed-circuit OWC wave energy converter", in: *Energies*, MDPI, 2019.

- **Paper D:**
  P. Benreguig, J. Murphy, Modelling approaches of a closed-circuit OWC wave energy converter, in: *Journal of Marine Science and Engineering, Special Issue "Advances in Ocean Wave Energy Conversion"*, MDPI, 2019.

- **Paper E:**
  P. Benreguig, J. Murphy, "Modelling Air Compressibility in OWC Devices with Deformable Air Chambers", in: *Journal of Marine Science and Engineering, Special Issue "Advances in Ocean Wave Energy Conversion"*, MDPI, 2019.

- **Paper F:**
  P. Benreguig, J.F. Kelly, V. Pakrashi, J. Murphy, "Wave-to-Wire model development and validation for two OWC type wave energy converters", in: *Energies*, MDPI, 2019.

- **Paper G:**
  P. Benreguig, M. Vicente, J. Murphy, "Non-isentropic study of a closed-circuit oscillating-water-column wave energy converter", in: *Ocean Engineering*, Elsevier, 2020.

## Publications not appended in this thesis

Another publication made during the PhD research time that is not appended to this thesis is mentioned here. This publication was not appended since it represents preliminary research carried out before the publication of Paper F. The author of this thesis carried out the research work and the rest of co-authors supervised the work and collaborated in the reviewing process.

- P. Benreguig, M. Vicente, S. Crowley, J. Murphy, "Wave-to-wire model of the Tupperwave device and performance comparison with conventional OWC", in: *Proceedings of the 3rd international conference on renewable energies offshore (RENEW)*. Lisbon, Portugal, 2018.

# Chapter 1

# Introduction

## 1.1 Context

Human activities producing greenhouse gases (GHG) emissions are estimated to have caused approximately 1.0°C of global warming above pre-industrial levels and it is likely to reach 1.5°C between 2030 and 2050 if it continues to increase at the current rate. Global climate change has already had visible effects on the environment: Sea levels rise and oceans become warmer. Longer, more intense droughts threaten crops, wildlife and freshwater supplies. Climate-related risks to health, livelihoods, food security, water supply, human security, and economic growth are projected to increase with global warming of 1.5°C and increase further with 2°C [1]. Limiting global warming to 1.5°C is projected to lower those risks and is the objective of the landmark agreement reached in Paris in 2015 by the parties of the UNFCCC (United Nations Framework Convention on Climate Change) to accelerate and intensify the actions and investments needed for a sustainable low carbon future. According to the IPCC (Intergovernmental Panel on Climate Change), this goal is achievable only if global net anthropogenic GHG emissions to reach net zero around 2050. This would require large-scale global transformations in the way in which energy is produced, agricultural systems are organized, and food, energy and materials are consumed [2]. But countries pledges to reduce their emissions are currently not in line with limiting global warming to 1.5°C [1].

With regard to the energy system transformation, it is evident that a growth in the share of energy derived from low-carbon-emitting renewable sources toward a 100% is a necessity. A scenario studied in [3] for powering the world with renewable energy by 2050 consists of using a mix of renewable energy sources such as: solar energy (57.5%), wind energy (37.1%), hydro-power (4%), geothermal energy (0.7%), wave energy (0.6%) and tidal energy (0.1%). Hydro-power and marine energies represent minor contribution but bring a variety of sources which enables to ensure that suitable sources can be found worldwide. Moreover, the complementarity of the sources will overcome

issues with the intermittent availability of solar and wind power.

The methodologies used in [3] to conclude on the cost-effective feasibility of a fully decarbonize energy system are largely questioned and criticised in [4] and [5]. A number of other studies claim the feasability of 100% renewable energy system but the principle barriers are neither technological nor economic, but instead are primarily political, institutional and cultural [6].

Although wave energy world-wide was assessed in 2002 to potentially produce 10% of the world electricity demand [7], it has a minor production share in the optimistic scenario of [3] from 2017 and represents only 0.6% of the world electricity supply. Technological solutions to produce electricity from ocean waves exist and have been proven to be technically feasible. However, their cost, so far, remains considerably higher than wind and solar technologies [8]. They are therefore not commercially viable yet. This is due to a number of challenges associated with harnessing wave energy such as the irregularity in wave parameters (amplitude, period and direction), structural loading, offshore maintenance, reliability, survivability, etc. [7]. To accelerate the wave energy sector, extensive R&D is required, at both fundamental and application level, in order to improve power performance of the particular technologies and to establish their competitiveness in the global energy market.

Among the wide variety of wave energy technologies, the Oscillating Water Columns (OWC) concept is one of the most promising [9]. An OWC device consists of a fixed or oscillating hollow structure, open to the sea below the water surface, that traps air above the inner free-surface; wave action alternately compresses and decompresses the trapped air and forces it to flow through a turbine coupled to a generator. Different concepts OWC devices can be distinguished on the basis of their working principle for harnessing the pneumatic energy of the air trapped in the device by the turbine. In the early 1980s, one concept was recognized as the most promising and has, since then, concentrated most research interest. In this concept, which will be referred as "conventional OWC", the air alternately flows from the chamber to the atmosphere through a bidirectional turbine. This thesis involves research and development of a novel OWC concept, entitled Tupperwave, that uses non-return valves and two large fixed-volume accumulator chamber to generate a smooth and continuous unidirectional air flow through a unidirectional turbine. This device is not open to the atmosphere and the air circulates in closed-circuit. This new concept aims at increasing efficiency and power quality of OWC devices for enhanced commercial competitiveness.

Part of the work within this thesis was carried out in the frame of the Tupperwave project which has been supported by OCEANERA-NET European Network. The Tupperwave project was a European collaborative project involving researchers from Ireland (MaREI Centre and CADFEM), Spain (Prodintec) and Portugal (WavEC). This thesis reflects the major findings of both numerical and physical studies carried out in the frame and in

parallel of the Tupperwave project.

## 1.2 Objectives and scope

This thesis investigates the innovative Tupperwave OWC concept for wave energy conversion purposes. The main objectives of this thesis are to:

- Develop and understand the behaviour of a novel closed-circuit OWC wave energy converter
- Develop a numerical modelling approach to assess the full behaviour of the wave energy converter from wave to wire
- Development of innovative physical modelling methods adapted to the nature of the concept
- Identify the critical component of the concept and address the risk associated with the device operation
- Assess the relevance of the new concept relative to existing concepts.

## 1.3 Outline

Seven publications have been included in the appendices of the document, and are the main publications produced during this work. They describe the research work and findings carried out during the PhD. They are referred in this document as Papers A, B, C, D, E, F and G. A brief summary of the work carried out in each appended publication is given in section 1.4. A conference paper made during this time is not appended to the thesis since it represents preliminary research of paper D. A list of publications is provided in page 14 of the document where both, the appended and not appended publications, are enumerated.

Chapter 2 presents a brief literature review of the wave energy resource and technologies and focuses on OWC wave energy converters, dealing with its history, deployments, and numerical modelling. Chapter 3 presents the strategy and the work carried out in this thesis to investigate the Tupperwave concept. It refers to Papers A to G for more details. Finally, chapter 4 summarises the main conclusions and suggests ideas for future work.

## 1.4 Summary of attached papers

Paper A describes the Tupperwave concept and applies it to a floating spar buoy OWC structure. A preliminary numerical model of the device in time-domain was built to determine the device primary conversion from hydrody-

namic power to pneumatic power, allowing an initial optimization of the device main design parameters. A set of design parameters were chosen which maximize the pneumatic average power output flowing through the turbine whilst minimizing the power fluctuations, in regular and irregular sea states. Finally, the resulting pneumatic power is compared to the pneumatic power created by a conventional OWC with the same structure geometry, revealing clear potential benefits of the Tupperwave concept in terms of pneumatic power smoothness.

Paper B presents the fabrication and testing campaign of the Tupperwave device which was carried out at 1/24th scale to prove the concept working principle and validate the numerical model that had previously been developed. An appropriate and challenging scaling method was applied to the floating device to correctly model the air compressibility in the Tupperwave PTO. In parallel, a model scale conventional OWC was also built using the same axisymmetric structure and tested in the same wave conditions. The results provide a direct comparison between the two physical models pneumatic power performances. An in-depth analysis of the valve behaviour is shown, revealing the importance of their efficiency for the Tupperwave device performance.

Paper C describes and validates the time-domain numerical models from wave to pneumatic power of the Tupperwave device and corresponding conventional OWC. The tank testing campaign of the two devices at 1/24th scale is described. Unexpected elastic deformation of the accumulator chambers of the physical model is observed and the effects on the modelling are investigated. The tank testing results are used to validate the numerical models. In this manner, the work contributes to the development of Wave-to-Wire models for a conventional OWC and the Tupperwave device.

Paper D describes the various methods used for the modelling of the Tupperwave device within the Tupperwave project. The device was modelled with two different numerical methods: the method presented in paper A and a method using Computational Fluid Dynamic (CFD) implemented by the company CADFEM. The device was also physically modelled at model scale as described in paper B. The modelling outcomes are compared in the paper. An analysis on the dependence of the device efficiency on the valves and turbine aerodynamic damping was carried out, using both physical and numerical approaches.

Paper E investigates a new method for modelling air compressibility at model scale based on physical observations made in paper C. The method uses variable volume chambers which mimic air compressibility by storing energy in the form of strain energy. This new method, relative to the existing method, facilitates practical implementation at small ($<$1/25th) and medium scale ($<$1/10th). Various applications to this method are identified and described, including the presentation of a novel OWC concept using variable volume chamber accumulators.

Paper F completes the time-domain numerical models from wave to pneumatic power previously developed in paper D by the addition of turbine and generator models, along with their control laws, to encompass all power conversion stages from wave to electrical power. The turbine models are based on physical testing results obtained from the literature. Hardware-in-the-Loop was used to physically model the last power conversion stage from mechanic to electrical power and hence validate the control law and the generator numerical model. The dimensioning methodology for turbines and generators for power optimisation is explained. The validated Wave-to-Wire numerical models of the conventional OWC and the Tupperwave device were used to assess and compare the performances of these two OWC type wave energy device concepts in the wave climate of the EMEC test site in Scotland. The benefits of pneumatic power smoothing by the Tupperwave device are discussed and the required efficiency of the non-return valves is investigated. The results demonstrate the potential of the Tupperwave device to outperform the conventional OWC.

Paper G describes and improves the wave-to-wire models of the Tupperwave device developed in papers D and E, by including a more advanced thermodynamic model. The new thermodynamic model is based on the energy conservation law, taking account of heat creation as well as heat dissipation across the device walls. Such modelling had yet not been carried out in the literature for closed-circuit OWC devices and this improvement enables the determination of the air temperature evolution in the device chambers. The results show that the temperature increase of the air in the Tupperwave device does not represent a danger for the device operation.

To conclude, the work described in the papers summarized above, investigates numerically and physically a novel concept of OWC wave energy converter to prove its working principle, understand its operational behaviour and assess its relevance relative to benchmark technologies.

# Chapter 2

# Literature Review

The aim of this section is to give a general overview of wave energy resource, existing technologies and modelling methods.

## 2.1 Wave Energy Review

### 2.1.1 Wave energy resource and characterisation

Waves are produced by the wind blowing over a surface of water. As the wind blows, pressure and friction perturb the equilibrium of the water surface and transfer energy from the air to the water, forming waves. In the ocean, these waves range from a few centimeter to up to 30 meters high.

The basic theory to describe the ocean waves propagating in water is the Airy wave theory (also referred to as linear wave theory) and dates back from the 19th century. The theory assumes that the fluid layer has a uniform mean depth, and that the fluid flow is inviscid, incompressible and irrotational [10]. In Airy's wave theory, single wave components are sinusoidal (also referred as regular). In the case of a single sinusoidal wave of amplitude $A_0$ and period $T$ propagating at an angle $\beta$ with the x-axis, the free surface elevation $\eta$ at the point M(x,y) located on the water plane area at the time t is:

$$\eta(x,y,t) = A_0 cos\Big(k\big(xcos\beta + ysin\beta\big) - \omega t - \phi_0\Big) \tag{2.1}$$

where $k = \frac{2\pi}{\lambda}$ is the wave number with $\lambda$ referring to the wave length; $\omega = \frac{2\pi}{T}$ is the angular frequency; $\phi_0$ is the phase reference. The average energy flux transported by a regular wave is proportional to the square of the amplitude and to the period. Typical mean wave periods in the Atlantic ocean are of 5 to 15 seconds. In deep water, the wavelength can be approximated by $\lambda \simeq 1.56T^2$ and common wavelength are thus of 40 to 350 meters. Since ocean waves are typically 1 to 3 meters outside of storm conditions, the horizontal scale of ocean waves is therefore much larger than the vertical

scale.

In reality, ocean waves are not regular but highly irregular: Height and period vary stochastically wave after wave and the wave crests are not straight lines. The surface elevation in an irregular sea state can be described as the superposition of an infinite number of regular waves, of various amplitudes $A_i$, frequencies $\omega_i$, directions $\beta_i$ and phase reference $\phi_i$:

$$\eta(x,y,t) = \sum_{n=1}^{\infty} A_i cos\Big(k_i\big(xcos\beta_i + ysin\beta_i\big) - \omega_i t - \phi_i\Big) \tag{2.2}$$

In that case, the sea state is commonly characterised by its energy spectrum, resulting from a spectral analysis. The form of the spectrum indicates the amount of energy transported by the different wave frequencies. Observations on ocean waves have revealed that ocean wave energy spectra show characteristics forms. The most commonly used spectrum is the Pierson-Moscowitz (PM) spectrum. This spectrum assumes that the wind blew steadily for a sufficiently long time over a large area and the waves have come into equilibrium with the wind. This is the concept of a fully developed sea. The PM spectrum is described by its spectral variance density:

$$S_{PM}(f) = \frac{\alpha g}{\omega^5} e^{-\beta\left(\frac{\omega_p}{\omega}\right)^4} \tag{2.3}$$

where $g$ is the gravitational acceleration, $\alpha = 0.0081$, $\beta = 0.74$ and $\omega_p = \dfrac{g}{U_{19.5}}$ is the peak frequency with $U_{19.5}$ being the wind speed at a height of 19.5m above the sea surface (height of the anemometers on the weather ships used by Pierson and Moskowitz in 1964).

Subsequent research completed during the Joint North Sea Wave Observation Project (JONSWAP) showed that the wave spectrum is never fully developed. It continues to develop through non-linear, wave-wave interactions even for very long times and distances. The JONSWAP spectrum is refined expression of the PM spectrum which takes into account additional parameters:

$$S_{JONSWAP}(f) = \frac{\alpha g}{\omega^5} e^{-\frac{5}{4}\left(\frac{\omega_p}{\omega}\right)^4} \gamma^r \tag{2.4}$$

with:

$$r = e^{-\dfrac{(\omega-\omega_p)^2}{2\sigma^2\omega_p^2}} \tag{2.5}$$

where $\alpha = 0.076\Big(\dfrac{U_{10}^2}{gF}\Big)^{0.22}$, $\omega_p = 22\Big(\dfrac{g^2}{U_{10}F}\Big)^{1/3}$, $\gamma = 3.3$ is the peak enhancement factor, $U_{10}$ is the wind speed at a height of 10m above the sea surface, $F$ is the distance (fetch) over which the wind blows with constant velocity, and $\sigma = \begin{cases} 0.07, & \text{if } \omega \leq \omega_p \\ 0.09, & \text{if } \omega > \omega_p \end{cases}$.

The spectrum formulations can also be expressed with two other parameters instead of the wind speed, namely: the significant wave height $H_s$, the peak period $T_p$ which determines the wave frequency transporting the most power. The significant wave height is defined traditionally as the mean wave height (trough to crest) of the highest third of the waves (also noted $H_{1/3}$).

It is usefull to define the moments of the spectrum $m_n$ as:

$$m_n = \int_0^\infty S(\omega)\omega^n d\omega \tag{2.6}$$

The spectral significant wave height $H_{m_0}$ is an approximation of the significant wave height derived from the 0-th order spectral moment:

$$H_{m_0} = 4\sqrt{m_0} = 4\sqrt{\int_0^\infty S(\omega)d\omega} \simeq H_s \tag{2.7}$$

or equivalently calculated as four times the standard deviation of the surface elevation:

$$H_{m_0} = 4\sigma_\eta = 4\sqrt{\int_0^\infty (\eta(t) - \overline{\eta})^2 dt} \tag{2.8}$$

With these new parameters, the JONSWAP formulation becomes:

$$S_{JONSWAP}(f) = \alpha \frac{5}{16} \frac{H_s^2}{T_p^4} \frac{1}{f^5} e^{-\frac{5}{4}\frac{1}{(T_p f)^4}} \gamma^{e^{-\frac{(fTp-1)^2}{2\sigma^2}}} \tag{2.9}$$

with $\sigma = 0.07$ if $f < \frac{1}{T_p}$ and $\sigma = 0.09$ if $f > \frac{1}{T_p}$, and $\gamma$ the frequency spreading coefficient.

The Bretschneider spectrum is also commonly used in the context of wave energy:

$$S_{Bretschneider}(f) = \frac{5}{16} \frac{H_s^2}{T_p^4} \frac{1}{f^5} e^{-\frac{5}{4}\frac{1}{(T_p f)^4}} \tag{2.10}$$

Once created, waves can travel thousands of kilometres with little energy loss. Ocean waves transport a large amount of energy near the free surface. The average energy flux transported by an irregular wave in deep water per meter of wave front can be approximately calculated as [11]:

$$J_\infty = \frac{\rho g^2}{64\pi} H_s^2 T_e \simeq 0.49 H_s^2 T_e \qquad \text{[kW/m]} \tag{2.11}$$

where $T_e$ is the wave energy period defined as:

$$T_e = \frac{m_{-1}}{m_0} \tag{2.12}$$

For a JONSWAP spectrum with a peak enhancement factor $\gamma = 3.3$, the peak period is $T_p = 1.12 T_e$.

The energy transported by the waves is therefore proportional to the square of the significant wave height and to the peak period of the waves. $H_s = 3m$ and $T_p = 11s$ represent common wave conditions off the west coast of Ireland [12]. In these conditions, the energy transported by the waves in one meter wave front is of the order of 40 kW and is equivalent to:

- the power transported by a 12 m/s wind (strong breeze, 25 knots) across a $30m^2$ vertical area;
- the power of direct solar insulation reaching 40 $m^2$ horizontal earth surface for the sun at the zenith;
- the power transported by a 2 m/s tidal current across a 10 $m^2$ vertical area;

This shows the high energy density of wave energy, which is the highest among renewable energy sources [7].

The wave energy resource is unequal around the globe. The global distribution of annual mean wave power is presented in figure 2.1. Greatest resources are located at high latitudes ($\pm 50°$) in both hemisphere. Large seasonal variations are however observed. Depending on the sea state ($H_s$;$T_p$), the energy transported by the waves can vary from 1kW/m in calm seas to 1MW/m under extreme conditions. Of course, only a very small proportion can be harnessed but this still represents a very large amount of energy.

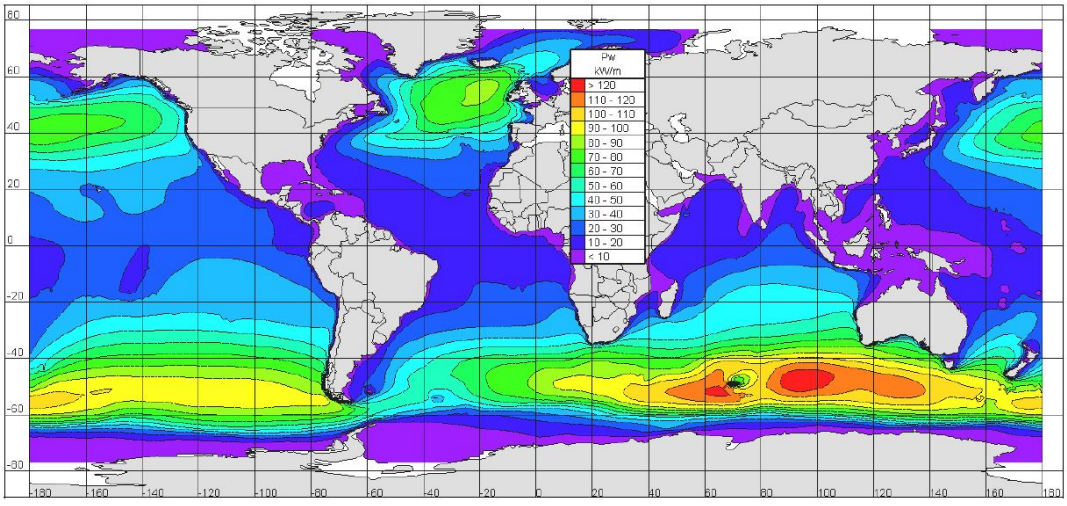


Figure 2.1: Global distribution of annual mean wave power [13]

In the next section, a brief review of existing technologies to harness wave power is given as well as an historical contextualisation.

## 2.1.2 Harnessing wave energy

### 2.1.2.1 History of wave energy development

Since the very first patent about a wave energy technology was filed in France in 1799 by a father and a son named Girard [14], the number of technological concept have been increasing significantly. In Japan in the 1940s, Yoshio Masuda developed a navigation buoy powered by wave energy, which were commercialized in Japan in 1965 and later in the USA. The buoy equipped with an air turbine, which was later named as a (floating) oscillating water column (OWC). The oil crisis in the 1970s resulted in a major change in how renewable energy was regarded and raised the interest from governments in large-scale energy production from the waves. In 1976, Masuda promoted the construction of such a device type in Japan, and called the Kaimei. At that time, the theoretical knowledge of wave energy absorption was however at a very early stage and the power output of the Kaimei was low. Research on large-scale wave energy conversion developed all over the world. Specialised conferences and large-scale experiments started to appear in the UK, Norway, Japan, and India.

From 1991, the European Commission decided to include wave energy in their R&D program on renewable energies [14]. This was followed by a period of great confidence with private investors and large industrial groups participating in wave energy projects. A number of wave energy companies emerged and tested large-scale prototypes in real sea conditions and energy was produced from waves: 131 large-scale prototypes were tested between 1978 and 2017; 47% were deployed for more than a year without major problems and demonstrated technical feasibility [8]. Figure 2.2 shows the outcomes of the demonstration projects.

However, from 2012 to 2016, a number of major wave energy companies went bankrupt or had to put their activities on hold. The bankruptcy of the Pelamis company in 2014, followed a year later by the company Aquamarine, was probably the biggest shock for the wave energy industry since they were considered as the leaders at the time. Since then, the general confidence in wave energy is dramatically declined.

The conclusions made in [8] are that, it is technically possible to produce electricity from waves, but harnessing wave energy in a commercially viable way represents the real technological challenge. So far, no technology has proved its ability to harvest wave energy at a cost that allows for commercial opportunities to be found. This is due to the nature of wave power and the harsh environment. The main challenges are [7]:

- obtaining maximum efficiency in irregular wave amplitude, phase, direction and over the large range of wave frequencies and available power.

- converting the large wave forces and slow motion (frequency around

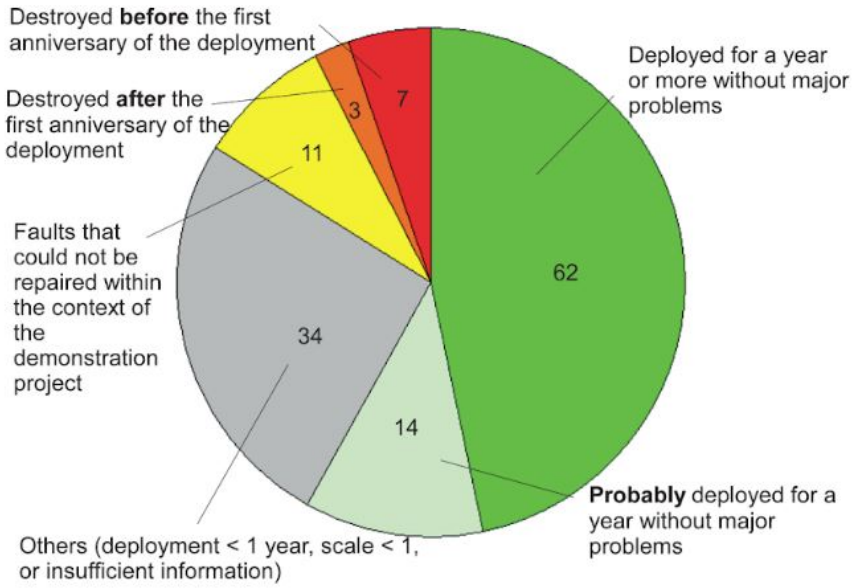


Figure 2.2: Distribution of large-scale demonstrators (1/3 to 1 scale) of wave energy converters from 1978 to the present day depending on the outcome of the demonstration projects [8]

0.1Hz) into a low torque fast rotary motion adapted to an electrical generator (typically 1000rpm=16Hz).

- achieving long term (20-30 years) resistance to extreme weather conditions which can lead to structural loading as high as 100 times the average loading.

Other non-technical issues like government policies, economics and environmental impacts also represent barriers to the development of wave energy conversion, however this thesis is mainly concerned with technological aspects of wave energy conversion.

Lessons were however learned from the past failures, and especially regarding the technology development methodology which had been so far focused on the feasibility and technical maturity of the devices, leaving aside the economic viability criterion. To solve this issue, the idea recommended by Weber in [15], is to prioritize the Technology Performance Level (TLP), i.e. the reduction of the cost of energy, before increasing the maturity of a particular technology. This idea has been applied by several researchers and funding agency and this could represent a turning point in the wave energy industry. Also, some developers have found there place in niche markets where other sources of energy are less competitive. For example, the company Albatern focuses on markets such as offshore power supply equipment and aquaculture. The project 1kW GATOR by the companies Technology

For Ideas (TFI) and Exceedence also target the aquaculture market. Others developers combine a wave energy conversion technology to wind energy technology to build hybrid wind-wave platforms on the model of the company Floating Power Plant.

#### 2.1.2.2 WEC technologies

The challenge of harnessing wave energy has inspired many inventors and more than one thousand patents had been registered by 1980 [16]. Since then, the number of technologies does not decrease as new concepts replace or outnumber those that are being abandoned.

WEC technologies use different methods to extract energy from the waves. A classification method was suggested in [14] based on the conversion principle, see figure 2.3. Within this classification, three main families of devices are identified: Oscillating Water Columns (OWCs), overtopping devices and wave-activated bodies. Each family is subdivided into fixed or floating structures and further subdivided in concept variations (structure shape and PTO type). Wave-activated bodies can be further divided according to their motion (heave, pitch, surge, yaw).

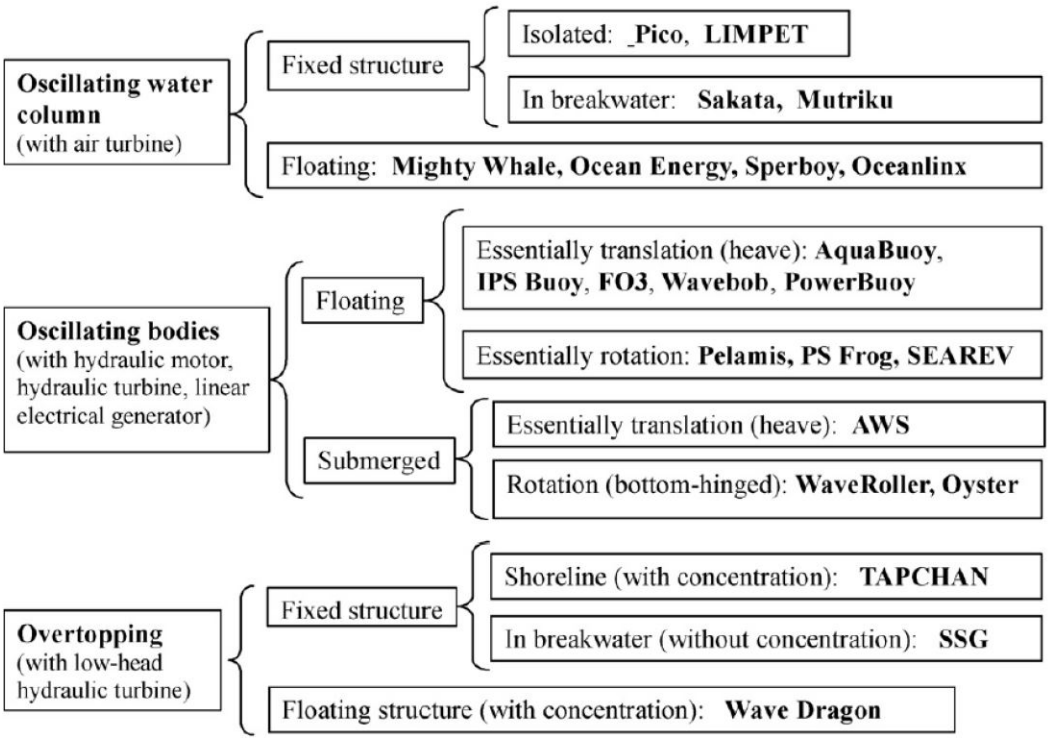


Figure 2.3: A classification of wave energy technologies [14]

OWC devices consist mainly of a partially immersed hollow structure, open at the bottom. Air is trapped between the Internal Water Surface (IWS) and the upper part of the structure. An opening in the upper part of the

structure ensures that the air interchanges in and out of the air chamber. This opening in fitted with a turbine. When excited by the waves, the IWS alternatively compresses and decompresses the air, converting hydraulic power from the wave into pneumatic power. The air turbine harnesses the pneumatic power and drives a generator which creates electricity. Figure 2.4 displays a schematic of a bottom-standing OWC.

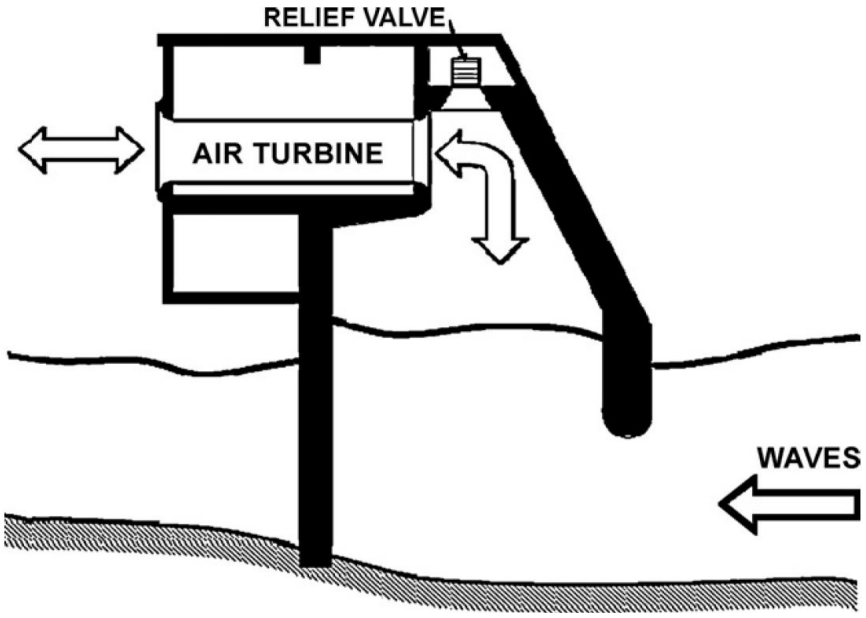


Figure 2.4: Cross-sectional view of a bottom-standing OWC [14]

Oscillating bodies are defined by a main moving body reacting against a frame of reference which is either fixed, or floating but with a much larger inertia than the main moving body. Then, between the relative movement of the two bodies, a Power Take-Off (PTO) system composed of a hydraulic motor or turbine, or a linear electrical generator, extracts the kinetic energy of the motion. Figure 2.5 displays the schematics of two different oscillating WEC principles.

Finally over-topping devices are based on a structure located above the free-surface that waves overflow filling a tank from where the potential energy is extracted by means of a low-head hydraulic turbine. Figure 2.6 displays the principle of overtopping devices.

Other types of devices were developed since the classification given in figure 2.3 and more recent concepts do not fit in the three main families of WECs. For example, the bulge wave technology which consists of a rubber tube filled with water, moored to the seabed heading into the waves. The passing wave causes pressure variations along the length of the tube, creating a bulge. As the bulge travels through the tube it grows, gathering energy which can be used to drive a standard low-head turbine located at the bow. See figure 2.7a. The rotating mass technology, presented in figure 2.7b, is

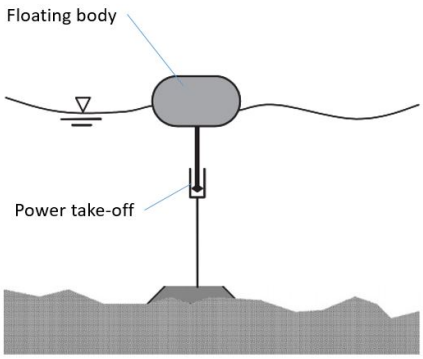


(a) Heaving buoy reacting against a fixed anchor [17]

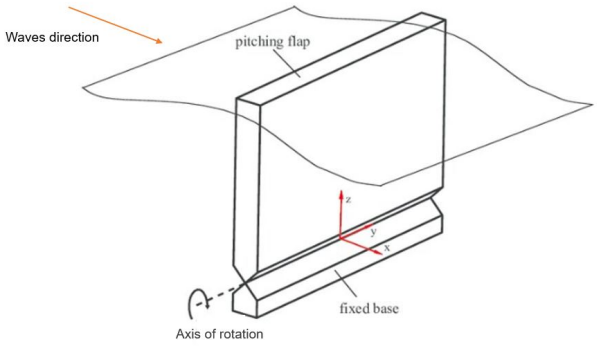


(b) Schematic of flap WEC [18]

Figure 2.5: Two examples of oscillating bodies wave energy converters

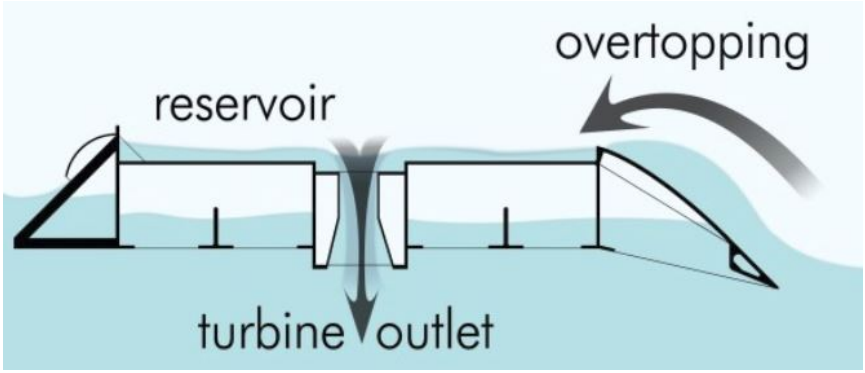


Figure 2.6: Cross-sectional view of an overtopping device [14]

another example of technology which uses two forms of rotation to capture energy by the movement of the device heaving and swaying in the waves. This motion drives either an eccentric weight or a gyroscope causes precession. In both cases the movement is attached to an electric generator inside the device.

Other marginal devices have a unique and very different design to the more well-established types of technology [20].

#### 2.1.2.3 Grid integration

In order to maintain the stability and the power quality of their electrical network, network operators have established grid codes that describe the requirements that any generating power plant needs to meet before they are allowed to make a connection on the grid. These requirements are usually in the form of limits for the two main following criteria [21, 22]:

- **Harmonic distortion:** The network has a set frequency and all com-

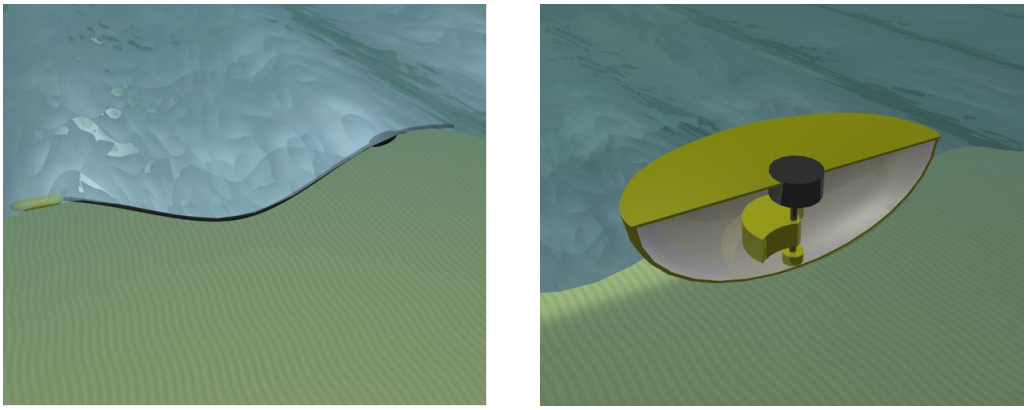

(a) Bulge wave device principle (b) Rotating mass device principle

Figure 2.7: Other wave energy converter concepts [19]

ponents should be connected synchronously to maintain the frequency and the phase of the network;

- **Voltage fluctuation:** Rapid voltage variations over several cycles may deteriorate the local power quality as well as introduce a certain degree of instability in a power system. Voltage variations in the frequency range 0.1-25Hz, also called flickers, can cause disturbance to the customers.

The exact tolerated level of fluctuation varies from country to country and also depends on the local network strength and operator.

All WEC technologies described in the previous section aim at driving an electrical generator which is either linear or rotary. Most commonly in WECs, variable-speed rotary generators are used in association with power electronic converters. The power electronic converters, which are AC-DC-AC back-to-back converters, decouple the electric machine from the electric network adapt the output power signal to meet the grid frequency requirements [23].

However, the reciprocating motion induced by ocean waves creates large mechanical power fluctuations, which, if no power smoothing mechanism is used, are directly transformed into large electrical power fluctuations by the generator. The fluctuating electrical power generated by the WEC may cause undesired voltage fluctuations on the grid. Hence, reducing the power fluctuations created by an oscillating WEC to fulfil the requirements of the grid represents a significant challenge for the wave energy device developers.

Wave energy converters are designed to be deployed in arrays and it was shown in [24] that the spatial scattering of several devices in a farm has a significant smoothing effect on the overall electricity production. Further smoothing is required to meet the electrical grid requirements and this can be achieved using costly conventional energy storage techniques. These include compressed air storage, hydrogen storage, super capacitors, batteries

and flywheels [25]. The stability of the WEC farm power output naturally also depends on the capacity of each individual WEC to produce a relatively smooth electrical power. Some WECs produce smoother electrical power than others depending on their working principles which can have inherent short-term energy storage mechanisms. Smoother electrical power production by individual WECs can reduce the total expenditure costs by [26]:

- reducing the need for the farm energy storage to a minimum because smooth overall electrical power is produced;
- reducing the required rating for components such as generators, cables and transformers because lower peak powers are reaches by the individual WECs.

Thus, the choice of a WEC type for a farm should not only rely on its power production performance but also on its capacity to inherently smooth its electrical power output.

### 2.1.3 Modelling of WECs

The modelling of wave energy conversion into electricity by a WEC is complex and involves, in most cases, several branches of physics such as hydrodynamics, thermodynamics, and electronics.

#### 2.1.3.1 Wave-to-Wire numerical model

To help understanding the behaviour of WECs, precise mathematical models are crucial for the development of successful wave energy converters. The energy generated from ocean waves passes through several conversion stages before it is converted into electricity and delivered into the electricity grid. Numerical models therefore need to encompass all power conversion stages to provide accurate prediction of the WECs power production, hence further allow the assessment of the energy price. Such models are called wave-to-wire models and are critical in the process of increasing the Technology Performance Level (TLP).

A review of wave-to-wire models for different types of WECs and PTOs was published in [23]. Depending on the power take-off (PTO) system implemented in the WEC, the path from ocean waves to the electricity grid can be divided into between two and four conversion stages: absorption-, transmission-, generation- and conditioning-stage. Figure 2.8 illustrates a power take-off (PTO) system with the four conversion stages highlighting the potential control inputs that includes a hydraulic transmission system.

A number of wave-to-wire models were built in [12] to compare the power performances of several WECs on various sites and establish a benchmarking of WECs. An investigation on wave-to-wire models was carried out in

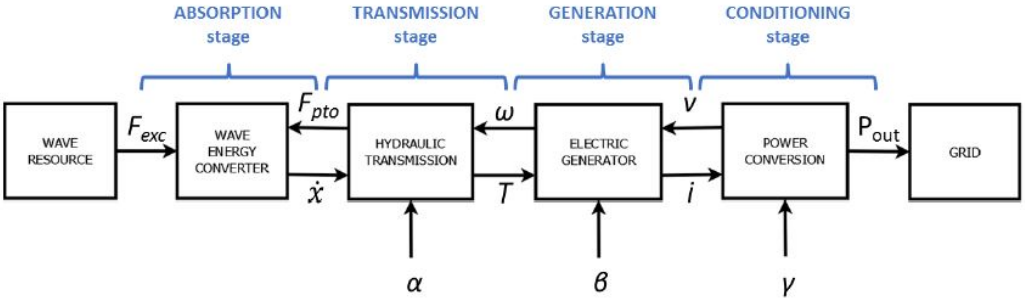


Figure 2.8: Diagram of a wave energy converter with a hydraulic power take-off, including potential control inputs [23]

[27] to assess what stages need to be accurately modelled and what stages can be simplified. A High-Fidelity Wave-to-Wire model (HFW2W), where all the important components of the different conversion stages from ocean waves to the electricity grid are incorporated, was compared to a reduced Wave-to-Wire model (rW2W), where only the most relevant dynamics are included, for the optimisation of control parameters and power production assessment. The result showed that the rW2W model, in which the generation and conditioning stages were significantly simplified, provided very similar results to the HFW2W model and reduced the computational time by an order of magnitude. However, it was observed that reductions in the model complexity for the wave-structure hydrodynamic interactions and the Power Take-Off (PTO) system may lead to significant fidelity reductions.

While the modelling of the PTO system is specific to each type of WECs, the hydrodynamics of wave-structure interactions is common for the modelling of all WECs.

#### 2.1.3.2 Wave-structure interaction

Various approaches were developed to study wave-structure interactions.

**Linear wave theory**

The theory for wave-structure interactions was initially developed before the mid-1970s, for the study of ships dynamics. The main theoretical tool developed at the time was the linear wave theory, already introduced briefly in section 2.1.1, and is still used now. The following description of the linear wave theory is based on [8, 28]. Within the linear wave theory, the wave-structure interaction is decomposed into different phenomena:

- **Buoyancy:** In the absence of waves, the body floats on the surface due to the buoyancy force which acts against gravity and is equal to the weight of the fluid displaced by the body.

- **Wave excitation:** In the presence of waves and in absence of body displacement, the unsteady pressure field generated by the incoming and diffracted waves induces excitation forces on the immersed body surface.
- **Radiation:** In the absence of incident waves, the unsteady motion of the body in the water generates waves on the surface of the water. This results in a radiation force applying on the body.

Within the potential theory, the water is assumed as an inviscid and incompressible fluid, and the flow is irrotational. These assumptions enable the description of the flow by a velocity potential function $\phi$, such that the velocity field is the gradient of the potential:

$$v(x,y,z,t) = \nabla\Phi = \begin{bmatrix} \partial\Phi/\partial x \\ \partial\Phi/\partial y \\ \partial\Phi/\partial z \end{bmatrix} \tag{2.13}$$

The flow velocity potential verifies the Laplace equation and a number of boundary conditions. Significant simplification through linearisation of the boundary conditions can be obtained when further assumptions are made:

– the wave steepness should be small, i.e. the wave height is significantly larger than the wave length;

– the displacement of the body around its mean position should be small relative to its size.

In practice, the velocity potential flow is solved numerically. This requires numerical codes based upon the Boundary Element Method (BEM) such as the commercially-available software WAMIT [29] or the open-source solver NEMOH [30]. The computational domain is discretized into numerous cells or boundary elements and then the velocity potential is calculated for each element. Such techniques are widely used in linear and weakly non-linear wave-structure interaction problems due to low computational cost and mature numerical techniques.

More details about the linear wave theory equations and resolution in frequency and time domain are given in Appendix H. Despite the restrictive assumptions, the linear potential flow theory applies very well for applications to WECs in small to moderate sea states. For more energetic sea states, the use of computational fluid dynamic is required.

#### Computational fluid dynamic

Computational Fluid Dynamics (CFD) is based on the numerical integration of the Navier-Stoke equations that are a set of equations derived from the conservation laws (mass, energy, momentum, and angular momentum, all of

which are conserved in a closed volume). These equations together with the continuity equation constitute what is often regarded as the fundamental set of fluid flow equations. The main difference from the potential flow models is the inclusion of viscous effects and two-phase flow (air entrainment in breaking waves) making them a good tool for the simulation of extreme wave loading and turbulence. A number of commercial codes are available such as the commercial codes CFX and Fluent distributed by the company ANSYS or the open-source software OpenFOAM by the company OpenCFD.

Their high demand in computational time makes them unsuitable to model an event of more than a few minutes long or multiple case scenarios with several devices. CFD models are therefore often used for extreme sea states or for validation of linear potential models in specific cases. Nevertheless, with the rapid development of high performance computing technology, the use of CFD tools is becoming increasingly important in engineering design work.

The comparisons between linear potential and CFD models prove the accuracy of linear potential models. Nevertheless, for larger sea states significant discrepancies appear as the linearity assumptions do not remain valid and other non-linear effects, such as vortex shedding, become important.

#### Physical experimentation

Since physical models are the natural reproduction of the physical processes, they are ideal for the study of wave-energy converters. However, building and testing a device at a relatively large scale (1:1, 1:2 or 1:3) is a long and expensive process. Tests are therefore first carried out at laboratory scale where the dimension of the scaled device are in the order of one meter. The device is usually scaled using Froude scaling and the scale chosen must be large enough to ensure a large Reynolds number (larger than $10^5$). Under such conditions, the effects of the viscous forces on the structures can be negligible and similarity between laboratory scale and full scale is achieved [31]. The scale is then stepwise incremented to increase the Technology Readiness Level (TRL) of the device [32]. Figure 2.9 displays a diagram of the TRLs.

Unlike in numerical modelling, it is impossible to include all power conversion stages in a single experimental test at laboratory scale. Building a scaled PTO and electrical generator adapted to the very low level of power available at laboratory scale is not possible. Physical experimentation is generally used to refine or validate numerical models and the validation of a wave-to-wire model is therefore achieved by validating separately each conversion stage of the model with specific physical experiments [33]. Physical tests in a wave basin usually only deal with the absorption stage and the wave-structure interaction while the WEC PTO is usually tested on a simulation bench together with the electrical generator. As an example, the wave-to-wire numerical model of a heaving buoy WEC is validated in a series of 3 publications corresponding with the validation of the hydrodynamic model

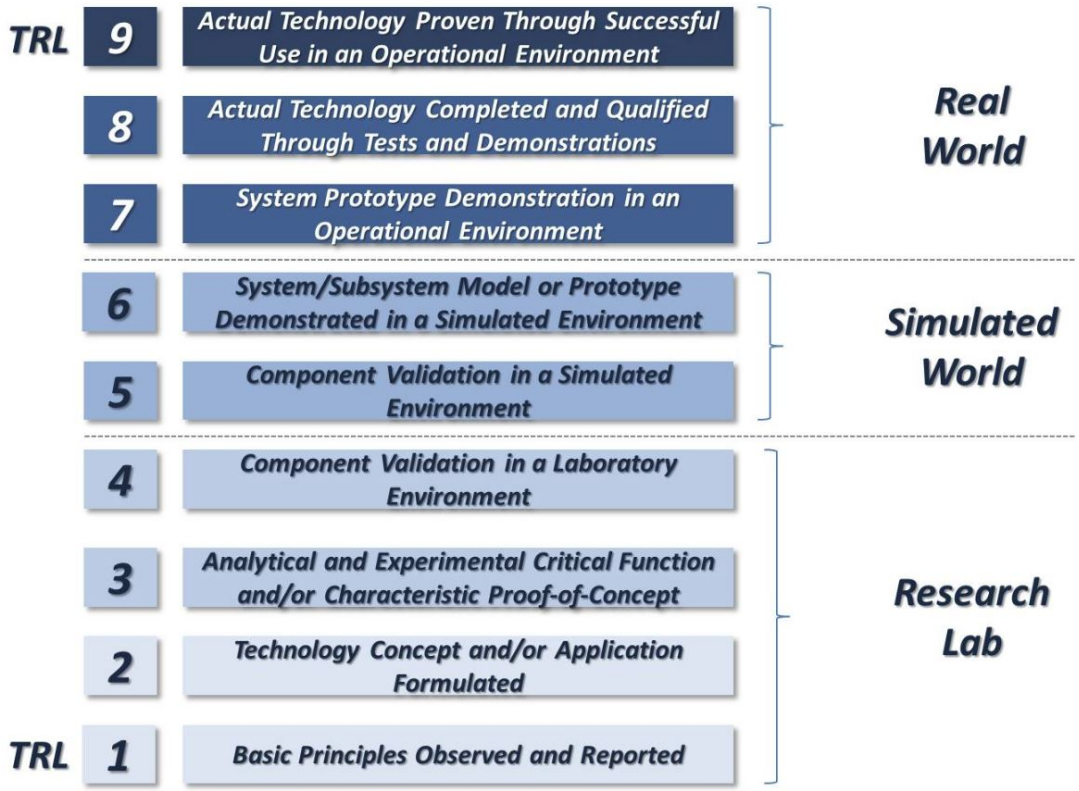


Figure 2.9: Technology Readiness Level diagram

[34], the transmission stage [35] and the generation and conditioning stage [33].

## 2.2 Oscillating Water Column devices

OWCs are a major class of wave energy converters. The main advantage of the OWC concept versus most other WEC concepts is its simplicity leading to low operational costs and straightforward maintenance. Indeed, the only moving part of the energy conversion mechanism is the rotor of a turbine, located above water level, rotating at a relatively high velocity and directly driving a conventional electrical generator. The simplicity of OWC devices is of particular interest in the transmission stage. Unlike for oscillating body WECs, the high loads and slow velocity of the absorbed wave power are not transmitted to a solid body, but are first converted into pneumatic power and further converted into mechanical power by the turbine with low loads and high velocity. The air chamber in the OWC structure therefore acts as a smooth non-mechanical transmission and gearbox which prevents:

- high loading on mechanical parts;
- the use of end-stops which are critical in terms of loads;

- the use of a mechanical gearbox for connecting to the generator.

This simplicity naturally increases the reliability of the device concept. Moreover, the concept is easily adaptable to different locations: in breakwaters, cliffs, beaches, near-shore and off-shore.

OWC WECs are the focus of this thesis and this section provides an overview of their development and modelling methods.

### 2.2.1 History and development

The first OWC device was a navigation buoy developed in the 1960s by Yoshio Masuda and already mentioned in section 2.1.2.1. Masuda's navigation buoys were equipped with a conventional unidirectional air turbine, which required a system of rectifying valves, see figure 2.10. Masuda then extended the working principle of the OWC for larger scale electrical power production and created the Kaimei device: Kaimei was a large barge (80 m $\times$ 12 m, 820 ton) that had thirteen OWC open bottom chambers built into the hull, see figure 2.11. The device was deployed off the coast of Japan for a two years at the end of the 1970s. Various arrangement of non-return valves and unidirectional turbine were tested on the Kaimei device to rectify the air flow across unidirectional turbines. The results showed that there were challenges associated with the use of non-return valves in large OWC devices. Other types of turbine which do not require rectification of the flow, namely self-rectifying turbines, were tested on the Kaimei [9]. Self-rectifying turbines are able to harness both directions of air flow while rotating in the same direction and are described in section 2.2.3. As non-return valves were regarded as impractical after the experience of the Kaimei, the use of self-rectifying turbines became the normal way to proceed.

In Europe, studies to develop large scale WECs were initiated in the early 1970s, shortly after the oil crisis, and followed world wide. OWC devices were largely investigated and went through extensive research. Their simplicity allowed rapid advancement since 63% of WECs tested in the sea, up to 2001, were OWCs [8]. Among the numerous prototypes of OWC devices deployed in real sea conditions, we can distinguish:

- fixed-structure OWCs: e.g., the LIMPET shoreline plant [36], the PICO power plant [37], the Mutriku wave power plant [38] and the recently built Yongsoo plant [39];
- floating structure: e.g., the OE buoy [39], the Mighty Whale concept [40] or the Mk3 from the company Oceanlinx [9].

A major achievement in developing OWC devices was the construction of the Pico plant on the island of Pico in Azores, Portugal, see figure 2.12. It was the first wave energy plant designed to permanently supply electrical

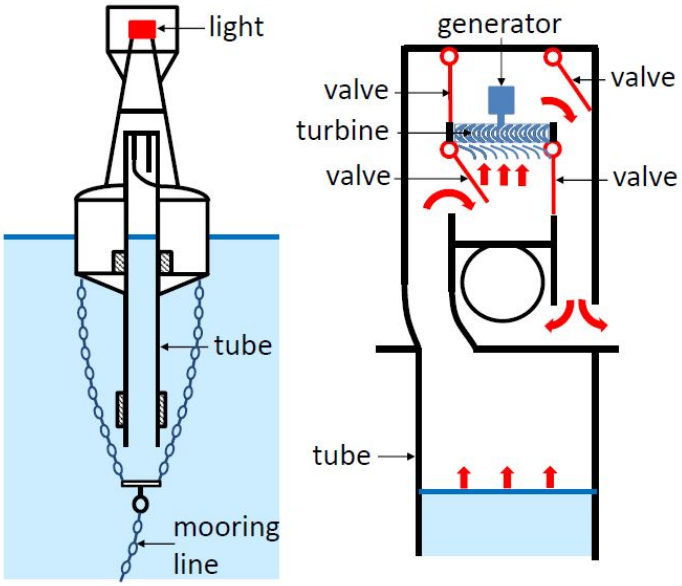


Figure 2.10: Layout of Masuda's navigation buoy and details of the air flow through the turbine and rectifying valves [9]


Figure 2.11: The Kaimei, a multi-OWC barge [9]

energy to a grid. The plant operated for the first time in 1999, and was still supplying energy to the Pico islands grid in early 2018 (with intermissions due to maintenance and technical problems), before it partially collapsed due to structural weaknesses. The plant was both used as a supplier of energy to the island grid, and as an infrastructure for research and training [41]. The plant was equipped with a relief valve (or bypass valve), connecting the OWC chamber to the atmosphere, in parallel to the turbine [42]. This valve is normally closed and opens in very energetic sea states. When it opens, the flow splits between the turbine and the bypass valve, reducing the flow through the turbine in order to alleviate the load on this latter and avoid stall conditions. Such valve is a common feature in OWC devices.

More recently, with the building of a breakwater to resolve problems of access to the harbour at Mutriku, Spain, the Basque government decided to incorporate an infrastructure into the breakwater to harness wave energy, and the OWC technology was selected [38], see figure 2.14. The Mutriku power plant was commissioned in 2011 and serves as a new real-sea infrastructure for the testing of air turbines [43]. In addition, the Marmok-A5 OWC device was completed at the BiMEP site, Basque country, in 2016. The Marmok is a 5m diameter (max), 41.8m long and 162.2t hollow floating spar buoy which provides an additional testing infrastructure for air turbines but also mooring systems and control algorithms [44]. Currently, a state-of-art turbine for OWC devices (namely the biradial turbine) is being tested on the Marmok buoy in the framework of the H2020 OPERA project [45].

Figure 2.12: Back view of the 400 kW OWC plant on the island of Pico, Azores, Portugal, 1999 [9]

In 2019, the deployment of the OE buoy by the Irish company Ocean Energy will take place off the coast of Hawaii at full scale. The OE buoy is a BBDB floating OWC device which has undergone three full phases of scaled testing, at 1:50, 1:15 and 1:3 scale. The full scale device, displayed in figure 2.15, is 826-ton and measures 38 by 18 meters with a draft of 9 meters. For its first deployment off the coast of Hawaii, the buoy will be equipped with a 400kW generator. The structure itself was however built for larger powers and will be equipped with a generator up to 1MW rated power when deployed on a test site with a more energetic wave climate.

Figure 2.13: Mutriku breakwater with integrated OWC chambers [9]


Figure 2.14: The MARMOK-A-5 device deployed at BiMEP [44]

### 2.2.2 OWC working principles

Wave energy converters, and by extension OWC devices, can be characterised into a number of sub-categories:

- Operational concepts;
- Location with respect to the shoreline (onshore, nearshore, offshore);
- Deployment state (fixed, floating, submerged);
- Orientation with respect to the incident wave (attenuator, terminator, point absorber).

OWC devices are most commonly classified regarding their location, their

Figure 2.15: Picture of the OE buoy, from Ocean Energy website (oceanenergy.ie)

deployment state, as well as their structure shape. Figure 2.16 displays various types of OWC device location and shapes.

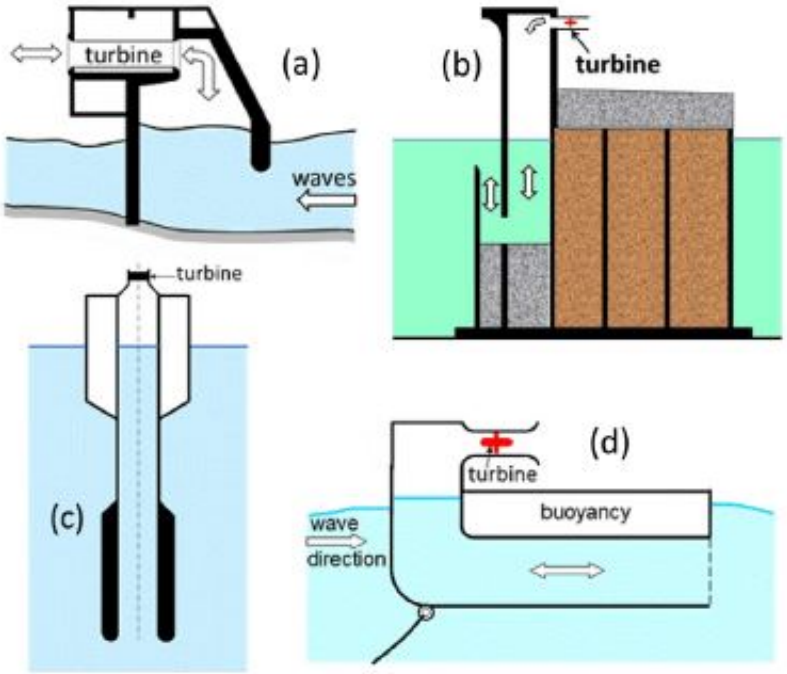


Figure 2.16: Various types of OWC wave energy converters: (a) bottom-standing for near shore; (b) Integrated into a breakwater; (c) OWC spar-buoy for near shore of offshore locations; (d) Backward-bent-duct-buoy (BBDB)

Nevertheless, a number of different OWC working principles exist. In this

section, OWC devices are distinguished based on their operational concept: mono- and multi-chamber structure; the type of turbine used; the use (or not) of non-return valves; the nature of the air flow (closed or open).

#### 2.2.2.1 Mono-chamber OWCs

Mono-chamber OWC devices are single stand-alone OWC chambers. They are either equipped with a bidirectional turbine (also called self-rectifying turbine) or with a unidirectional turbine.

**OWC with self-rectifying turbine**

Most OWC devices developed so far are equipped with self-rectifying turbines located on top of the structure and the air alternately flows from the chamber to the atmosphere and back through the turbine. Two processes are distinguished: the exhalation, where the air is blown out of the chamber through the turbine due to a rise of the water column; and the inhalation, where the air is sucked from the atmosphere into the chamber through the turbine due to a fall of the water column. Figure 2.17 presents a schematic of the working principle. This is the most established type of OWC and will be referred in this thesis as "conventional OWC". The Pico plant [41], the Marmok spar buoy [44] and the OE buoy and most OWC devices cited in section 2.2.1 are conventional OWC devices.

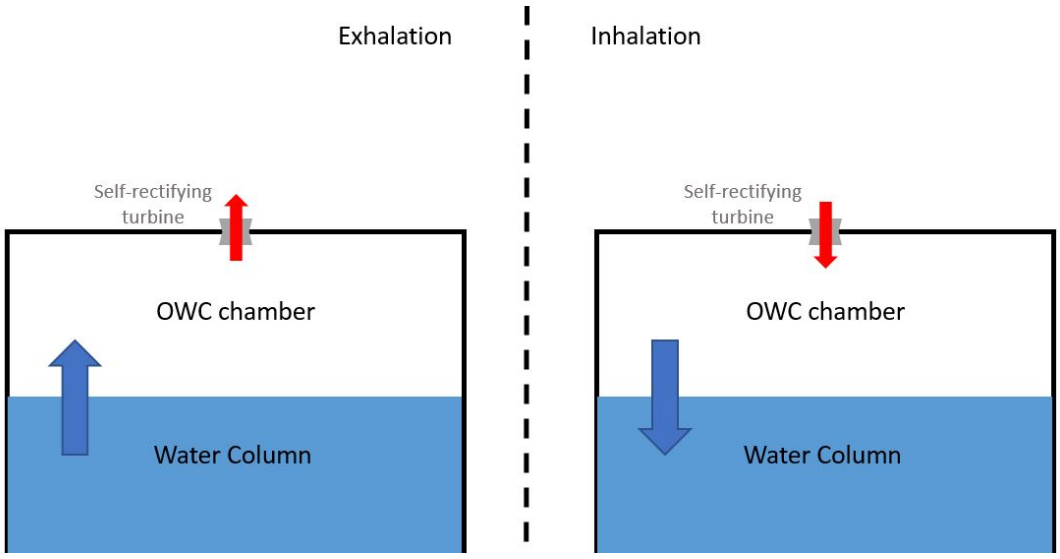


Figure 2.17: Working principle of conventional OWC device with self-rectifying turbine

Figure 2.18 displays another kind of OWC device using a self-rectifying turbine. Here, the device is a hollow structure that contains air and water. The structure is split in two chambers and the water can flow between the

two chambers through a large opening in the bottom of the wall. The chambers also connect in the dry area by a self-rectifying turbine which allows air to flow from one chamber to the other. The WEC structure is designed to pitch and surge with the waves which causes the water to flow from one chamber to the other and forces the air to flow across the turbine. The SEWEC wave energy device uses this principle [46]. Having the air turbine protected from the corrosive and mechanical effects of sea water is cited as an advantage of this type of OWC.

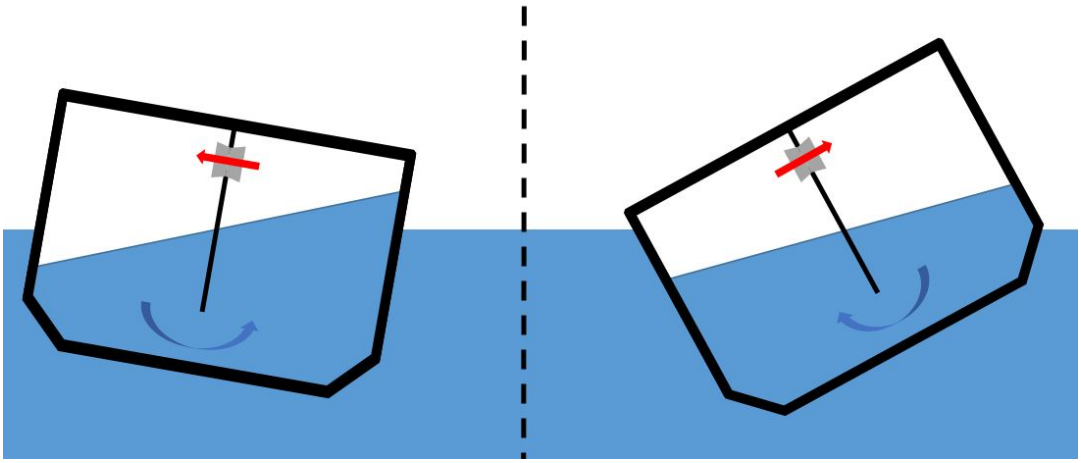

Figure 2.18: Working principle of enclosed OWC with self-rectifying turbine

**OWC with unidirectional turbine**

A number of OWC working principles use unidirectional turbines, which reach higher efficiencies than the self-rectifying turbines. When air flows across a unidirectional turbine in the direction the turbine was designed for, it is said that the turbine works in direct mode. Alternatively, when the air flows in the opposite direction across the turbine, the turbine works in reverse mode.

In the twin-turbine concept, see figure 2.19, the OWC chamber is connected to the atmosphere via two unidirectional turbines oriented in opposite directions: One is oriented from the OWc chamber to the atmosphere and the other from the atmosphere to the OWC chamber. The two turbines can be coupled to a common electrical generator or, alternately, each turbine is coupled to its own generator. In this arrangement, for a given excess pressure in the OWC chamber (either positive or negative), most of the air flows across the turbine in direct mode while a smaller part of the air flows across the other turbine in reverse mode. The issue with such a working principle is this part of the flow across the turbine in reverse mode is not harnessed and even produces a negative torque which reduces the system efficiency. When axial turbines are used, about one third of the flow crosses the turbine is re-

verse mode [47]. Radial turbines are more adapted to this working principle as they achieve higher blockage of the flow in reverse mode and hence lead to a higher system efficiency [48].

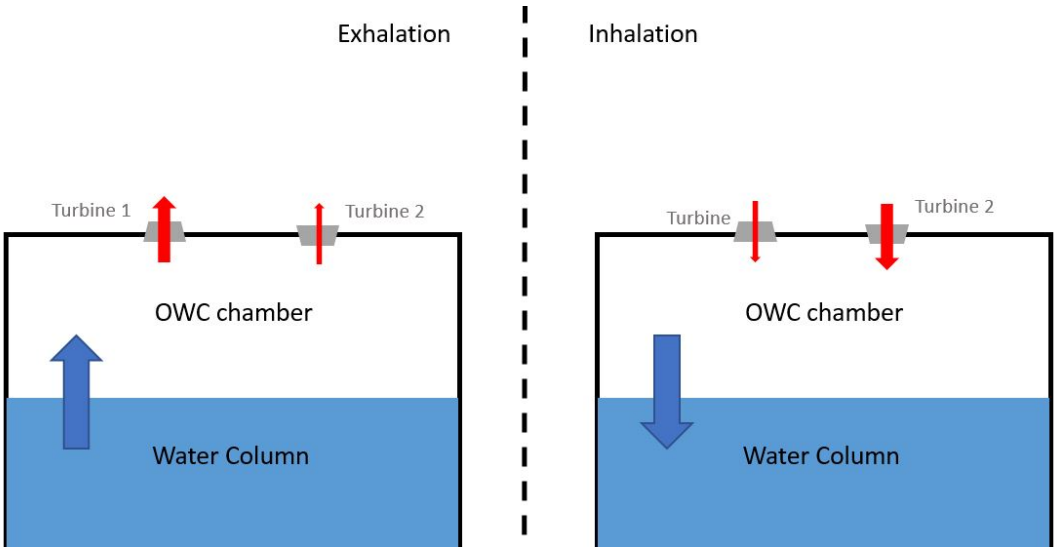


Figure 2.19: Working principle of twin-turbine OWC devices []

Apart from the twin-turbine configuration, unidirectional turbines are most commonly used in association with non-return valves. There are a number of ways to rectify the reciprocating air flow into a unidirectional flow across a unidirectional turbine using non-return valves:

- **Masuda's principle:** Figure 2.20 presents the working principle used in Masuda's navigation buoy. It has single unidirectional turbine and four valves are used to rectify the flow across the turbine. The air goes either from the atmosphere into the chamber or from the chamber into the atmosphere and always has to flow across two valves in series with the turbine.

- **Vented OWC:** Figure 2.21 displays the working principle of the vented OWC device. The OWC chamber is connected to the atmosphere via a unidirectional turbine and a non-return valve, oriented in opposite direction. As represented in figure 2.21, the air flow across the turbine in direct mode during exhalation and across the valve during inhalation. During the inhalation process, the turbine is subject to a reverse pressure head and, similarly as in the twin-turbine configuration, part of the flow may cross the turbine in reverse mode and create negative torque. It is also possible to swap the orientation of the turbine and the valve and have the turbine working in inhalation. This later orientation was chosen by the Australian company Wave Swell Energy for its vented OWC device, currently under development [49].

- **Double turbine:** Figure 2.22 shows a working principle involving two unidirectional turbines and two valves. Each turbine is associated with a valve in series. The two turbine-valve sets are oriented in opposite directions and connect the OWC chamber to the atmosphere. The two turbines can be coupled to a common electrical generator or, alternately, each turbine is coupled to its own generator. This working principle is currently being studied commercially but no official information was released.

- **Tupperwave:** Figure 2.23 displays the Tupperwave working principle which rectifies the air flow in a closed-circuit. The OWC chamber is connected to two accumulator chambers via non-return valves. When the water level rises in the OWC chamber, a high-pressure is built in the high-pressure chamber (HP chamber). This process is called exhalation by analogy to the other principles, even though the air is not exiting in the atmosphere. When the water level falls, a low pressure in built in the low-pressure chamber (LP chamber). This process corresponds to the inhalation. The resulting pressure difference between the HP and LP chamber creates a unidirectional flow across the turbine. This working principle will be studied in detail in this thesis. In section 2.3, the potential advantages presented by the Tupperwave concept against the other concepts will be discussed.

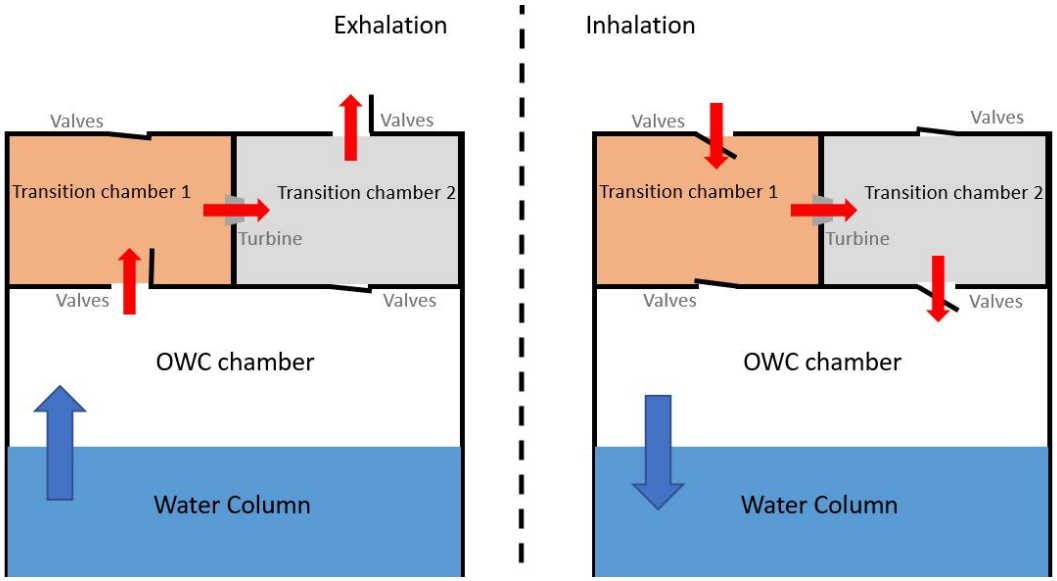


Figure 2.20: Working principle of Masuda's navigation buoy

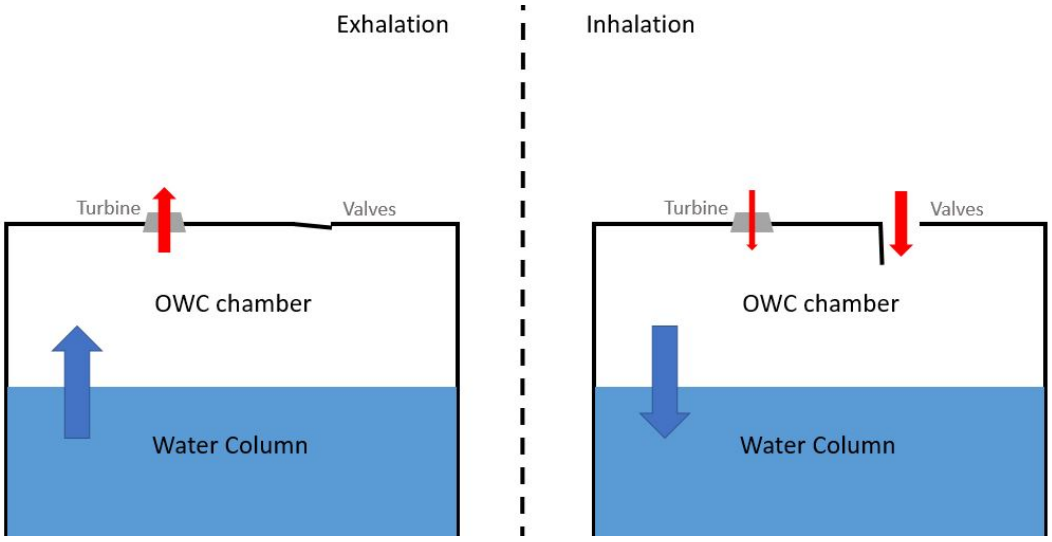


Figure 2.21: Working principle of the vented OWC

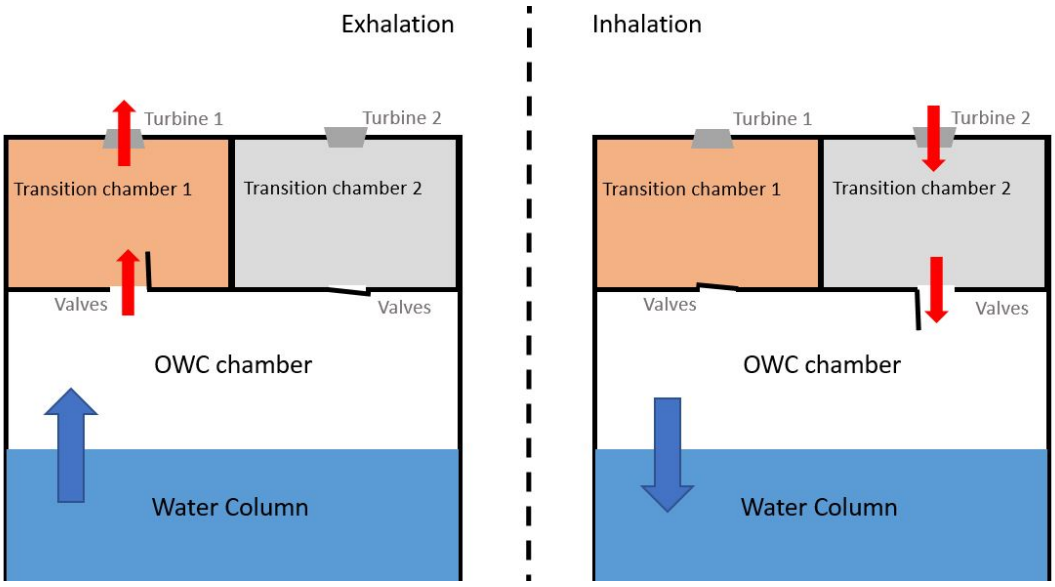


Figure 2.22: Working principle of OWC device using two sets of unidirectional turbine and valves

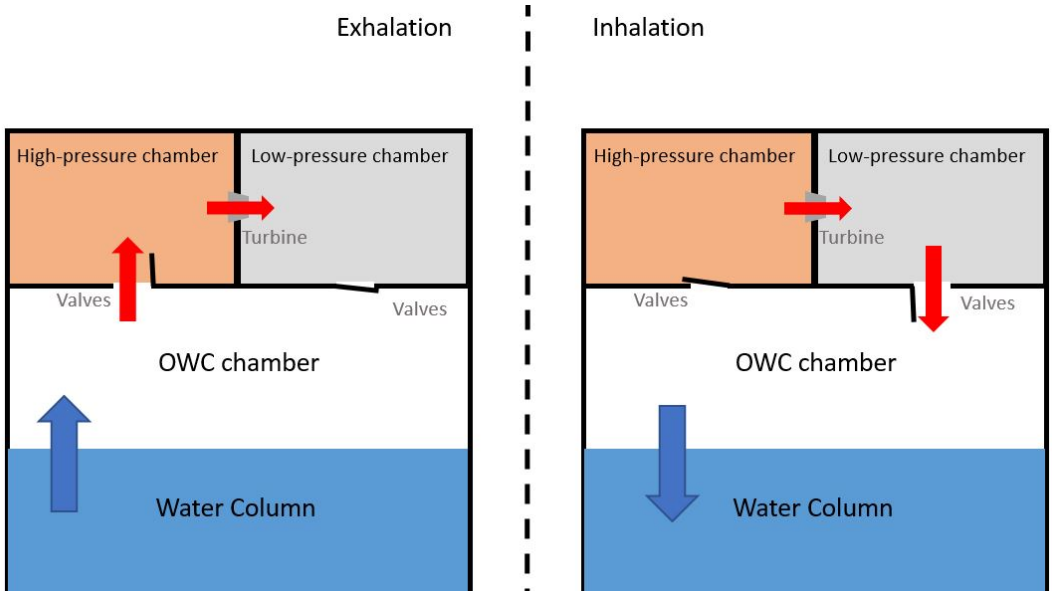


Figure 2.23: Working principle of the Tupperwave device

Finally, figure 2.24 gives a classification of the mono-chamber OWC principles.

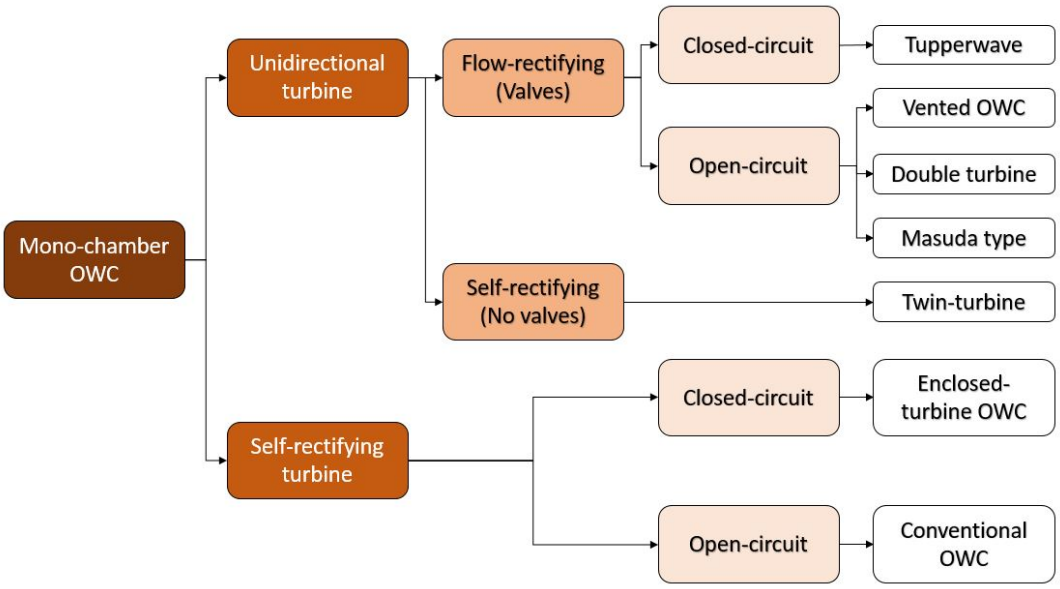


Figure 2.24: Classification of mono-chamber OWC concepts based on type of turbine used

Historically, non-return valves were regarded as unpractical for large scale devices after the experience of the Kaimei. The large size of the valves was incompatible with the fast opening and closing required, in the order of the second. Therefore, mono-chamber OWC devices using non-return valves (flow-rectifying OWCs) are not extensively studied in the literature [9].

#### 2.2.2.2 Multi-chamber OWCs

Multi-chamber OWCs are an arrangement of OWC systems gathered in a single structure, which can either be fixed or floating. They can be divided in three main categories of operational concepts [50]:

- **OWC array:** The structure is divided into many OWC chambers each one with its own turbine-generator. Any OWC concept presented in the previous section can be applied in each chamber. As an example, the Mutriku power plant [38] is an OWC array, included into a breakwater.
- **Segmented OWC:** Every chamber has its own turbine and all turbine are coupled to a single generator. Since the mechanical outputs of the turbines are offset, their combination is relatively continuous. The objective of such concept is to reduce the cost of electrical material and to smoothen the electrical power output. As an example, figure 2.25 presents the working principle of a two-chamber segmented OWC studied in [51].

- **Modular OWC:** All chambers cooperate to produce a unidirectional airflow through a single unidirectional turbine and generator system with the use of non-return valves. The objective is to reduce both turbine and generator costs as well as smoothing the flow across the turbine. Most modular OWCs work in close-circuit with a similar principle to the Tupperwave concept: all chambers are connected to a high- and a low-pressure ducts via non-return valves and all chambers participate to build a differential of pressure in the HP and LP ducts. The unidirectional turbine is connecting the two ducts. The Seabreath [52], LEANCON [53] and ShoreSWEC [54] all use this working principle. Figure 2.26 displays a schematic of the Seabreath device.

  Another unique modular OWC concept is the Waves2Watts converter, see figure 2.27. The device is being studied in Lancaster University, UK [55]. In this device, the chambers are arranged in series along the length of the structure in the direction of wave propagation. The wave excitation cause the water column inside the separate chambers to rise and fall individually. Unidirectional air valves mean that chambers are pneumatically coupled to allow airflow in the same direction the propagation wave. This is an open system as the air is drawn from the atmosphere and returns to the atmosphere. The intention of the Waves2Watts WEC is to build a high-pressure differential with respect to atmospheric pressure with the multi-stage compression process.

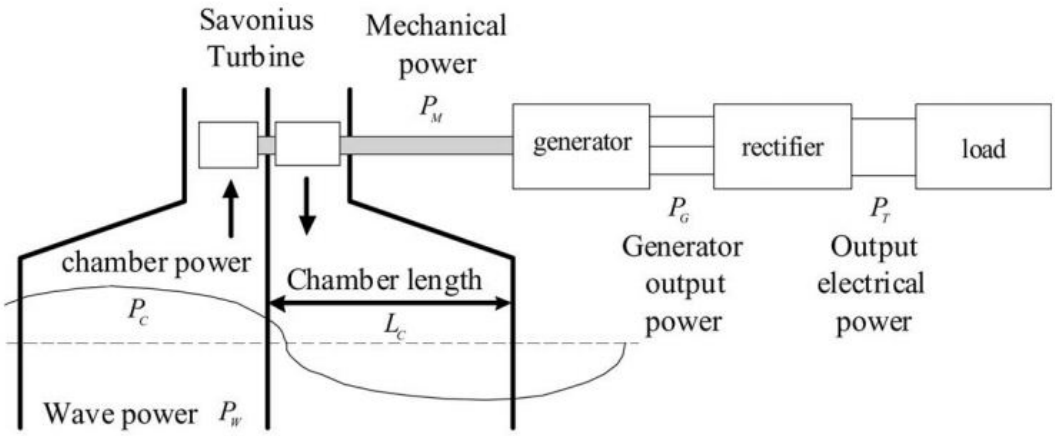


Figure 2.25: Schematic of two-chamber segmented OWC studied in [51]

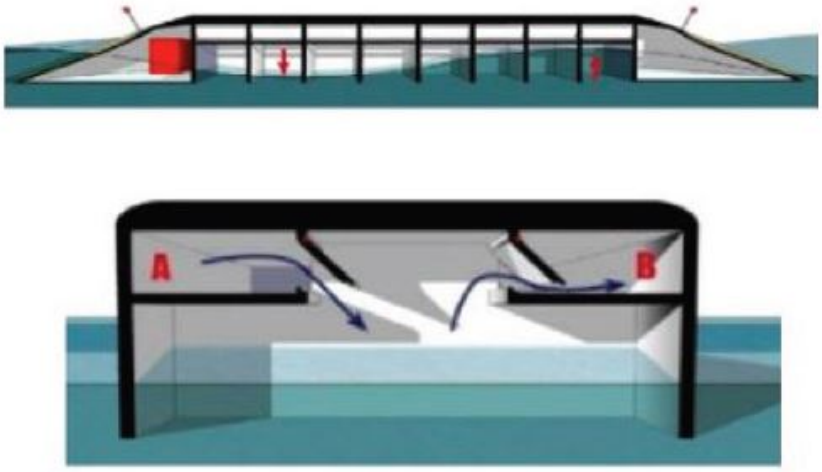


Figure 2.26: Schematic of two-chamber segmented OWC studied in [51]

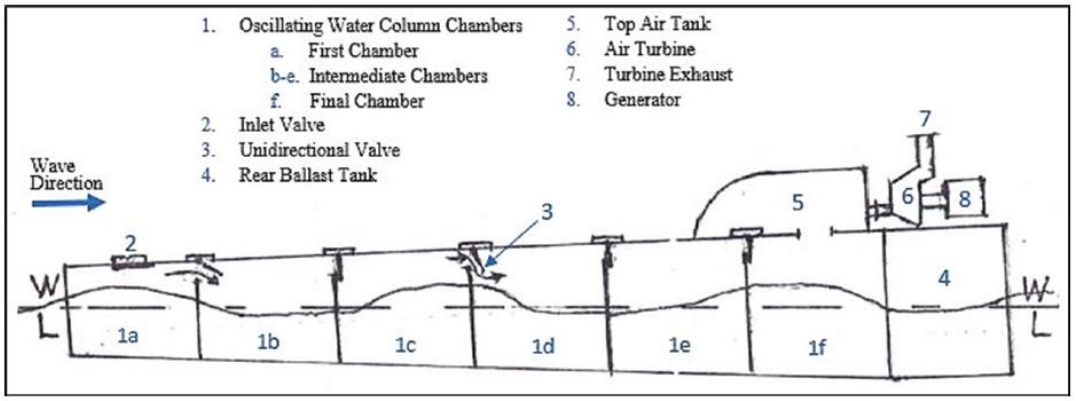


Figure 2.27: Annotated original design sketch of the W2W concept [56]

### 2.2.3 Air turbines

Single stage conventional turbines can be used to equip flow-rectifying OWCs as seen in section 2.2.2.1. These turbines were thoroughly developed for steam and gas turbines and are known to attain high efficiencies, up to 90%, in unidirectional flows. However most flow-rectifying OWCs require large non-return valves that have been regarded as unpractical in large plants, where flow rates may be of the order of $10^2 m^3.s^{-1}$ and the required response time is typically less than one second [9]. Surprisingly, very little or no research on non-return valves for OWC devices was carried out.

Research focused on the development of bidirectional or self-rectifying turbines which can keep the same direction of rotation regardless of the generated bidirectional airflow. Most OWC prototypes tested so far have been equipped with self-rectifying air turbines. A extensive review on such turbines can be found in [57].

The first self-rectifying turbine was the Wells turbine invented in 1976. The blades of the Wells turbines are shaped as aerofoils of symmetrical cross section. Several variants of the Wells turbine have studied: with or without guide vanes, single or multi-stages, etc. Figure 2.28 displays rotor geometries for Wells turbines. Peak efficiencies up to about 0.75 were found to be attainable in model testing of some Wells turbines, but their efficiency drops very sharply for high pressure head because of aerodynamic stalling that takes place at excessive angle of incidence.

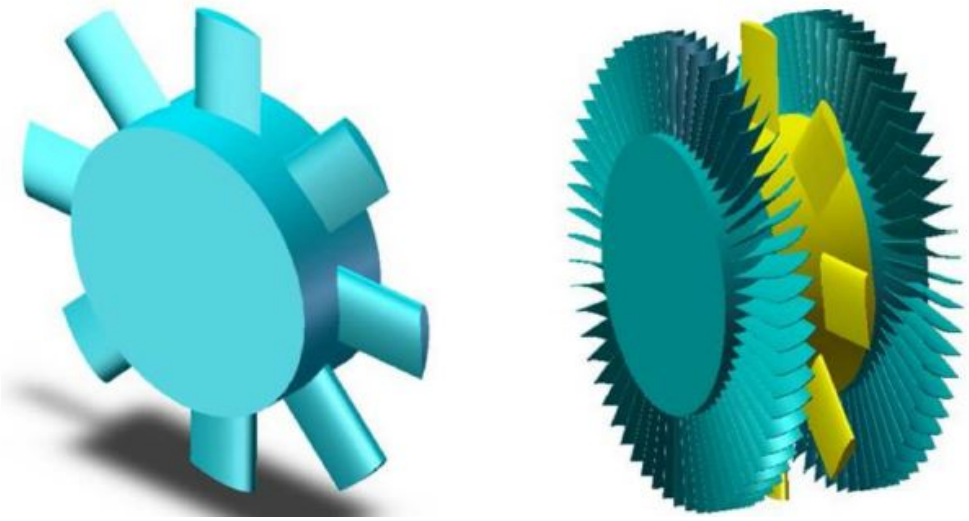

Figure 2.28: Wells turbines. Monoplane without (left) and (with) guide vanes [57]

The most popular alternative to the Wells turbine is the self-rectifying impulse turbine invented in 1975. Its rotor is basically identical to the rotor of a conventional single-stage steam turbine of axial-flow impulse type, but since the turbine flow is required to be bidirectional, there are two rows of guide vanes placed symmetrically on both sides of the rotor, instead of a single row. Like for the Wells turbine, the guide-vanes and the rotor are symmetrical relatively to the rotors plane. Figure 2.29 displays the rotor and guive-vane geometry for an axial impulse turbine. The efficiency curve of such turbines does not experience stall effects. However, the presence of guide vanes downstream of the rotor of an impulse turbine may introduce severe aerodynamic losses. As a result, the peak efficiency of an impulse is less than that of the Wells turbine and is about 44%. Variations such as pitching guide-vanes to avoid losses in the downstream guide-vanes were studied and showed to improve the turbine efficiency up to 59% [58].

In order to overcome the drawbacks of the Wells and impulse turbines, other more sophisticated turbines were developed. The biradial turbine, see figure 2.30, developed by Instituto Superior Tcnico in Lisbon, is an impulse

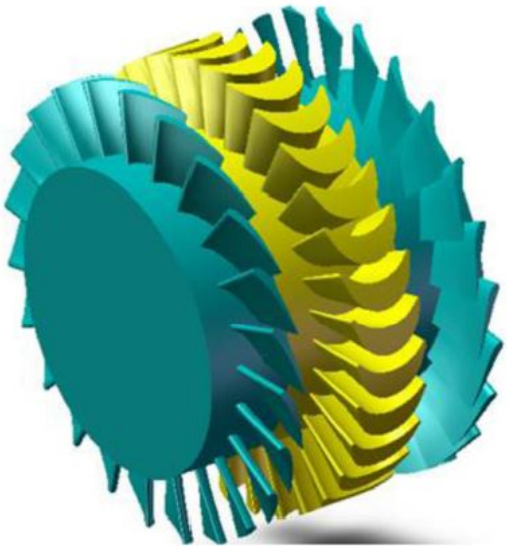

Figure 2.29: Axial-flow impulse turbine [57]

turbine for bidirectional flows that is symmetrical with respect to a plane perpendicular to its axis of rotation. The entrance of fluid into the rotor through any of the two axially offset apertures is centripetal, and the exit flow is centrifugal. The rotor is surrounded by a pair of radial-flow guide-vane rows, each row being connected to the corresponding rotor opening by a duct whose walls are flat discs. As for the axial-flow self-rectifying impulse turbine, the guide-vanes downstream of the rotor introduce aerodynamic losses. As a way of reducing such losses, the guide vanes are radially offset from the rotor. Another way is to install a mechanism to quickly remove and insert the guide-vanes from the flow path, so that the downstream guide vanes are prevented from obstructing the flow coming out of the rotor [59]. This mechanism is relatively sophisticated as the guide-vanes need to be instantaneously removed/inserted every 3 to 6 seconds. The particular geometry of the biradial turbine makes the mechanism feasible because only a short linear displacement of the guide-vane along the turbine axis is necessary. The axial translational motion of the guide vane set can be produced by hydraulic, pneumatic, electrical or other action. Model testing of this turbine revealed a peak efficiency of 79% in constant flow conditions, which is the highest efficiency obtained with a self-rectifying turbine so far. The turbine was recently tested on the Mutriku power plant within the OPERA project and is currently being tested on the Marmok buoy.

The twin-rotor turbine is another turbine also currently developed by Instituto Superior Técnico. The turbine associates a pair of conventional radial-inflow rotors mounted on the same shaft, mounted in opposite direction, and axially offset from each other. Each rotor is complemented by the corresponding guide vane rows at its inlet, similar to a conventional unidirectional turbine. Innovative curved-duct manifolds separate the two rotors and en-

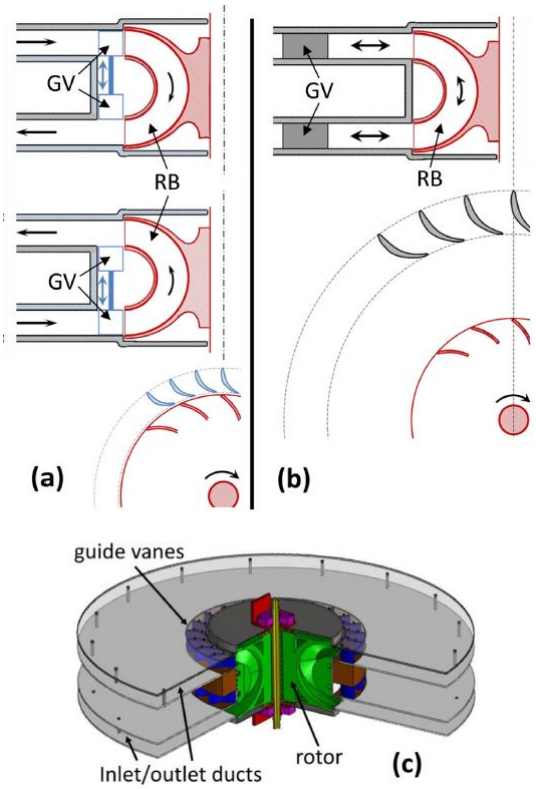


Figure 2.30: Biradial impulse turbine: (a) version 2, with axially-sliding guide vanes; (b) version 1, with radially-offset fixed guide vanes; (c) perspective view of version 2. GV guide vanes, RB rotor blades [57]

able the installation of a two-position axially-sliding cylindrical valve that is operated, for a given direction of flow, to orientate the flow only through the rotor in direct mode and prevent air from flowing in the other rotor in reverse mode. The passive rotor (the one with no flow) absorbs a part of the twin-rotor produced energy (windage loss) which may be significant. Figure 2.31 displays a schematic of the twin-rotor turbine. Model testing of this turbine revealed a peak efficiency of 73.9% in constant flow conditions [60]. Without the losses in the passive rotor, the turbine would reach 86.6%.

The valve can also obstruct the entrance to both rotors and be used to apply latching control on the OWC plant. Latching is known to be an effective way of substantially increasing the amount of energy absorbed from the waves by oscillating body devices and many developers attempt to implement this control with their turbine. Figure 2.32 describes the three positions that the valve can take in the manifolds.

Originally, self-rectifying turbines were invented to prevent the use of non-return valves which can introduce maintenance or reliability issues. In the biradial and twin-rotor turbine, the axially sliding guide-vane or valve mechanisms can introduce similar issues but are less critical due to the relatively small size and stroke of the guide-vanes/valves.

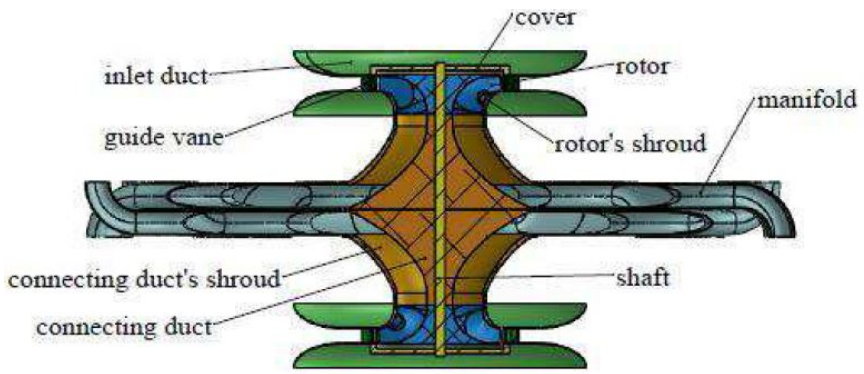


Figure 2.31: Three-position axially-sliding valve in the twin-rotor turbine [60]

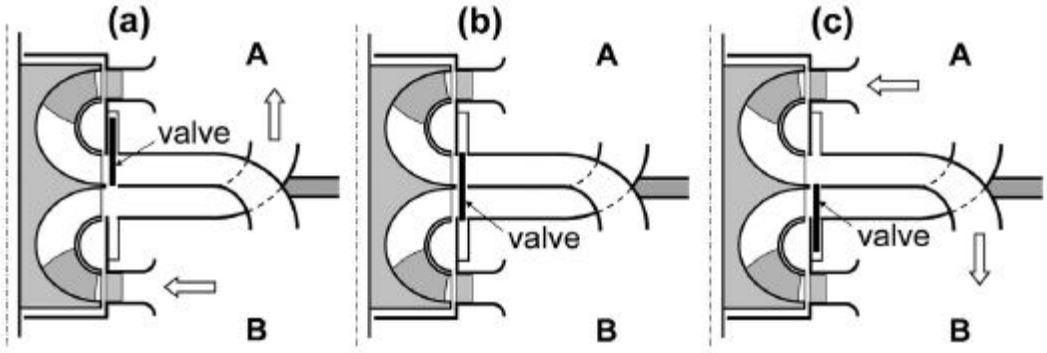


Figure 2.32: Three-position axially-sliding valve in the twin-rotor turbine [57]

Although bidirectional turbines are mostly tested at model scale in constant and unidirectional flow conditions, the flow in real-sea conditions is highly fluctuating and changes direction every half wave period. In those conditions, the average turbine efficiency is lower than the maximum efficiency established in model testing. It is possible to estimate the average efficiency of an OWC turbine under irregular sea wave conditions using a stochastic approach in which the pressure oscillations in the OWC air chamber are assumed to be a random Gaussian process [61, 60]. The other possibility is to build a time domain model of the OWC device. In real-sea conditions, the average efficiency of a bidirectional turbine is 5 to 10% lower than its maximum efficiency.

The aerodynamic noise produced by a turbine may be a serious issue for the public acceptance of OWC devices, especially near inhabited areas, as is the case of some shoreline plants or OWCs integrated into harbour breakwaters. Noise levels increase with machine size and especially with flow velocity and rotor blade speed. Studies showed that the Wells turbine is particularly noisy, especially under stalled condition. Impulse turbines are slightly better in that sense [62, 63]. Turbines in closed-circuit OWC devices are not

open to the atmosphere, see section 2.2.2 (enclosed OWC and Tupperwave), and are expected to produce less noise.

### 2.2.4 Numerical modelling of OWCs

The numerical modelling of OWC devices involves the modelling of different phenomenon: the device hydrodynamic response to the passing waves, the thermodynamic response of the plenum chamber(s) of the OWC device, which convert the absorbed wave energy to pneumatic energy, the behaviour of the turbine, which converts the pneumatic energy to mechanical energy, and the controller and generator system, which converts the mechanical energy to the electrical energy. The relative motion of the internal water column with the structure generates pressure changes in the OWC chamber. The evolution of the pressure is governed by thermodynamic equations and also by the behaviour of the turbine-generator system which enables an air flow in reaction to the pressure change. All phenomena are therefore coupled and need to be modelled inter-dependently.

#### 2.2.4.1 Hydrodynamics

There are two main methodologies to model the hydrodynamics of an OWC device [9]:

- **The uniform pressure distribution approach:** This approach is based on the decomposition of the flow rate of air displaced by the internal water column $q$ into the sum of the radiation flow rate $q_r$ due to the oscillating pressure $p$ in the chamber in the absence of incident waves distribution, and the excitation flow rate $q_e$ due to the incident wave field if $p = 0$. This decomposition resembles the decomposition of the wave-structure interactions from the linear wave theory. This approach is realistic because no assumption is made on the interior free surface, which, in reality is generally warped. This method was for example implemented in [64, 65].

- **The rigid-piston approach:** Here, the internal water surface of the OWC is assumed as a thin piston-like rigid body. The adoption of the rigid piston model is a way of taking advantage of the linear wave theory and the boundary element method developed to describe the interaction between waves and rigid floating bodies, see section 2.1.3.2. For this reason, the rigid-piston approach is very popular in OWC numerical modelling. With this method, the modelling of a floating OWC becomes a two-body problem: the floating structure and the rigid-piston which oscillate relatively to each other.

Figure 2.33 presents illustrates the two different approaches described. In this thesis, the rigid-piston approach will be adopted and described in the papers introduced in chapter 3 and attached in Appendix.

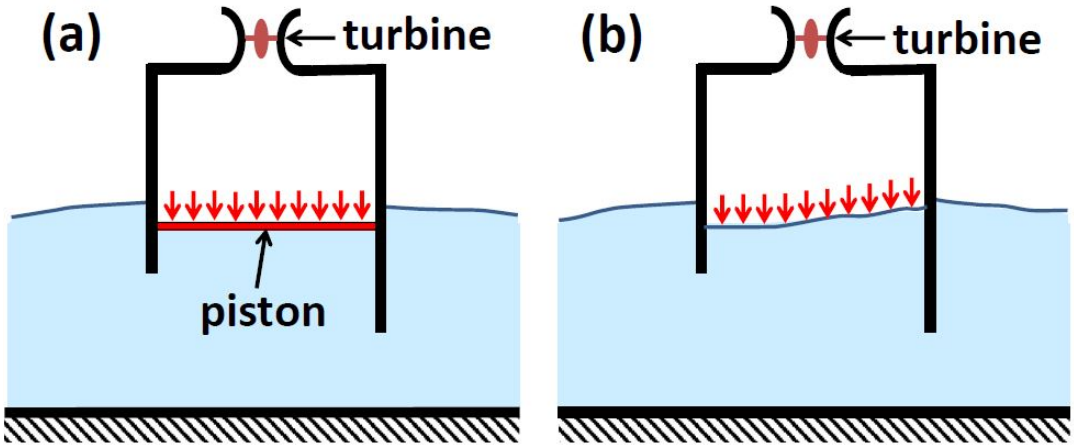


Figure 2.33: Schematic representation of OWC modelling: (a) piston model; (b) free-surface uniform pressure model [9]

#### 2.2.4.2 Thermodynamics

The volume of the OWC chamber is generally large enough to avoid ingestion of water by the air turbine or valves in rough sea conditions. In the case of fixed structure, tidal effects also need to be taken into account for the choice of the chamber's height which can be 3 to 10 meters. The quick volume variation of the large OWC chamber due to the internal water surface rise/fall cause a temporary compression or expansion of the air. This is called the spring-like effect of air compressibility and it increases with the chamber volume. This effect plays an important role in a full-sized OWC converter. It was analysed for the first time in [66] and is since then commonly taken into account in studies on OWC devices. Neglecting the spring-like effect in the numerical or physical modelling of an OWC, i.e. assuming the air as incompressible, may lead to substantially unrealistic overvalues for the converter performance. For a perfect gas, the relationship between air pressure and density variations is given by [67]:

$$\dot{\rho} = \frac{1}{\gamma R_s T}\dot{p} - \frac{\rho}{c_p}\dot{s} \tag{2.14}$$

where $\rho$ is the air density; $\gamma$ is the air heat capacity ratio; $R_s$ is the specific gas constant; $p$ is the excess pressure in the OWC chamber relative to atmospheric conditions; $c_p$ is the heat capacity at constant pressure and $s$ is the specific entropy of the air.

When the thermodynamic processes are assumed isentropic, the specific entropy of the system remains constant and 2.14 becomes:

$$\dot{\rho} = \frac{1}{\gamma R_s T}\dot{p} \tag{2.15}$$

As in [66], the simple isentropic relationship 2.15 between air pressure and density is commonly used to model the spring-like effect of the air. The

isentropic assumption is strong and assumes that the transformations are adiabatic and reversible. The adiabatic assumption is, in most cases, reasonable because the temperature oscillations in the air chamber are relatively small and their time scales (a few seconds) are too short for significant heat exchanges to occur across the chamber walls and across the air-water interface, in comparison with the energy flux in the turbine. The reversible assumption however is only reasonable if the turbine is perfectly efficient which is impossible in real life because of friction losses which are sources of irreversibility. The complex aerodynamic and thermodynamic processes were analysed in more detail in [68] by distinguishing the inhalation and exhalation process and taking the losses of the turbine into account. If the air chamber is connected to the atmosphere through the turbine, the air is partly replaced at each inhalation, and so the specific entropy (hence, the temperature) cannot increase significantly. The conclusions of [68] show that the isentropic assumption provides very satisfactory results for the numerical modelling of conventional OWC devices, compared to the more advance non-isentropic model.

For OWC devices working in closed circuit, the potential for large temperature increase represents an issue which has discouraged many developers from taking this type of technology further. The topic of the temperature increase in closed-circuit OWC devices has not yet been considered in the literature but is studied in this thesis.

#### 2.2.4.3 Turbine

The main objective in the modelling of the turbine is to correctly represent the relationship between the flow rate across the turbine and its pressure head. This relationship depends on the turbine type, geometry, size and rotational speed. Typically, this relationship is established during model scale testing of the turbine and extended to the full-scale device for numerical modelling.

For the physical model testing of a turbine, care is generally taken that the tests results are applicable to larger scales and avoid scaling effects. The main concern is to reproduce correctly the flow characteristics which are characterised by two main dimensionless numbers: The Reynolds number and Mach number. They are the dominant similarity parameters and need to be of similar values than in the full scale conditions. The Reynolds number is physically a measure of the ratio of inertia forces to viscous forces and is generally high for turbines in real sea conditions. Model scale tests therefore need to be carried out with a high enough Reynolds number, higher than the critical Reynolds number ($\simeq 2 \times 10^5$), after which the turbine performances reach an asymptotic behaviour. The Mach number is the ratio of the flow velocity to the speed of sound. For Mach numbers higher than 0.3, the flow is compressible. For Mach number below 0.3, the assumption of incompressible flow is valid. Practically, model tests are mostly carried out

for high enough Reynolds number but rarely for Mach number higher that 0.3 due to the limited capacities of common test rigs. In most studies, Mach and Reynolds number effects are ignored and the flow through the turbine is considered as approximately incompressible. Thus, the model scale results can be applied to a geometrically similar turbine of different size, rotating at different speed and with a fluid of different density [69].

Hence, a practical way of representing the relationships between flow and pressure head is to use non-dimensional variables: the dimensionless flow coefficient $\Phi$, dimensionless pressure head $\Psi$ and dimensionless turbine power output $\Pi$ which are defined as [9]:

$$\Phi = \frac{w_t}{\rho_{in}\Omega D^3}; \quad \Psi = \frac{\Delta p_t}{\rho_{in}\Omega^2 D^2}; \quad \Pi = \frac{P_m}{\rho_{in}\Omega^3 D^5} \tag{2.16}$$

where $P_m$ is the air turbine power output, $D$ its size (rotor diameter), its rotational speed $\Omega$, its pressure head $\Delta p_t = p_{in} - p_{out}$ between inlet and outlet, $w_t$ the air mass flow rate flowing across a turbine.

Under the assumption of incompressibility, the non-dimensional pneumatic power available to the turbine is $\Phi\Psi$ and the efficiency of the turbine in converting this power into mechanical power is $\eta = \frac{\Pi}{\Phi\Psi}$. Typically, the efficiency of a turbine reaches a maximum for a given value of dimensionless flow coefficient $\Phi_{opt}$. In order to maximise the turbine efficiency, the dimensionless flow coefficient should be maintained close to $\Phi_{opt}$ by adjusting the rotational speed depending on the pneumatic energy level available to the turbine.

#### 2.2.4.4 Generator and power electronics

The highly variable energy sources of the waves suggest that the use of variable-speed generators in wave energy converters is preferable. The generator is generally connected in direct-drive to the turbine and performs the final power conversion stage and converts the mechanical power of the turbine into electricity. The generator also enables the control of the turbine to maximise its efficiency. Various turbine control strategies exists in order to track the maximum power point [70]. In general, this is achieved by controlling the torque applied by the generator on the turbine. This method is called optimal torque control and is simple, fast, and efficient.

The efficiency of the generator is maximum when it operates close to its rated power. In that case, generators usually reach efficiencies of about 95%. The efficiency however drops very sharply for partial loads and the generator rated power should be chosen carefully to maximise its efficiency over the wave climate of the site. This drop in efficiency at partial load should also be taken into account in numerical modelling [71].

Due to the frequency requirements of the grid, variable-speed generators cannot be directly connected to the grid. Therefore, power electronic con-

verters are required to adapt the frequency of the generated electric power to the frequency of the grid. The efficiency of power electronic converters is very close to unity except for very small loads [33] and their dynamics can be neglected in numerical models for outpower assessments [27].

## 2.3 Summary and motivations

This section summarizes pertinent points obtained from the literature review which show why the innovative Tupperwave OWC concept constitutes a topic of study that will enhance knowledge of wave energy extraction technologies.

OWC devices have good advantages compared to other wave energy converter technologies, mainly due to their simplicity and adaptability. There are a number of different concepts for extracting wave power with an OWC and two-main groups are opposed based on the type of turbine used: Unidirectional or self-rectifying. Conventional OWCs, equipped with a self-rectifying turbines, were extensively studied in the literature, resulting in accurate design and modelling knowledge and a number of sea trials. OWCs can be modelled numerically by modelling the different power conversion stages inter-dependently and each stage can be validated against scaled physical model tests. The thermodynamics in the OWC chamber can be described with satisfactory accuracy by using the isentropic relationship between air pressure and density, hence neglecting irreversible thermodynamic processes.

Despite recent improvements and sophisticated mechanisms, self-rectifying turbines are not as efficient as unidirectional turbines which are a well-known and simpler technology and hence likely to be cheaper. Rectifying the flow with non-return valves to use a unidirectional turbine therefore remains an interesting option.

Among the flow-rectifying OWC concepts, the innovative closed-circuit Tupperwave concept has the following advantages:

- It is equipped with only two valves and one turbine-generator system. Thus, investment costs are likely to be less than for the other concepts, except maybe the vented OWC which has only one turbine and one valve.
- The turbine is not open to the atmosphere and is likely to generate less noise.
- The device can potentially create a smooth and continuous flow across the turbine.

This last point is unique to the Tupperwave concept and constitutes its main advantage. It can allow the turbine to work at a rather steady state which can have a positive impact on its efficiency. Moreover, the electrical power

produced by the generator is likely to be smoother than for the other concepts. The reduction of electrical power fluctuations is linked with an improvement in power quality and a reduction in voltage fluctuations on the network which is a general problem with wave energy converters.

Previous developments of similar concepts were hindered by two problematic aspects, which have not been the focus of advanced academic research:

- Experience from the literature have shown that there are challenges associated with the use of large non-return valves including aerodynamic losses, time response limitations, and, operation and maintenance issues. But no specific research was carried out to overcome those challenges.

- Irreversible thermodynamic processes occurring in the closed-circuit OWC device may result in an increase in air temperature, which would represent an operational risk. But this phenomenon was neither effectively observed nor studied so far and results in a lack of understanding of closed-circuit OWCs.

Thus, the Tupperwave concept is a promising concept as it may increase wave power conversion capacities of OWC devices but has not been thoroughly studied to date. Moreover, studying this concept will address the obvious shortcomings of the current knowledge on OWC technologies.

# Chapter 3

# Investigation

As highlighted in section 2.3, the literature review has shown that there are incentives to investigate the Tupperwave concept in order to advance knowledge of OWC devices. In this chapter, the different papers, listed in section 1.3 and included in Appendix A to G, are combined together to present the research work achieved for this thesis to investigate the innovative Tupperwave OWC concept described in section 2.2.2.

The strategy to investigate the Tupperwave concept is first established in section 3.1. The work carried out according to the established strategy is then presented in section 3.2.

## 3.1 Strategy

With respect to the literature review, a clear strategy was established to investigate the relevance of Tupperwave concept.

Figure 3.1 displays the schematic of the Tupperwave working principle as it was first presented on the Tupperwave project proposal. This schematic represented the starting point of the work presented in this thesis.

The proposed overall strategy of study was the development of numerical wave-to-wire models of two OWC devices:

- one device based on the Tupperwave concept;
- one device based on the conventional OWC concept, to be used as benchmark since it is the most developed concept to date.

This numerical tool would enable to simulate the two devices in the same wave climate to compare their behaviours and performances. For a fair comparison, the two devices use the same OWC structure and state-of-art turbine technologies.

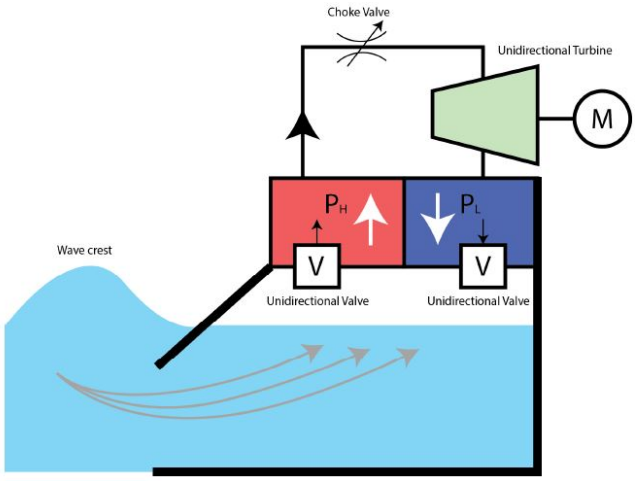


Figure 3.1: Tupperwave working principle as first presented on the project proposal

The development of the wave-to-wire numerical models is split in three stages with incremental modelling difficulty and accuracy:

- **Stage 1** describes the devices in their conversion from wave to pneumatic power. The isentropic assumption is used for the thermodynamics. Model scale testing in wave basin is used to validate this stage. The main objective is to gain understanding on the Tupperwave device behaviour and provide a base for the wave-to-wire model.
- **Stage 2.a** completes the previous work by adding the power conversion from pneumatic to electrical power, leading to a full wave-to-wire model. With this model, the overall power performance of the device can be assessed. The validation of the second part of the power conversion chain is achieved by hardware-in-the-loop simulations on an electro-mechanical rig testing.
- **Stage 2.b** enhances the wave-to-wire modelling by improving the thermodynamic modelling. A non-isentropic modelling method is developed to take into account irreversible processes and to investigate the temperature increase in the device.

Table 3.1 describes the three stages of the wave-to-wire numerical developments and their associated objectives. Figure 3.2 displays a schematic representation of the strategy.

| Stages | Thermodynamic assumption | Validation method | Objectives |
|---|---|---|---|
| (1) From wave to pneumatic power | Isentropic | Tank testing | • Validate working principle numerically and physically<br>• Gain understanding of the Tupperwave device behaviour<br>• Compare devices pneumatic power production<br>• Provide base for wave-to-wire numerical model |
| (2.a) From wave to electrical power | Isentropic | Electro-mechanical rig testing | • Complete the device modelling from wave to wire<br>• Identify critical parameters of the valves and quantify power losses<br>• Compare devices electrical power performance |
| (2.b) From wave to electrical power | Non-isentropic | - | • Assess air temperature increase in the Tupperwave device<br>• Assess relevance of the isentropic assumption relative to the non-isentropic results for the modelling of closed-circuit OWCs |

Table 3.1: Numerical model development stages for the Tupperwave device and conventional OWC with corresponding validation method and objectives

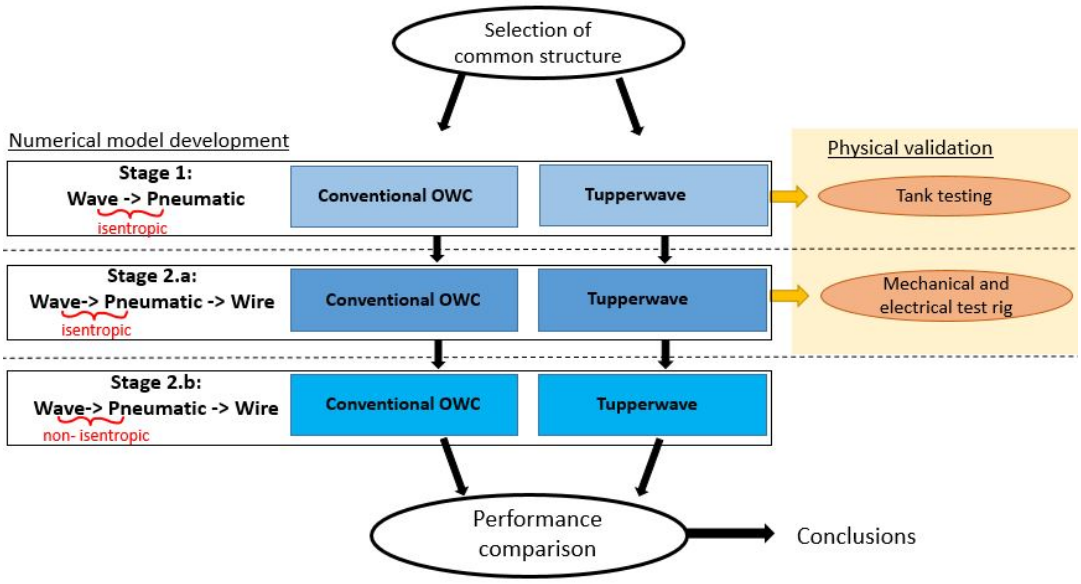


Figure 3.2: Simplified illustration of the strategy employed to study the Tupperwave device

## 3.2 Model development and validation

This section is divided in two main subsections corresponding to Stage 1 and Stage 2 of the numerical model development strategy described in section 3.1. The subsections are divided in numbered paragraphs and each paragraph is built around one paper attached in the appendix of this thesis, except paragraph 3.2.1.4 which presents unpublished material.

### 3.2.1 From wave to pneumatic power

For the first step of the concept study, the working principle was to be understood and proven. Thus, in this section, the energy conversion chain from wave power to electrical power of the device is not studied entirely, but only from wave power to pneumatic power. The rest of the power conversion chain, from pneumatic to electrical power, achieved by a unidirectional air turbine and a generator, will be considered later in section 3.2.2.

#### 3.2.1.1 Numerical model

The first objective of the work was to select a suitable type of structure to support the Tupperwave concept. A literature review on the existing Oscillating Water Column devices (OWCs) was done in order to decide which device structure was most adapted to support the Tupperwave concept. The market seems to be more open to floating OWCs rather than fixed ones. While fixed structure OWCs are only adapted for locations with either remote coast lines with strong wave resource and convenient bathymetry or breakwaters, floating structures can be installed in bigger offshore areas to form farms. The maximum water depth location is only limited by mooring and can exceed a hundred meters. Moreover, floating OWCs can achieve greater conversion from wave energy to pneumatic energy because of the relative motion of the device itself and the water column. The structure and the water column having different resonance frequencies, it is possible to tune the design so that the device is efficient on a wide range of frequency centred on the dominant wave frequency of the site. It was therefore decided to use a floating OWC design for the Tupperwave project.

A report prepared for the British Department of Trade and Industry [72] compared different types of floating OWCs for electricity generation in an Atlantic environment and considered the spar buoy to be the lowest risk and most economic option for further development. Even though the spar buoy shows a slightly lower efficiency than the buoys in unidirectional swell, the spar buoy is equally efficient in spread seas than in unidirectional seas because of its axisymmetric shape. The spar buoy also exhibits the best motion characteristics for survivability in extreme waves and was considered superior to the other two designs. The material considered for buoy construction are steel, concrete and possible a steel-concrete hybrid solution. Steel is

adapted for the construction of a prototype but concrete may be better for a multiple build scenario.

The Tupperwave concept was hence adapted to a spar buoy to carry out the study. The chosen spar buoy geometry was taken from a previous model tested in UCC during the Marinet Round Robin project, see figure 3.3. This geometry showed satisfactory stability and a peak power conversion for 8 seconds wave period at full scale equivalent [73].

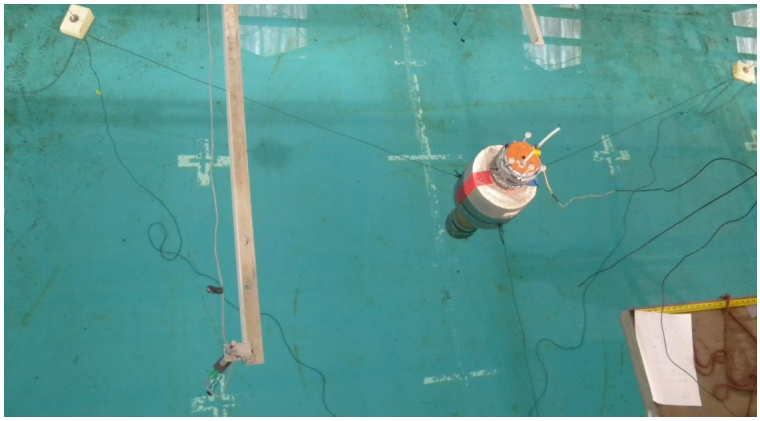

Figure 3.3: Marinet Round Robin test setup for spar buoy OWC in LIR-NOTF wave basin, 01/2015 [73]

A first numerical model of the Tupperwave device was developed in paper A to determine the primary conversion capacity of the device from wave to available pneumatic power by the turbine. The model used the potential flow theory to model the hydrodynamics. The thermodynamics was modelled considering isentropic transformations of air in the different chambers and the turbine was modelled as a simple orifice. Coupled hydrodynamic and thermodynamic equations were solved in time domain using the Ordinary Differential Equations (ODEs) solver ode45 from Matlab. The working mechanism of the device was analysed in details in regular waves and a general understanding of the concept was achieved. In parallel the corresponding conventional OWC was also modelled. The numerical model allowed the optimisation of two important design parameters of the Tupperwave device, namely the volume of the HP and LP chambers and the damping coefficient of the turbine, to maximise the wave-to-pneumatic power conversion and provide the smoothest pneumatic power.

The results of the optimisation from paper A showed that the volume of the accumulator chambers plays an important role in the pneumatic power smoothing of the device without influencing the average power production: Larger chambers enable smoother pneumatic power production. The size of the chambers is obviously limited by the available volume on the device. Floating structures are therefore particularly suited to the Tupperwave device because of the existing large volume of the float which can be used for

the accumulator chambers. This justifies the choice of a floating structure such as the Spar buoy for the Tupperwave concept. For the chosen spar buoy, the maximum possible size of the HP and LP chamber is 950m$^3$ and was used then for the remainder of the work. A range of damping coefficient for the turbine was found to maximise both pneumatic power output and minimise the power fluctuations. The same spar buoy working as a conventional OWC was also modelled. Figure 3.4 displays the conventional spar buoy OWC and the adaptation of the Tupperwave working principle to the chosen spar buoy.

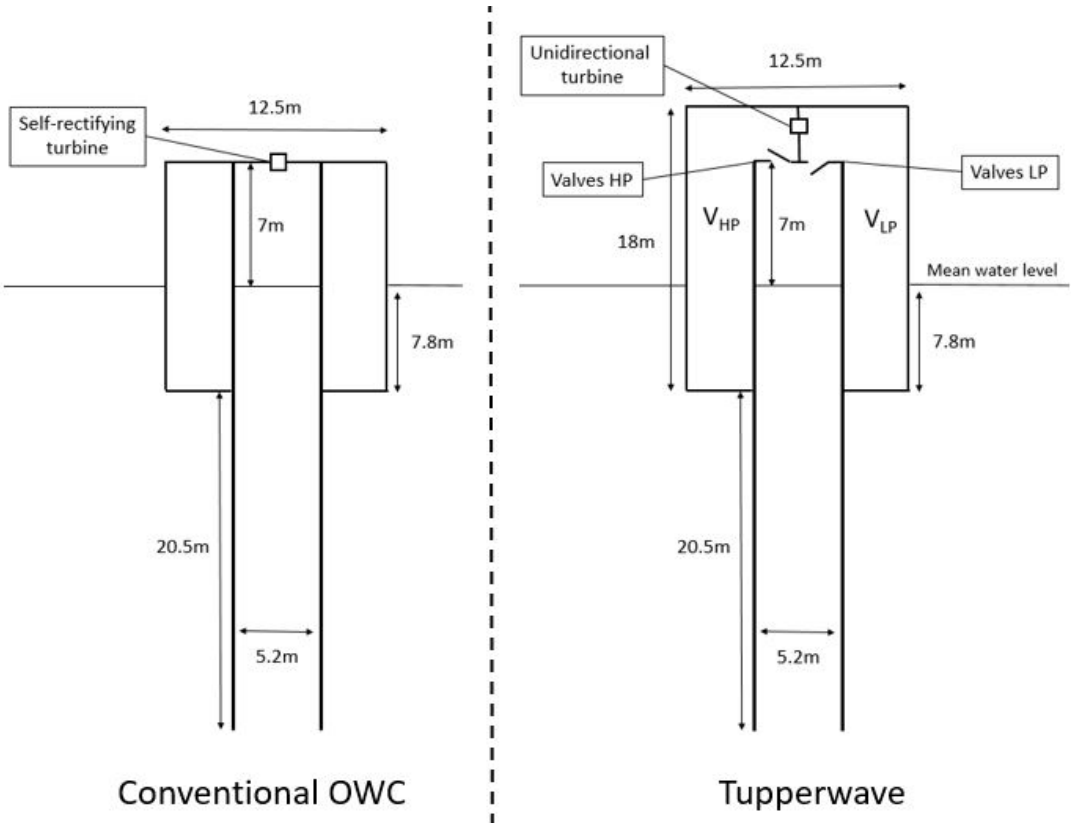


Figure 3.4: Adaptation of the Tupperwave working principle to the chosen spar buoy geometry

The results of the numerical models showed that the pneumatic power made available to the turbine in the Tupperwave device is much smoother than in the conventional OWC, as can be seen in figure 3.5.

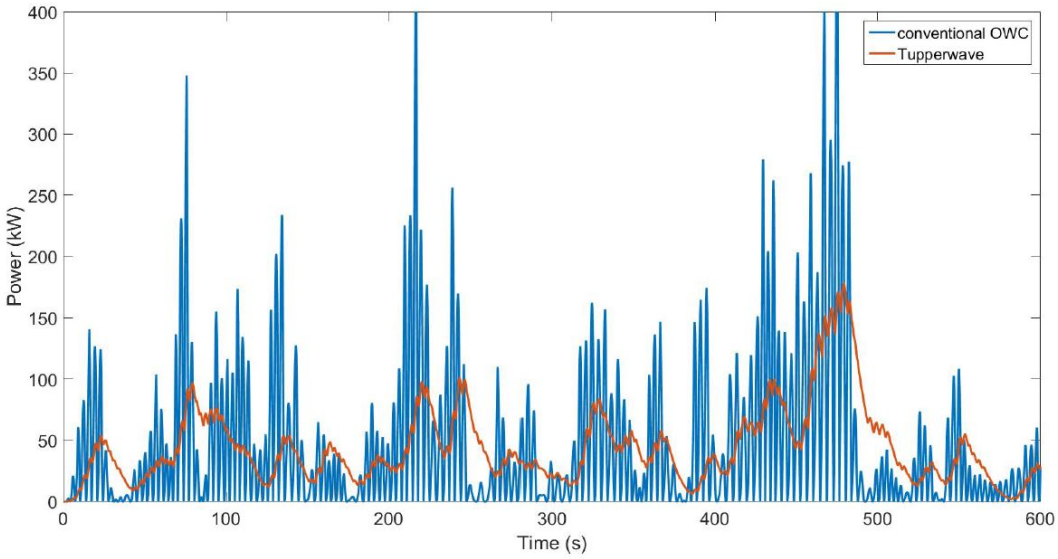


Figure 3.5: Numerical results of pneumatic power made available to the turbine in irregular waves $H_s$=2m and $T_p$=8s

#### 3.2.1.2 Tank testing

A tank testing campaign of the optimised device was then carried out at 1/24th scale, both to prove the device concept on an experimental basis, and to provide validation to the numerical model.

Paper B describes the physical model construction, experimental setup and the tank testing results. A single spar buoy was built and was used both for the Tupperwave device and for the corresponding conventional OWC. The underwater part of the device was scaled using Froude similarity law with a scaling factor $\epsilon = 0.0415 \simeq 1/24$. The air compressibility effects occurring in the HP and LP chambers of the Tupperwave device are essential for the device working principle but do not scale properly if the chambers' volumes are scaled using the Froude similarity law. It was attempted to model them by using a method suggested and applied in [74]: The volumes of the chambers were scaled by $\epsilon^2$, and not by $\epsilon^3$ as the Froude similarity law suggests. External additional fixed-volume accumulator chambers were connected to the device with flexible pipes to obtained the required volumes for the HP and LP chambers. Figure 3.6 displays a schematic of the two model scale devices tested.

The tank testing campaign physically demonstrated the significant pneumatic power smoothing potential of the Tupperwave device. The power performances of both models were compared both in terms of average pneumatic power and quality (or smoothness). The results showed that the Tupperwave device absorbs slightly less power from the waves as compared to the conventional OWC. Moreover the valves lead to important pneumatic power losses and dissipated up to 50% of the absorbed wave power. This re-

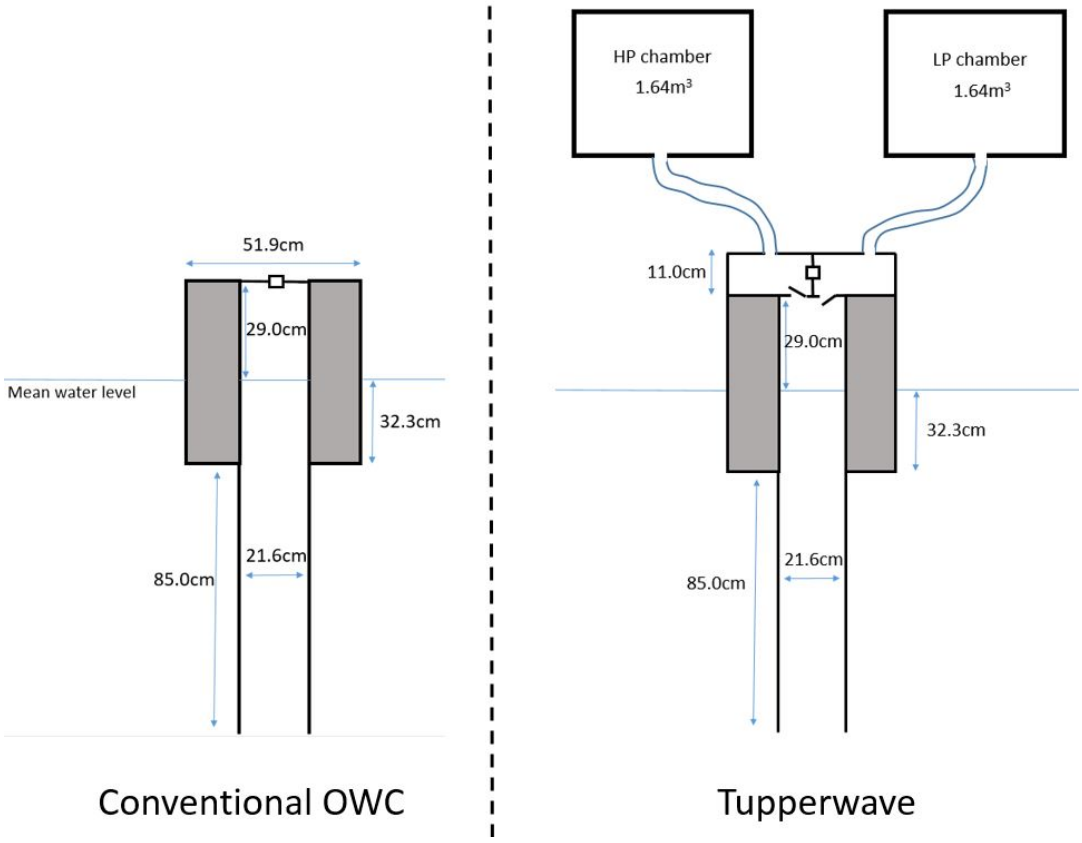


Figure 3.6: Schematic of the model scale conventional OWC and Tupperwave devices

sulted in a lower average pneumatic power production by the Tupperwave device. The Tupperwave device produced in average only about 30 to 40% of the available pneumatic power produced by the conventional OWC device. Figure 3.7 compares the pneumatic power made available to the turbine in the physical models in irregular waves equivalent to a sea state of $H_s$=3m and $T_p$=10.6s.

The valves used in the Tupperwave device were passive valves, opening mechanically when a certain pressure threshold is reached. The experiment revealed that the valves may not always open fully above this threshold. As a consequence, the level of opening and hence the damping of passive valves vary with the pressures reached in each experiment, i.e. with the device excitation from the waves. Larger valves damping were obtained when the device was far from resonance (low wave excitation), resulting is very significant pneumatic power losses and hence reducing the range of wave frequencies were the device is efficient. The experiment showed the importance of the valve design to maximise power conversion.

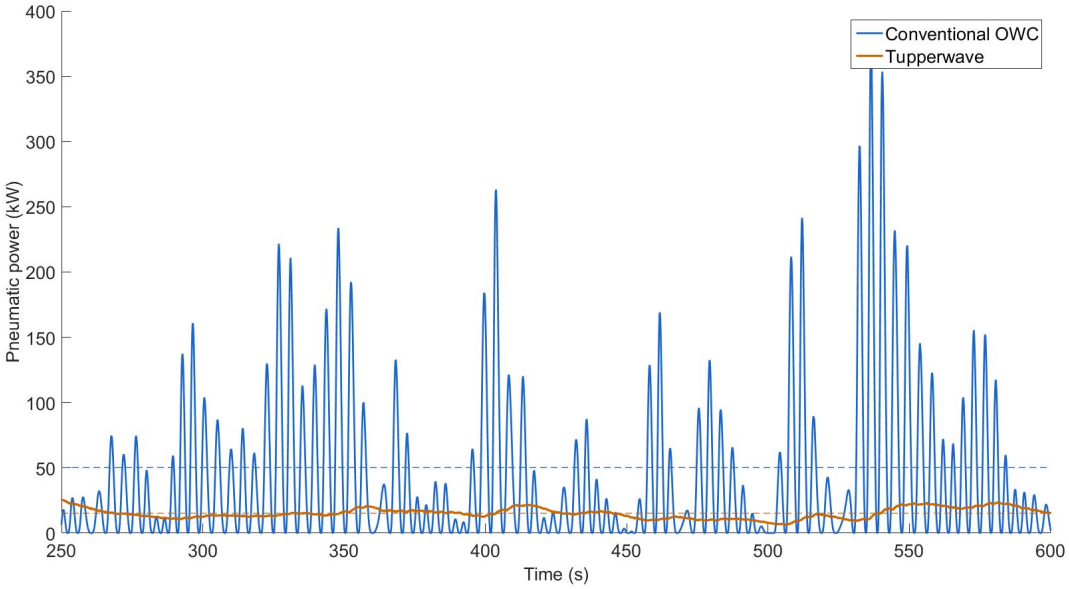


Figure 3.7: Physical results, at full scale equivalent, of pneumatic power made available to the turbine in irregular waves $H_s$=3m and $T_p$=10.6s. Solid lines: Time-series; Dash lines: Average values.

#### 3.2.1.3 Numerical model validation

Paper C compares the tank testing results to the numerical models. For the conventional OWC, good agreement is obtained between numerical and physical results. For the Tupperwave device, good agreement is initially obtained on the hydrodynamic part (buoy and IWS heave motion) but not on the thermodynamic aspects (pressures in the chambers). The comparison revealed that physical model was oversmoothing the pneumatic power available to the turbine relative to the numerical predictions. The reason for that was the unexpected deformation of the HP and LP chambers of the physical model under their excess pressure relative to the atmosphere which caused additional pressure smoothing effects. As a consequence, the air compressibility effects in the chambers were not represented as initially intended. It was not possible to fix the chambers in the time frame and budget of the physical testing campaign, so the numerical model was corrected to take into account the chambers deformation. Once corrected, the numerical results were in good agreement with the physical results which validated the numerical model. Figure 3.8 compares the time series of the pressure drop across the orifice of the Tupperwave device in the irregular sea state $\{H_s$=3m; $T_p$=8.485s$\}$ obtained by the physical model, the initial numerical model, and the corrected model. Although unintentional, the fact that the HP and LP chambers of the physical model deformed under pressure lead to better pneumatic power smoothing which is highly desirable. This observation lead to innovative ideas described in paragraph 3.2.1.5.

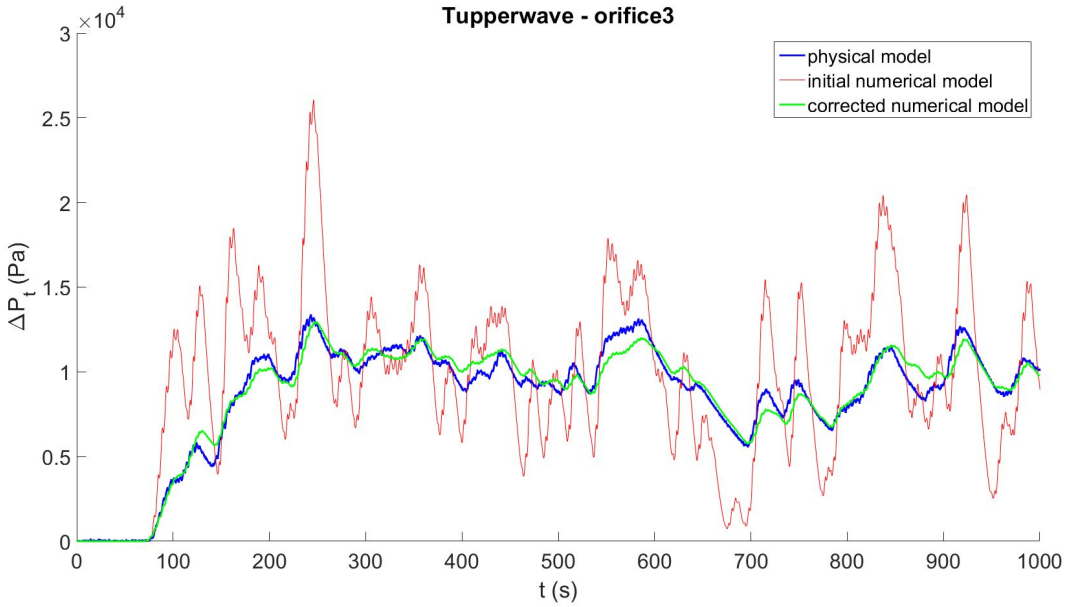


Figure 3.8: Pressure drop time series across orifice 3 of the Tupperwave device obtained by the physical model, the initial numerical model, and the corrected model in the irregular sea state {Hs=3m; Tp=8.5s}

We note that the lower pneumatic power production by the Tupperwave device observed in tank testing does not necessarily imply a lower electrical power production. The remainder of the power conversion chain from pneumatic power to electrical power provided to the grid has not been considered so far. It is likely that the Tupperwave device shows a better conversion efficiency than the conventional OWC in the second part of the conversion chain since it is equipped with a unidirectional turbine of higher efficiency than the self-rectifying turbine of the conventional OWC. To find out if the gain in turbine efficiency due to the use of a unidirectional turbine is sufficient to, at least, make-up for the pneumatic power losses by the valves, it was necessary to complete the numerical models to integrate all power conversion stages from wave power to electrical power produced. This is described in section 3.2.2.

Within the frame of the Tupperwave project, the Tupperwave device was also modelled numerically using Computational Fluid Dynamics (CFD) by the company CADFEM Ireland. The device was modelled in 3D using the software package ANSYS CFX V19.1. Difficulties in modelling the complete floating device were encountered and the outcome of the CFD study were very limited. The device was only modelled at a fixed position in the waves (not freely floating) and a single simulation was ran fully: The device was simulated in 2m high waves with 8 second period. Nevertheless, the CFD results were used to provide more validation to the numerical model described

in papers A and C. In total, in the frame of the Tupperwave project, three different modelling approaches were implemented to model the Tupperwave device:

- numerically using potential flow theory (paper A and C);
- numerically using CFD;
- physically at 1/24th scale in wave basin (paper B).

These approaches are summarized and compared in paper D. The CFD approach is the most advanced numerical method and should enable detailed modelling of the device including non-linear and viscous effects neglected in the potential flow model. But the limited outcome did not make the most of the method's potential. Nevertheless, the CFD simulation results provided an additional validation to the potential flow model. Among the three approaches, the numerical model using potential flow theory reveals to be the most efficient and most adapted to run parametric studies.

Based on both physical and numerical results, Paper D also investigates the capacity of the device to convert the absorbed wave power into available pneumatic power. The efficiency of the valves was analysed in regular waves and a formula to approximate their average efficiency was derived. The formula showed that the pneumatic damping of the valves should be small compared to the pneumatic damping of the turbine, and that the opening pressure of the valves should also be small compared to the average pressure head across the turbine.

#### 3.2.1.4 CFD investigation on the valves

The experience of the non-return valves gained during the tank testing is valuable as it showed that the pneumatic losses across the valves can have a very detrimental impact on the Tupperwave power production. This experience is however not representative of what is achievable with well designed valves at full scale. CFD represent a particularly useful tool to study the flow through the valves. The valves in the CFD model carried out by CADFEM, presented in the previous paragraph, were round orifices of 1.8m diameter. Two orifices connected the OWC chamber to the HP chamber and two orifices connected the LP chamber to the HP chamber. The opening pressure of the valves was set to 0 Pa. With such valves, the pneumatic power losses in the valves were only of 5%, meaning that 95% of the absorbed wave power was effectively made available to the turbine. This is a promising result as it is much better than the 50% pneumatic power losses obtained during the tank testing. However, the valves in CFD model were modelled with an idealistic representation since, in reality, the valve design is likely to be much more complex and the opening pressure will be a non-null value. Hence, 95% is probably the maximum achievable efficiency for the valves that is un-

likely to be achieved in a realistic scenario.

A non-return can be described by three parameters: its opening pressure $p_0$, its opening area $A_v$ and the discharge coefficient $\alpha \in [0;1]$. When subject to a pressure head $\Delta p_v$ larger than $p_0$, the valve opens. Due to the constriction of the flow, the air flows across the effective opening area $\alpha A_v$ smaller than the opening area $A_v$. The value of the discharge coefficient is unknown and depend on the shape of the valve. The valve has in general, a similar behaviour as an orifice. The relationship between pressure drop $\Delta p$ and mass flow rate $q$ can be expressed as:

$$\Delta p_v = \frac{1}{2\rho_{in}(\alpha A_v)^2} w_{v,in\rightarrow out}^2 \qquad \text{for} \qquad \Delta p_v > p_0 \tag{3.1}$$

Larger effective opening area enables larger flow of air at a lower pressure head and hence less resistance to the flow and less pneumatic power losses. In order to have a better idea of the valves parameters achievable at full scale, to input in the numerical model described in paper A and C, another CFD study was carried out. A numerical test rig was built using the software ANSYS Fluent to analyse the relationship between flow rate and pressure head across various valve set-ups. The rig has the similar geometry as the OWC chamber: it is a vertical column of 5.2 meter diameter split horizontally into 2 parts by a wall equipped with valves. The study was carried out in 2D, thus, it was assumed that the column was 1 meter wide. For simplicity, the dynamics of the valve was not represented and the valve was always open. Figure 3.9a displays the test rig with a large perfect valve represented as an opening of 1.6m wide. In order to reproduce similar conditions to which the valves are submitted to, pressure boundary conditions were set on each side of the valve to create a flow across the valve. At the boundary condition 1, atmospheric pressure is imposed and at the boundary condition 2, a sinusoidal pressure is imposed of the form: $p_{BC2} = p_{atm} + Acos(\omega t)$, with $A$ being the pressure oscillation amplitude, set to $10^4$ Pa. The flow and the pressure drop across the valve are monitored and the effective area of the valve is assessed.

Eight smaller valves, of 0.2m width positioned in parallel, were also tested. Their equivalent width is equal to the width of the larger valve. Figure 3.9b displays the eight valves in parallel. In order to come closer to the shape of an actual valve, a flap was added to the eight valves. The valves were tested in two opening state: fully open with flap at $90^o$ and partially open with flap at $45^o$, see figure 3.10. When equipped with a flap, the effective area of the valves was assessed only in direct mode (from down to up in figure 3.10).

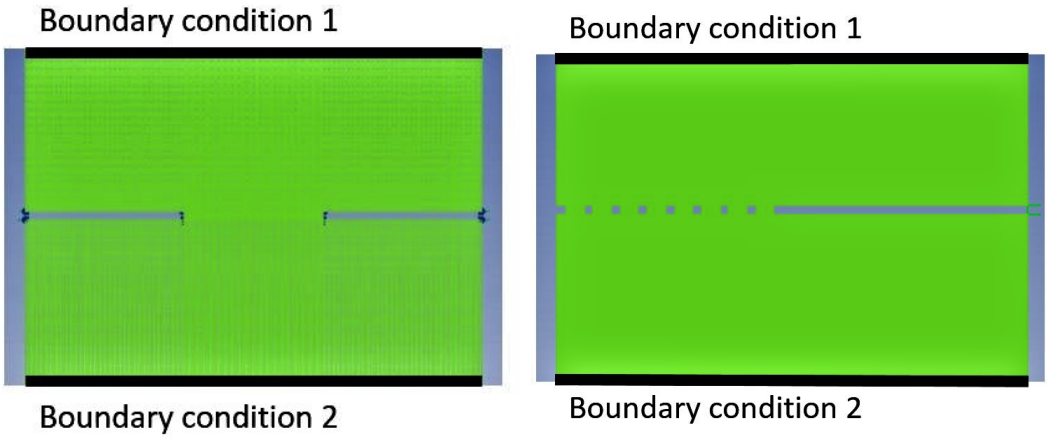


(a) Single 1.6m wide valve

(b) Eight 0.2m wide valves in parallel

Figure 3.9: Numerical test rig for valves built on ANSYS FLUENT

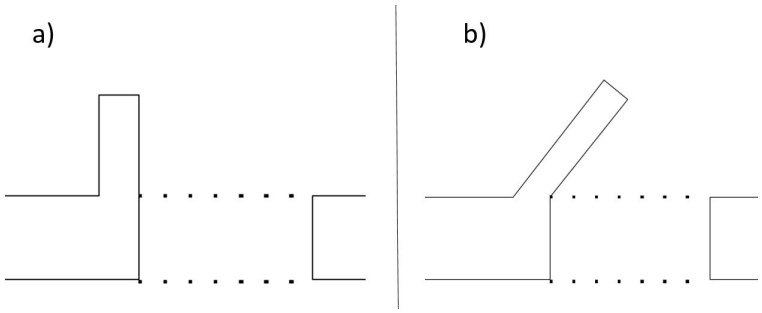


Figure 3.10: Schematic of flap-type valve: a) fully open, flap at $90^o$; b) partially open, flap at $45^o$

The total effective opening area obtained are given in table 3.2.

Table 3.2: Effective opening area of the tested valve set-ups

| Valve | | $\alpha A(\mathrm{m}^2)$ |
|---|---|---|
| 1 large perfect valve | | 0.69 |
| 8 small perfect valves | No flap | 1.34 |
| | Flap $90^o$ | 1.30 |
| | Flap $45^o$ | 0.22 |

From these results, the following observations can be made:

- Despite their same equivalent width, 8 smaller valves offer almost twice the effective opening area as the larger valve.
- When their flaps are fully open, the behaviour of the valves is as they had no flap.
- When partially opened, the effective opening area of the valve reduces significantly and they offer much larger resistance to the flow.

From those observations, and in the context of the Tupperwave device, the following conclusions were drawn:

- Numerous smaller valves would offer larger opening area and hence cause less pneumatic power losses.
- Care should be taken so that the valves open fully and not partially. This requires a very fast opening response time of the valves.

Those two points are compatible since smaller valves can exhibit faster opening time than bigger valves. Moreover, if passive valves are considered, small opening pressure can be achieved with small valves. For example, the small valves considered above are 0.2m wide and 1m length. A pressure difference of 150Pa on both sides of the valves represents a 30 N force and is equivalent to 3 kgf. If the flap is sufficiently light, such force will open it. Considering that the CFD numerical test rig is only 1m deep, a total valve effective opening area of 1.3m$^2$ with an opening pressure of 150 Pa therefore seems to be largely achievable on the side of HP and LP chamber in the Tupperwave device. The parameters $\alpha A_v = 1.3\,\mathrm{m}^2$ and $p_0 = 150\,\mathrm{Pa}$ were subsequently in-putted as a case study in the wave-to-wire numerical model developed in section 3.2.2.

#### 3.2.1.5 Applications of deformable air chambers

The observations made in paper C led to the consideration that the slight elastic deformation of an air chamber under the change of inner excess pressure relative the atmosphere acts as a pneumatic energy storing mechanism in the form of strain energy. Based on that consideration, two innovative ideas are presented in paper E:

- A new method to physically model air compressibility is described which has the potential to simplify the implementation of air compressibility modelling relatively to the existing method which uses large volume external accumulator chambers. The new method uses variable volume chambers which mimic air compressibility by storing energy under the form of strain energy and hence either reduce or suppress the need for large volume external accumulator chambers.

- A new closed-circuit OWC concept, named Uilleann, is presented. The Uilleann concept is based on the Tupperwave concept but uses variable volume chamber instead of fixed volumes. The Uilleann concept has the potential to outperform the Tupperwave device in terms of pneumatic power smoothing and extend the concept of closed-circuit OWC to onshore or smaller wave energy converters. An invention disclosure form was submitted to UCC.

### 3.2.2 From wave to wire

In this section, the numerical models of the Tupperwave device and of the corresponding conventional OWC described in paper C are completed into wave-to-wire models, encompassing all power conversion processes.

#### 3.2.2.1 Version 1: Isentropic model

Paper F describes the development of the first version of the wave-to-wire models. The numerical models described in paper C, which assumed the isentropic relationship between air density and pressure, are used as bases for the isentropic wave-to-wire models. The rest of the power conversion chain, from pneumatic to electrical power, is added to the model by including realistic turbine and generator models as well as a control strategy. In the purpose of a fair and up-to-date power performance comparison between the Tupperwave and conventional OWC devices, both devices are equipped with the current state-of-the-art turbine technologies suiting both devices. The turbine models are taken from experimental tests reports from the literature. The generators and their control strategies were the same for both devices and chosen to suit them equally. The dimensioning for turbines and generators is optimised to maximise the power conversion of the devices.

In order to validate the last power conversion stage of the wave-to-wire models, the mechanical to electrical power conversion occurring at full scale in the two devices studied was physically emulated on an electrical test rig. This is achieved using Hardware-In-the-Loop (HIL) to simulate physically and in real time the turbine action on a real generator. The hardware used is a rotatory test rig composed of two coupled electrical machines. One is used as a motor and acts as the prime mover (turbine). The other is acting as the electrical generator and is connected to the local electrical grid using an off-the-shelf AC-to-AC converter. A picture of the rig is shown in figure 3.11. The results successfully validated the numerical models.

Once the Tupperwave and conventional OWC wave-to-wire models were validated against physical testing for all power conversion stages, their results are used to compare the two devices performances in the wave climate of the EMEC wave energy test site. The results prove that the smoother pneumatic power produced by the Tupperwave device, allows its turbine to work very close to maximum efficiency while the turbine of the conventional OWC

Figure 3.11: Rotary test rig of the Lir-NOTF, used to emulate the turbine-generator systems of the devices

is working in average 10 percent away from its maximum efficiency. Figure 3.12 illustrates this fact on a given sea state. The second consequence of the

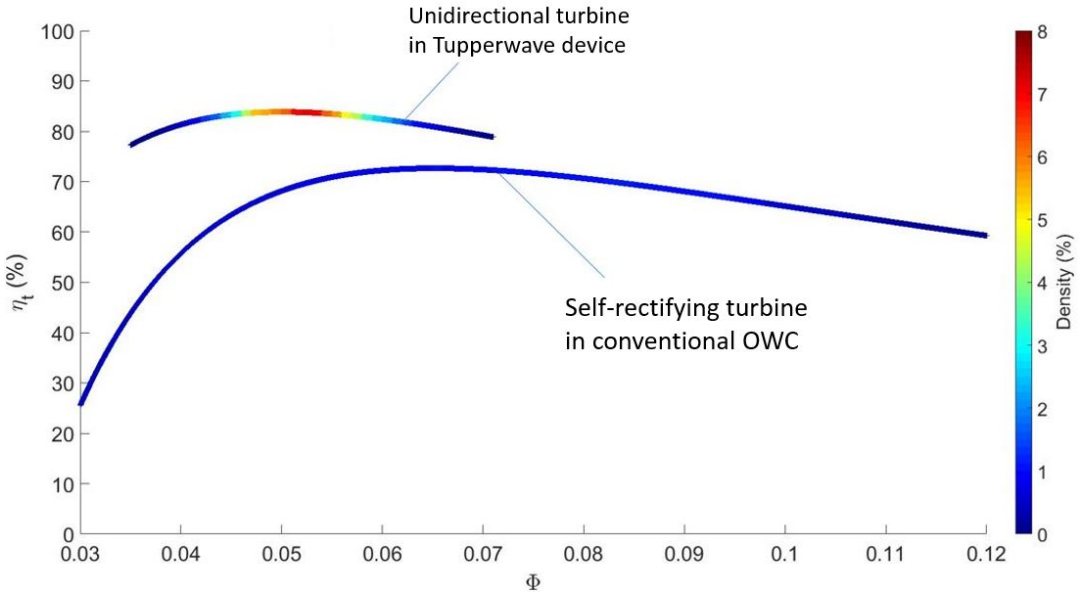


Figure 3.12: Percentage of occurrence of turbines working points in sea state Hs=3m, Tp=9s.

smoother pneumatic power produced by the Tupperwave device is that the device produces a smoother electrical power than the conventional OWC, as illustrated in figure 3.13, enhancing power quality delivered to the grid.

We note that the smoother mechanical power generated by the turbine of the Tupperwave device has however no consequence on the generator effi-

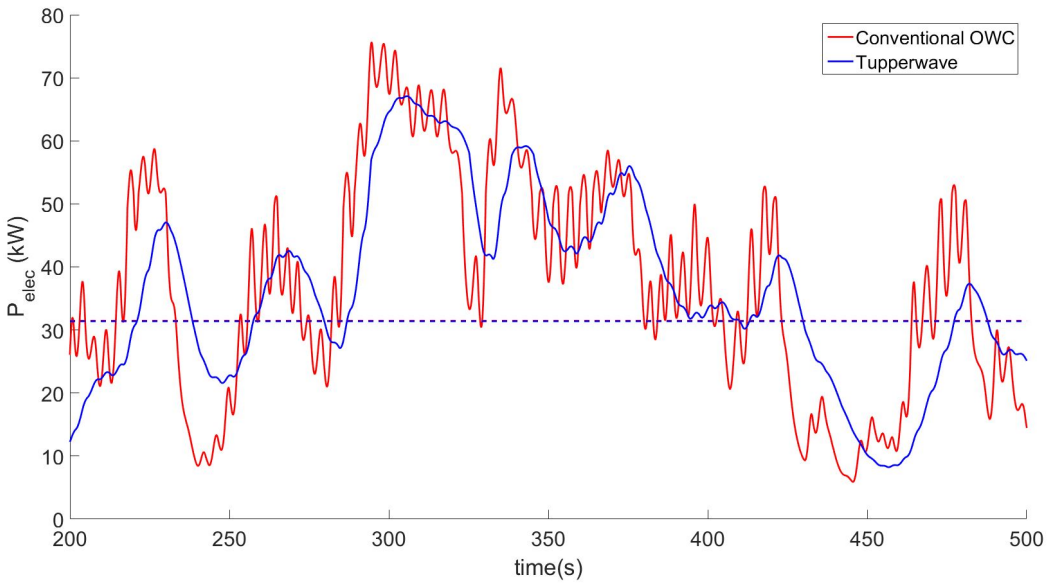


Figure 3.13: Electrical power produced by the conventional OWC and Tupperwave device (case2) in sea state Hs=3m, Tp=9s. Solid lines: Time-series; Dash lines: Average values.

ciency in converting the mechanical power into electrical power. The generators in both devices reach similar efficiency.

Finally, in terms of power production, the Tupperwave device has the potential to outperform the conventional OWC device if more than 80% of the absorbed wave power is effectively converted into useful pneumatic power by the non-return valves. Moreover, when simulated with a valve opening area of 1.3m$^2$ and opening pressure of 150Pa, which was identified as achievable in section 3.2.1.4, the Tupperwave device outperforms the electrical power production of the conventional OWC by about 20% annually. The actual feasibility and practicability of large-scale non-return valves able to achieve such efficiency is to be investigated in future work.

#### 3.2.2.2 Version 2: Non-isentropic model

The Tupperwave device works with a closed-circuit of air. The repetition of thermodynamic cycles and viscous losses occurring across the valves and turbine can lead to a temperature rise of the air in the device, which represents a potential issue for the safe operation of the device if high temperature are reached. In order to study the air temperature rise in the device, a second version of the wave-to-wire numerical model of the Tupperwave device was developed in paper G. The model is identical to the model described in paper F except that the thermodynamic part of the model now accounts for the energy dissipation across the turbine and the valves, the heat transfers between the inner air and the environment, and the solar radiations on the

device. Such irreversible thermodynamic processes lead to the creation of entropy, hence the name of non-isentropic model.

Realistic assumptions were made on the device walls heat conductivity and the results confirmed that the temperature of the air in the device rises. But the large surface area of the chambers outside walls allows sufficient heat transfer to the environment to limit the temperature increase to a certain threshold depending on the sea state, on the walls thermal conductivity, and on the level of solar irradiance. Figure 3.14 displays the temperature of the air in the HP and LP chambers in the case of a concrete buoy structure and shows the asymptotic increase of the running average of the temperature by a couple of degrees in a moderate sea state. The temperature elevation of the air in the device remains lower than 15°C, even in very energetic sea states. This result show that the temperature rise in the chamber does not represent an issue for the device operation.

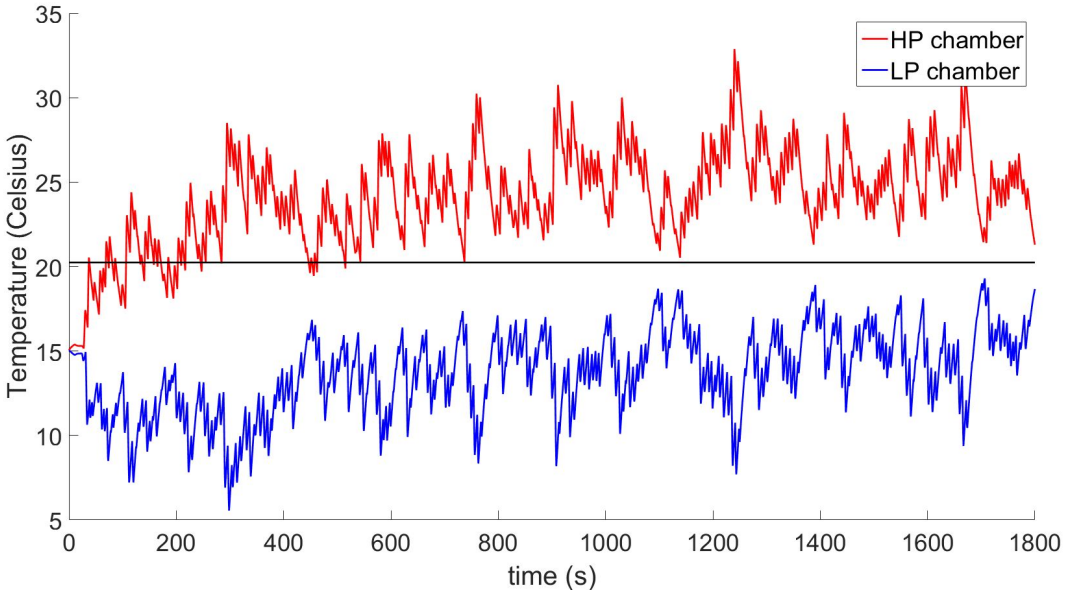


Figure 3.14: Air temperature in HP and LP chambers assuming heat transfers across the concrete buoy structure and with the water column for sea state Hs=3m, Tp=9s

An non-isentropic version of the conventional OWC numerical model was also developed. As the conventional OWC is open to the atmosphere, the temperature increase of the air within the OWC chamber is lower than in the Tupperwave device and was limited to 3°C in very energetic sea states.

Finally, it was found that the isentropic version of the models provide very similar predictions (within 1%) of the devices performances in terms of electrical power production than the more complex non-isentropic model. It is therefore recommended to use the simpler isentropic version for the purpose of assessing the device performance. The temperature evolution is how-

ever only predictable using the non-isentropic model.

This chapter described the work carried out to investigate the innovative Tupperwave OWC concept. The concept was adapted to a floating spar buoy and a numerical wave-to-wire model of the device was developed and validated physically. Using this numerical tool, the device performances were compared to existing state-of-art technologies and the critical aspects of the concept were identified and addressed.

# Chapter 4

# Conclusions and recommendations

In this chapter, the main achievements and conclusions of the work are summarized. Finally recommendations of the further work are suggested.

## 4.1 Achievements and conclusions

The research in this thesis led to the following **achievements**:

- A novel concept of closed-circuit OWC wave energy converter, entitled Tupperwave, was proven and investigated numerically and physically. A device based on this concept was designed and optimised to maximise its power conversion performance. The novel concept was shown to have the capacity to outperform state-of-the-art existing technologies in terms of electrical power production and power quality.

- A numerical modelling approach was developed to assess the full behaviour of the device in time domain and encompass all power conversion stages from wave to electrical power. The approach was incremental in difficulty and included scaled physical model testing for validation. This gradual development enabled detailed analysis of the device critical components and operational risks. Such progressive approach is effective and particularly adequate for the study of a novel device.

- The design of non-return valves used in this novel concept was identified as crucial for the overall efficiency. The lack of previous research available in the literature on valves for such application was addressed by identifying critical design parameters for the good operation of the device.

- A non-isentropic thermodynamic study of the close-circuit OWC device was developed for the first time and addressed a topic so far ignored in the literature. The temperature increase of the air in the closed-circuit device was shown to be bound to reasonable temperatures with

no associated operational risks. Moreover, the isentropic approach was shown to provide very satisfactory power performance estimations of the close-circuit OWC device and is simpler to implement.

- A new method to reproduce air compressibility effects during model scale testing of OWC devices was suggested and demonstrated. The new method uses deformable air chambers to mimic pneumatic power storing due to air compressibility and hence facilitates the implementation relative to the existing method.

- Another innovative OWC wave energy conversion concept was invented. The Uilleann concept is similar to the Tupperwave concept as it is a closed-circuit OWC using accumulator chambers and a unidirectional turbine. The accumulator chambers are however deformable to increase short term pneumatic power storage and enhance the pneumatic power smoothing capacity of the device.

These achievements led to a number of **conclusions relative to the Tupperwave concept** which are summarized below:

- The working principle of the Tupperwave concept enables the creation of a smooth and continuous unidirectional air flow across a unidirectional turbine with the intermediate of fixed-volume accumulator chambers and non-return valves.

- Large accumulator chamber volumes increase the pneumatic power smoothing without affecting the power performance. The concept is therefore particularly adapted to floating structures where the buoyancy volume is available.

- The non-return valves in the Tupperwave concept are the most critical components for the device conversion efficiency as they can induce important pneumatic power losses. Their design should enable:

  1. large opening area;
  2. low opening pressure;
  3. quick response to open fully.

- Rather than a single large valve, numerous smaller valves associated in parallel facilitate the achievement of the three design conditions enumerated above.

- The smoothing of the pneumatic power achieved by the Tupperwave device has two major benefits:

  1. it enables the unidirectional pneumatic turbine to operate close to maximum efficiency most of the time;

2. it improves the electrical power quality delivered to the grid.

- The turbine in the Tupperwave device is likely to be cheaper than the turbine in the conventional OWC, due to:

  1. its simple and well-established unidirectional turbine technology;
  2. its diameter which is twice smaller.

- The Tupperwave device has the potential to convert more power than the existing state-of-the-art OWC technology provided that the valves are sufficiently well designed. If the valves dissipate less than 20% of the absorbed wave power, the gain in turbine efficiency balances out the pneumatic power losses in the valves. In the ideal case where the valves dissipate no power, the Tupperwave device outperforms the conventional OWC in terms of electrical power production by a maximum of 20%.

- Relative to the conventional OWC, the Tupperwave device produces better quality electrical power with lower output power fluctuations.

- Due to the reduced level of load fluctuations on the generator, less use of the security system protecting the electrical equipment is required in the Tupperwave device than in the corresponding conventional OWC.

- The air in the Tupperwave device raises in temperature due to the pneumatic power dissipation into heat occurring in the valves and turbine. The large surface of the device wall allow sufficient heat transfer with the outside to restrain the average inner air temperature increase in the device to reasonable levels ($< +15^{o}$C), which does not raise concern for the device operability.

## 4.2 Further recommended work

Following the work achieved in this thesis, directions for further research are recommended:

- Further research on the Tupperwave concept should focus on the non-return valves. The priority of the research would be to identify the best and most reliable possible design for the valves and conclude on the achievable performance of the valves for a given available surface. Once assessed, the valves parameters would only need to be imputed in the developed numerical models to conclude on their efficiency in the Tupperwave device. The recommended layout path is the multiplication of small size valves (10-50cm) in parallel forming a one-way porous surface. Such layout would have several advantages: Maximum use of the available wall surface is possible; Small opening pressure and

fast opening are easily achievable; Small valves are easier to manufacture and replace when faulty. Passive valves which open with pressure head were considered in this thesis and are the recommended option for their simplicity of use. Active valves (electrically activated) require control algorithms and are likely to be more expensive and less reliable. Active valve however would enable latching control of the buoy which could increase the device's power absorption from the waves. Latching control on the Tupperwave device would represent an interesting topic of study.

- It was shown that Tupperwave and conventional OWC have slightly different hydrodynamics. Hence, a hydrodynamic optimisation of the spar buoy structure for the Tupperwave device would be of interest to improve its wave absorption capacity. The Tupperwave concept could also be adapted to other buoy structures such as a BBDB type structure to see if it is suitable.

- For the improvement of the developed numerical model of the Tupperwave device, a number of aspects should be regarded:

  1. extend the hydrodynamic component to a 6 degrees of freedom motion;

  2. include moorings;

  3. improve the valves model by including their dynamics (non-instanteneous opening) and use physically proven values for opening area and effective opening pressure;

  4. non-steady heat transfers across the walls could be considered in the case of non-isentropic modelling.

- For further experimental testing of the Tupperwave device, if the same air compressibility method was to be implemented, extreme care should be taken to ensure that the walls of the additional accumulator chambers are perfectly rigid. The suggested new modelling method using deformable air chamber could also be implemented.

- The new method for modelling the air compressibility effects at model should be validated and demonstrated. For that, the new method and the existing method could be implemented in parallel for the physical modelling of a fixed OWC device. The OWC device should also be modelled numerically at full scale. The comparison of all the results would enable the demonstration of the new method. It should be kept in mind that the success of the new method depends on the design and calibration of the deformable accumulator chamber(s).

- The results of the non-isentropic model should be validated against experimental work. This is a challenging task since very small air temperature increase is expected at model scale. Moreover, the method for modelling air compressibility using large external accumulator chambers offers a much larger wall surface, across which thermal exchanges can happen, than at full scale. The new air compressibility modelling method would reduce the wall surface and, with thermally isolated deformable accumulator chambers, may enable sufficient air temperature increase to be detected for the numerical model validation.

- The Uilleann concept should be investigated in further details to prove its superior pneumatic power smoothing capacity and find in which applications it is better adapted than the Tupperwave device.

- Finally, a techno-economic study of the Tupperwave, Uilleann and corresponding OWC device would enable the definitive conclusion on their relative economic profitability.

# Bibliography


[1] Intergovernmental Panel on Climate Change. Special report: Global warming of 1.5 $^{o}$C. `https://www.ipcc.ch/sr15/`. Accessed: 2019-01-14.

[2] Intergovernmental Panel on Climate Change. *Climate change 2014: Mitigation of climate change*, volume 3. Cambridge University Press, 2015.

[3] Mark Z Jacobson, Mark A Delucchi, Zack AF Bauer, Savannah C Goodman, William E Chapman, Mary A Cameron, Cedric Bozonnat, Liat Chobadi, Hailey A Clonts, Peter Enevoldsen, et al. 100% clean and renewable wind, water, and sunlight all-sector energy roadmaps for 139 countries of the world. *Joule*, 1(1):108–121, 2017.

[4] Benjamin P Heard, Barry W Brook, Tom ML Wigley, and Corey JA Bradshaw. Burden of proof: A comprehensive review of the feasibility of 100% renewable-electricity systems. *Renewable and Sustainable Energy Reviews*, 76:1122–1133, 2017.

[5] Christopher TM Clack, Staffan A Qvist, Jay Apt, Morgan Bazilian, Adam R Brandt, Ken Caldeira, Steven J Davis, Victor Diakov, Mark A Handschy, Paul DH Hines, et al. Evaluation of a proposal for reliable low-cost grid power with 100% wind, water, and solar. *Proceedings of the National Academy of Sciences*, 114(26):6722–6727, 2017.

[6] Mark Diesendorf and Ben Elliston. The feasibility of 100% renewable electricity systems: A response to critics. *Renewable and Sustainable Energy Reviews*, 93:318–330, 2018.

[7] Alain Clément, Pat McCullen, António Falcão, Antonio Fiorentino, Fred Gardner, Karin Hammarlund, George Lemonis, Tony Lewis, Kim Nielsen, Simona Petroncini, et al. Wave energy in europe: current status and perspectives. *Renewable and sustainable energy reviews*, 6(5):405–431, 2002.

[8] Aurelien Babarit. *Ocean Wave Energy Conversion: Resource, Technologies and Performance*. Elsevier, 2017.

[9] António FO Falcão and Joao CC Henriques. Oscillating-water-column wave energy converters and air turbines: A review. *Renewable Energy*, 85:1391–1424, 2016.

[10] Alex DD Craik. The origins of water wave theory. *Annu. Rev. Fluid Mech.*, 36:1–28, 2004.

[11] RPF Gomes, JCC Henriques, LMC Gato, and AF de O Falcão. Hydrodynamic optimization of an axisymmetric floating oscillating water column for wave energy conversion. *Renewable Energy*, 44:328–339, 2012.

[12] Aurélien Babarit, Jorgen Hals, MJ Muliawan, Adi Kurniawan, Torgeir Moan, and Jorgen Krokstad. Numerical benchmarking study of a selection of wave energy converters. *Renewable Energy*, 41:44–63, 2012.

[13] Andrew M Cornett et al. A global wave energy resource assessment. In *The Eighteenth International Offshore and Polar Engineering Conference*. International Society of Offshore and Polar Engineers, 2008.

[14] António FO Falcão. Wave energy utilization: A review of the technologies. *Renewable and sustainable energy reviews*, 14(3):899–918, 2010.

[15] Jochem Weber. Wec technology readiness and performance matrix–finding the best research technology development trajectory. In *Proceedings of the 4th International Conference on Ocean Energy, Dublin, Ireland*, pages 17–19, 2012.

[16] Michael E McCormick. *Ocean wave energy conversion*. Courier Corporation, 2013.

[17] Johannes Falnes. A review of wave-energy extraction. *Marine structures*, 20(4):185–201, 2007.

[18] Clayton E Hiles, Scott J Beatty, and Adrian de Andres. Wave energy converter annual energy production uncertainty using simulations. *Journal of Marine Science and Engineering*, 4(3):53, 2016.

[19] Aquaret, delivering knowledge and understanding. `http://www.aquaret.com/indexea3d.html?option=com_content&view=article&id=203&Itemid=344&lang=en#Animations`. Accessed: 2019-01-22.

[20] Wave devices. `http://www.emec.org.uk/marine-energy/wave-devices/`. Accessed: 2019-01-21.

[21] Anne Blavette. *Grid integration of wave energy and generic modelling of ocean devices for power system studies*. PhD thesis, University College Cork, 2013.

[22] EIRGRID. Power quality requirements for connection to the transmission system. Technical report, 2015.

[23] Markel Penalba and John Ringwood. A review of wave-to-wire models for wave energy converters. *Energies*, 9(7):506, 2016.

[24] J Tissandier, A Babarit, AH Clément, et al. Study of the smoothing effect on the power production in an array of searev wave energy converters. In *The Eighteenth International Offshore and Polar Engineering Conference*. International Society of Offshore and Polar Engineers, 2008.

[25] Dara O'Sullivan, Darren Mollaghan, Anne Blavette, and Raymond Alcorn. *Dynamic characteristics of wave and tidal energy converters & a recommended structure for development of a generic model for grid connection*. PhD thesis, Ocean Energy Systems-Implementing Agreement (OES-IA), International Energy , 2009.

[26] D OSullivan, F Salcedo, A Blavette, M Santos, and AW Lewis. Case studies on the benefits of energy storage for power quality enhancement: oscillating water column arrays. In *Proceedings of the 4th International Conference on Ocean Energy (ICOE2012), Dublin, Ireland*, volume 1719, 2012.

[27] Markel Penalba and John V Ringwood. A reduced wave-to-wire model for controller design and power assessment of wave energy converters. In *Proceedings of the 3rd international conference on renewable energies offshore RENEW, Lisbon*, 2018.

[28] Gareth Thomas. The theory behind the conversion of ocean wave energy: a review. In *Ocean wave energy*, pages 41–91. Springer, 2008.

[29] Chang-Ho Lee. *WAMIT theory manual*. Massachusetts Institute of Technology, Department of Ocean Engineering, 1995.

[30] Aurélien Babarit and Gérard Delhommeau. Theoretical and numerical aspects of the open source bem solver nemoh. In *11th European Wave and Tidal Energy Conference (EWTEC2015)*, 2015.

[31] Wanan Sheng, Raymond Alcorn, and Tony Lewis. Physical modelling of wave energy converters. *Ocean Engineering*, 84:29–36, 2014.

[32] Thomas Vyzikas. Application of numerical models and codes. 2014.

[33] Markel Penalba, José-Antonio Cortajarena, and John Ringwood. Validating a wave-to-wire model for a wave energy converterpart ii: The electrical system. *Energies*, 10(7):1002, 2017.

[34] Giuseppe Giorgi, Markel Penalba Retes, and John Ringwood. Nonlinear hydrodynamic models for heaving buoy wave energy converters. 2016.

[35] Markel Penalba, Nathan Sell, Andy Hillis, and John Ringwood. Validating a wave-to-wire model for a wave energy converterpart i: The hydraulic transmission system. *Energies*, 10(7):977, 2017.

[36] T Heath, TJT Whittaker, and CB Boake. The design, construction and operation of the limpet wave energy converter (islay, scotland). In *Proceedings of 4th European wave energy conference*, pages 49–55, 2000.

[37] JRM Taylor and NJ Caldwell. Design and construction of the variable-pitch air turbine for the azores wave energy plant. In *Proceedings of the Third European Wave Power Conference, Patras, Greece*, volume 30, 1998.

[38] Y Torre-Enciso, I Ortubia, LI López de Aguileta, and J Marqués. Mutriku wave power plant: from the thinking out to the reality. In *Proceedings of the 8th European wave and tidal energy conference, Uppsala, Sweden*, volume 710, page 319329, 2009.

[39] The Executive Committee of Ocean Energy Systems (OES). An overview of ocean energy activities in 2017. Technical report, 2017.

[40] Y Washio, H Osawa, Y Nagata, F Fujii, H Furuyama, T Fujita, et al. The offshore floating type wave power device" mighty whale": open sea tests. In *The Tenth International Offshore and Polar Engineering Conference*. International Society of Offshore and Polar Engineers, 2000.

[41] AFO Falcão, LMC Gato, AJNA Sarmento, and A Brito-Melo. The pico owc wave power plant: Its life from conception to closure 1986–2018. In *Advances in Renewable Energies Offshore: Proceedings of the 3rd International Conference on Renewable Energies Offshore (RENEW 2018), October 8-10, 2018, Lisbon, Portugal*, page 475. CRC Press, 2018.

[42] A Brito-Melo, F Neumann, AJNA Sarmento, et al. Full-scale data assessment in owc pico plant. In *The Seventeenth International Offshore and Polar Engineering Conference*. International Society of Offshore and Polar Engineers, 2007.

[43] JCC Henriques, W Sheng, AFO Falcão, and LMC Gato. A comparison of biradial and wells air turbines on the mutriku breakwater owc wave power plant. In *ASME 2017 36th International Conference on Ocean, Offshore and Arctic Engineering*, pages V010T09A037–V010T09A037. American Society of Mechanical Engineers, 2017.

[44] SD Weller, D Parish, T Gordelier, B de Miguel Para, EA Garcia, P Goodwin, D Tornroos, and L Johanning. Open sea owc motions and mooring loads monitoring at bimep. 2017.

[45] Opera-h2020. `http://opera-h2020.eu/`. Accessed: 2019-02-08.

[46] Wesley Scharmen. Wave energy prize-1/50th testing-sewec. Technical report, Marine and Hydrokinetic Data Repository (MHKDR); Ricardo Detroit Technical , 2015.

[47] Bruno Pereiras, Pablo Valdez, and Francisco Castro. Numerical analysis of a unidirectional axial turbine for twin turbine configuration. *Applied Ocean Research*, 2014.

[48] Laudino Rodríguez, Bruno Pereiras, Jesús Fernández-Oro, and Francisco Castro. Optimization and experimental tests of a centrifugal turbine for an owc device equipped with a twin turbines configuration. *Energy*, 2019.

[49] Alan Fleming, Gregor MacFarlane, Scott Hunter, and Tom Denniss. Power performance prediction for a vented oscillating water column wave energy converter with a unidirectional air turbine power takeoff. In *Proceedings of the 12th European Wave and Tidal Energy Conference*, pages 1204–1. EWTEC, 2017.

[50] Nicola Delmonte, Davide Barater, Francesco Giuliani, Paolo Cova, and Giampaolo Buticchi. Oscillating water column power conversion: A technology review. In *Energy Conversion Congress and Exposition (ECCE), 2014 IEEE*, pages 1852–1859. IEEE, 2014.

[51] Min-Fu Hsieh, I-Hsien Lin, David G Dorrell, Ming-June Hsieh, and Chi-Chien Lin. Development of a wave energy converter using a two chamber oscillating water column. *IEEE Transactions on Sustainable Energy*, 3(3):482–497, 2012.

[52] Luca Martinelli, Paolo Pezzutto, and Piero Ruol. Experimentally based model to size the geometry of a new owc device, with reference to the mediterranean sea wave environment. *Energies*, 6(9):4696–4720, 2013.

[53] Jens Peter Kofoed and Peter Frigaard. Hydraulic evaluation of the leancon wave energy converter. *Department of Civil Engineering, Aalborg University, Aalborg. DCE Technical Reports*, 2008.

[54] James Rattray Joubert. Design and development of a novel wave energy converter. *Stellenbosch University*, 2013.

[55] Simeon Doyle and George Athanasios Aggidis. Investigation into multi-oscillating water column wave energy converters and a novel concept. 2018.

[56] Kiffin. R. Floating multistage air compressor with turbine, 2012. US Patent 4466244 A.

[57] António FO Falcão, João CC Henriques, and Luís MC Gato. Self-rectifying air turbines for wave energy conversion: A comparative analysis. *Renewable and Sustainable Energy Reviews*, 91:1231–1241, 2018.

[58] A Thakker, J Jarvis, and A Sahed. Design charts for impulse turbine wave energy extraction using experimental data. *Renewable Energy*, 34(10):2264–2270, 2009.

[59] AF de O Falcão, LMC Gato, and EPAS Nunes. A novel radial self-rectifying air turbine for use in wave energy converters. part 2. results from model testing. *Renewable energy*, 53:159–164, 2013.

[60] Bárbara S Lopes, Luís MC Gato, António FO Falcão, and João CC Henriques. Test results of a novel twin-rotor radial inflow self-rectifying air turbine for owc wave energy converters. *Energy*, 170:869–879, 2019.

[61] AFO Falcão and RJA Rodrigues. Stochastic modelling of owc wave power plant performance. *Applied Ocean Research*, 24(2):59–71, 2002.

[62] M Takao, T Setoguchi, K Kaneko, S Raghunathan, and M Inoue. Noise characteristics of turbines for wave power conversion. *Proceedings of the Institution of Mechanical Engineers, Part A: Journal of Power and Energy*, 216(3):223–228, 2002.

[63] Ralf Starzmann. *Aero-acoustic analysis of Wells turbines for ocean wave energy conversion*. VDI Verlag, 2012.

[64] AFO Falcão, AJNA Sarmento, et al. Wave generation by a periodic surface pressure and its application in wave-energy extraction. In *Proceedings of the 15th International Congress of Theoritical and Applied Mechanics, Toronto, ON, Canada*, pages 17–23, 1980.

[65] DV Evans. Wave-power absorption by systems of oscillating surface pressure distributions. *Journal of Fluid Mechanics*, 114:481–499, 1982.

[66] AJNA Sarmento and AFO Falcão. Wave generation by an oscillating surface-pressure and its application in wave-energy extraction. *Journal of Fluid Mechanics*, 150:467–485, 1985.

[67] AFO Falcão and JCC Henriques. The spring-like air compressibility effect in owc wave energy converters: Hydro-, thermo-and aerodynamic analyses. In *ASME 2018 37th International Conference on Ocean, Offshore and Arctic Engineering*, pages V11AT12A038–V11AT12A038. American Society of Mechanical Engineers, 2018.

[68] AFO Falcao and PAP Justino. Owc wave energy devices with air flow control. *Ocean Engineering*, 26(12):1275–1295, 1999.

[69] Cesare Hall and S Larry Dixon. *Fluid mechanics and thermodynamics of turbomachinery*. Butterworth-Heinemann, 2013.

[70] Majid A Abdullah, AHM Yatim, Chee Wei Tan, and R Saidur. A review of maximum power point tracking algorithms for wind energy systems. *Renewable and sustainable energy reviews*, 16(5):3220–3227, 2012.

[71] Elisabetta Tedeschi, Matteo Carraro, Marta Molinas, and Paolo Mattavelli. Effect of control strategies and power take-off efficiency on the power capture from sea waves. *IEEE Transactions on Energy Conversion*, 26(4):1088–1098, 2011.

[72] Department of Trade and Industry. Nearshore floating oscillating water column: Prototype development and evaluation. Technical report, 2005.

[73] Florent Thiebaut. Experimental testing in lir national ocean test facility. Technical report, University College Cork, Lir Round Robin, 2015.

[74] António FO Falcão and João CC Henriques. Model-prototype similarity of oscillating-water-column wave energy converters. *Int. J. Mar. Energy*, 6:18–34, 2014.

[75] Gunnar Mork, Stephen Barstow, Alina Kabuth, and M Teresa Pontes. Assessing the global wave energy potential. In *ASME 2010 29th International conference on ocean, offshore and arctic engineering*, pages 447–454. American Society of Mechanical Engineers, 2010.

[76] S Raghunathan. The wells air turbine for wave energy conversion. *Progress in Aerospace Sciences*, 31(4):335–386, 1995.

[77] Bruno Pereiras, Francisco Castro, Abdelatif El Marjani, and Miguel A Rodríguez. An improved radial impulse turbine for owc. *Renewable Energy*, 36(5):1477–1484, 2011.

[78] Y Masuda and T Miyazaki. Wave power electric generation study in japan. In *International Symposium on Wave and Tidal Energy*, volume 1, page 6, 1978.

[79] V Jayashankar, S Anand, T Geetha, S Santhakumar, V J Kumar, M Ravindran, T Setoguchi, M Takao, K Toyota, and S Nagata. A twin unidirectional impulse turbine topology for owc based wave energy plants. *Renewable Energy*, 34(3):692–698, 2009.

[80] Wanan Sheng, Raymond Alcorn, and Anthony Lewis. Assessment of primary energy conversions of oscillating water columns. ii. power take-off and validations. *Journal of Renewable and Sustainable Energy*, 6(5):053114, 2014.

[81] C-H Lee, JN Newman, FG Nielsen, et al. Wave interactions with an oscillating water column. In *The Sixth International Offshore and Polar Engineering Conference*. International Society of Offshore and Polar Engineers, 1996.

[82] James Lighthill. Two-dimensional analyses related to wave-energy extraction by submerged resonant ducts. *Journal of Fluid Mechanics*, 91(2):253–317, 1979.

[83] WE Cummins. The impulse response function and ship motions. Technical report, David Taylor Model Basin Washington DC, 1962.

[84] Z Yu and J Falnes. State-space modelling of a vertical cylinder in heave. *Applied Ocean Research*, 17(5):265–275, 1995.

[85] Reinder André Habing. Flow and plate motion in compressor valves. 2005.

[86] Thomas Kelly, Thomas Dooley, John Campbell, and John Ringwood. Efforts towards a validated time-domain model of an oscillating water column with control components. In *Proceedings of the 11th European Wave and Tidal Energy Conference*. European Wave and Tidal Energy Conference 2015, 2015.

[87] T Kelly, T Dooley, J Campbell, and J V Ringwood. Comparison of the experimental and numerical results of modelling a 32-oscillating water column (OWC), v-shaped floating wave energy converter. *Energies*, 6(8):4045–4077, 2013.

[88] H B Bingham, D Ducasse, K Nielsen, and R Read. Hydrodynamic analysis of oscillating water column wave energy devices. *Journal of Ocean Engineering and Marine Energy*, 1(4):405–419, 2015.

[89] Wanan Sheng, Raymond Alcorn, and Anthony Lewis. Primary wave energy conversions of oscillating water columns. In *Proceedings of 10th European Wave and Tidal Energy Conference, 2-5th Sep 2013, Aalborg, Denmark.* European Wave and Tidal Energy Conference, 2013.

[90] Pierre Benreguig, Florent Thiebaut, and Jimmy Murphy. Pneumatic orifice calibration, investigation into the influence of test rig characteritics on calibration results. *CORE Conference, Glasgow*, 2016.

[91] Wanan Sheng and Anthony Lewis. Power takeoff optimization to maximize wave energy conversions for oscillating water column devices. *IEEE Journal of Oceanic Engineering*, 2017.

[92] Luca Martinelli, Piero Ruol, Enrico Fassina, Francesco Giuliani, and Nicola Delmonte. A wave-2-wire experimental investigation of the new seabreath wave energy converter: The hydraulic response. *Coastal Engineering Proceedings*, 1(34):29, 2014.

[93] JR Joubert and JL Van Niekerk. Recent developments in wave energy along the coast of southern africa. In *European Wave Tidal Energy Conference*, pages 1096–1100, 2009.

[94] Ken O Connell, Florent Thiebaut, Ger Kelly, and Andrew Cashman. Development of a free heaving owc model with non-linear pto interaction. *Renewable Energy*, 117:108–115, 2018.

[95] Miguel Vicente, Pierre Benreguig, Sarah Crowley, and Jimmy Murphy. Tupperwave-preliminary numerical modelling of a floating owc equipped with a unidirectional turbine. In *Proc. of 12th European Wave and Tidal Energy Conference Series*, 2017.

[96] António FO Falcão, Luís MC Gato, João CC Henriques, João E Borges, Bruno Pereiras, and Francisco Castro. A novel twin-rotor radial-inflow air turbine for oscillating-water-column wave energy converters. *Energy*, 93:2116–2125, 2015.

[97] Ajit Thakker, Zia Usmani, and TS Dhanasekaran. Effects of turbine damping on performance of an impulse turbine for wave energy conversion under different sea conditions using numerical simulation techniques. *Renewable energy*, 29(14):2133–2151, 2004.

[98] António FO Falcão, João CC Henriques, and Luís MC Gato. Comparisons of self-rectifying air turbines for owc wave energy converters.

[99] JE Borges. A three-dimensional inverse method for turbomachinery: Part iiexperimental verification. *Journal of Turbomachinery*, 112(3):355–361, 1990.

[100] NW Bellamy. The circular sea clam wave energy converter. In *Hydrodynamics of Ocean Wave-Energy Utilization*, pages 69–79. Springer, 1986.

[101] Shawn Ryan, Cam Algie, Gregor J Macfarlane, Alan N Fleming, Irene Penesis, Andrew King, et al. The bombora wave energy converter: A novel multi-purpose device for electricity, coastal protection and surf breaks. In *Australasian coasts & ports conference 2015: 22nd Australasian coastal and ocean engineering conference and the 15th Australasian port and harbour conference*, page 541. Engineers Australia and IPENZ, 2015.

[102] Barbara Lopes. Construction and testing of a double rotor self-rectifying air turbine model for wave energy recovery systems. language of reference: Portuguese. Ms thesis, Tecnico Lisboa, Portugal, 2017.

[103] JE Borges. *Three-dimensional design of turbomachinery*. PhD thesis, University of Cambridge, 1986.

[104] Yoshio Masuda and Michael E McCormick. Experiences in pneumatic wave energy conversion in japan. In *Utilization of ocean waves Wave to energy conversion*, pages 1–33. ASCE, 1986.

[105] James F Kelly, William MD Wright, Wanan Sheng, and Keith OSullivan. Implementation and verification of a wave-to-wire model of an oscillating water column with impulse turbine. *IEEE Transactions on Sustainable Energy*, 7(2):546–553, 2016.

[106] DV Evans. The oscillating water column wave-energy device. *IMA Journal of Applied Mathematics*, 22(4):423–433, 1978.

[107] Alexander H-D Cheng and Daisy T Cheng. Heritage and early history of the boundary element method. *Engineering Analysis with Boundary Elements*, 29(3):268–302, 2005.

[108] António FO Falcão, João CC Henriques, and José J Cândido. Dynamics and optimization of the owc spar buoy wave energy converter. *Renewable energy*, 48:369–381, 2012.

[109] JCC Henriques, AFO Falcao, RPF Gomes, and LMC Gato. Air turbine and primary converter matching in spar-buoy oscillating water column wave energy device. In *ASME 2013 32nd International Conference on Ocean, Offshore and Arctic Engineering*, pages V008T09A077–V008T09A077. Citeseer, 2013.

[110] Reza Taghipour, Tristan Perez, and Torgeir Moan. Hybrid frequency–time domain models for dynamic response analysis of marine structures. *Ocean Engineering*, 35(7):685–705, 2008.

[111] Giuseppe Giorgi and John V Ringwood. Consistency of viscous drag identification tests for wave energy applications. In *Proceedings of the 12th European Wave and Tidal Energy Conference (EWTEC). Cork*, 2017.

[112] JR Morison, JW Johnson, SA Schaaf, et al. The force exerted by surface waves on piles. *Journal of Petroleum Technology*, 2(05):149–154, 1950.

[113] Wanan Sheng, Raymond Alcorn, and Anthony Lewis. On thermodynamics in the primary power conversion of oscillating water column wave energy converters. *Journal of Renewable and Sustainable Energy*, 5(2), 2013.

[114] I López, B Pereiras, F Castro, and Gregorio Iglesias. Optimisation of turbine-induced damping for an owc wave energy converter using a rans–vof numerical model. *Applied Energy*, 127:105–114, 2014.

[115] Pierre Benreguig, Jimmy Murphy, Miguel Vicente, and Sarah Crowley. Wave-to-wire model of the tupperwave device and performance comparison with conventional owc. In *Proceedings of the RENEW 2018 3rd International Conference on Renewable Energies Offshore, Lisbon, Portugal*, 2018.

[116] Gaelle Duclos, Alain H Clément, Gontran Chatry, et al. Absorption of outgoing waves in a numerical wave tank using a self-adaptive boundary condition. *International Journal of Offshore and Polar Engineering*, 11(03), 2001.

[117] Wanan Sheng, Raymond Alcorn, and Anthony Lewis. A new method for radiation forces for floating platforms in waves. *Ocean Engineering*, 105:43–53, 2015.

[118] MATLAB. *version 7.10.0 (R2010a)*. The MathWorks Inc., Natick, Massachusetts, 2010.

[119] Adi Kurniawan, JR Chaplin, DM Greaves, and Martyn Hann. Wave energy absorption by a floating air bag. *Journal of Fluid Mechanics*, 812:294–320, 2017.

[120] SOLIDWORKS. *version 2017*. Dassault Systmes SE, https://www.solidworks.com/.

[121] Capricorn, hypair balance, product technical data sheet (ver. 001/08.2013). http://www.capricorn.pl/upload/files/20150904/napowietrzacz-hipair-balance-karta-techniczna-en.pdf, 2013.

[122] Pierre Benreguig, Jimmy Murphy, and Wanan Sheng. Model scale testing of the tupperwave device with comparison to a conventional owc. In *Proceedings of the ASME 2018 37th International Conference on Ocean, Offshore and Arctic Engineering OMAE2018, Madrid, Spain*. American Society of Mechanical Engineers (ASME), 2018.

[123] Neil Hodgins, Ozan Keysan, Alasdair S McDonald, and Markus A Mueller. Design and testing of a linear generator for wave-energy applications. *IEEE Transactions on Industrial Electronics*, 59(5):2094–2103, 2012.

[124] Joseph Prudell, Martin Stoddard, Ean Amon, Ted KA Brekken, and Annette Von Jouanne. A permanent-magnet tubular linear generator for ocean wave energy conversion. *IEEE Transactions on Industry Applications*, 46(6):2392–2400, 2010.

[125] NJ Baker and Markus A Mueller. Direct drive wave energy converters. *Rev. Energ. Ren.: Power Engineering*, 1:1–7, 2001.

[126] Pierre Benreguig, Miguel Vicente, Adrian Dunne, and Jimmy Murphy. Modelling approaches of a closed-circuit owc wave energy converter. *Journal of Marine Science and Engineering*, 7(2):23, 2019.

[127] Bárbara S Lopes, Luís MC Gato, António FO Falcão, and João CC Henriques. Test results of a novel twin-rotor radial inflow self-rectifying air turbine for owc wave energy converters. *Energy*, 2018.

[128] Barbara Lopes. Construction and testing of a double rotor self-rectifying air turbine model for wave energy recovery systems. language of reference: Portuguese. Ms thesis, Tecnico Lisboa, Portugal, 2017.

[129] Chang-Ho Lee and J Nicholas Newman. Wamit user manual. *WAMIT, Inc*, 2006.

[130] Pierre Benreguig, Miguel Vicente, Sarah Crowley, and Jimmy Murphy. Non-isentropic study of a closed-circuit oscillating-water-column wave energy converter. *Ocean Engineering*, 195:106700, 2020.

[131] William Finnegan and Jamie Goggins. Numerical simulation of linear water waves and wave–structure interaction. *Ocean Engineering*, 43:23–31, 2012.

[132] MC Silva, M d A Vitola, WT Pinto, and CA Levi. Numerical simulation of monochromatic wave generated in laboratory: Validation of a cfd code. In *23 Congresso Nacional De Transporte Aquaviário, Construção Naval e Offshore, Rio de Janeiro, Brazil, Oct*, pages 25–29, 2010.

[133] Pierre Benreguig, James Kelly, Vikram Pakrashi, and Jimmy Murphy. Wave-to-wire model development and validation for two owc type wave energy converters. *Energies*, 12(20):3977, 2019.

[134] Hendrik Tennekes, John Leask Lumley, JL Lumley, et al. *A first course in turbulence*. MIT press, 1972.

[135] Pierre Benreguig, Vikram Pakrashi, and Jimmy Murphy. Assessment of primary energy conversion of a closed-circuit owc wave energy converter. *Energies*, 12(10):1962, 2019.

[136] C Maunsell and T Murphy. Effects of air compressibility in oscillating water column physical modelling. *Final Year Project Report at HMRC*, 2005.

[137] Jochem Weber. *Optimisation of the hydrodynamic-aerodynamic Coupling of an Oscillation Water Column wave energy device*. PhD thesis, University College Cork, 2006.

[138] J Weber. Representation of non-linear aero-thermodynamic effects during small scale physical modelling of owc wecs. In *Proceedings of the 7th European Wave and Tidal Energy Conference*, pages 11–14, 2007.

[139] Ahmed Elhanafi, Gregor Macfarlane, Alan Fleming, and Zhi Leong. Scaling and air compressibility effects on a three-dimensional offshore stationary owc wave energy converter. *Applied energy*, 189:1–20, 2017.

[140] Aggelos S Dimakopoulos, Mark J Cooker, and Tom Bruce. The influence of scale on the air flow and pressure in the modelling of oscillating water column wave energy converters. *International Journal of Marine Energy*, 19:272–291, 2017.

[141] I Zabala, JCC Henriques, A Gomez, AFO Falcão, A Amezaga, Rui PF Gomes, and LMC Gato. Assessment of a spar buoy oscillating-water-column wave energy converter including a fully dynamic model.

[142] Wikipedia. Uilleann pipes. Online; accessed 12-December-2018.

[143] Balazs Czech and Pavol Bauer. Wave energy converter concepts: Design challenges and classification. *IEEE Industrial Electronics Magazine*, 6(2):4–16, 2012.

[144] AF de O Falcão, LMC Gato, and EPAS Nunes. A novel radial self-rectifying air turbine for use in wave energy converters. part 2. results from model testing. *Renewable energy*, 53:159–164, 2013.

[145] RK Rajput. *A textbook of engineering thermodynamics*. Firewall Media, 2010.

[146] François-Xavier Faÿ, João C Henriques, James Kelly, Markus Mueller, Moahammad Abusara, Wanan Sheng, and Marga Marcos. Comparative assessment of control strategies for the biradial turbine in the mutriku owc plant. *Renewable Energy*, 2019.

[147] Erik Dick. *Fundamentals of turbomachines*, volume 109. Springer, 2015.

[148] Judith A Rea, James F Kelly, Raymond Alcorn, and Dara O'Sullivan. Development and operation of a power take off rig for ocean energy research and testing. *Proceedings of the Ninth EWTEC 2011, Southampton, UK*, 2011.

[149] James F Kelly and Ross Christie. Applying hardware-in-the-loop capabilities to an ocean renewable energy device emulator. In *Ecological*

*Vehicles and Renewable Energies (EVER), 2017 Twelfth International Conference on*, pages 1–7. IEEE, 2017.

[150] Dara L OSullivan and Anthony W Lewis. Generator selection and comparative performance in offshore oscillating water column ocean wave energy converters. *IEEE transactions on energy conversion*, 26(2):603–614, 2011.

[151] Anne Blavette, Dara L O'Sullivan, Antony W Lewis, and Michael G Egan. Impact of a wave farm on its local grid: Voltage limits, flicker level and power fluctuations. In *2012 Oceans-Yeosu*, pages 1–9. IEEE, 2012.

[152] C Josset and AH Clément. A time-domain numerical simulator for oscillating water column wave power plants. *Renewable energy*, 32(8):1379–1402, 2007.

[153] Beatriz M Marino, Natalia Muñoz, and Luis P Thomas. Calculation of the external surface temperature of a multi-layer wall considering solar radiation effects. *Energy and Buildings*, 174:452–463, 2018.

[154] Richard Edwin Sonntag, Claus Borgnakke, Gordon John Van Wylen, and Steve Van Wyk. *Fundamentals of thermodynamics*. Wiley New York, 1998.

[155] Guide A environmental design. The Chartered Institution of Building Services Engineers (CIBSE), London, 2006. available at: `https://www.cambeep.eng.cam.ac.uk/References/cibse` (accessed June 14, 2019).

[156] M. Bahrami. Forced convection heat transfer. Simon Fraser University SFU, British Columbia, Canada, 2019. available at: `https://www.sfu.ca/~mbahrami/ENSC%20388/Notes/Forced%20Convection.pdf` (accessed June 14, 2019).

[157] T Namèche and J Vassel. Thermal balance in temperate climate of aerated and natural lagoons; language of reference: French. *Revue des sciences de l'eau/Journal of Water Science*, 12(1):65–91, 1999.

[158] Lixia Guo, Lei Guo, Ling Zhong, and Yueming Zhu. Thermal conductivity and heat transfer coefficient of concrete. *Journal of Wuhan University of Technology-Mater. Sci. Ed.*, 26(4):791–796, 2011.

[159] Matthew J. Hancock. The 1-d heat equation. MIT OpenCourseWare, Massachusetts Institute of Technology, 2006. available at: `https://ocw.mit.edu/courses/mathematics/18-303-linear-partial-differential-equations-fall-2006/lecture-notes/heateqni.pdf` (accessed June 17, 2019).

[160] Marcel Suri, Thomas Huld, ED Dunlop, and Tomas Cebecauer. Photovoltaic solar electricity potential in European countries. Institute for Environment and Sustainability, 2006. available at: `http://re.jrc.ec.europa.eu/pvgis/download/PVGIS-EuropeSolarPotential.pdf`.

[161] Majid A Bhinder, Aurélien Babarit, Lionel Gentaz, Pierre Ferrant, et al. Effect of viscous forces on the performance of a surging wave energy converter. In *The Twenty-second International Offshore and Polar Engineering Conference*. International Society of Offshore and Polar Engineers, 2012.

[162] Majid A Bhinder, Aurélien Babarit, Lionel Gentaz, and Pierre Ferrant. Assessment of viscous damping via 3d-cfd modelling of a floating wave energy device. In *Proceedings of the 9th European Wave and Tidal Energy Conference, Southampton, UK*, 2011.

[163] T Francis Ogilvie. Recent progress toward the understanding and prediction of ship motions. In *5th ONR Symp. on Naval Hydrodynamics*, 1964.

# Appendices

# Appendix A

# Paper A

# Tupperwave - initial numerical modelling and optimization

*Published in*

Proceedings of EWTEC 2017

*Authors*

Miguel Vicente[2], Pierre Benreguig[1], Sarah Crowley[2], Jimmy Murphy[1]

[1]*MaREI Centre (ERI), University College Cork, Haulbowline Road, Ringaskiddy, Ireland*
[2]*WavEC - Offshore Renewables, Rua Dom Jerónimo Osório, nº. 11, 1º, 1400-119 Lisboa, Portugal*

# Abstract

The TUPPERWAVE project is supported by the European Commission's Ocean-EraNet program. It aims to design and validate an innovative Oscillating Water Column (OWC) Power Take-Off (PTO) concept at laboratory scale. A conventional OWC typically generates a highly fluctuating bidirectional air flow through a self-rectifying turbine. To reduce both the pneumatic power fluctuations through the turbine and the acoustic impact, the TUPPERWAVE concept generates unidirectional air flow in a closed circuit, which can be converted into electricity via a conventional, high efficiency, unidirectional turbine. The principle is based on the use of a pair of non-return valves, two additional chambers above the water column and a unidirectional turbine harnessing energy from the resulting air flow between the two chambers. The concept was adapted to a floating axisymmetric structure. Numerical time-domain models have been developed by UCC and WavEC to determine the device's primary conversion from hydrodynamic to pneumatic power. Comparison of the output from the two models showed good agreement and allowed an initial optimization of the PTO main design parameters. A set of design parameters were chosen which maximize the pneumatic average power output flowing through the turbine whilst minimizing the power fluctuations, in regular and irregular sea states. When compared to a conventional OWC with the same structure geometry, the optimised Tupperwave device was shown to produce similar pneumatic average power with much lower fluctuations.


## A.1 Introduction

Climate change and its relation with global energy consumption is a topic of the utmost importance, and the need to tackle this problem is increasingly urgent. Given some estimates of ocean waves energy potential ([75]), the harvesting of this form of renewable energy may contribute to the decrease of fossil fuels consumption. Amongst a variety of wave energy converters (WEC) concepts, the oscillating water column (OWC) is one of the most studied and more promising The technology has been thoroughly reviewed in several works such as in [9]. The OWC concept presents some interesting characteristics: the absence of submerged moving parts and, more importantly, the adaptableility to different scenarios. The structure may be fixed or floating, and it may be designed in such a way so it better suits the water depth and the typical wavelength of a specific location, be it onshore or offshore.

The conventional OWC concept comprises a partially submerged hollow structure, with an aperture below through which sea water enters in the chamber. The alternated rise and fall of the water inside the chamber in-

duces the compression and expansion of the air entrapped above the water. The chamber is connected to the atmosphere through a system of ducts and a turbine and the air is then successively forced to go outwards and inwards through the turbine. In turn, an electric generator converts the rotation of the turbine into electricity.

In order to deal with the inwards and outwards flows, the majority of OWC prototypes are equipped with self-rectifying bidirectional turbines, such as the Wells or impulse turbines (see [76] and [77]). This type of turbine has a lower efficiency than a conventional unidirectional turbine. Also, as the airflow changes direction every couple of a seconds, the pneumatic power fluctuations through the turbine are important and induce difficulties in terms of control and power quality. Moreover, as the turbine is opened to the atmosphere, significant acoustic noise can be created. More conventional unidirectional turbines have a better efficiency, but require a complicated system of valves and ducts ([78]). Such systems have been successfully used in small devices such as navigation buoys but were, so far, considered as unpractical for larger power scale devices where flow rates may be of the order of 100 $m^3/s$. The use of unidirectional turbines has been tested in different configurations, as it is the case of the twin turbines in [79], the SeaBreath [52], or the ShoreSWEC [54].

The goal of the Tupperwave project is to design and validate in laboratory an innovative OWC concept that mitigates the aforementioned negative features of the conventional OWCs devices equipped with self-rectifying turbines. The Tupperwave concept consists in generating a unidirectional air flow in a closed circuit, by adding two reservoirs to the conventional OWC chamber, a high pressure chamber and a low pressure chamber. Each of these chambers is connected with the OWC chamber through a system of non-return valves, and connected between them by a unidirectional turbine. Fig. E.2 describes schematically the working principle of the device under study.

The motion of the water column alternatively pushes air into the high pressure chamber through the valve $H$ when going up, and sucks air out from the low pressure chamber through valve $LP$ when going down. The air flows rather steadily from the high pressure to the low pressure chamber across an unidirectional turbine.

This paper presents a preliminary study which consists in a numerical model to simulate the device's dynamics, and its application for optimization purposes. As a reference case, it was assumed the Tupperwave concept to be integrated in a floating axisymmetric structure, with identical dimensions as the spar OWC developed by HMRC (now MaREI), UCC, under the Marinet project (see fig. A.2). It had shown good pitching stability and therefore would provide a good support for the Tupperwave PTO system.

A time-domain model was implemented in order to understand how various design factors would affect the overall device behaviour and resulting power output. The conversion from hydrodynamic power to pneumatic

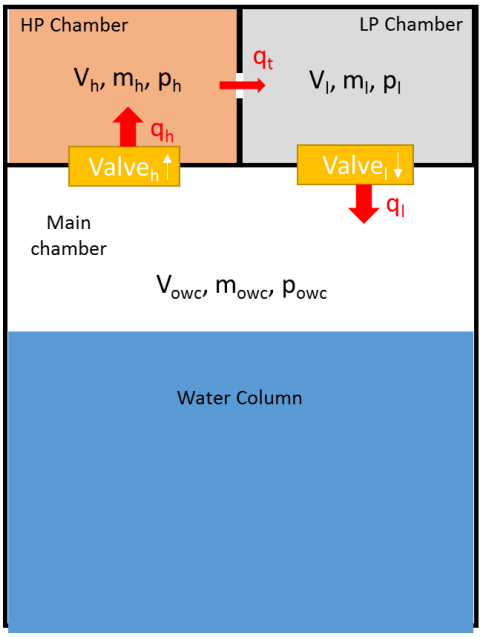


Figure A.1: Schematic diagram of the Tupperwave device concept

power was modelled based on the linear wave theory and linearised isentropic thermodynamic equations. Only heave motion was considered, and the unidirectional valves and the turbine were modelled as a simple orifice. Furthermore, it was assumed the valves completely open and close instantaneously.

A wide range of numerical simulations were carried out to test a set of design parameters, including the volumes of the three chambers, and the valve and turbine flow coefficients. Two methods to determine the radiation force were implemented - corresponding results are presented and compared. A mathematical description of the time-domain model is presented in more detail in section A.2. Section A.3 presents the results of the numerical time-domain model where simulations were run for both regular and irregular waves. Results are shown for relevant quantities, namely, the relative body and water column displacements, the air pressure within the chambers, the mass flow rate across the turbine, and the pneumatic power. The most important criteria for selecting the best configuration were considered to be a high average power, a low power fluctuation, and a reasonable maximum relative displacement value. Conclusions are summarized in section A.4.

## A.2 Model Description

In order to mathematically describing the dynamics of the Tupperwave device, several simplifications have been made. The hydrodynamics component is based on linear water wave theory, under the assumption that the

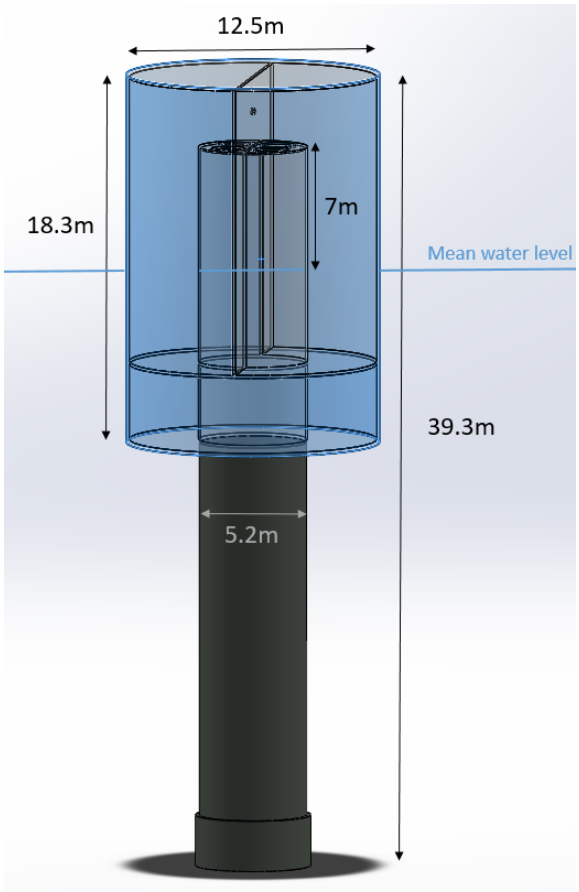


Figure A.2: Solidworks design of the optimised Tupperwave device

body motions and the wave steepness are sufficiently small. Furthermore, in the pressure dynamics, the isentropic expression relating the pressure to the density is linearised under the assumption that changes in air pressure within each of the chambers are small relative to its equleilibrium value [80]. As a further simplification, only the vertical motion of the floater, also known as the heaving mode, is considered ; only this mode contributes to the power conversion. Regarding the motion of the internal water column, the approach of the generalized modes presented in [81] is adopted. The dynamic boundary condition for the chamber internal free surface is represented by a superposition of modal distributions of the vertical velocity as shown in [82]. Assuming the chamber length is small compared with the typical wavelength, it is sufficiently accurate to consider only the vertical piston mode. Therefore, two motion degrees of freedom have to be taken into account: the heaving mode of the floater and the vertical piston mode of the OWC.

The ordinary differential equations which drive the two degrees of freedom may be written in the following matrix form:

$$M\ddot{z} = F_{exc}(t) + F_{rad}(t) + F_{hs}(t) + F_{pto}(t) \tag{A.1}$$

where $M$ is the system's mass matrix, z is the vertical coordinate of the system, $F_{exc}$ represents the excitation force inflicted by the incoming waves, $F_{rad}$ is the hydrodynamic radiation force imposed by the motion of both the body and the water column, and $F_{hs}$ is the hydrostatic restoring force. $F_{pto}$ is the force induced by the power take-off equipment. No forces due to mooring lines are considered in this work.

### A.2.1 Hydrodynamics

Under the linear theory, the hydrostatic restoring force is simply proportional to the amplitude of the heaving motion. The proportional factor is $\rho g$ times the respective horizontal cross section of the wetted surface. In regular waves the wave elevation profile has a sinusoidal form. The excitation force is therefore sinusoidal and frequency dependant. The hydrodynamic coefficients (added mass and hydrodynamic damping) are also frequency dependant. Excitation force and hydrodynamic coefficients were computed using the boundary element code WAMIT [29] taking into account a description of the free-surface elevation profile. For the case of irregular waves, the excitation force is expressed as the sum of a significant set of regular waves, each with a random phase, and whose amplitude is specified by a wave spectral model.

Regarding the radiation term, it is expressed as follows:

$$F_{rad}(t) = A_{\infty}\ddot{z}(t) - \int_0^t K(t-\tau)\,\dot{z}(\tau)\,d\tau, \tag{A.2}$$

where $A_{\infty}$ is the system's added mass at infinite frequency and $K$ is the system impulse response function. The impulse response function was calculated from the hydrodynamic coefficients using Cummins' equations ([83]). Two approaches were considered in this work for computing the convolution integral in eq. A.2: one was to directly compute the integral at each simulation time step. The other was to use a state-space model to approximate the convolution integral. The convolution integral is represented by a set of first order linear differential equations, by using Prony's method, as explained in [84].

### A.2.2 Power Take-Off component

The physical model representing the Tupperwave's closed circuit, which converts the wave power to pneumatic power, is here mathematically described. As shown in figure E.2, there are three chambers: a conventional OWC chamber, a high pressure chamber (HP) and a low pressure chamber (LP), with their corresponding air pressures, respectively, $p_{owc}$, $p_h$ and $p_l$. There are two non-return valves, valve $h$ and valve $l$. When $p_{owc} > p_h$, valve $h$ opens and air flows from the OWC to the HP chamber through the non-return valve.

Then the air is transferred through a turbine, from the HP chamber to the LP chamber. Then when $p_{owc} < p_l$, valve $l$ opens and the air flows from the LP back to the OWC chamber. Referring to eq. A.1, the term $F_{pto}$ results from the difference in air pressure inside the OWC chamber acting upon both, the internal structure of the WEC and the OWC surface:

$$F_{pto}(t) = \pm S_{owc}\left(p_{owc}(t) - p_{owc,0}\right), \tag{A.3}$$

where $S_{owc}$ is the OWC chamber cross section, $p_{owc}$ is the instantaneous air pressure in the chamber, and $p_{owc,0}$ is its pressure in equilibrium conditions. Note that the action of the air pressure on the structure and on the OWC piston mode is the same, but with opposite directions; in the equation, the plus sign corresponds to the structure, and the minus sign to the piston mode.

In order to express the air pressure in the OWC chamber, as well as the pressure in the other two chambers (high and low pressure chambers), and ultimately the pneumatic power, the mass balance for each of the chambers is taken into account:

$$\dot{m}(t) = \frac{\partial\left(\rho(t)V(t)\right)}{\partial t} = \rho(t)\frac{\partial V(t)}{\partial t} + V(t)\frac{\partial \rho(t)}{\partial t}, \tag{A.4}$$

where $\dot{m}$ is the mass flow rate for a given container, $\rho$ is the fluid density (air, in this case), and $V$ is the volume of the container. Assuming that the expansion/decompression of air within a given container is reversible, the isentropic relation can be applied

$$\frac{p}{\rho^{\gamma}} = \frac{p_{ref}}{\rho_{ref}^{\gamma}}. \tag{A.5}$$

where $p_{ref}$ and $\rho_{ref}$ are air pressure and density in reference conditions. Considering that the pressure of air in a given container fluctuates about an equilibrium value,

$$p(t) = p_{ref} + p'(t) \tag{A.6}$$

Then using the isentropic relation in equation (A.5), and taking the atmospheric pressure $p_0$, to be the reference pressure $p_{ref}$, the density within the container can be written as

$$\rho = \rho_0\left(1 + \frac{p'}{p_0}\right)^{\frac{1}{\gamma}}, \tag{A.7}$$

where the "$(t)$" notation has been suppressed. The excess pressure $p'$ being much smaller than the atmospheric pressure, the expression of the air density can be linearised as:

$$\rho = \rho_0\left(1 + \frac{p'}{\gamma p_0}\right) \tag{A.8}$$

The derivative of the density $\rho$ with respect to time is then given by

$$\frac{d\rho}{dt} = \frac{\rho_0}{\gamma p_0}\frac{dp'}{dt} \tag{A.9}$$

The mass balance within a container can be expressed as:

$$\dot{m} = \rho\frac{\partial V}{\partial t} + V\frac{\partial \rho}{\partial t}, \tag{A.10}$$

substituting in the expression for the rate of change of the density from equation (A.9), it becomes

$$\dot{m} = \rho\frac{\partial V}{\partial t} + \frac{\rho_0 V}{\gamma p_0}\frac{dp'}{dt} \tag{A.11}$$

Applying equation (A.11) to each of the three aforementioned chambers, the following linearized expressions (A.12), (A.13), (A.14) may be written, respectively, for the OWC chamber, the HP chamber and the LP chamber:

$$-Q_h + Q_l = -\rho_{owc}S_{owc}\frac{\partial z}{\partial t} + V_{owc}\frac{\rho_{owc0}}{\gamma}\frac{\partial}{\partial t}\left(\frac{p_{owc}}{p_{owc0}}\right), \tag{A.12}$$

where $Q_h$ is the mass flow rate from the OWC chamber to the high pressure chamber, $Q_l$ is the mass flow rate from the low pressure chamber to the OWC chamber (both flows through the respective non-return valve), $S_{owc}$ is the cross section area of the OWC chamber, and $z_r$ is the relative vertical displacement between the floater and the water column inside the chamber.

$$Q_h - Q_t = V_h\frac{\rho_{h0}}{\gamma}\frac{\partial}{\partial t}\left(\frac{p_h}{p_{h0}}\right), \tag{A.13}$$

where $Q_t$ is the mass flow rate across the unidirectional turbine.

$$Q_t - Q_l = V_l\frac{\rho_{l0}}{\gamma}\frac{\partial}{\partial t}\left(\frac{p_l}{p_{l0}}\right). \tag{A.14}$$

Subinhedices *owc*, *h* and *l* represent, respectively, the OWC, the high pressure and the low pressure chambers, and the subhindindex 0 represents the corresponding equilibrium value (atmospheric conditions).

The non-return valves connecting the OWC chamber to each of the other chambers are not always open. They are opened only for pressure difference values above a given positive threshold. Otherwise there is no flux of air passing through. In this article, the valve are assumed to be perfect and the pressure threshold at which the valves open is 0. The valves are also assumed to be either fully opened or fully closed.

Following [85], and [86], the mass flow rate through the valves is assumed to be proportional to the square root of the pressure drop and is modelled via,

$$\begin{cases} Q_v = C_v L_g h_{max}\sqrt{2\rho_{air}\left(p_{up} - p_{down}\right)}, & \text{for } p_{up} > p_{down} \\ Q_v = 0 & , \text{ for } p_{up} < p_{down} \end{cases} \tag{A.15}$$

where $C_v$ is the discharge coefficient for the valve, $L_g$ is the total edge length of the valve plate and $h_{max}$ the maximum valve opening. The pressures $p_{up}$ and $p_{down}$ are, respectively, the upstream and down stream pressures across the valve. [85] performs experimental tests on a model valve for which $L_g = 471.2$mm and $h_{max} = 3.14$mm. The expression used by [85] is slightly more complicated, and requires the instantaneous height of the valve opening, but here the same simplified approach of [86] is considered, which assumes that the valve is either completely open or completely closed. For a fully open valve, [85] empirically determines the discharge coefficient to be 0.69, whereas [87] uses a value of 0.5.

Hence, applying equation (A.15) to each mass flow rate through the valves gives:

$$\begin{cases} Q_h = C_{v,h} L_g h_{max} \sqrt{2\rho_{air} \left(p_{owc} - p_h\right)}, & \text{for } p_{owc} > p_h \\ Q_h = 0 & \text{, for } p_{owc} < p_h \end{cases} \tag{A.16}$$

and

$$\begin{cases} Q_l = C_{v,l} L_g h_{max} \sqrt{2\rho_{air} \left(p_l - p_{owc}\right)}, & \text{for } p_l > p_{owc} \\ Q_l = 0 & \text{, for } p_l < p_{owc} \end{cases} \tag{A.17}$$

As a simplification in this preliminary analysis, similarly to the valves, the flow through the turbine is also modelled as an orifice - assuming that the relationship between the mass flow rate and pressure drop is quadratic:

$$Q_t = \sqrt{\frac{p_h - p_l}{k_t}}. \tag{A.18}$$

Here $k_t$ is the turbine flow coefficient, which may be expressed as

$$k_t = \left(2\rho_{air} A^2 C_t^2\right)^{-1}, \tag{A.19}$$

where $A$ is the area of the orifice and $C_t$ the discharge coefficient. In the case of a conventional OWC, it is generally agreed that $A$, the orifice area should be between 0.5-2% of the OWC chamber area $S_{owc}$, see [88] and [89] for example. But it will be seen in section A.3 that a smaller orifice area is required in the case of the Tupperwave device. The value taken for $C_t$, varies but is typically between 0.5-1: [86] uses 0.6, whereas according to [87], the measured value for the discharge coefficient for a smooth venturi ranges from 0.95 to 0.97, but then went on to use a value of 0.9 in their own model.

Finally, the pneumatic power available at the turbine is given by

$$P_{prs} = \frac{1}{\rho_{air}} Q_t \left(p_h - p_l\right). \tag{A.20}$$

## A.3 Numerical Model Results

In this section the most relevant results from the numerical model presented in the previous section are displayed. Since two approaches were used for the radiation term computation, their results first need to be compared. The results in regular waves are then presented and commented. It includes a description of the method to optimise the main design parameters. Finally the performance of the optimized Tupperwave device is compared against a conventional OWC device.

### A.3.1 Comparison of the two approaches for the radiation force

Since WavEC and MaREI used two different methods to compute the convolution integrals of the radiation force (eq. A.2), it is necessary to compare the results from both approaches. A standard hydrodynamic model verification procedure is to carry out a decay test. In order to take into account only the system's hydrodynamics, the main OWC chamber is fully open to the atmosphere, and thus there is no effect from the PTO (no damping nor stiffness). The decay test is carried out in flat water - no excitation force. The OWC floating structure is initially positioned 1m above its floatation equilibrium point and is released at $t = 0$s. The hydrostatic restoring force and gravity lead to an oscillatory motion around the equilibrium, whose amplitude is increasingly attenuated by the hydrodynamic damping, until the motion is not significant any more. The water surface also gets slightly excited by the motion of the structure. For each body, the time interval between consecutive crests should correspond to their expected resonance period. Figure A.3 shows the decay test results obtained with both models.
The displacements given by the two methods are very similar but do not overlap exactly. The structure's motion is quicker damped in MaREI's model and the water column is slightly more excited. These small differences between the results of the two methods might not be significant once the PTO behaviour is included in the model.

When considering the PTO, the time series in regular waves did not overlap exactly but showed good similarities. Figure A.4 compares the two models results of the average pneumatic power output in 2m height regular waves for a device equipped with a turbine damping coefficient of $k_t = 300\text{kg}^{-1}.\text{m}^{-1}$ and chambers volume of $V_{lp} = V_{hp} = 750\text{m}^3$ and $V_{owc} = 150\text{m}^3$.

The power output results in regular waves show good agreement. Two main peaks are observed corresponding to the two bodies resonance frequencies. The first peak corresponds to the spar resonance period while the second peak corresponds to the water column resonance period. Assuming as acceptable the similarity between the results from both models for the radiation terms, only MaREI's results will be used hereinafter.

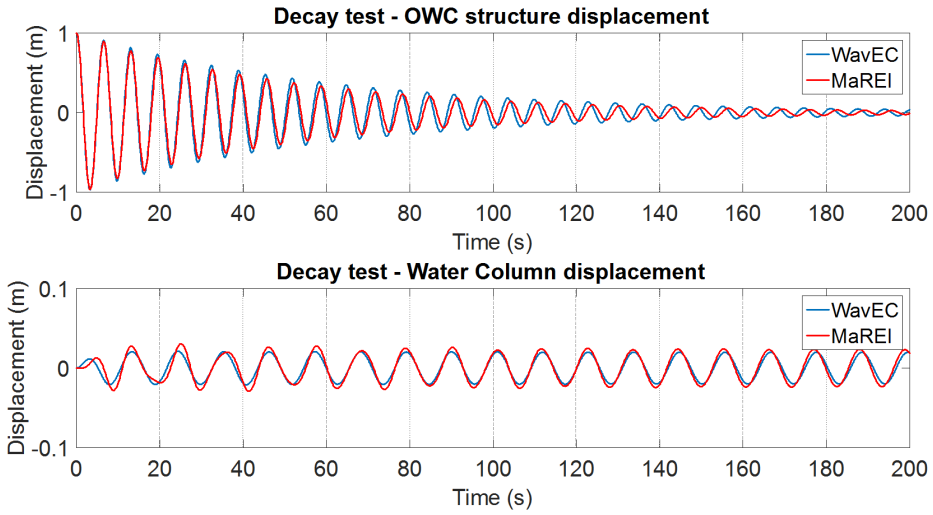


Figure A.3: Decay test for both methods of computing the radiation force

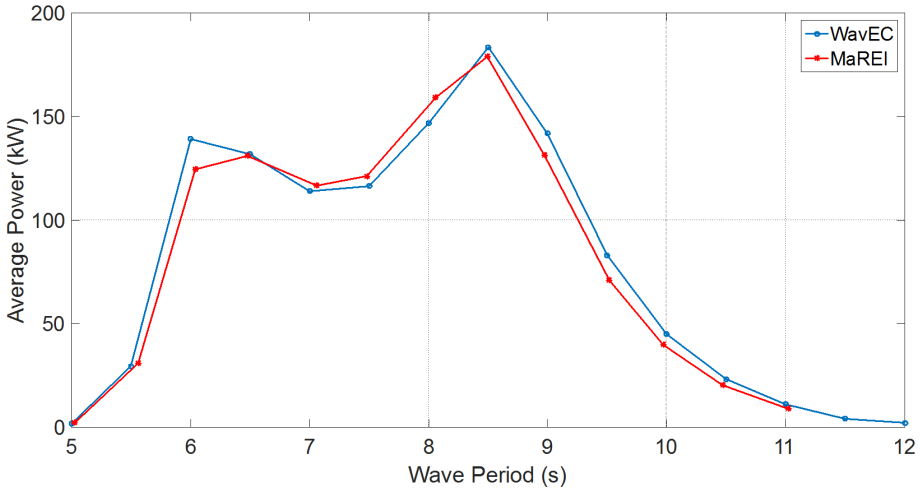


Figure A.4: Pneumatic power output of the device in 2m high regular waves assessed with both WavEC and MaREI's models

### A.3.2 Regular Waves Results

Figure A.5 gives the pressures, mass flows and volume time series of the Tupperwave device on a regular waves case: 2 meter high waves and 8.5 seconds period. At $t < 0s$, the device is floating on flat water and the chambers pressures are all at atmospheric pressure. At $t = 0s$ the waves start interacting with the device, and the OWC spar structure and the water column begin moving relatively to each other. The volume $V_{owc}(t)$ of the main OWC chamber starts oscillating. The pressure in the HP chamber rises while the pressure in the LP chamber decreases. The mass flow rate through the turbine slowly increases. After roughly 70 seconds, $V_{owc}(t)$ follows a sinusoidal

motion. The system has reached a stable regime and all variables will keep on oscillating periodically. The pressure drop between HP and LP chambers is relatively constant overtime and so is the mass flow rate flowing through the turbine.

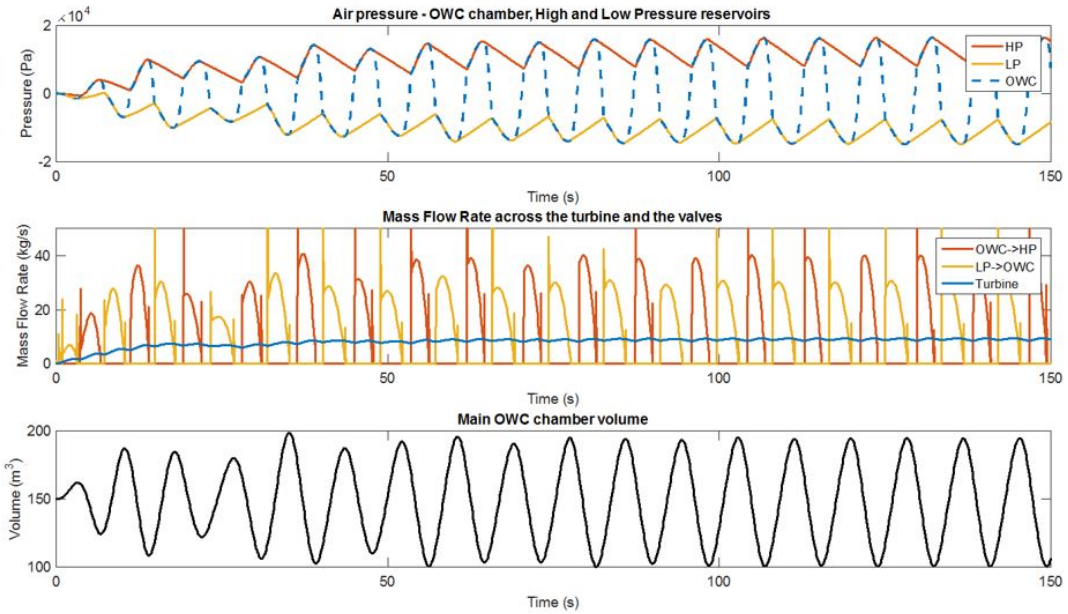


Figure A.5: 2m high Regular waves - pressures, mass flow rates and main chamber volume -series - $[V_{owc}, V_h] = [150, 750]\text{m}^3$, $k_t = 300\text{kg}^{-1}.\text{m}^{-1}$, $T = 8.5\text{s}$

In order to fully understand what is going on in the device, a breakdown of the device working cycle is given in figure A.6, which displays the pressures in the chambers and the volume of the OWC main chamber. At $t = t_1$, the main OWC chamber volume $V_{owc}$ reduces and the pressure $p_{owc}$ rises. Both valves are closed as $p_l < p_{owc} < p_h$. As $p_h > p_l$, chamber HP slowly discharges into chamber LP through the turbine. $p_h$ slowly reduces while $p_l$ slowly increases. At $t = t_2$, $p_{owc}$ gets slightly higher than $p_h$. Valve $h$ opens and air flows from the OWC chamber to the HP chamber. Since the damping induced by the opened valve is very small, the pressure drop through the opened valve is close to zero, and $p_{owc}(t) \approx p_h(t)$ during this phase. As $V_{owc}$ keeps reducing, $p_h$ increases. At $t = t_3$, $V_{owc}$ starts to expand. Immediately the pressure in the main OWC chamber reduces and valve $h$ closes. Air continues to be transferred from HP chamber to the LP chamber through the turbine. Pressure $p_{owc}$ collapses quickly until $t = t_4$ where $p_{owc}$ reaches $p_l$. Valve $l$ opens and air flows from the LP chamber into the OWC chamber. Symmetrically to the phase $t_2 < t < t_3$, , the air flows easily from chamber LP into the OWC chamber as $V_{owc}$ further expands, and $p_l$ reduces. At $t = t_5$, V reverts again its evolution and starts reducing. p rises and valve $l$ closes. The cycle repeats then from $t_5$ to $t_9$, and so on.

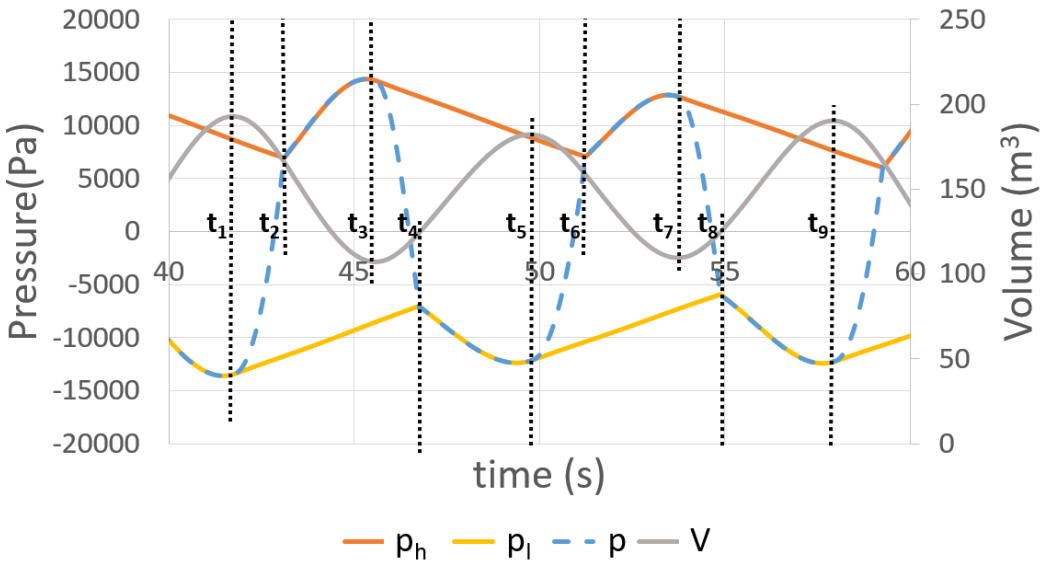


Figure A.6: Tupperwave cycle breakdown - [Vowc, Vh] = [150, 750]$m^3$, Kt = 300$kg^{-1}.m^{-1}$, $T = 8.5s$

In the end, the pressure difference between the two chambers is kept relatively constant by the motion of the water column in the moving structure. The high pressure chamber almost constantly discharges into the low pressure chamber. The airflow rate through the turbine is unidirectional and can be harnessed with a conventional unidirectional turbine. As opposed to in a conventional OWC where the mass flow stops at each period to change direction, the mass flow rate through the turbine in the Tupperwave device is relatively constant.

From a more energetic point of view. The high and low pressure chambers act as accumulators. They store, under the form of pressure, the important pneumatic energy generated in half a period by the rising or falling water column and release it at a much slower pace though the turbine. Thus, the lull of pneumatic power, observed in conventional OWC, when the water column is changing direction, is almost erased.

The pneumatic power to be harnessed is therefore much smoother compared to a conventional OWC (see section A.3.4). A smooth power output is a great asset as it simplifies the turbine control strategy as well as the power electronic work that needs to be done before sending the power onto the grid.

### A.3.3 PTO Optimization

Ideally, the pneumatic power should be as high and as smooth as possible. An optimisation work has been undertaken to maximise the power output as well as the power smoothing of the Tupperwave device. The parameters to be optimized are the chambers volumes, and turbine flow coefficient.

The relative computational ease with which the simulations are run on Matlab allows to use a brute force optimisation method. The valves flow coefficients were desirably small, corresponding to their large area, limited by the available surface. Both chambers HP and LP were assumed to have the same volume $V_h$. The tested chambers volumes are constrained by the total volume of the floater. Different values for the PTO damping $k_t$ and for the chambers volumes $V_{owc}$ and $V_h$ were tested.

As explained in section A.2, the turbine is simply modelled by an orifice. Technically the damping is unlimited as it is related to the size of the turbine and that the damping increases when the size of the orifice decreases. In order to provide the reader a better idea of the tested damping coefficients, table A.1 gives the damping coefficient $k_t$ for different orifice diameters with a discharge coefficient C=0.74 [90].

Table A.1: Diameter and theoretical damping of chamfered orifices with C=0.74.

| orifice diameter [cm] | Surface orifice [$m^2$] | $k_t$ [$kg^{-1}.m^{-1}$] |
|---|---|---|
| 59.0 | 0.273 | 10 |
| 46.9 | 0.173 | 25 |
| 39.4 | 0.122 | 50 |
| 33.1 | 0.0863 | 100 |
| 30.0 | 0.0705 | 150 |
| 25.2 | 0.0498 | 300 |
| 20.0 | 0.0315 | 750 |
| 15.0 | 0.0177 | 2386 |

The optimisations criteria were to maximize the power output and the power smoothing. In order to characterise the power smoothing an additional variable called power fluctuation $f_p$ was used:

$$f_p = \frac{std(P)}{\bar{P}} = \frac{1}{\bar{P}} \cdot \sqrt{\left( \frac{1}{t_{final}} \int_0^{t_{final}} (P(t) - \bar{P})^2 \, dt \right)} \tag{A.21}$$

Optimising the smoothing is equivalent to minimizing the power fluctuation around its average value.

Due to the huge amount of tested cases, results here presented are limited to the most relevant. Although it is not explicitly displayed, one outcome

of the simulations was that $V_{owc}$ should be small compared with $V_h$. The following results correspond to $V_{owc} = 150\text{m}^3$.

Focussing on the HP and LP volume and on the turbine flow coefficient, each couple $(k_t; V_h)$ was simulated in regular waves for periods ranging from 5 to 12 seconds. The wave height tested were 1, 2 and 4m. The simulation time was 250 seconds, but the relevant quantities are computed only for the stable regime, which is assumed to be reached after 100 seconds. Double entry tables displaying the average power and the power fluctuation were then generated to visually identify the optimum $(k_t; V_h)$ couple.

In order to choose a couple $(k_t; V_h)$ that satisfies the most wave periods between 5 and 12 seconds, an averaging of the power output and of the power fluctuation over all periods tested was performed for each configuration. Results obtained with 2m high waves are displayed in tables A.2 and A.3. The colour formatting allows to easily spot the higher power and lower power fluctuation. The green areas in tables A.2 and table A.3 show respectively the higher power and the lower fluctuation. Highlighted in bold are the values of $k_t$ and $V_h$ that combine high power output and low fluctuation.

Table A.2: Average Power output in 2m high regular waves for period from 5 to 11s

Power [kW]

| | $k_t$ [$\text{kg}^{-1}.\text{m}^{-1}$] | | | | | | | |
|---|---|---|---|---|---|---|---|---|
| $V_{01}$ [$\text{m}^3$] | 10 | 25 | 50 | 100 | 150 | **300** | **750** | 2386 |
| 300 | 49.9 | 64.6 | 72.3 | 78.5 | 82.1 | 87.3 | 89.6 | 79.0 |
| 400 | 50.7 | 61.7 | 70.7 | 78.2 | 82.1 | 87.7 | 90.3 | 79.5 |
| 500 | 51.4 | 61.0 | 69.4 | 77.6 | 81.8 | 87.8 | 90.5 | 79.6 |
| **750** | 49.7 | 59.2 | 67.4 | 76.1 | 80.9 | 87.4 | 90.5 | 79.4 |
| **950** | 49.0 | 58.0 | 66.2 | 80.2 | 83.8 | 90.0 | 90.2 | 78.8 |
| **1000** | 48.8 | 57.7 | 66.0 | 75.1 | 80.0 | 87.0 | 90.1 | 78.7 |

Table A.3: Average power fluctuation table in 2m high regular waves for period from 5 to 11s

Fluctuation [%]

| $V_{01}$ [m$^3$] \ $k_t$ [kg$^{-1}$.m$^{-1}$] | 10 | 25 | 50 | 100 | 150 | **300** | **750** | 2386 |
|---|---|---|---|---|---|---|---|---|
| 300 | 84.9 | 71.0 | 57.5 | 44.8 | 38.0 | 27.9 | 18.3 | 10.9 |
| 400 | 80.3 | 63.3 | 49.4 | 36.8 | 30.3 | 21.6 | 13.9 | 8.3 |
| 500 | 75.1 | 57.5 | 43.3 | 30.9 | 25.1 | 17.5 | 11.2 | 6.8 |
| **750** | 66.6 | 46.5 | 32.4 | 21.7 | 17.3 | 11.9 | 7.6 | 5.3 |
| **950** | 60.6 | 40.0 | 26.7 | 13.8 | 11.4 | 7.3 | 6.1 | 4.8 |
| **1000** | 59.4 | 38.6 | 25.6 | 16.7 | 13.1 | 9.0 | 5.8 | 4.8 |

Table A.3 clearly shows that $V_h = 950\text{m}^3$ provides the best power smoothness for the range of $k_t$ highlighted. Table A.2 shows that the average power extraction of the device in regular waves depends mostly on the damping coefficient. Also, the power fluctuations decrease with the damping coefficient. $k_t = 750\text{kg}^{-1}.\text{m}^{-1}$ reveals to be the most efficient on average for all wave periods for 2m high waves and provides an average power fluctuation of 6.1% once associated with $V_h = 950\,\text{m}^3$.

The results obtained with 1m and 4m high waves showed that the optimized turbine damping value $k_t$ decreases when the wave height increases. For 2 meter high waves, the optimized turbine damping is close to 2386 $\text{kg}^{-1}.\text{m}^{-1}$ while for 4 meter high waves it is closer to 300 $\text{kg}^{-1}.\text{m}^{-1}$. Also the pneumatic power output of the device showed to be increasing linearly with the wave height squared.

The optimal PTO damping therefore depends on the sea state and needs to be tuned accordingly [91]. In the case of an actual unidirectional PTO turbine, the damping can be tuned by controlling the turbine rotational speed or the pitching of the blades. Similarly to conventional OWC devices, it was observed that, for a certain wave height, higher PTO damping show better efficiency in long period waves ($\sim$ 8.5s) while lower PTO damping are more efficient in short period waves ($\sim$ 6.5$s$). For two meter high waves, the value $k_t = 300\text{kg}^{-1}.\text{m}^{-1}$ is almost equally efficient for wave period from 6 to 9 seconds as will be observed in the next section (table A.7).

The PTO configurations $[k_t = 300 - 2386\text{kg}^{-1}.\text{m}^{-1}; V_h = 950\text{m}^3]$ provide in average good power output and power smoothness among all value tested in 1 to 4 meter high waves for wave periods from 5 to 11 seconds. A visualisation of this configuration is shown in Figure 7.

Table A.4: Average mean power per wave height squared and average power fluctuation for [$k_t = 300\text{kg}^{-1}.\text{m}^{-1}$;$V_h = 950\text{m}^3$] for wave heights $H$=1,2, and 4m, for wave periods $T$=5-11s.

| Wave height [m] | H=1 [m] | H=2 [m] | H=4 [m] |
|---|---|---|---|
| Average mean power [kW/m$^2$] | 20.13 | 21.77 | 21.99 |
| Average power fluctuation [-] | 13.69 | 9.43 | 6.71 |

### A.3.4 Performance comparison with conventional OWC

In parallel to the modelling of the Tupperwave device, a conventional OWC was modelled using the same OWC spar structure. The bidirectional PTO turbine was also modelled by an orifice. The orifice damping was optimised to maximize the power output using the same brute force method described in the previous section. An optimized damping coefficient for the conventional OWC in 2 meter high regular waves was of $k_t = 25\text{kg}^{-1}.\text{m}^{-1}$. The PTO damping required in the Tupperwave device is higher than for the conventional OWC. The turbine adapted to the Tupperwave device is likely to be smaller and therefore cheaper.

Figure A.7 and A.8 compare respectively the power and dispersion curves of the conventional OWC and the Tupperwave device.

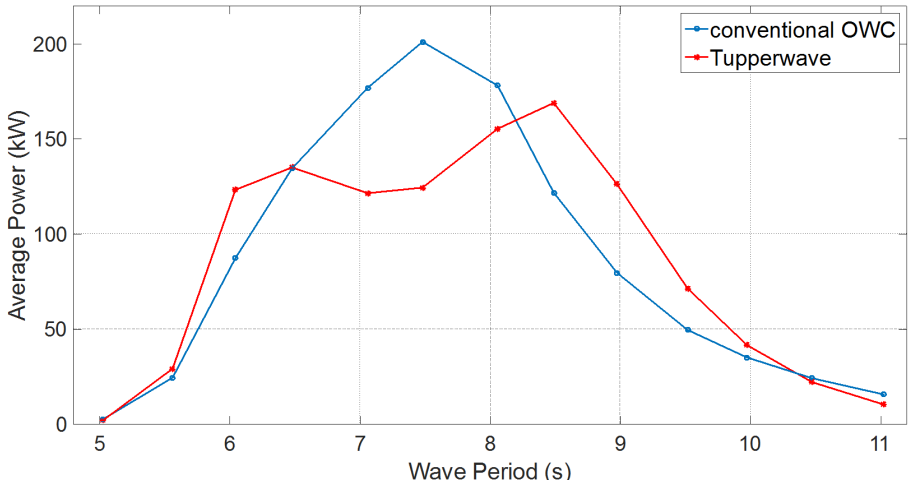


Figure A.7: Pneumatic Power in 2 meter high regular waves for conventional OWC and optimized Tupperwave device

While the power outputs of the two devices are of similar order, the power fluctuation around its average value is 8 times smaller for the Tupperwave

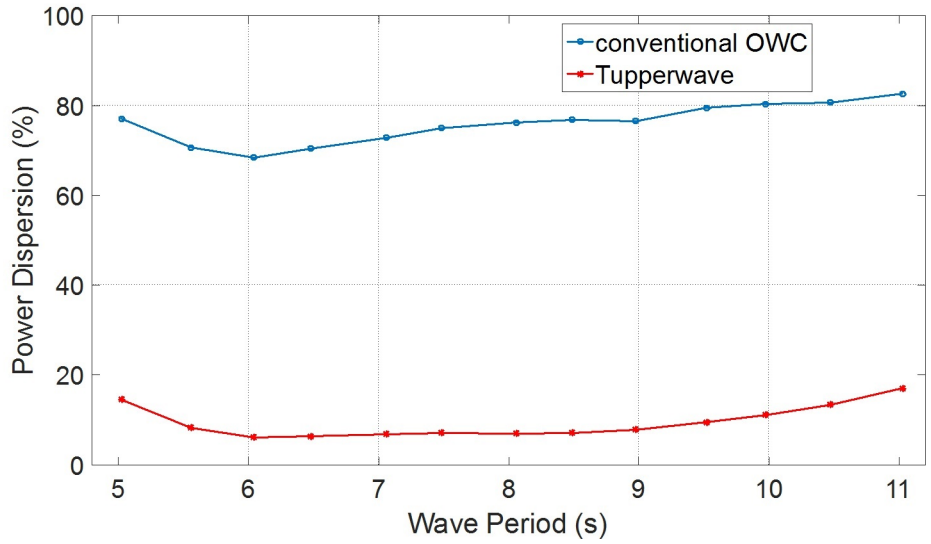


Figure A.8: Power fluctuation in 2 meter high regular waves for conventional OWC and optimized Tupperwave device

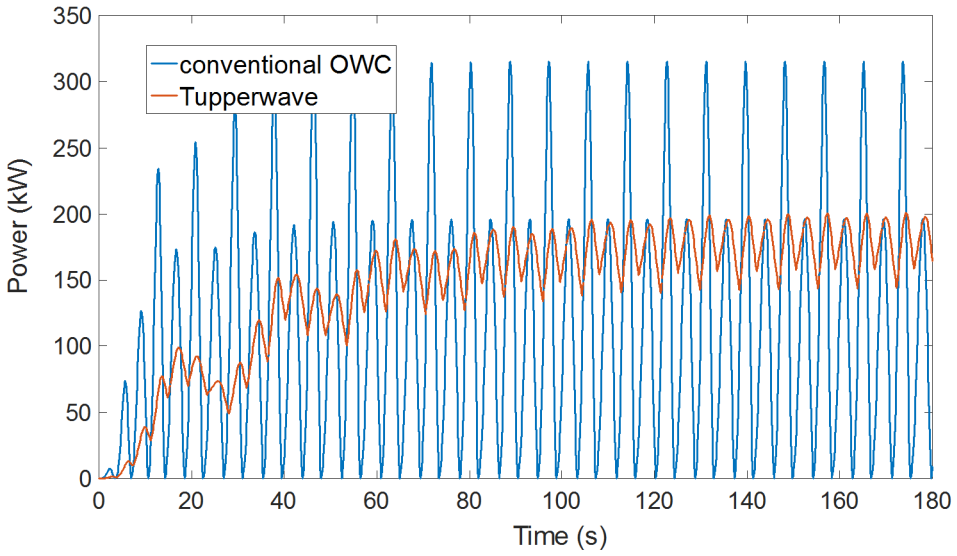


Figure A.9: Pneumatic power generation by Tupperwave device $\{[Vowc, Vh] = [150, 750]\text{m}^3, k_t = 300\text{kg}^{-1}.\text{m}^{-1}\}$ and conventional OWC device $\{k_t = 25\text{kg}^{-1}.\text{m}^{-1}\}$ in 2m high regular waves of period $T = 8.5\text{s}$

device. The Tupperwave device delivers a better power quality than a conventional OWC.

To illustrate the difference in power quality, figure A.9 displays the power time series of the conventional OWC and the Tupperwave device in 2 meter high regular waves of 8.5s period. While the conventional OWC's power oscillate between 0 and its highest peaks every half-period, the Tupperwave

device's power shows smaller oscillations. For this wave period, the Tupperwave device also shows a higher average power than the conventional OWC once the stable regime is reached as shown in figure A.7.

Figure A.10 displays the power time series of the conventional OWC and the Tupperwave device in irregular sea state of Hs=2m and Tp=8s. The pneumatic power across the Tupperwave's PTO is not only smoothened in-between wave periods but also in-between the wave groups.

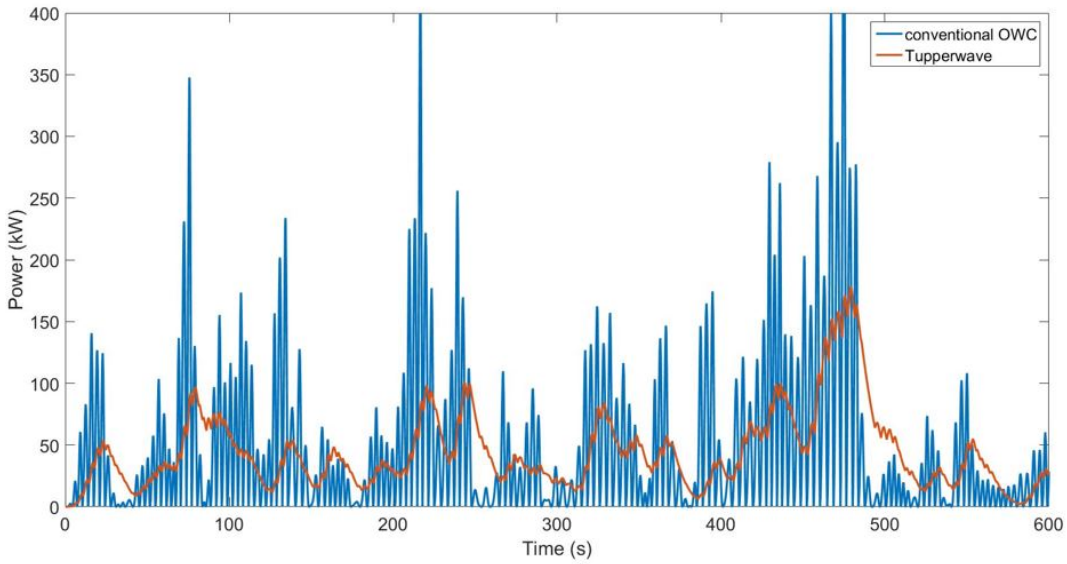


Figure A.10: Pneumatic power generation by Tupperwave device $\{[Vowc, Vh] = [150, 950]\text{m}^3, k_t = 750\text{kg}^{-1}.\text{m}^{-1}\}$ and conventional OWC device $\{k_t = 25\text{kg}^{-1}.\text{m}^{-1}\}$ in 2m significant height irregular waves of period $T = 8\text{s}$

## A.4 Conclusions

This works presented the innovative Tupperwave's OWC concept adapted onto a floating spar type OWC structure and a numerical model to assess its performance. A optimisation of the Tupperwave PTO main parameters has been performed to maximise the average pneumatic power output and minimize the power fluctuations in regular waves. Once optimised, the Tupperwave device showed good performances, both in regular and in irregular waves, particularly regarding the power fluctuation criterion: Tupperwave's unidirectional air flow show much lower fluctuation when compared against the highly fluctuating bidirectional air flow from the conventional OWC, which corresponds to a higher pneumatic power quality. The efficiency of unidirectional turbines being higher than self rectifying turbine, more pneumatic power is expected to be converted into electrical power. Also, because

of the low power fluctuations, the Tupperwave concept might require a less complex turbine control system and a more efficient power electronics equipment.

Despite some assumptions that simplify the numerical model, results look physically acceptable. Nevertheless, near future work within the Tupperwave project will be focussed on improving the thermodynamics modelling, and also characterizing the unidirectional turbine. CFD simulations are currently being carried out under the Tupperwave project by CADFEM Ireland. Their results will be compared to the numerical results presented in this article. The device will also be tested at small scale in the LIR National Ocean Test Facility in Cork in the summer 2017, which will be an opportunity to validate the numerical model.

## Acknowledgment

The authors would like to acknowledge funding received through OCEANERA-NET European Network (OCN/00028).

# Appendix B

# Paper B

# Model Scale Testing of the Tupperwave device With Comparison to a Conventional OWC

*Published in*

Proceedings of the ASME 2018 International Design Engineering Technical Conferences & Computers and Information in Engineering Conference

*Authors*

Pierre Benreguig[1], Jimmy Murphy[1], Wanan Sheng[1]

[1]*MaREI Centre (ERI), University College Cork, Haulbowline Road, Ringaskiddy, Ireland*

# Abstract

A model testing campaign of the Tupperwave device was carried out to prove the working principal and validate a numerical modelling that had previously been developed. An appropriate and challenging scaling method was applied to the floating device to correctly model the air compressibility in the Tupperwave PTO. In parallel, a model scale conventional OWC was also buleannilt using the same axisymmetric structure geometry and both devices were tested and compared. The testing showed that the Tupperwave device produced less average useful pneumatic power than the conventional OWC. The primary losses were attributed to pneumatic power dissipation through the valves. The pneumatic power delivered by the Tupperwave device was however significantly smoother.
The paper describes the experimental set-up and the methods used to assess the devices performance. The results provide a direct comparison between the two physical models pneumatic power performances and an in-depth analysis of the valves behaviour is shown.


## B.1 Introduction

Wave energy has the potential of playing an important role in the world renewable energy mix [75]. A large variety of wave energy converters (WEC) exist but a technology to efficiently and economically harness wave energy has not emerged yet.
Among this variety of WECs, the Oscillating Water Column (OWC) is one of the most studied and shows interesting characteristics. The OWC device comprises of a partly submerged structure open at its bottom, inside which air is trapped above the water free surface. The hydraulic energy from the waves is first transferred to the air contained in the OWC chamber as pneumatic energy and then converted into mechanical and electrical energy by an air turbine and a generator. The success of the OWC largely depends on the performance and reliability of the air turbine.
Conventionally, the turbine connects the OWC chamber to the atmosphere. An alternating air flow is created through the turbine resulting from the rising and falling of the water column. Various types of pneumatic PTO systems can be used to harness this alternating air flow [9]. In order to deal with the inwards and outwards flows, the majority of OWC prototypes are equipped with self-rectifying bidirectional turbines, such as the Wells or impulse turbines. This type of turbine has a lower efficiency than a conventional unidirectional turbine. Also, as the airflow changes direction every couple of a seconds, the pneumatic power fluctuations through the turbine are important and induce difficulties in terms of control and power quality. Moreover, as the turbine is opened to the atmosphere, significant acoustic noise can be

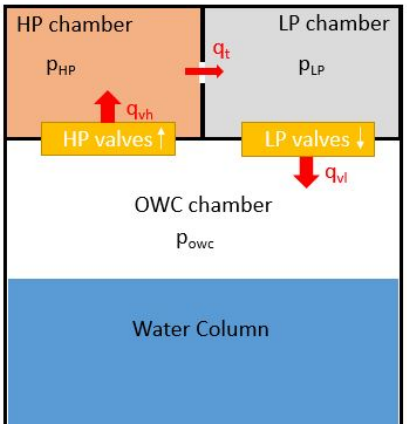


Figure B.1: Schematic diagram of the Tupperwave device concept

created.

An alternative consists of creating a closed-circuit air flow in the device driven by the rising and falling of the water column and using rectifying non-return valves. The air flow is then harnessed with a high-efficiency unidirectional turbine. This closed-circuit method has been tested in different multi-chambers OWC devices, as is the case of the LEANCON [53], the SeaBreath [92], or the ShoreSWEC [93]. Those very large multi-chamber devices work on the assumption that similar quantities of air are being blown from a chamber and sucked into another chamber at the same time.

The goal of the Tupperwave project is to design and validate at laboratory scale an innovative OWC concept that uses air compressibility in two large fixed volume accumulator chambers to generate a smooth unidirectional air flow in a closed circuit. Each of these chambers is connected with the OWC chamber through a system of non-return valves, and connected between them by a high efficiency unidirectional turbine. Figure E.2 describes schematically the working principle of the device under study. The motion of the water column alternatively pushes air into the high pressure chamber (HP chamber) through the HP valves when rising, and sucks air out from the low pressure chamber (LP chamber) through LP valves when falling. The air flows rather steadily from the HP chamber to the LP chamber across an unidirectional turbine.

For the development of such a system, the concept was applied in a floating axisymmetric structure, with submerged dimensions based on a device previously tested in the MaREI Center as part of the Marinet project [94]. The PTO characteristics, mainly the accumulator chamber volumes and the turbine damping coefficient, were previously investigated in [95] to maximise the average pneumatic power whilst minimizing their fluctuations. It showed that the Tupperwave device could potentially create as much useful

pneumatic power as a conventional OWC of the same geometry.

As a second step of the project, a tank testing campaign of the device at model scale was carried out in the Lir-National Ocean Test Facility's Deep Ocean Basin. The device was built at a scale of 1/24 and equipped with all necessary instrumentation to fully monitor its behaviour. A model scale conventional OWC was also tested using the same axisymmetric structure geometry. The two devices were tested in the same conditions both in fixed and floating states in regular and irregular sea states. The Tupperwave working principle relies on compressibility which is not scalable with Froude similarity law. Another scaling method for the HP and LP chambers was used. The multiple objectives of the physical testing were:

1. to prove the device working principal and assess the device power production
2. to show the feasibility of small scale testing of such floating device despite complex compressibility effects
3. to compare the Tupperwave and conventional spar OWC model pneumatic power performances
4. to validate the numerical models developed in [95].

This paper presents the design, fabrication and tests of the Tupperwave model scale device and compares the performance with the tested conventional OWC. The validation of the numerical model is not in the scope of this article.

## B.2 Physical model design and fabrication

In order to fairly compare the Tupperwave device to the conventional OWC, a single Spar buoy was built and both PTOs were built to fit on this same Spar. The following sections describe the Spar and PTO design and fabrication for both devices.

### B.2.1 Floating Spar

The spar buoy concept is the simplest concept for floating OWC. It is an axisymmetric device consisting basically of a submerged vertical tail tube open at both ends, fixed to a floater that moves essentially in heave. The single heave motion makes it simple to model: The system can be represented as a two body system (structure + water column) moving relatively in the vertical direction. The geometry of the spar buoy at full scale is shown in fig. 2a. For the model scale, all dimensions were multiplied by a scaling factor $\varepsilon = 0.0415$ which is close to 1/24th scale. The Spar model was built using a aluminium

cylinder of 21.59cm internal diameter and 6.35mm thick. A 6mm aluminium plate was welded on top to support the different PTOs. The floatation consisted of high density foam. A 14kg lead ring was attached at the bottom of the float to ballast the device. The 3D-design of the spar is shown in fig. 2b.

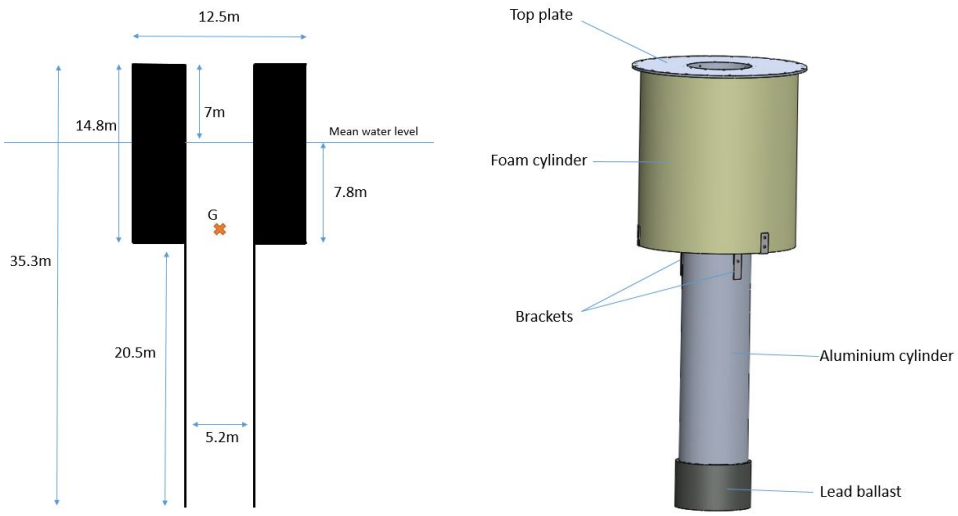


(a) Full Scale Dimensions (b) Model Scale 3D design

Figure B.2: SCHEMATIC OF THE SPAR BUOY

### B.2.2 Conventional OWC Power-Take-Off

The PTO of the conventional Spar OWC was chosen to be a self-rectifying impulse turbine. This type of turbine is commonly modelled physically by an orifice plate. Assuming constant air density under the testing conditions, the pressure $\Delta p_t$ and air mass flow rate $\dot{m}_t$ across the thin orifice plate are related by the following equation:

$$\Delta p_t = k_t \dot{m}_t{}^2 \tag{B.1}$$

$k_t$ is called orifice damping coefficient. The numerical modelling carried out previously in [95] showed that the damping coefficient of 25 $\mathrm{Pa.s^2.kg^{-2}}$ was close to optimal for the full scale device. For the model device, the damping coefficient was also scaled down using Froude scaling and 3 different orifice plates with damping coefficients close to this value were built and tested. Their exact damping coefficient were determined experimentally prior to testing in the OWC by forcing a known sinusoidal air flow across the orifice and measuring the pressure drop.

The orifice plate was simply screwed on top of the column using a rubber joint between the orifice plate and the top plate to insure airtightness.

### B.2.3 Tupperwave Power-Take-Off

The Tupperwave PTO is composed of non-return valves, 2 accumulators and a unidirectional impulse turbine. Each reservoir is connected to the OWC chamber through a system of non-return valves and connected to one another by the turbine.

#### B.2.3.1 Scaling method of HP and LP chambers

Since the device working principal relies on air compressibility in the HP and LP chambers, the right scaling method needs to be used for the down-scaling of the chambers. The scale ratio $\varepsilon$ is 0.0415. A scaling method suggested to scale down the OWC chamber volume to properly represent the spring-like effect of the air in the OWC chamber is suggested in [74]. Assuming the turbines to be equally efficient at model and full scale, the ratio between the OWC chamber volume at model scale and full scale is given by:

$$\frac{V_{0_M}}{V_{0_F}} = \varepsilon^2.\delta^{-1} \tag{B.2}$$

$\delta$ is defined as the ratio between the water densities $\rho_w$ at full and small scale ($\delta = \frac{\rho_{w_M}}{\rho_{w_F}} = 0.97$). Using the same derivation method as used in [74] it can be shown that this same method is applicable for the scaling of the accumulators chambers.

This scaling law for the chambers size requires much bigger size chamber than the Froude similarity would require. In the full scale device, the HP and LP chambers are 950 $m^3$ each. Froude scaling would give 0.068 $m^3$ for each chamber at small scale. The scaling suggested by equations C.18 gives 1.69 $m^3$ per chamber. Unlike for the full scale, it is impossible to fit both chambers on the device as their volume largely exceed the overall volume of the device. The alternative at small scale is to locate the main volume of the HP and LP chambers outside of the device and connect them to two smaller chambers on the device with flexible pipes.
Two 1 $m^3$ IBC tanks per chamber were used and were partially filled with water in order to match the required volume of air per accumulator.

Figure B.3 shows the Tupperwave model in regular waves connected to both HP and LP accumulators on the pedestrian bridge. Care was taken to reduce the influence of the flexible pipes on the motion of the buoy and part of the pipes weight was supported by bungee ropes.

##### B.2.3.1.1 Remark on OWC chamber scaling method

Since the air compressibility in the HP and LP chamber is essential in the Tupperwave device working-principle, efforts were made to physically model it

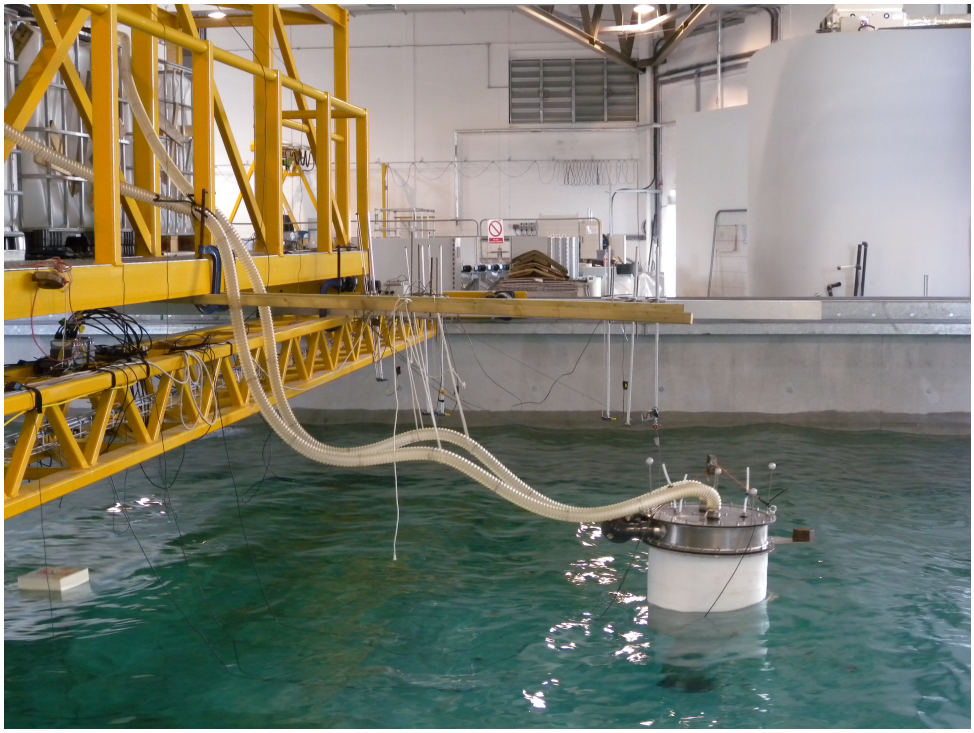

Figure B.3: TUPPERWAVE IN IRREGULAR WAVES

by using the scaling method described above. However, the air compressibility in the full scale 148 $m^3$ OWC chamber, is not essential for the device working-principle and was therefore not modelled. This would have required a third flexible pipe connecting the OWC chamber to another 0.264 $m^3$ reservoir on the bridge and would have increase the testing difficulty even more. The OWC chamber was therefore downscaled with Froude similarity to 0.011 $m^3$. Thus, this needs to be kept in mind that dynamic similarity of the air spring-like effect in the OWC chamber of the full scale device was not achieved in this testing. The study of the exact consequences of such modelling on the device behaviour is of interest for a future work.

#### B.2.3.2 Turbine

The unidirectional turbine chosen for the Tupperwave device is also of impulse type and modelled using orifice plates located inbetween the two smaller chambers on the device. The numerical modelling carried out previously in [95] showed that the optimized turbine damping coefficient was in the range of $300 - 750$ $Pa.s^2.kg^-2$ for the full scale device. For the model scale device 3 orifice plates were built around those values scaled down using Froude similarity law. Their exact damping coefficient were also determined experimentally prior to testing.

#### B.2.3.3 Valves

The Tupperwave's working principle relies on the use of non-return valves. The valves are a key component of the PTO because they are likely to cause pneumatic power losses. They can either be passive or active. Passive valves are usually less complex to implement and more robust than active valves but may not be as efficient.
For the physical model, passive valves were chosen for their simplicity. The most appropriate valves found on the market for the small scale physical model were the Capricorn MiniHab HypAirBalance, see fig. 4. They are passive normally closed air admittance valves from the plumbing market. A rubber membrane contained in the valve obstructs with gravity the opening of the valve. When sufficient pressure is applied, the rubber membrane is lifted up and the valve opens. Their opening pressure is about 70Pa (1686Pa at full scale) and their relatively small size allowed their use in the small scale physical model.

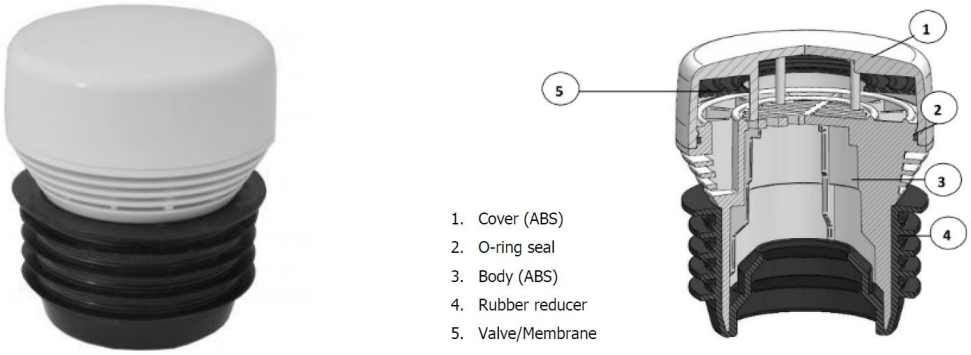


(a) Picture (b) Section

Figure B.4: MINIHAB HYPAIRBALANCE FROM CAPRICORN USED IN TUPPERWAVE SMALL SCALE MODEL

Their only drawback is the fact that, since they are gravity operated, they only work properly when positioned the right way up in vertical position. The HP valves therefore had to be positionned on a U-shaped PVC duct. Since a larger valve opening area reduces the valves damping, it is beneficial to maximise the number of valves on each side. Because of the necessary U-shaped PVC set-up for the HP valves, only 2 valves could be fitted between the OWC chamber and the HP chamber. In order to keep the device symmetrical, 2 valves were also fitted on the other side, between the LP chamber to the OWC chamber.

The damping of the valves will be discussed later in the article.

Table B.1: DEVICES MASS PROPERTIES

| | Model scale | Full scale |
|---|---|---|
| Total mass (kg) | 58.4 | $817.10^3$ |
| COG (m) | 0.892 | 21.49 |
| COB (m) | 0.961 | 23.16 |
| Ixx (kg.m$^2$) | 23 | $1,87.10^8$ |
| Iyy (kg.m$^2$) | 23.5 | $1,91.10^8$ |
| Izz (kg.m$^2$) | 2 | $1.62.10^7$ |

#### B.2.3.4 Devices mass properties

The conventional OWC PTO being lighter than the Tupperwave PTO, the conventional OWC was ballasted such that both device have the exact same mass properties. The mass properties of the device are given in table C.1.

## B.3 Experimental setup

The device was tested in the LIR-NOTFs Deep Ocean Basin in fixed and floating configuration under regular and irregular sea states. The fixed configuration was only tested in the scope of the numerical model validation and is not described in this article.

### B.3.1 Wave Basin

The dimensions of the LIR-NOTFs Deep Ocean Basin are 35m long, 12m wide and 3m deep. It has a movable floor plate to allow the water depth be adjusted, making it suitable for circa. 1/15 scale operational conditions and 1/50 scale survival waves in Atlantic conditions. Equipped with 16 hinged force feedback paddles capable of a peak wave generation condition of Hs = 0.6m, Tp = 2.7s and Hmax = 1.1m. An instrument bridge runs across the width of the basin and is used to support the electrical instrumentation and cables. A pedestrian bridge spans the basin as well and was used to support the four IBC tanks. For the tests the water depth was set to 2.075m, equivalent to 50m at full scale.

Table B.2: Tested Bretschneider sea states

| | Hs (m) | | Tp (s) | |
|---|---|---|---|---|
| Bretschneider | Full scale | Model | Full scale | Model |
| B1 | 2 | 0.083 | 5.66 | 0.083 |
| B2 | 3 | 0.1245 | 7.07 | 0.1245 |
| B3 | 3 | 0.1245 | 8.49 | 0.1245 |
| B4 | 5 | 0.2075 | 8.49 | 0.2075 |
| B5 | 3 | 0.1245 | 10.61 | 0.1245 |
| B6 | 5 | 0.2075 | 10.61 | 0.2075 |
| B7 | 5 | 0.2075 | 12.73 | 0.2075 |
| B8 | 3 | 0.1245 | 14.14 | 0.1245 |

### B.3.2 Test Plan

The devices were tested in both regular and irregular sea states. For the regular sea states, 2 wave heights (2 and 4m at full scale equivalent) were tested with periods ranging from 5 to 14s. A set of irregular sea states of various significant wave heights and peak periods was also tested. Table B.2 displays the characteristics of the irregular wave tests.

The regular wave tests were 125 seconds long, which is equivalent to 10 minutes at full scale. The irregular wave tests are 7 minutes long which is equivalent to 35 minutes at full scale. This allows a full representation of the Bretschneider sea state.

For the analysis of regular wave tests, averaging of the key variables is made over several waves once a steady state is reached, practically between 90 and 115s at model scale. The average values in irregular sea states are calculated over the full time of the simulation.

### B.3.3 Moorings

The device is moored with a 3 point mooring arrangement of catenary type with 120 degrees between any two mooring lines. There are 2 bow mooring lines and 1 stern line.

### B.3.4 Device Monitoring

Both devices were equipped with a number of instrument to monitor the devices' behaviours. They were connected to a National Instrument Compact Rio data acquisition system which recorded at a sampling rate of 32Hz and stored the data on a text file. Pressure sensors, wave probes and 3D-cameras allowed to fully monitor the movements, pressures and flows of the device.
For the measurement of the internal water surface relatively to the buoy (IWS), a wave probe was located in the water column.
The air flows through the orifices and valves were calculated using the measured pressures. The mass flow $\dot{m}_t$ across the thin orifice plate representing the turbine was calculated using eq. B.1 by:

$$\dot{m}_t = \sqrt{\frac{\Delta p_t}{k_t}} \tag{B.3}$$

$k_t$ is called orifice damping coefficient.
The same mathematical model was used for the valves:

$$\dot{m}_v = \begin{cases} \sqrt{\frac{\Delta p_v - p_{thres}}{k_v}} & if \quad p_v > p_{thres} \\ 0 & if \quad p_v < p_{thres} \end{cases} \tag{B.4}$$

$k_v$ is called valve damping coefficient and $p_{thres}$ is the valve opening pressure (70Pa).

The pneumatic power flowing through the orifice PTO $P_t$ and through the valves $P_v$ is calculated as the product of the volumetric flow and the pressure drop:

$$P = Q.\Delta p = \frac{\dot{m}}{\rho_0}.\Delta p \tag{B.5}$$

The available hydraulic power $P_{hydro}$ is the power of the force applied by the IWS on the air contained in the OWC chamber:

$$P_{hydro} = S.\frac{dx_{IWS}}{dt}.p_{owc} \tag{B.6}$$

where $S$ is IWS area, $x_{IWS}$ is the position of the IWS relatively to the buoy and $p_{owc}$ is the excess pressure of the air in the OWC chamber.

The available hydraulic power $P_{hydro}$ is the hydraulic power extracted from the waves by the device and converted into available pneumatic power. $P_v$ is the pneumatic power dissipated in the valves. $P_t$ is the useful pneumatic power or pneumatic power available to the turbine.

## B.4 Results and analysis

In this section, the Tupperwave device behaviour is first described and the power losses in the valves are estimated. The performance of the Tupper-

Table B.3: Device natural period of oscillations

| Natural oscillation period (s) | Small scale | Full scale |
|---|---|---|
| Heave | 1.37 | 6.7 |
| Pitch | 4.48 | 22.0 |
| Roll | 4.43 | 21.7 |

wave device are then compared to the conventional OWC tested in parallel. All results are given at full scale equivalent to give the reader a more significant perspective of the devices performances.

## B.4.1 Tupperwave Device Behaviour

### B.4.1.1 Decay tests

Decay tests for the heave, pitch and roll motion of the device were performed. The PTO was not installed on top of the water column in order to suppress all water column damping which can influence the buoy movement. The natural periods of oscillation in these three degrees of freedom are given in table B.3. The slight difference in the pitch and roll natural oscillation periods can be explained by the difference in moment of inertia due to the location of the Tupperwave orifice and its counter-balancing weight.

### B.4.1.2 Regular Waves

The Tupperwave device creates in regular waves a constant pressure difference between the HP and LP chamber which generates a smooth unidirectional flow across the orifice PTO. Among the 3 orifices tested, the device showed the best performance when equipped with a 9.2mm diameter of damping coefficient $1.24.10^8$ Pa.s$^2$.kg$^{-2}$ which is equivalent to 367 Pa.s$^2$.kg$^{-2}$ at full scale. The graphs of the pressure, mass flow and power time series obtained with this orifice for 2m high regular waves with 9 seconds period are given in fig. B.5. $p_{owc}$, $p_{HP}$ and $p_{LP}$ are the excess pressures relatively to the atmosphere in the OWC chamber, the HP chamber and the LP chamber respectively. $q_t$, $q_{vh}$, and $q_{vl}$ are the mass flows across the orifice and the HP and LP valves respectively (see fig. E.2).
The power time series show that the Tupperwave PTO system tranforms the highly fluctuating available hydraulic power into a smooth pneumatic power across the orifice. But the two signals do not have the same average value. It is clear that there has been losses in the transformation process.

Figure B.6 displays the average available hydraulic power and the average pneumatic power available to the turbine in 2 and 4 meter high waves

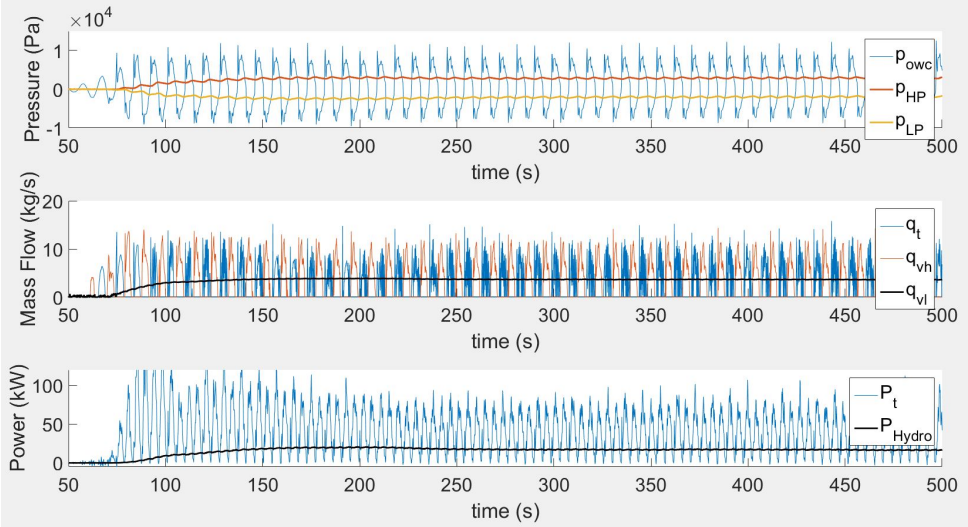


Figure B.5: Tupperwave device - 2 meter-high and 9seconds period regular waves - Pressure, mass flow and power time series

once the steady state was reached. The device produces the most useful pneumatic power for wave periods around 6.5-8.5s. The device does not convert all hydraulic power into useful pneumatic power.

Figure D.16 compares the average available hydraulic power to the sum of the average dissipated pneumatic power in the valves ($\overline{P}_{v_{hp}}$ and $\overline{P}_{v_{lp}}$) and in the orifice ($\overline{P}_t$), and shows that the available hydraulic power is entirely dissipated. This shows that the difference between the hydraulic power and the useful pneumatic power observed in fig. B.6 is equal to the power dissipated in the HP and LP valves.

The valves efficiency is defined as the ratio between the average pneumatic power available to the turbine over the average available hydraulic power of the water column:

$$\eta_{valves} = \frac{\overline{P_t}}{\overline{P_{hydro}}} \tag{B.7}$$

Figure D.16 has shown that:

$$\overline{P}_{hydro} = \overline{P}_t + \overline{P}_{v_{hp}} + \overline{P}_{v_{lp}} \tag{B.8}$$

Assuming that the valves have the same damping $k_v = k_{v_{hp}} = k_{v_{lp}}$, it can be shown that the valves efficiency can be approximated from the turbine and valve damping characteristics using the equation:

$$\eta_{valves} \simeq \frac{1}{1 + 2^3.\frac{k_v}{k_t} + 2.\frac{p_{thres}}{\overline{\Delta p_t}}} \tag{B.9}$$

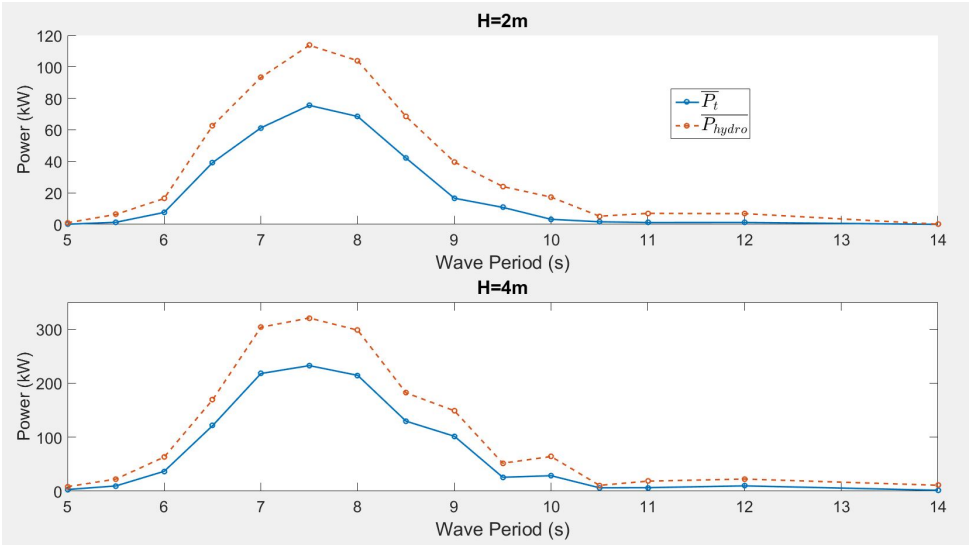


Figure B.6: Tupperwave device - average available hydraulic power and useful pneumatic power

Figure B.8 compares the actual efficiency to the estimation obtained with Eqn. D.24 for H=2m and H=4m. Equation D.24 gives a good approximation of the actual valves efficiency. This formula shows that in order to maximise the Tupperwave valves efficiency, the opening pressure of the valves need to be small compared to the average pressure drop across the orifice and the damping coefficient of the valves needs to be small compared to the damping coefficient of the turbine.

The valves efficiency is maximised between 6.5-8.5s seconds where the spar buoy and water column excitation is maximum. Outside of this range, the efficiency quickly drops and the hydraulic power from the water column is not transferred to the air in the OWC chamber. The device is also more efficient in higher waves. A maximum of 72.5% efficiency is reached for H=4m. This is due to the passive valves that require sufficient pressure to open fully. Higher valve efficiency (up to 80%) was obtained for the orifice with higher damping coefficient $k_t$ which created higher average pressure drop $\overline{\Delta p_t}$ across the turbine. These features clearly increase the efficiency according to equation D.24. But this orifice allowed less hydraulic power to be extracted from the waves and produced in the end less pneumatic power. Figure B.9 displays the average damping coefficient $k_v$ of the HP valves obtained for the different wave periods. The damping coefficient of the valves reaches a plateau around 5 $\mathrm{Pa.s^2.kg^{-2}}$ between 6.5 and 8.5s wave period. It is larger outside of this range and thus the valves efficiency decreases. For H=4m, the valves open fully on a larger range of wave periods. The dependence of the valves efficiency on the bodies excitation is clearly a drawback to passive valves because it reduces the device performance bandwidth.

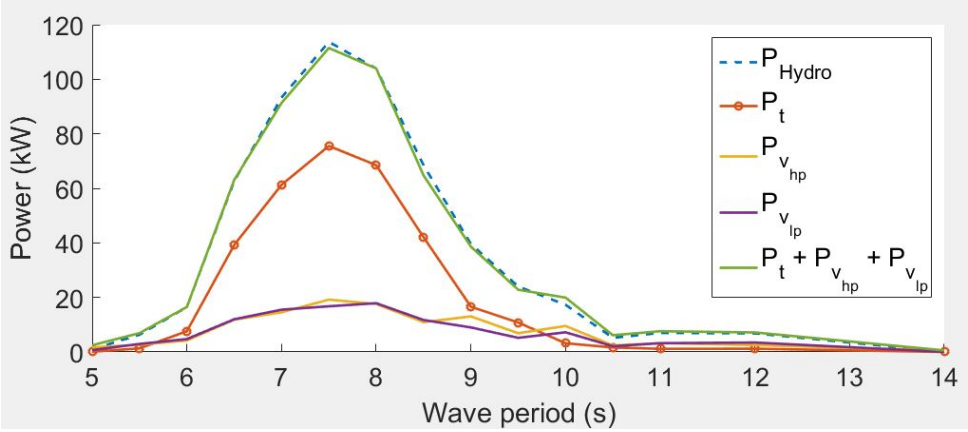


Figure B.7: Tupperwave device - average hydraulic power and pneumatic dissipated powers

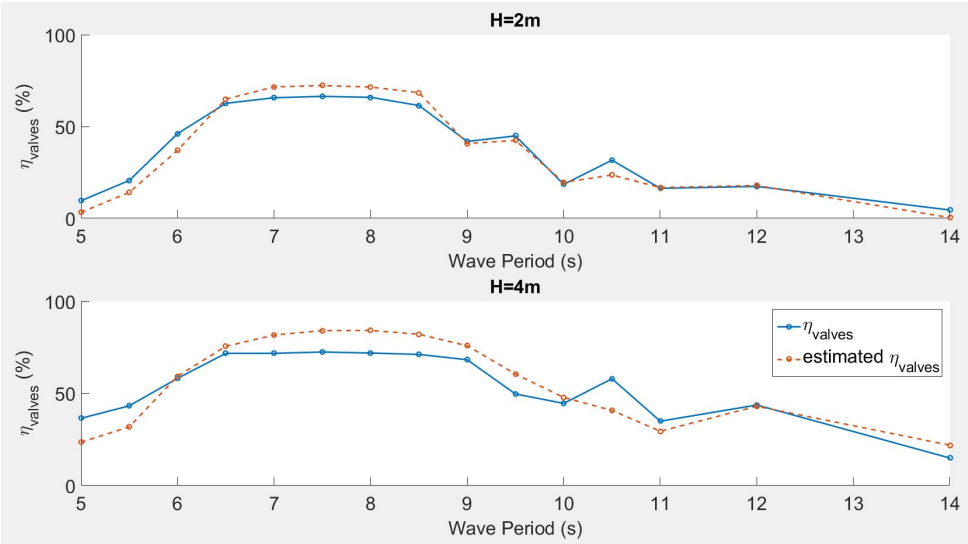


Figure B.8: Tupperwave device - regular waves - valves efficiency

The Tupperwave model creates a steady pressure head across the orifice and converts the highly fluctuating hydraulic power extracted from the waves into a smooth pneumatic power across the orifice. A maximum of 15kW of pneumatic power per meter square wave height is obtained for wave periods between 7 and 8s at full scale equivalent. The damping coefficient of the passive valves varies with the bodies excitations and significant pneumatic power dissipation happens in the valves. For the best performing orifice, a maximum of 72.5% of the hydraulic power extracted from the waves is actually converted into useful pneumatic power. A formula to estimate the valves efficiency from the valves characteristic was derived and showed the importance of the opening pressure and damping coefficient in the valves efficiency. The valves used in these tests are plumbing valves that

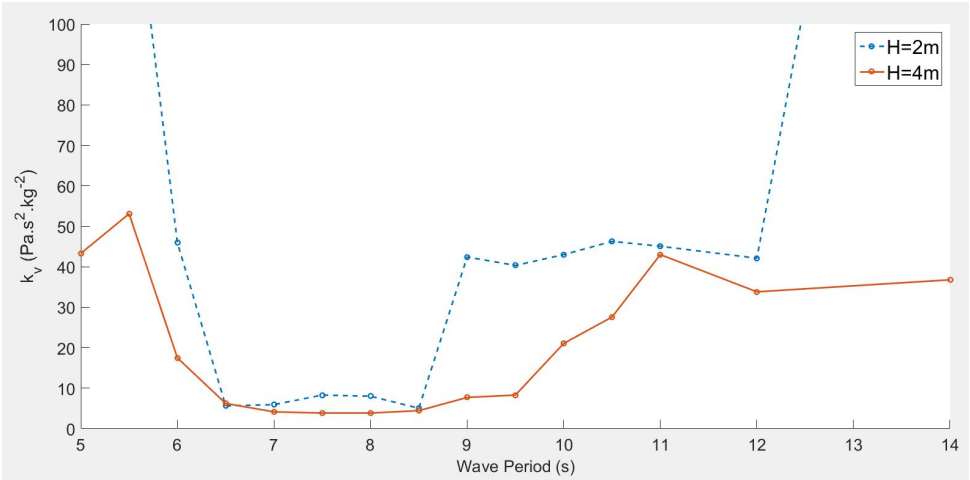


Figure B.9: Tupperwave device - regular waves - Hp valves damping coefficient

have not been designed for such application. It is therefore believed that it is possible to improve the Tupperwave device performances by improving the valves and reduce significantly the amount of losses.

### B.4.2 Tupperwave Device and Conventional OWC Power Performances

In this section, the performances of the floating conventional OWC and floating Tupperwave are compared. The devices were built using the same Spar OWC structure in order to provide a fair comparison in terms of power performance. Both devices are compared with their respective orifice that maximised their pneumatic power output.

#### B.4.2.1 Regular waves

The conventional OWC and Tupperwave device behave differently in converting the wave energy into useful pneumatic energy. Average pressure head and air flow rate across the turbines are compared in fig. B.10. The maximum and minimum values of the pressures and flow rates in steady state are also displayed such that to understand their fluctuations.
The conventional OWC produces large flows and small pressure drops compared to Tupperwave device. The pressure drops and flows produced by the conventional OWC are largely fluctuating from 0 to twice their average value while the fluctuations from the Tupperwave device are barely visible. The turbine requirements of both devices are therefore very different. The Tupperwave turbine is likely to be smaller because of the reduced flow.

Figure B.11 compares available hydraulic power and pneumatic power available to the turbine for the conventional OWC and the Tupperwave model

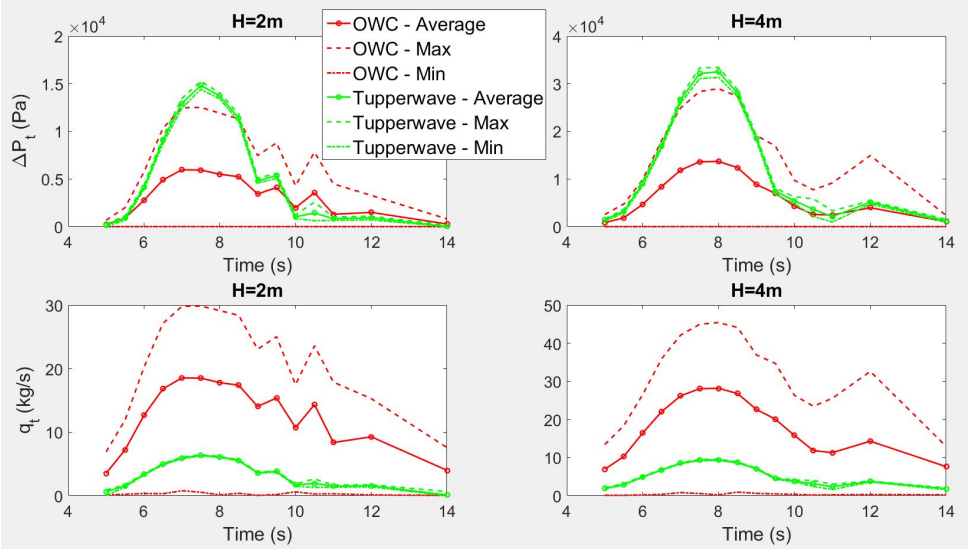


Figure B.10: Tupperwave device and conventional OWC - regular waves - pressure head and mass flow across the orifice

at H=2m and 4m. The Tupperwave model extracts less hydraulic power from the waves than the conventional OWC. The conventional OWC converts entirely the available hydraulic power into useful pneumatic power. The Tupperwave model converts only 60-70% of the hydraulic power into useful pneumatic power. The Tupperwave model produces in the end between 30 and 70% of the useful pneumatic power generated by the conventional OWC for wave periods from 6 to 9 seconds. The useful pneumatic power produced by the Tupperwave device is however much smoother than for the conventional OWC. Figure B.12 displays the average, maximum and minimum values of the useful pneumatic power in steady state. The standard deviation of the pneumatic power around its average value is of 2% for the Tupperwave device against 87% for the conventional OWC.

Various types of self-rectifying turbines have been developed for the pneumatic to electrical power conversion in conventional OWCs. The most recent and most efficient prototypes are the biradial and twin-rotor turbine. Their efficiencies in constant air flows was assessed experimentally to be 75% and 80% respectively. In real flow conditions, their efficiency is lower and the maximum efficiency of the biradial turbine in irregular flow conditions was estimated of 70% [59, 96]. Older versions of fixed-guide vanes self-rectifying impulse turbines have reached 40% efficiency in real flow conditions [97, 98]. The Tupperwave device uses a single-stage unidirectional turbines, such turbines reach 85% efficiency in constant flow conditions [99, 96]. The flow in the Tupperwave device is relatively constant as can be seen in the previous section. Hence, the turbine is likely to operate at maximum efficiency most

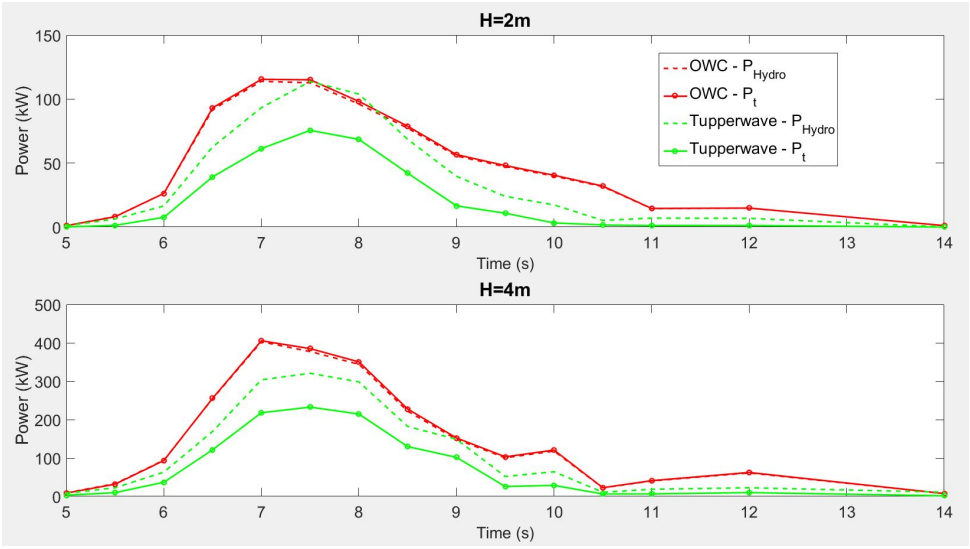


Figure B.11: Tupperwave device and conventional OWC - regular waves - Hydraulic and pneumatic power output

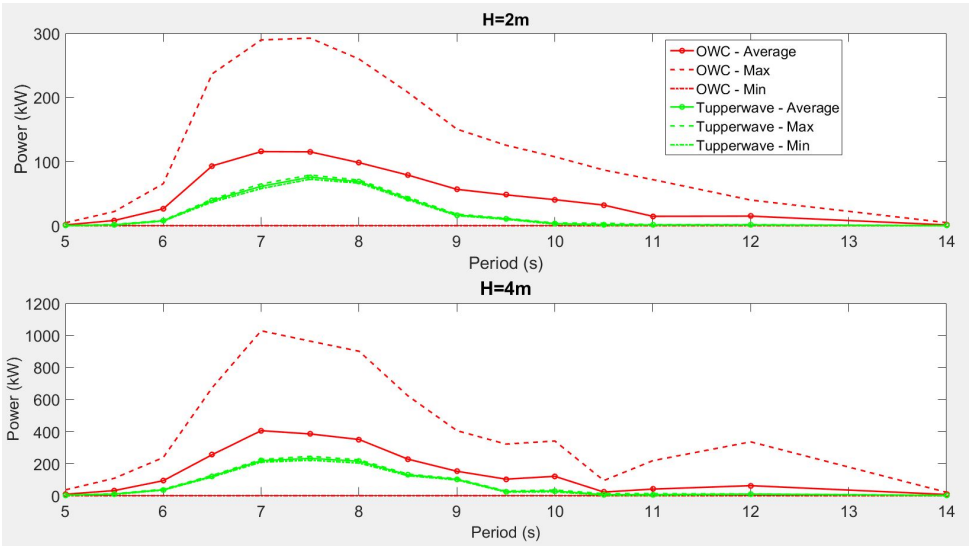


Figure B.12: Tupperwave device and conventional OWC - regular waves - Pneumatic power output

of the time.
From the useful pneumatic power obtained in tank testing, it is possible to approximate the electrical power that would be created if the devices were equipped with a turbine. This is done by multiplying the useful pneumatic power created in the tank testing to the assumed turbines efficiencies with the assumption that the generators are 100% efficient. The comparison between the theoretical electrical power produced in regular sea states by both devices is shown in fig. B.13. This method showed that the Tupperwave

device produces less electrical power than the conventional OWC equipped with the most efficient self-rectifying turbine. However, the valves used in the testing have not been designed for this purpose and are causing 20 to 50% pneumatic power losses depending on the device excitation. A proper design of appropriate valves would enhance the electrical power production of the Tupperwave device.

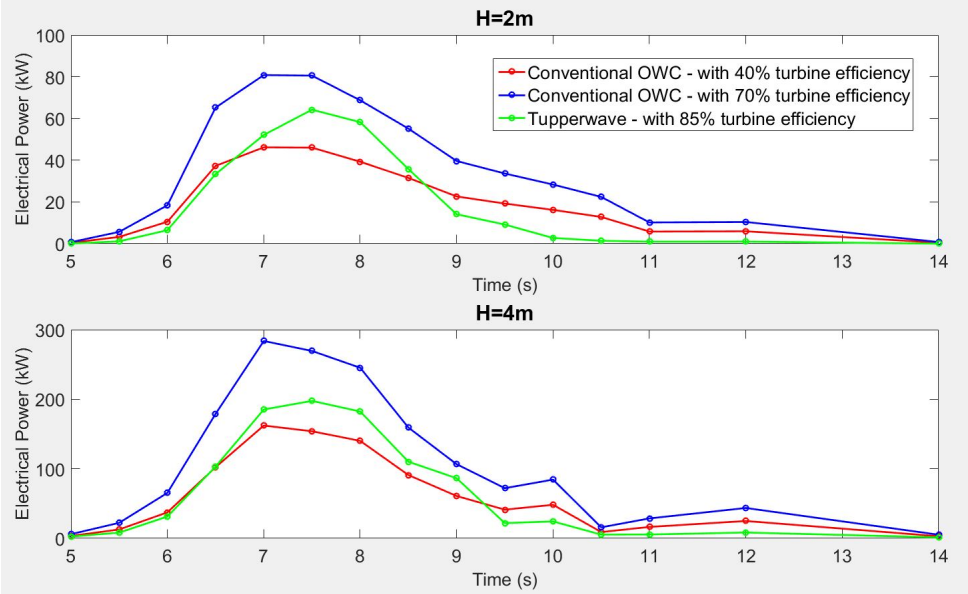


Figure B.13: Tupperwave device and conventional OWC - regular waves - Electrical power output assuming turbines

### B.4.2.2 Irregular waves

The comparison of power performances between conventional OWC and Tupperwave in irregular sea states is shown in fig. B.14. The results of the Tupperwave device compared to the conventional OWC are not as good as for the regular waves. The Tupperwave device produces in the end only about 35% of the useful pneumatic power produced by the conventional OWC. The efficiency of the Tupperwave valves for the irregular sea states shown to be about 50%. This is due to the fact that the part of the energy contained in the irregular wave series is transported by the smaller waves for which the valves do not open properly or do not open at all. The valves used in these tests are the cause of the poor performance of the Tupperwave device in irregular sea states. The smoothing of the pneumatic power is however still remarkable as shown in fig. B.15.

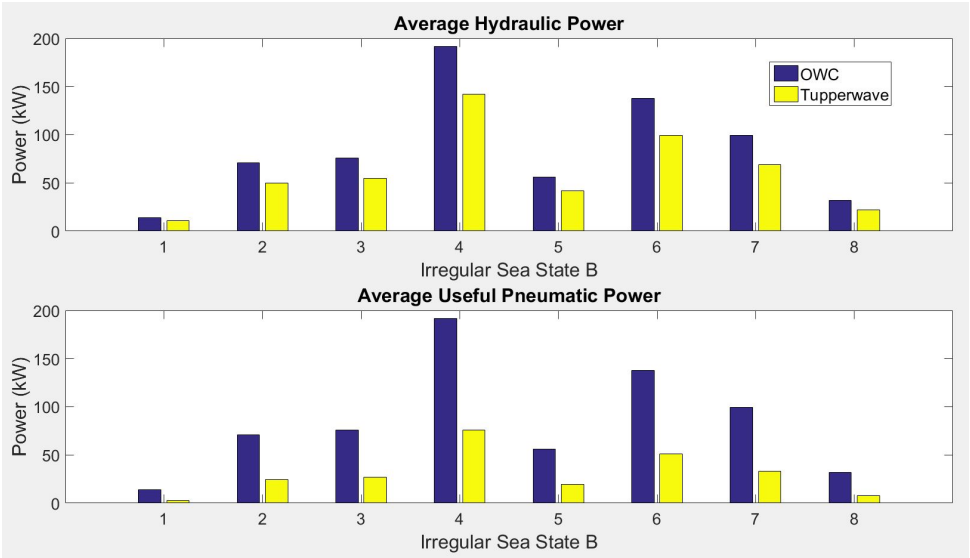


Figure B.14: Tupperwave device and conventional OWC - irregular waves - Hydraulic and pneumatic power output

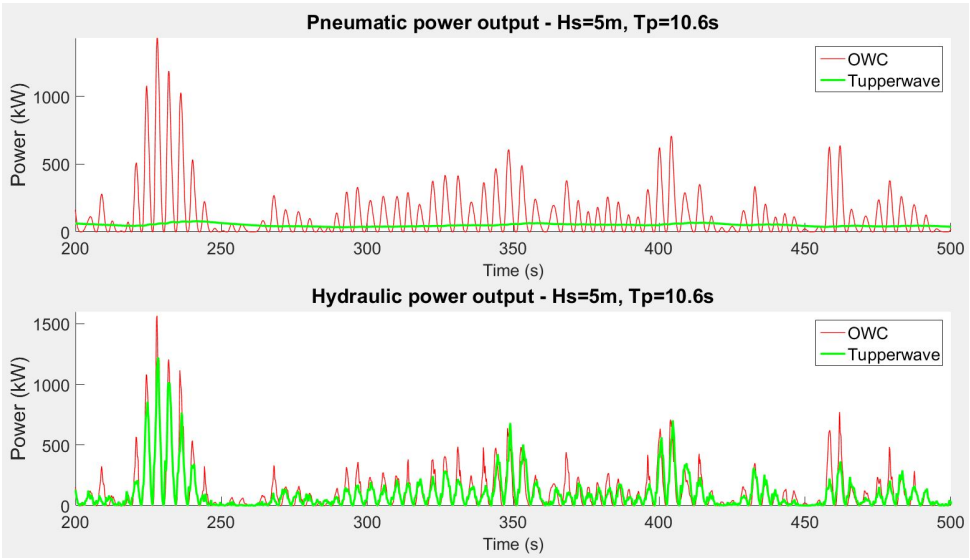


Figure B.15: Tupperwave device and conventional OWC - irregular waves - Hydraulic and pneumatic power time series

## B.5 Conclusion

A 1/24th scale Tupperwave device was built and tested in the Lir-NOTF's Deep Ocean Basin. The scaling method used to correctly simulate the air compressibility in the high and low pressure chambers involved big reservoirs and flexible pipes to connect the device to the reservoirs. A conventional Spar buoy OWC was also built on the same geometry as the Tupperwave model in order to provide a fair comparison between the two devices

pneumatic power performances. Both devices were tested in regular and irregular sea states. Their behaviour and pneumatic power outputs were monitored and compared.
In regular waves, the smoothing of the pneumatic power by the Tupperwave PTO is significant: 2% pneumatic power fluctuation around the mean value across the turbine is obtained against 87% for the conventional OWC. The Tupperwave device produced however less useful pneumatic power. It produced in average 30 to 70% of the useful pneumatic power produced by the conventional OWC. The main losses are the pneumatic power dissipation through the valves. The efficiency of the valves used in these tests to convert water column hydraulic energy into useful pneumatic energy was in the range of 50% to 80% depending on the orifice and on the device excitation.
In irregular sea states the Tupperwave device produced about 35% of the useful pneumatic energy produced by the conventional OWC. The main reason for that is the poor efficiency of the valves which only worked properly for high-energetic wave groups and did not allow energy extraction from the waves for the rest of the spectrum.
The valves used in the Tupperwave model were basic air admittance valves found on the plumbing market. These valves were not designed specifically for this purpose and there is therefore large room for improvement. Nevertheless, the Tupperwave device produced decent pneumatic power in regular waves with remarkable smoothness which would allow the unidirectional turbine to be fully efficient with relatively simple control law. These tests revealed the importance of the valves for the Tupperwave power performance. A formula to estimate the passive valves efficiency from the orifice and valves characteristics was suggested. Low damping and quick opening is key to maximise the power production. Well designed valves are the conditions for Tupperwave device to be competitive against conventional OWCs equipped with high-end self-rectifying turbines in terms of power production.
Future work will focus on the validation of the numerical model developed in [95] using the tank testing results described in this article. A Wave-to-Wire numerical model will then be developed to accurately compare the electrical power performance of the Tupperwave device to the conventional OWC.

# Acknowledgment

The authors would like to acknowledge funding received through OCEANERA-NET European Network (OCN/00028).

# Appendix C

# Paper C

# Assessment of primary energy conversion of a novel OWC wave energy converter

*Published in*

Energies, MDPI

*Authors*

Pierre Benreguig[1], Vikram Pakrashi[2], Jimmy Murphy[1]

[1]*MaREI Centre (ERI), University College Cork, Haulbowline Road, Ringaskiddy, Ireland*
[2]*Department of Civil, Structural and Environmental Engineering, Trinity College, Dublin, Ireland*

# Abstract

Tupperwave is a wave energy device based on the Oscillating-Water-Column (OWC) concept. Unlike a conventional OWC which creates a bidirectional air flow across the self-rectifying turbine, the Tupperwave device uses rectifying valves to create a smooth unidirectional air flow which is harnessed by a unidirectional turbine. This paper deals with the development and validation of time-domain numerical models from wave to pneumatic power for the Tupperwave device and the conventional OWC device using the same floating spar buoy structure. The numerical models are built using coupled hydrodynamic and thermodynamic equations. The isentropic assumption is used to describe the thermodynamic processes. A tank testing campaign of the two devices at 1/24th scale is described and the results are used to validate the numerical models. The capacity of the innovative Tupperwave OWC concept to convert wave energy into useful pneumatic energy to the turbine is assessed and compared to the corresponding conventional OWC.


## C.1 Introduction

Waves are an ocean energy resource which has the potential to contribute in the offshore renewable energy mix. A multitude of different devices have been invented to convert the wave power into electrical power, but the challenges involved in the development of an economically sustainable solution are huge. No device for large-scale energy production from the waves has yet reached the stage of commercialisation. The barriers include high maintenance costs and survivability in extreme sea states amongst others. Oscillating-Water-Columns (OWCs) are among the most promising wave energy devices because of their relative simplicity. The only moving part being the turbine connected in direct drive to the generator, low levels of maintenance are expected. Moreover, the air contained in the OWC chamber flows across the turbine at high speed transforming the slow motion and high forces from the waves into a fast rotational speed and low torque at the turbine. This primary conversion of the wave power into pneumatic power acts as a non-mechanical gear-box and constitutes a huge advantage in terms of maintenance and survivability. This feature is not exclusive to OWC device and is found in other wave energy converters that use air as a conversion fluid and flexible membranes such as the sea clam [100] and the Bombora device [101] amongst others. OWC devices are among the most studied type of wave energy technologies and their principle is used in various forms.

For the most common form of OWC devices, the air flow across the turbine is bidirectional and the turbine is self-rectifying. Such turbine can harness both flow direction but is not as efficient as a unidirectional turbine. State-of-the-art self-rectifying air turbines reach a maximum efficiency in the

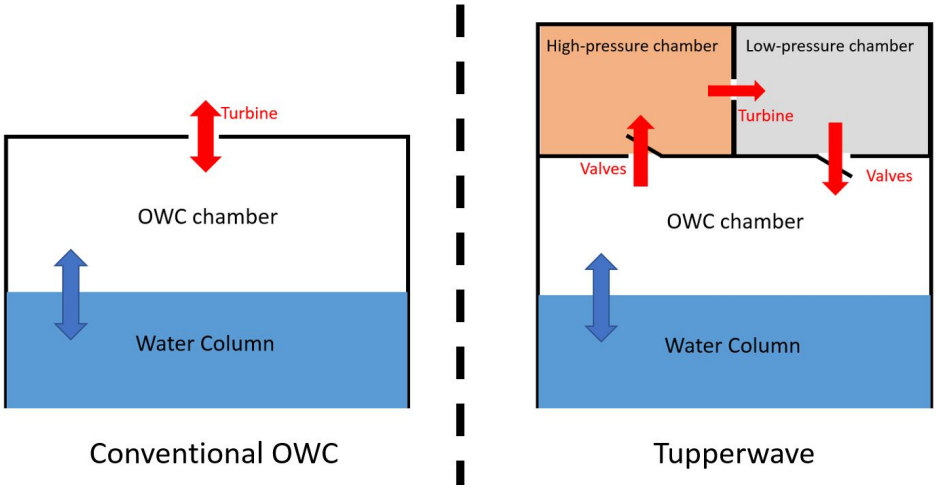


Figure C.1: Schematic diagram of the conventional OWC and Tupperwave device concepts

order of 70-75% in constant flow conditions during scaled tests [57]. In real-sea conditions, the air flow across the turbine is highly fluctuating since it stops and changes direction every 3 to 5 seconds. In such conditions, the average efficiency of self-rectifying turbines is 5 to 10% lower than their maximum efficiency [57]. Other forms of OWCs use non-return valves to rectify the flow in a single direction across a unidirectional turbine. Single stage unidirectional turbines reach 85-90% efficiency in constant flow conditions [102, 103]. The use of rectifying valves was successful for Masuda's commercial navigation buoy (1965) powered by wave energy [9], but the experience of the Kaimei device [104] in 1986 revealed that there are challenges associated with the use of valves in larger scale devices for power production where air flow rates are in the order of $100\,m^3.s^{-1}$. Such flow rates necessitates large valve dimensions which are unsuited for the fast opening and closing response tim e required for the valves. The moderate success of the Kaimei was also due to the limited theoretical knowledge of wave energy absorption available at the time [14].

The idea of using a high-efficiency unidirectional turbine in a OWC device is however still appealing since it could potentially increase the device efficiency. The Tupperwave principle suggests another approach on the use of non-return valves for the generation of a closed-circuit air flow. The Tupperwave concept for OWCs consists of self-rectifying valves, two large air chambers that act as accumulators and a unidirectional turbine. The Tupperwave principle is described in Figure C.1 and can be applied to fixed or floating devices. Floating devices are however more suitable because the available buoyancy volume which can be divided in two parts and used as the high-pressure (HP) chamber and low-pressure (LP) chambers. In this article, the Tupperwave principle is applied to a floating axisymmetric structure in the

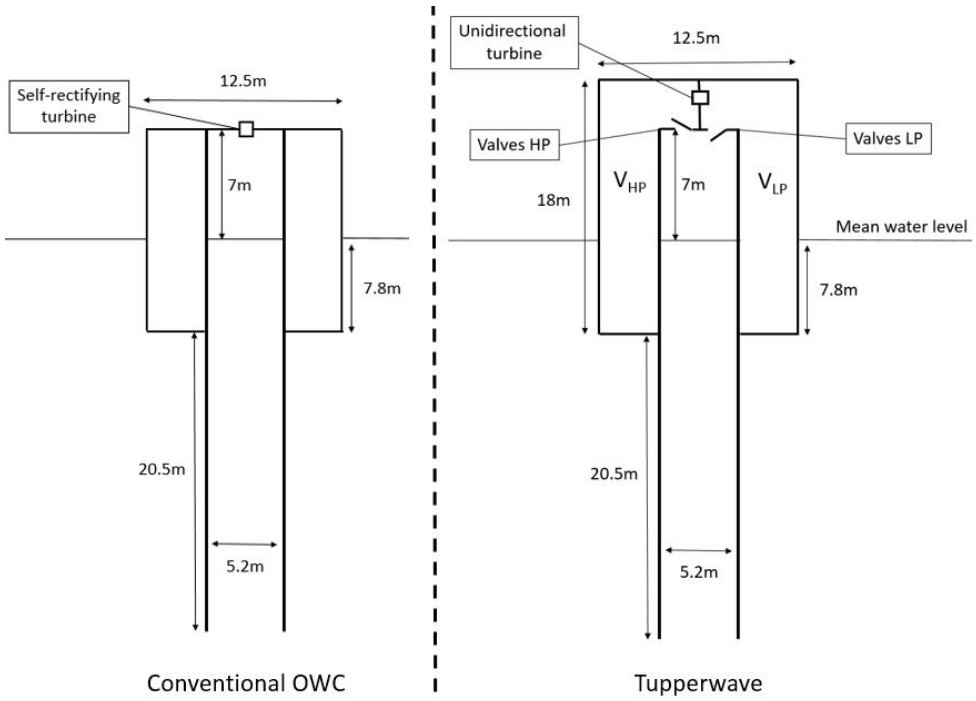


Figure C.2: 2D schematic of the full scale conventional OWC and Tupperwave devices

form of a spar buoy. In addition to a potential yield increase due to the high efficiency of the unidirectional turbine, this principle also aims at smoothing the flow across the turbine and hence maximise its efficiency and the power quality delivered by the device. An optimization study showed that the volume of these chambers should be maximized [95]. Thus, the whole buoyancy volume of the chosen spar buoy is used and each chamber is 950 $m^3$. Figure C.2 displays the schematic for the Tupperwave device at full scale as well as the corresponding conventional OWC using the same spar buoy geometry.

The power conversion chain of wave energy converters is achieved in various stages. In the case of OWC devices, the incoming wave power reaching the device is partly absorbed by the device. This absorbed power is then converted into useful pneumatic power available across the turbine. Finally, the power available to the turbine is converted into electrical power by the turbine and generator system. The development and validation of a model encompassing all power conversion stages is challenging due to complex interdependent physical phenomena happening at each stages and the cost of building a physical model with all the components [23]. Therefore, developers usually decide to separately study parts of the power conversion chain as in [35, 33, 105].

In this paper, the first two conversion stages are considered: the Tupperwave device and the corresponding conventional OWC (fig. C.2) are numerically modelled from wave to pneumatic power and the results are validated

against tank testing experiments. The objective is to assess, numerically and physically, the capacity of the Tupperwave device to convert wave power into smooth pneumatic power available to the turbine and compare it to the performance of the conventional OWC.

The hydrodynamic and thermodynamic equations forming the devices numerical models from wave to pneumatic power are presented in section C.2. Section C.3 describes the tank testing experiments carried out. Section C.4 compares the physical model performances and the numerical and experimental results of both devices for validation of the numerical models. Finally, the conclusions of the work are given in section C.5.

## C.2 Numerical models from wave to pneumatic power

The time-domain numerical models from wave to pneumatic power for the two devices studied in this research consist of a number of coupled differential equations obtained via hydrodynamic and thermodynamic considerations.

### C.2.1 Hydrodynamics

Both the Tupperwave device and the conventional OWC use the same spar buoy geometry. The hydrodynamic model is therefore the same for the two devices. The model is based on linear wave theory, using the assumptions that wave steepness and bodies motions are sufficiently small. To solve the linear hydrodynamic problems in the OWC device, several approaches have been developed. The two most popular approaches are the uniform surface pressure model [65] and the rigid piston model [106]. The former approach is exact because its makes no assumption on the generally warped Internal Water Surface (IWS) and assumes spatially uniform pressure on the IWS. The latter approach approximates the IWS to be a thin rigid piston moving along the column of the device. This approximation is reasonable when the radius of the IWS is small compared to the wavelength. With this approach, the problem becomes a two-rigid-body problem {Device floating structure - rigid piston} that can be solved using the Boundary Element Method (BEM) developed in the 1970s for the study of interaction between waves and floating bodies (ships) [107]. This approach is used in this research.

Spar buoys move essentially in heave due to the relatively large length of the submerged tail tube and the heave motion is the main contribution for the power conversion of the axisymmetric device. Hence, to simplify the problem, only the heave motions of the two bodies are considered. This assumption is reasonable and commonly adopted in the literature [80, 108, 109]. The vertical displacement of the device structure and rigid piston are respectively noted $(x_1, x_2)$ and the vertical axis is upward. The constant horizontal section of the IWS is noted $S_2$. The volume of the OWC chamber, noted V,

varies with the relative vertical displacement of the bodies. A dot over a variable indicates the variable's derivative taken with respect to time. When the device is floating at rest on calm water ($x_1 = x_2 = 0$), the OWC chamber has a volume of $V_0$. We therefore have:

$$\begin{cases} V = V_0 + S_2(x_1 - x_2) \\ \dot{V} = S_2(\dot{x}_1 - \dot{x}_2) \end{cases} \tag{C.1}$$

In order to establish a time-domain model of the system's dynamic response, the hybrid frequency-time domain method described in [110] is used. Each body is subjected to the Cummins equation [83]. The reciprocating pressure force $f_p$ due to the pressure building in the OWC chamber is added, along with the viscous drag force $f_d$. The coupled heave motions of the two-bodies can be written in time-domain as [80]:

$$\begin{cases} [m_1 + A_{11}(\infty)]\ddot{x}_1(t) + \int_0^t K_{11}(t-\tau)\dot{x}_1(t)d\tau + A_{12}(\infty)\ddot{x}_2(t) \\ \quad + \int_0^t K_{12}(t-\tau)\dot{x}_2(t)d\tau + c_1 x_1(t) = f_1(t) + f_p(t) + f_{d1}(t) + f_{m1}(t) \qquad (a) \\ A_{21}(\infty)\ddot{x}_1(t) + \int_0^t K_{21}(t-\tau)\dot{x}_1(t)d\tau + [m_2 + A_{22}(\infty)]\ddot{x}_2(t) \\ \quad + \int_0^t K_{22}(t-\tau)\dot{x}_2(t)d\tau + c_2 x_2(t) = f_2(t) - f_p(t) + f_{d2}(t) \qquad (b) \end{cases} \tag{C.2}$$

where $m_i$ are the bodies masses; $A_{ij}(\infty)$ are the bodies heaving added masses at infinite frequency (including the proper and crossed modes); $c_i$ are the hydrostatic stiffness terms and are calculated as $c_1 = \rho_w g S_1$ and $c_2 = \rho_w g S_2$, where $\rho_w$ is the water density, $g$ is the acceleration of gravity, $S_1$ is the constant horizontal cross sectional area of device structure at the undisturbed sea surface; $K_{ij}$ are the impulse response functions for heave motions; $f_i$ are the wave excitation forces; $f_{m1}$ is the force applied by the mooring system on the device structure.

The impulse response functions can be obtained by the following formula:

$$K_{ij}(t) = \frac{2}{\pi}\int_0^\infty B_{ij}(\omega)cos(\omega t)d\omega \tag{C.3}$$

where $B_{ij}$ is the radiation damping coefficient in the frequency domain.

The excitation forces are calculated as:

$$f_i(t) = \int_0^t K_{ex,i}(t-\tau)\eta(t)dt \tag{C.4}$$

where $\eta$ is the external wave elevation and $K_{ex,i}$ is the excitation force impulse response function calculated as:

$$K_{ex,i}(t) = \frac{1}{\pi}\int_0^\infty Re\{\tilde{F}_{ex,i}(\omega)e^{-i\omega t}\}d\omega \tag{C.5}$$

where $\tilde{F}_{ex,i}(\omega)$ is the excitation force coefficient from the waves on body $i$. The frequency domain coefficients $A_{ij}(\infty)$, $B_{ij}(\omega)$, $c_i$ and $\tilde{F}_{ex,i}(\omega)$ are calculated using the commercial BEM solver WAMIT [29].

The reciprocating pressure force is calculated as: $f_p = S_2 p_{owc}(t)$ and $p_{owc}$ is the excess pressure relatively to atmospheric pressure built in the OWC chamber. Because of the particular mooring system used in the experiments (see section C.3.2), the vertical component of mooring force was neglected in the numerical model.

The viscous drag forces have an important role in wave energy converter dynamics as their misestimation would lead to numerical prediction of unrealistic amplitude of motions, and thereby also energy absorption. The identification of drag coefficients for wave energy applications is particularly challenging because other sources of non-linearities may interfere with the isolation of the viscous drag force, causing uncertainties and inconsistency in the literature. Following the method suggested in [111], the drag force was calculated as $f_{di} = -C_{di}|\dot{x}_i(t)|\dot{x}_i(t)$ (based on Morison's equation [112]) where $C_{di}$ is the equivalent drag coefficient and is estimated as the one that minimizes the error between the physical measurements and the numerical model. As a result, this equivalent drag coefficient incorporates the viscous drag effects as well as all other non-linear effects such as changes of the wetted surface subject to viscous effects, splashes, mooring line drag, etc. The values $C_{d1} = 150\,\mathrm{N.s^2.m^{-2}}$ and $C_{d2} = 40\,\mathrm{N.s^2.m^{-2}}$ were found to obtain the best fit between the vertical displacement of the bodies predicted numerically and the ones obtained physically.

According to system G.1.a,b, the hydrodynamic system can be described by the 3 main variables $\{x_1, x_2, p_{owc}\}$. A third differential equation verified by $p_{owc}$ is necessary to solve the problem. This equation is established in the next section using thermodynamic equations.

## C.2.2 Thermodynamics

In this section, the general thermodynamic equations ruling an open air chamber are first described. They are then applied to the modelling of the conventional OWC and Tupperwave device.

### C.2.2.1 General equations

We consider the following open thermodynamic system: an air chamber of variable volume $V$ containing a mass $m$ of air at the density $\rho$, at the temperature $T$ and at pressure $p_{atm} + p$. The air mass flow rates $w_{in}$ and $w_{out}$ are the flows respectively in and out of the chamber and are functions of the air excess pressure $p$.

The mass balance equation in the system is:

$$\dot{m} = \rho\dot{V} + \dot{\rho}V = w_{in} - w_{out} \tag{C.6}$$

If the system is considered adiabatic and the transformations slow enough

to be reversible, the isentropic density-pressure relation is applicable:

$$\rho = \rho_{atm}\left(1 + \frac{p}{p_{atm}}\right)^{\frac{1}{\gamma}} \tag{C.7}$$

where $\rho_{atm}$ is the density of the air at atmospheric conditions and $\gamma$ is the isentropic expansion factor.

Moreover, in the case where the excess pressure remains small compared to the atmospheric pressure, it is possible to linearise the isentropic relationship between density and pressure. Once linearised, Equation G.11 leads to:

$$\rho = \rho_{atm}\left(1 + \frac{p}{\gamma p_{atm}}\right) \tag{C.8}$$

The derivation of Equation G.14 with respect to time gives:

$$\dot{\rho} = \frac{\rho_{atm}}{\gamma p_{atm}}\dot{p} \tag{C.9}$$

Finally, the combination of Equations G.9 and C.9 leads to the differential Equation G.16 governing the evolution of the pressure in an open air chamber during isentropic transformations:

$$\dot{p} = \frac{\gamma p_{atm}}{\rho_{atm} V}(w_{in} - w_{out} - \rho\dot{V}) \tag{C.10}$$

#### C.2.2.2 Conventional OWC thermodynamics

The air chamber in a conventional OWC device is commonly modelled in the literature using the linearized isentropic assumption. The main justification is that, the temperature oscillations in the air chamber are relatively small and their time scales (a few seconds) are too short for significant heat exchanges to occur across the chamber walls and across the air-water interface [9]. It was proven in [68] that the linearised isentropic assumption provides a satisfactory results for the modelling of conventional OWCs except possibly under very rough sea conditions. In this paper, the numerical model will be compared to model-scale experimental results where pressure and temperature oscillations are even smaller. The use of the linearised isentropic assumption is hence justified. Figure G.7 displays a schematic of the OWC thermodynamic system.

At model scale, the turbine (of impulse type) connecting the inside of the chamber to atmosphere is modelled using an orifice plate. In the conventional OWC, the flow is bidirectional through the orifice. Hence, the density of the air entering the turbine is either $\rho_{atm}$ during the inhalation process ($p_{owc} < 0$), or $\rho_{owc}$ during the exhalation process ($p_{owc} > 0$). Under the testing conditions, the maximum excess pressures observed in the OWC

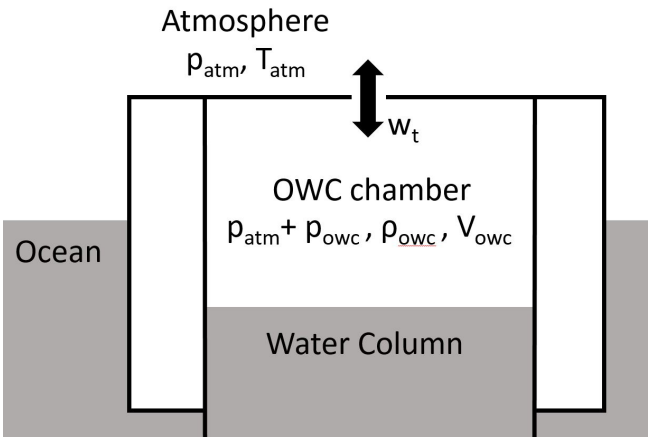


Figure C.3: Conventional OWC schematic with thermodynamic variables

chamber are $\pm 1250\,\text{Pa}$ for which, according to Equation G.14, $\rho_{owc}$ reaches the maximum values of $\rho_{atm} \pm 0.8\%$. Hence, the air in the OWC chamber can be considered as quasi-incompressible and the air flow rates are described using the volumetric flow rates ([113], [114]):

$$\Delta p = k_t q_t^2 \quad \text{with} \quad k_t = \frac{\rho_{atm}}{2(\alpha A_t)^2} \tag{C.11}$$

where $q_t$ is the volumetric flow rate across the orifice/turbine, $k_t$ is the turbine damping coefficient and $\alpha A_t$ is the effective area of the orifice representing the turbine.

Finally, according to equations G.16 and C.11, the relationship between the hydrodynamic body motions (see Equation C.1) and the excess pressure in the OWC chamber is:

$$\dot{p}_{owc} = \begin{cases} \dfrac{\gamma p_{atm}}{\rho_{atm} V_{owc}} \Big( - \rho_{owc} \sqrt{\dfrac{p_{owc}}{k_t}} - \rho_{owc} \dot{V}_{owc} \Big) & \text{for} \quad p_{owc} > 0 \\ \dfrac{\gamma p_{atm}}{\rho_{atm} V_{owc}} \Big( + \rho_{atm} \sqrt{\dfrac{p_{owc}}{k_t}} - \rho_{owc} \dot{V}_{owc} \Big) & \text{for} \quad p_{owc} < 0 \end{cases} \tag{C.12}$$

### C.2.2.3 Tupperwave device thermodynamics

In the Tupperwave device, air is exchanged between 3 different air chambers. Unlike for the conventional OWC where the OWC chamber is open to the atmosphere, the air in the Tupperwave device is flowing in a closed-circuit. This raises the issue of possible air temperature increase in the device due to heat created by viscous effects, mainly happening in the turbine. It was shown in [115] that the heat created is dissipated through the device walls and only slight temperature increase (¡1$^o$C) is observed in moderate sea states. At model scale, the temperature increase is expected to be negligible. Moreover, the pressures reached in the device are expected to be in the same order as in the conventional OWC. Hence the linearized isentropic

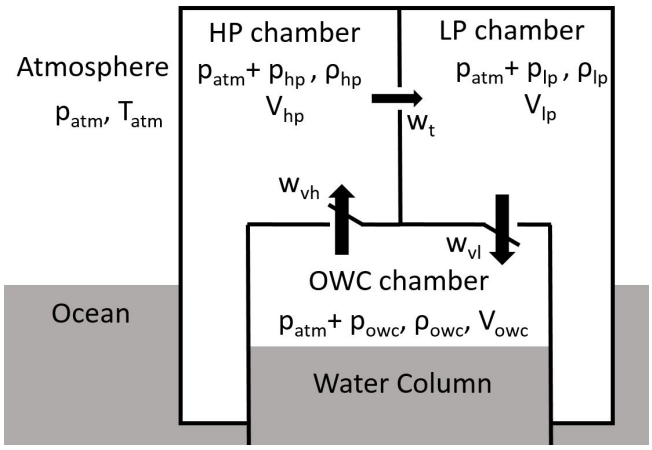


Figure C.4: Tupperwave device schematic with thermodynamic variables

assumption is assumed to be valid. Figure F.4 displays a schematic of the 3 chambers which constitute 3 interconnected thermodynamic systems.

Equation G.16.c can be directly applied to the 3 chambers:

$$\begin{cases} \dot{p}_{owc} = \dfrac{\gamma p_{atm}}{\rho_{atm} V_{owc}} (w_{vl} - w_{vh} - \rho_{owc} \dot{V}_{owc}) & (a) \\ \dot{p}_{hp} = \dfrac{\gamma p_{atm}}{\rho_{atm} V_{hp}} (w_{vh} - w_t) & (b) \\ \dot{p}_{lp} = \dfrac{\gamma p_{atm}}{\rho_{atm} V_{lp}} (w_t - w_{vl}) & (c) \end{cases} \tag{C.13}$$

where $w_t$, $w_{vh}$ and $w_{vl}$ are the mass air flow rates across the turbine, the HP valve and the LP valve. The sign convention for the volumetric flow rates is given by the arrows directions in Figure F.4.

As for the conventional OWC, the excess pressures reached in the different chambers at model scale do not exceed 1250 Pa. The variation of air density are therefore small and the flow across the orifice is considered as incompressible:

$$w_t = \rho_{hp} \sqrt{\frac{p_{hp} - p_{lp}}{k_t}} \tag{C.14}$$

The valves are non-return valves that close under a certain opening pressure $p_o$. When opened, their model is similar to orifice plates of effective opening area $\alpha A_v$ and damping coefficient $k_v = \dfrac{\rho_{atm}}{2(\alpha A_v)^2}$:

$$w_{vh} = \begin{cases} 0 & \text{if} \quad p_{owc} - p_{hp} < p_o \\ \rho_{owc} \sqrt{\dfrac{p_{owc} - p_{hp} - p_o}{k_v}} & \text{if} \quad p_{owc} - p_{hp} > p_o \end{cases} \tag{C.15}$$

$$w_{vl} = \begin{cases} 0 & \text{if} \quad p_{lp} - p_{owc} < p_o \\ \rho_{lp} \sqrt{\dfrac{p_{lp} - p_{owc} - p_o}{k_v}} & \text{if} \quad p_{lp} - p_{owc} > p_o \end{cases} \tag{C.16}$$

The system of equations F.6.a,b,c is coupled with the hydrodynamic system of equations G.1.a,b and completes the model for the Tupperwave device.

### C.2.3 Numerical solution

The conventional OWC is governed by the coupled equations G.1.a,b and F.5 while the Tupperwave device is governed by equations G.1.a,b and F.6.a,b,c.

The four convolution integrals $I_{ij}(t) = \int_0^t K_{ij}(t-\tau)\dot{x}_j(\tau)d\tau$ present in equations G.1.a,b are called memory effect integrals. Their values depend on the history of the system which implies their recalculation at each time step and is not practical for the system resolution. By using the conventional Prony's methods [116], it is possible to calculate each of these functions as the sum of $N_p$ additional unknowns $\{I_{ij,k},\, k = 1 : N_p\}$ which are the solutions of $N_p$ additional first order equations that will be solved along with the system of equations G.1.a,b. Details on the conventional Prony's method are given in Appendix A. Following the recommendations made in [117], $N_p = 4$ was taken for the approximation of the impulse function of heave motion, which adds 16 first order equations in the system.

The solution of these equations was obtained numerically using the ordinary differential equation solver ode45 from the mathematical software MATLAB [118].

## C.3 Physical modelling in wave tank

### C.3.1 Physical models design and fabrication

#### C.3.1.1 Scaling

The devices displayed in Figure C.2 were built at model scale. For dynamic similarity in the water, all underwater dimensions were multiplied by the scaling factor $\epsilon = 0.0415 \simeq 1/24$ according to Froude similarity law. However, if the volumes of the high- and low-pressure chambers were also scaled using Froude scaling (ie. multiplied by $\epsilon^3$), air compressibility effects occurring at full scale would not be reproduced at model scale [74]. Since the Tupperwave device working principle fully relies on air compressibility in the high- and low-pressure chambers, these effects had to be reproduced and a different scaling method was implemented for the volumes of the chambers.

As shown in equations F.6.b, the variation of mass in the HP chamber of volume $V_{hp}$ is only due to air compressibility and directly related to the change in pressure:

$$\dot{p}_{hp} = \frac{\gamma p_{atm}}{\rho_{atm} V_{hp}} \dot{m}_{hp} \tag{C.17}$$

Equation C.17 is valid both at full scale (subscribe F) and model scale (subscribe M). Hence:

$$\frac{\dot{p}_{hp,M}}{\dot{p}_{hp,F}} = \frac{p_{atm,M}\ \dot{m}_{hp,M}\ \rho_{atm,F}\ V_{hp,F}}{p_{atm,F}\ \dot{m}_{hp,F}\ \rho_{atm,M}\ V_{hp,M}} \tag{C.18}$$

For similitude to be achieved between full scale and model scale, Froude scaling laws need to be respected. This implies:

$$\begin{cases} \dfrac{\dot{p}_{hp,M}}{\dot{p}_{hp,F}} = \epsilon^{1/2} \\ \dfrac{\dot{m}_{hp,M}}{\dot{m}_{hp,F}} = \epsilon^{5/2} \end{cases} \tag{C.19}$$

Unless very specific infrastructures are used, the atmospheric conditions are the same at model scale as at full scale, hence:

$$\begin{cases} p_{atm,M} = p_{atm,F} \\ \rho_{atm,M} = \rho_{atm,F} \end{cases} \tag{C.20}$$

Combining Equation C.18 with Equations C.19 and C.20 leads to the necessary condition on the chamber volume to satisfy similarity regarding compressibility effects between full scale and model scale:

$$\frac{V_{hp,M}}{V_{hp,F}} = \epsilon^2 \tag{C.21}$$

The same condition needs to be satisfied for the LP chamber. At full scale, the HP and LP chamber are 950 $m^3$. At model scale, the volumes of the chambers therefore are 1.64 $m^3$. Unlike full scale, it is impossible to fit both chambers on the device as their volume largely exceed the overall volume of the device. The alternative at small scale is to locate the main volume of the HP and LP chambers outside of the device and connect them to two smaller chambers on the device with flexible pipes. Large reservoirs were used for the HP and LP chambers and located on the pedestrian bridge above the tank, see Figure E.5. The flexible pipes were chosen as lightweight and flexible as possible to reduce their influence on the floating device motion. Part of the pipes weight was supported by bungee ropes. A similar experimental setup was implemented in [119] to test a floating air bag wave energy converter at model scale.

This scaling method was suggested and applied in [74] to properly represent the spring-like effect of the air in the OWC chamber of a conventional OWC device. To implement this method, an additional flexible pipe connecting the OWC chamber to another reservoir outside of the device is required. It is however rarely implemented at model scale by conventional OWC developers since the air compressibility in the OWC chamber is not essential

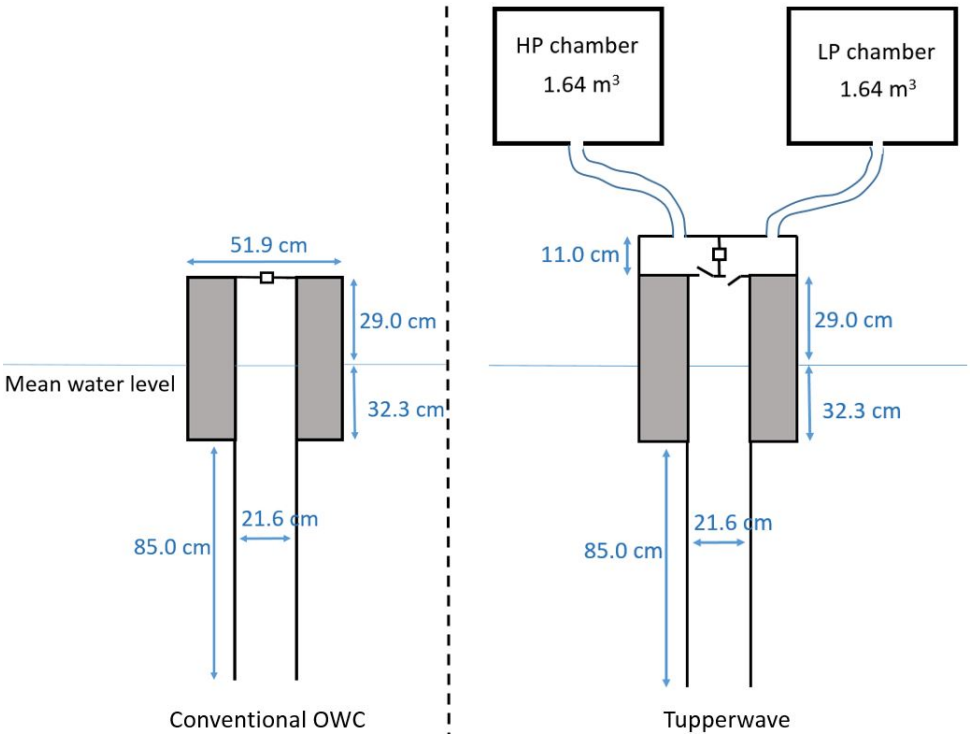


Figure C.5: Schematic of the model scale conventional OWC and Tupperwave devices

for the devices working principle and it increases even more the testing difficulty, especially for a floating device. Therefore, in the present experiments, the volume of the OWC chamber was simply scaled down by the factor $\epsilon^3$ using direct Froude scaling and the spring-like effect of the air in the OWC chamber was not physically modelled in both devices. The air in the OWC chamber is therefore quasi-incompressible in the conditions of the tests and it is acknowledged that the perfect similitude with the full scale devices is not achieved. The power conversion performances of the full scale devices can therefore not be directly obtained from the results of the model tests as it may result in unrealistic overestimations [67]. The present experiments are however still valuable to validate the Tupperwave concept and compare it to the conventional OWC.

Since both devices use the same Spar structure, a single spar was built and used for both device. Schematics of the physical models are shown in Figure C.5. The positions of the centre of gravity and centre of buoyancy as well as the moments of inertia were assessed using the computer-aided design software Solidworks [120]. The position of the centre of gravity was also assessed experimentally by hanging the device to a vertical rope and finding the balance point. The values obtained experimentally after five repeated tests verified the centre of gravity to be within $\pm 1$ mm from the position indicated by Solidworks. The moment of inertia around the horizontal

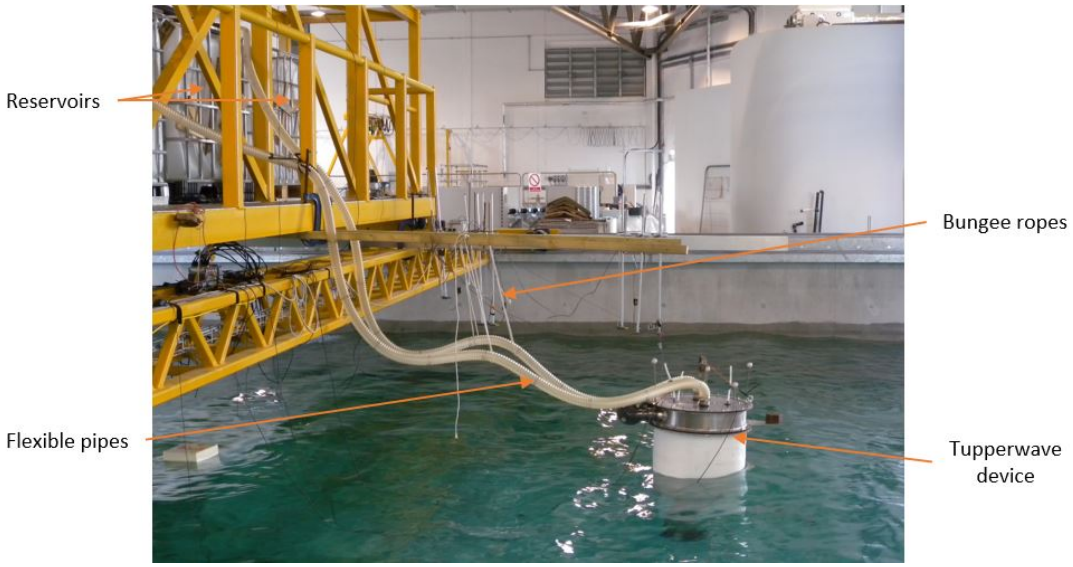


Figure C.6: Physical model of the Tupperwave device

axis Y parallel to the wave front was also verified using the bifilar pendulum method and the values obtained were within $\pm 0.1$ kg.m$^2$ from the value indicated by Solidworks. The conventional OWC being initially lighter than the Tupperwave device, it was ballasted such that both devices have the exact same mass properties. The mass properties of the device are given in Table C.1.

Table C.1: Devices mass properties

| | **Model scale** | **Full scale** |
|---|---|---|
| **Total mass (kg)** | 58.4 | $817 \times 10^3$ |
| **Distance device bottom - COG (m)** | 0.892 | 21.49 |
| **Distance device bottom - COB (m)** | 0.961 | 23.16 |
| **Ixx (kg.m$^2$)** | 23 | $1.87 \times 10^8$ |
| **Iyy (kg.m$^2$)** | 23.5 | $1.91 \times 10^8$ |
| **Izz (kg.m$^2$)** | 2 | $1.62 \times 10^7$ |

### C.3.1.2 Turbines

As mentioned in section C.2.2.2, the turbines were physically modelled using orifice plates. Preliminary numerical modelling showed that the optimal

damping coefficients at full scale to maximise the pneumatic power output were close to 38 $Pa.s^2.m^{-6}$ for the conventional OWC and 450 $Pa.s^2.m^{-6}$ for the Tupperwave device [95]. Three orifice plates per device were built around those values scaled down using Froude scaling. Their exact damping coefficients and effective areas were then experimentally assessed prior to testing by forcing a known flow across the orifice and measuring the pressure drop [90]. Table C.2 displays the orifice characteristics for the conventional OWC and the Tupperwave model scale devices. The damping coefficients are used during the tank testing to calculate the instantaneous volumetric flow across the orifice based on the measurement of the pressure drop according to Equation G.2.2.2.2.

Table C.2: Orifices characteristics for conventional OWC and Tupperwave device

| | **Model Scale** | | | **Full Scale** | |
|---|---|---|---|---|---|
| **Orifice** | **Diameter (mm)** | $\mathbf{k_t}$ **(Pa.s$^2$.m$^{-6}$)** | $\boldsymbol{\alpha}$**A (m$^2$)** | $\mathbf{k_t}$ **(Pa.s$^2$.m$^{-6}$)** | $\boldsymbol{\alpha}$**A (m$^2$)** |
| **OWC1** | 22.6 | $7.10 \times 10^6$ | $2.94 \times 10^{-4}$ | 21.1 | $1.71 \times 10^{-1}$ |
| **OWC2** | 20.6 | $10.4 \times 10^6$ | $2.42 \times 10^{-4}$ | 30.9 | $1.41 \times 10^{-1}$ |
| **OWC3** | 17.5 | $19.6 \times 10^6$ | $1.77 \times 10^{-4}$ | 58.3 | $1.03 \times 10^{-1}$ |
| **T1** | 11.5 | $0.70 \times 10^8$ | $9.33 \times 10^{-5}$ | 209 | $5.42 \times 10^{-2}$ |
| **T2** | 9.2 | $1.86 \times 10^8$ | $5.74 \times 10^{-5}$ | 552 | $3.33 \times 10^{-2}$ |
| **T3** | 7 | $4.85 \times 10^8$ | $3.55 \times 10^{-5}$ | 1439 | $2.06 \times 10^{-2}$ |

### C.3.1.3 Valves

The Tupperwave working principle relies on the use of non-return valves. The valves are key components because they are likely to cause pneumatic power losses. They can either be passive or active. Passive valves mechanically open when a certain pressure difference is reached across the valves, while active valves are electrically activated. For the physical model, passive valves were chosen for their simplicity. The most appropriate valves found on the market were the Capricorn MiniHab HypAirBalance, see Figure D.13.

They are passive normally closed air admittance valves from the plumbing market. A rubber membrane contained in the valve obstructs the opening of the valve due to gravity. When sufficient pressure is applied, the rubber membrane is lifted up and the valve opens. Their opening pressure is 70 Pa (equivalent to 1686 Pa at full scale) and their lightweight allowed their use in the small scale Tupperwave physical model.

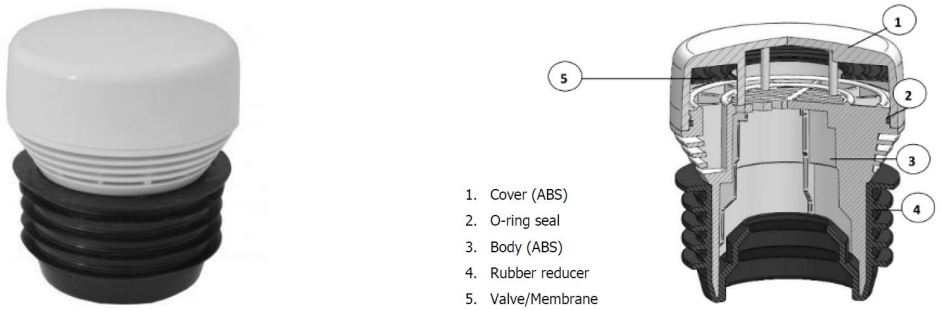


(a) Full device

(b) Section

Figure C.7: MiniHab HypAirBalance from Capricorn used in Tupperwave small scale model [121]

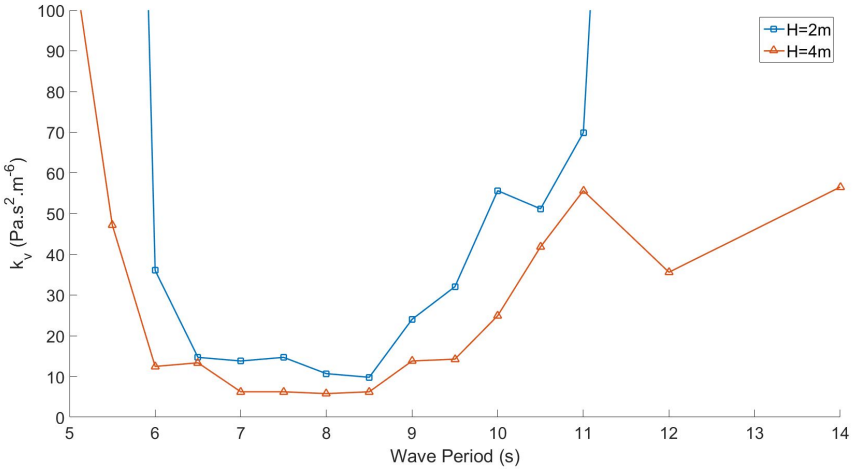


Figure C.8: HP valve damping coefficient in regular waves (full scale equivalent)

According to equations C.15 and C.16, lower values of the valve damping coefficient $k_v$ reduce the pressure drop across the valves and hence reduce the pneumatic power losses. The value of $k_v$ is therefore fundamental for the device efficiency. Unlike for the orifices, the damping coefficient of the valves were experimentally assessed during each tests by using equations C.15 and C.16 and monitoring the pressure drop and air flow across the valves. The air flow rate across the valves was calculated from the measurement of the IWS elevation achieved with wave probes located inside the water column. Different valve damping values were obtained depending on the tests undertaken. Figure D.14 displays the values of $k_v$ for the HP valve obtained in regular waves. Wave height, wave period and valve damping coefficients are given at full scale equivalent. Variations of $k_v$ with the wave height and wave period are observed. It was shown in [122] that the damping coefficient of those valves is highly dependant on the device excitation. Indeed, when

the device is well excited (for 6.5 s $< T <$ 8.5 s), large pressure drops and flows across the valves are created. The valves therefore open fully and their damping coefficient is small (large effective area). The lowest damping values reached by the valves were around $k_v = 7.5\,\text{Pa.s}^2\text{.m}^{-6}$ at full scale equivalent, which corresponds to an effective valve opening area of $0.286\,\text{m}^2$. This maximum opening area achieved is very small compared to the available $10.6\,\text{m}^2$ available between the OWC chamber and the HP chamber. When the device is poorly excited (for $T <$ 6.5 s and $T >$ 8.5 s), the valves do not open fully and create large damping (i.e. large losses). For $H = 4\,\text{m}$, the valves open fully on a larger range of wave periods than for $H = 2\,\text{m}$ since the device is more excited in bigger waves. The values of the valves damping coefficient assessed for each regular wave physical test were fed into the numerical model for the corresponding numerical test.

In irregular waves, the excitation of the device varies with the incoming wave groups. Hence, the instantaneous damping of the valves fluctuates along the simulation. The $k_v$ values in-putted in the numerical model for each irregular wave simulations were the average damping values obtained physically over the whole durations of the simulations.

## C.3.2 Experimental setup and test plan

The experiments took place in the Lir-National Ocean Test Facility (Lir-NOTF) of the MaREI centre in Cork, Ireland. The devices were tested under regular and irregular sea states in the Deep Ocean Basin which is 35 m long, 12 m wide, and has a movable floor with up to 3 m depth. For the regular sea states and at full scale equivalent, 2 wave heights (2 m and 4 m) were tested with periods ranging from 5 to 14 s. A set of 8 irregular sea states of various significant wave heights (2-5 m) and peak periods (5-14 s) was also tested. These sea states were chosen to represent a large variety of typical conditions in the Atlantic Ocean. The depth was set to 2.07 m, equivalent to 50 m at full scale.

The devices were moored using a 3 points mooring arrangement of catenary type with 120 degrees between any two mooring lines. There are two bow mooring lines and one stern line. Each line is divided in two parts: a steel chain connects the anchor to a surface buoy that can support the chain weight. A neutrally buoyant line then connects the surface buoy to the device at the mean water level. Figure C.9 shows a schematic of one mooring line. With such mooring configuration, the mooring forces applied on the device are principally horizontal, preventing the device from drifting in the waves, with a minimum impact on the heave motion from which the wave energy is absorbed. Therefore, the vertical component of the mooring force applied on the device was neglected in the numerical model presented in section C.2. The drag forces caused by the vertical motion of the neutrally buoyant lines with the device are taken into account in the numerical model

by the equivalent drag coefficient $C_d$.

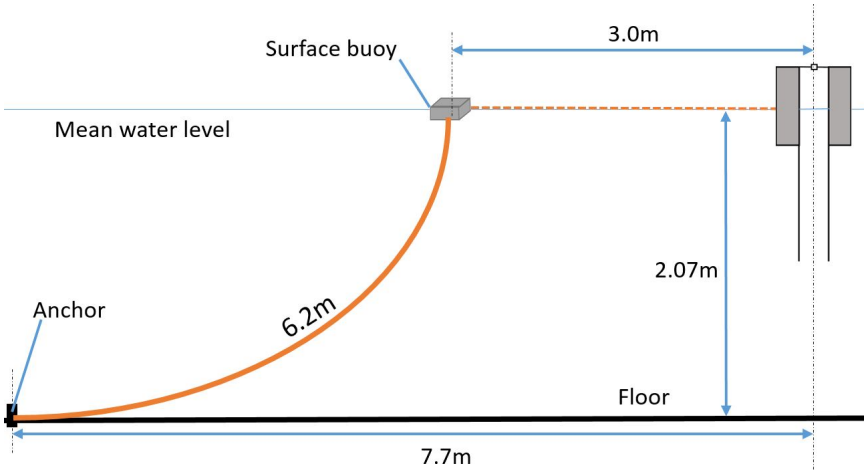


Figure C.9: Schematic of a mooring line. The device is moored by 3 mooring lines with 120 degrees between any two mooring lines.

The devices were fully monitored using 3D cameras, pressure sensors and wave probes allowing the measurement of the devices motions, IWS elevation, pressure drops and volumetric flow rates across orifices and valves. Wave probes located outside of the device measured the incoming wave elevation. A wave probe located inside the column of the device measured the relative elevation of the water column relatively to the buoy. Figure C.10 displays a picture of the device, from above, equipped with pressure sensors and reflective markers for the 3D cameras.

The power absorbed from the waves by the devices is the power applied by internal water surface (IWS) on the air contained in the OWC chamber, and was calculated, from those measurements, as:

$$P_{abs} = p_{owc}.\dot{V} = p_{owc}S_2\frac{dx_{IWS}}{dt} \tag{C.22}$$

where $x_{IWS} = x_2 - x_1$ is the position of the IWS relatively to the buoy. In testing conditions, the flows across the orifice or valves are incompressible. The pneumatic power available to the turbine $P_t$ or to a valve $P_v$ is therefore calculated as the product of the volumetric flow and the pressure drop:

$$P = \Delta p\, q \tag{C.23}$$

The regular wave tests were 125 seconds long, which is equivalent to 10 minutes at full scale. The irregular wave tests are 7 minutes long which is equivalent to 35 minutes at full scale. This allows a full representation of the Bretschneider sea state.

For the analysis of regular wave tests, averaging of the key variables is made over several waves once a steady state is reached, practically between 90 and 115 s at model scale. The average values in irregular sea states are calculated over the full time of the simulation.

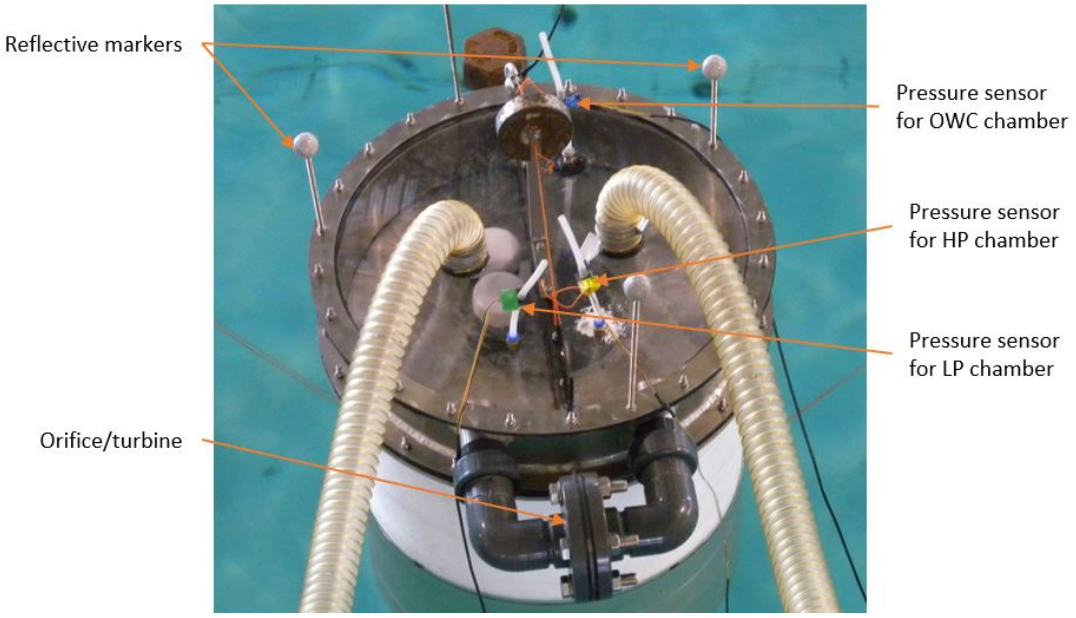


Figure C.10: Top view of the Tupperwave device

## C.4 Results and numerical model validation

Physical and numerical tests were carried out for the small scale devices, but all results are given in full scale equivalence to give the reader perspective.

### C.4.1 Correction in the Tupperwave numerical model

During the tests, it was observed that the reservoirs used for the HP and LP chambers of the Tupperwave physical model did not have perfectly rigid walls and that the walls moved very slightly due to the pressure building inside the chambers. The HP chamber was observed to inflate with the build-up of a positive excess pressure inside and the LP chamber was observed to deflate due to the negative excess pressure inside. Unfortunately, within the time frame and budget of the project, it was not possible to replace the chamber walls with stiffer material. As a result, the air compressibility in the HP and LP chambers was physically not modelled correctly and the varying volumes of the chambers caused a dampening of the pressure variations. This required a correction in the initial numerical model described in section C.2.2.3 to take into account the slight volumetric changes of the HP and LP chambers.

A simple linear model of the chamber volumetric deformation as a function of the excess pressure was chosen:

$$\begin{cases} V_{hp} = V_0 + Cp_{hp} \\ V_{lp} = V_0 + Cp_{lp} \end{cases} \tag{C.24}$$

where $C$ is the elastic stiffness of the chambers and $V_0 = 1.64\,\mathrm{m}^3$ is their initial volume.

The same stiffness value was applied to the two chambers and its value was calibrated using the experimental results. The value $C = 8.3 \times 10^{-5}\,\mathrm{m}^3.\mathrm{Pa}^{-1}$ was obtained by an iterative process to minimise the error with the experimental results in the different irregular sea states. Therefore, for an excess pressure of $p_{ref} = \pm 1000\,\mathrm{Pa}$ (close to maximum pressure observed in the chambers), the volume variations of the chamber is $dV_{ref=} \pm 0.083\,\mathrm{m}^3 << V_0$ which is equivalent to a $\pm 2\,\mathrm{cm}$ deformation of the edge lengths of the cubic chambers and corresponds with the approximate visual observations.

The system of equations F.6 describing the pressure evolution in the Tupperwave chambers is modified to take into account the HP and LP chambers deformations:

$$\begin{cases} \dot{p}_{owc} = \dfrac{\gamma p_{atm}}{\rho_{atm} V_{owc}}(w_{vl} - w_{vh} - \rho_{owc}\dot{V}_{owc}) & (a) \\ \dot{p}_{hp} = \dfrac{\gamma p_{atm}}{\rho_{atm} V_{hp}}(w_{vh} - w_t - \rho_{hp}\dot{V}_{hp}) & (b) \\ \dot{p}_{lp} = \dfrac{\gamma p_{atm}}{\rho_{atm} V_{lp}}(w_t - w_{vl} - \rho_{lp}\dot{V}_{lp}) & (c) \end{cases} \tag{C.25}$$

Figure C.11 compares the time series of the pressure drop $\Delta P_t = p_{hp} - p_{lp}$ across the orifice of the Tupperwave device in regular waves of 9 s period and heights of 2 m and 4 m obtained by the physical model, the initial numerical model, and the corrected model. In regular waves, the wave excitation on the device is steady and the excess pressures in the HP and LP chambers increased until they stabilized to certain values and reach a steady state. In the initial numerical model where the HP and LP chambers are perfectly rigid, the pressure drop between the chambers build-up quickly to reach steady state. Small pressure drop oscillations with a period of half a wave period are also visible and are due to the oscillatory motion of the water column. In the physical model, the chambers deformed gradually by a corresponding small volume $\pm\Delta V$ much less than the initial volume $V_0$ and consequently delayed the pressure evolution. Hence, the slight deformation of the chambers did not influence the end results in regular waves but simply delayed the system to reach steady state. The smaller oscillations are also attenuated.

In irregular waves however, the slight volumetric deformations of the chambers caused more visible effects. During a simulation, the pressures in the HP and LP chambers vary significantly when the device is excited by high or low energy wave groups. The chamber volumes are therefore changing between wave groups and dampen fast pressure variations. Figure E.6 compares the time series $\Delta P_t$ in the irregular sea state $\{H_s = 3\,\mathrm{m};\, T_p = 8.5\,\mathrm{s}\}$ obtained physically against the time series obtained with the initial and corrected numerical model. The pressures in the rigid-wall chambers from the initial numerical model vary more rapidly with the wave groups than in the chambers used in the physical tests. As a result of the chambers deformation,

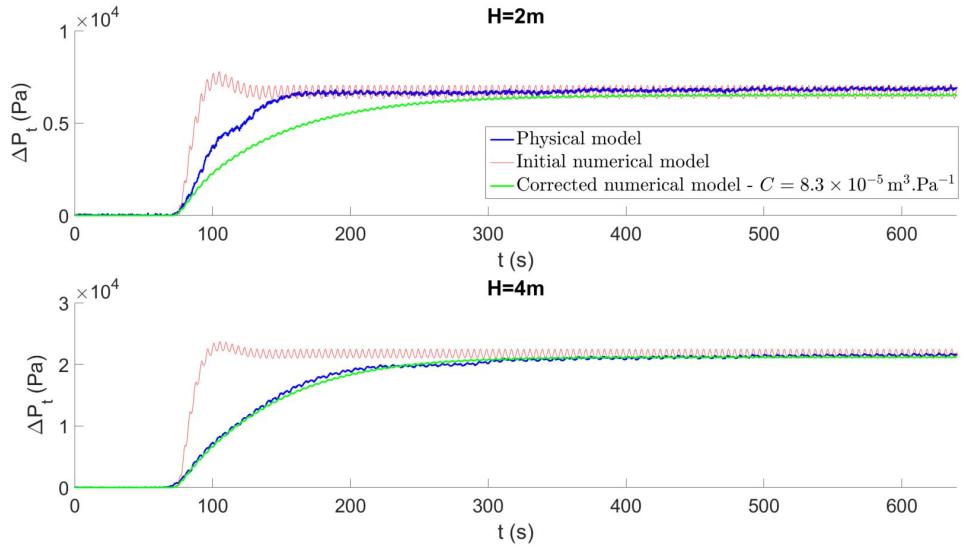


Figure C.11: Pressure drop time series across orifice 3 of the Tupperwave device obtained by the physical model, the initial numerical model, and the corrected model in the regular waves of 9 s period and heights of 2 m and 4 m

an extra and unrealistic smoothing effect of the pressure variations between the wave groups was observed in irregular waves. Accounting for the small volume variations of the HP and LP chambers in the numerical model very clearly enhances the fidelity with the physical model.

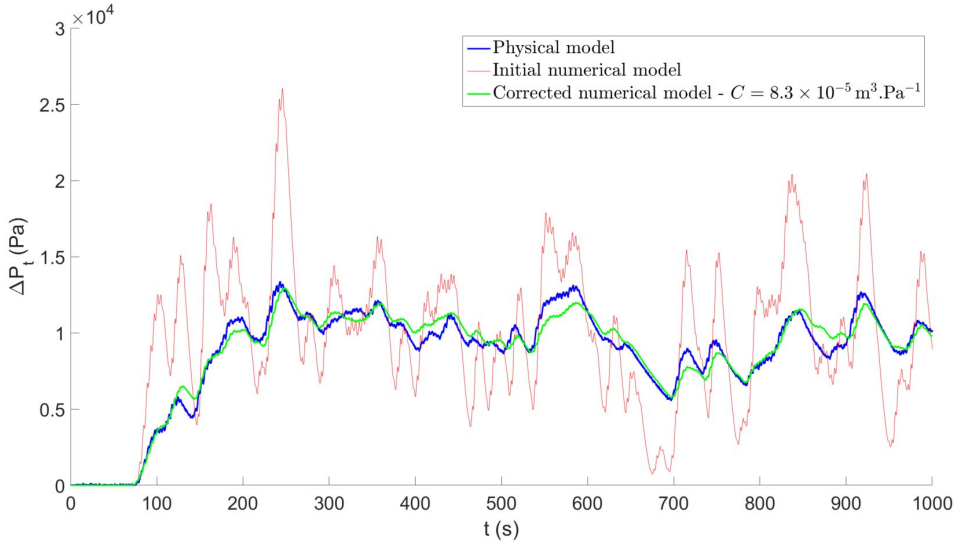


Figure C.12: Pressure drop time series across orifice 3 of the Tupperwave device obtained by the physical model, the initial numerical model, and the corrected model in the irregular sea state $\{H_s = 3\text{ m}; Tp = 8.5\text{ s}\}$

Figure C.13 displays the numerical results obtained with the following chamber stiffness values: $[4.2; 8.3; 12] \times 10^{-5}\,\text{m}^3.\text{Pa}^{-1}$, corresponding respec-

tively to $\pm[1; 2; 3]$ cm deformation of the chambers edge length for an excess pressure of $p_{ref} = \pm 1000\,\text{Pa}$. This figure shows the sensitivity of the results on the chambers stiffness value. With stiffer chambers ($C = 4.2 \times 10^{-5}\,\text{m}^3.\text{Pa}^{-1}$), the pressure variation are larger due to the smaller deformation of the walls. The pressure variations are more dampened with more flexible chambers ($C = 1.2 \times 10^{-4}\,\text{m}^3.\text{Pa}^{-1}$). Although the results are not extremely sensitive on the stiffness value, $C = 8.3 \times 10^{-5}\,\text{m}^3.\text{Pa}^{-1}$ obtains the closest results to the physical model for all sea states tested. Table C.3 displays the Pearson correlation coefficients between the time series obtained physically and the time series obtained with the initial and corrected numerical models. Values closer to 1 indicate a better correlation between physical and numerical results.

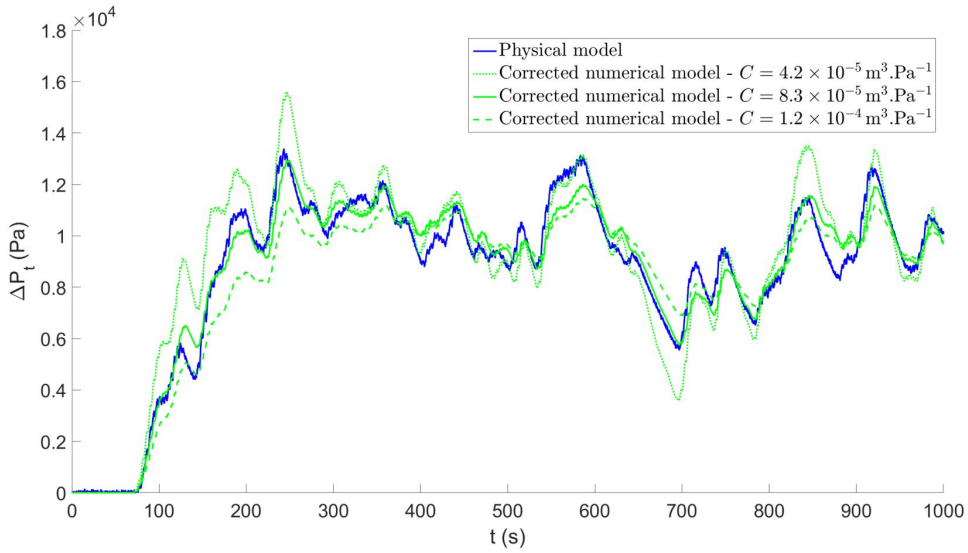


Figure C.13: Pressure drop time series across orifice 3 of the Tupperwave device obtained by the physical model and the corrected model in the irregular sea state $\{H_s = 3\,\text{m}; Tp = 8.5\,\text{s}\}$ with different chamber stiffness values

From an energy point of view, the pneumatic energy stored in the HP and LP chamber is not only stored in the form of pressure but also under the form of strain energy. This explains the lower pressure variations between wave groups and the average value of the pressure drop across the orifice is not impacted, see Figure E.6. In the next section, only the corrected numerical model of the model scale device accounting for the chambers deformation is used.

We note that the idea of storing pneumatic energy under the form of strain energy could be combined to the Tupperwave concept at full scale, by adding a spring and piston to the HP and LP chambers for example. This would enable to further improve the pneumatic power smoothing capacity of the device or to reduce the volumes of the reservoirs. Moreover, this would possi-

Table C.3: Pearson correlation coefficient between $\Delta P_t$ time series obtained physically and numerically for the various irregular sea states

| Sea state | | Pearson correlation coefficient (-) | |
|---|---|---|---|
| $H_s$ (m) | $T_p$ (s) | Initial model | Corrected model $C = 8.3 \times 10^{-5}\,\mathrm{m}^3.\mathrm{Pa}^{-1}$ |
| 2 | 5.7 | 0.72 | 0.85 |
| 3 | 7.1 | 0.68 | 0.93 |
| 3 | 8.5 | 0.69 | 0.93 |
| 5 | 8.5 | 0.65 | 0.94 |
| 3 | 10.6 | 0.70 | 0.94 |
| 5 | 10.6 | 0.65 | 0.93 |
| 5 | 12.7 | 0.62 | 0.93 |
| 3 | 14.1 | 0.70 | 0.86 |

bly introduce further control possibilities: changing the stiffness of the spring could enable the device to be tuned to the sea state to improve energy extraction (or de-tuned if desired). The concept variation of the Tupperwave device using variable volume HP and LP chambers will be investigated in further work and is not in the scope of this paper. With fixed volume chambers, the Tupperwave device is structurally and mechanically simple. History has shown that mechanical simplicity represents an advantage in the development of wave energy devices, particularly regarding the device cost, maintainability and reliability. Developers commonly claim the simplicity of their wave energy device as an advantage [123, 124, 125].

## C.4.2 Numerical model validation

For the validation process, the spar buoy and water column relative motions are first compared in regular waves. Figure C.14 displays the Response Amplitude Operator (RAO) of the bodies relative sinusoidal heave oscillations and their phase difference for the two devices. The numerical models agree generally well with the results obtained by the physical tests and the influence of the different orifice damping tested is well predicted. The phase difference between the bodies in the Tupperwave device for short wave period is less accurately predicted by the numerical model than for the conventional OWC. It is interesting to note that, for the two devices, smaller orifices restrict both the relative motion amplitude and the phase difference between

the bodies. In the conventional OWC, the larger damping of small orifices directly causes more resistance against the bodies relative motions. In the Tupperwave device, the larger damping of small orifices creates larger excess pressures in the HP and LP chamber which increase the necessary OWC chamber pressure to open the valves and thus causes more resistance against the bodies relative motions.

Also, in comparison to the conventional OWC, the response of relative motion amplitude in the Tupperwave device is narrower and the phase difference between the bodies is lower. This shows that the coupling between the structure and the water column is stiffer and the bodies are more constrained to oscillate together in the Tupperwave device.

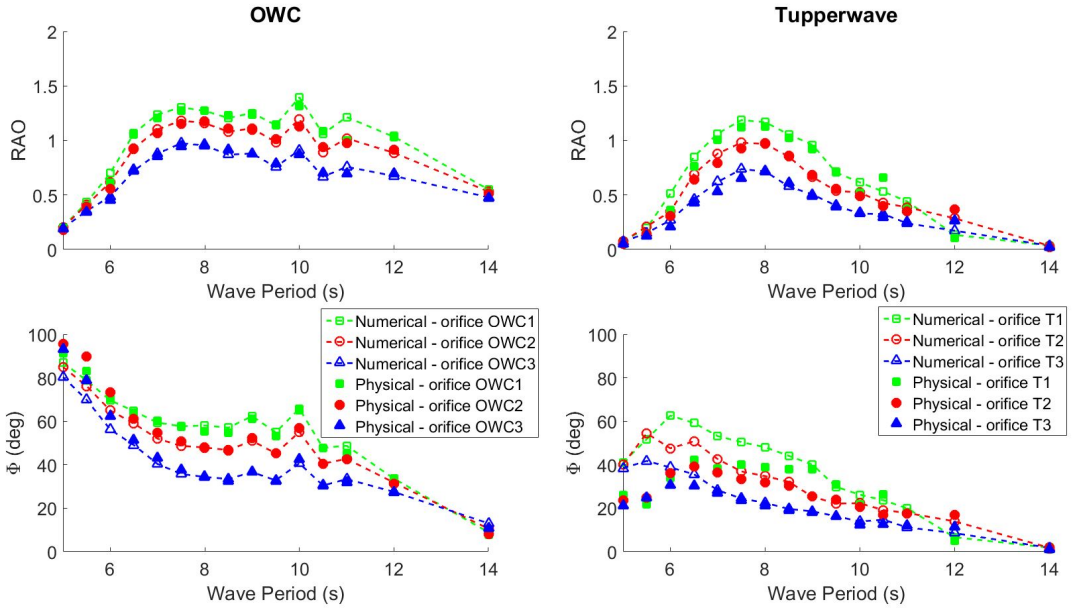


Figure C.14: RAO of the buoy and water column relative motion and their phase difference for the conventional OWC and Tupperwave device in regular waves ($H = 2$ m)

The average pressure drop and volumetric flow across the orifices in regular waves are compared in Figure C.15. Good agreement is obtained between numerical and physical results. In both devices, the pressure drop decreases with increasing orifice diameter and the flow across the orifice increases. The Tupperwave device produces larger pressure drops and lower flow rates across the turbine than the conventional OWC.

Figure C.16 displays the average pneumatic power normalized by the significant wave height squared obtained numerically and physically by the two devices in the 8 irregular sea states tested. Figure C.17 displays the time series of the pneumatic power for the irregular sea state $\{H_s = 3$ m; $T_p = 7.1$ s$\}$. The two devices are equipped with their most efficient orifices (OWC2 and T2).

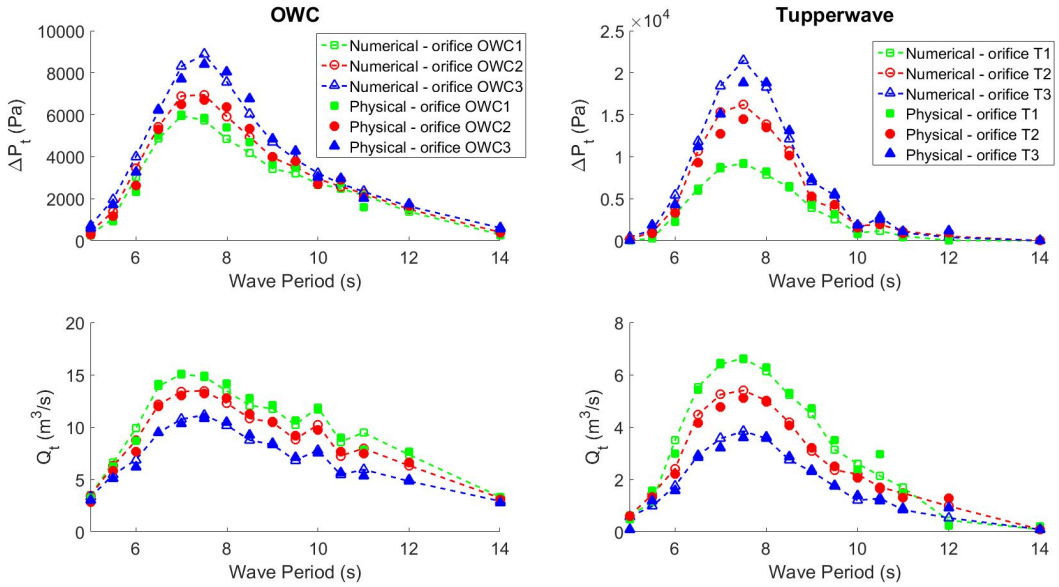


Figure C.15: Average pressure drop and volumetric flow rate across the orifice for the conventional OWC and the Tupperwave device in two-meter high regular waves

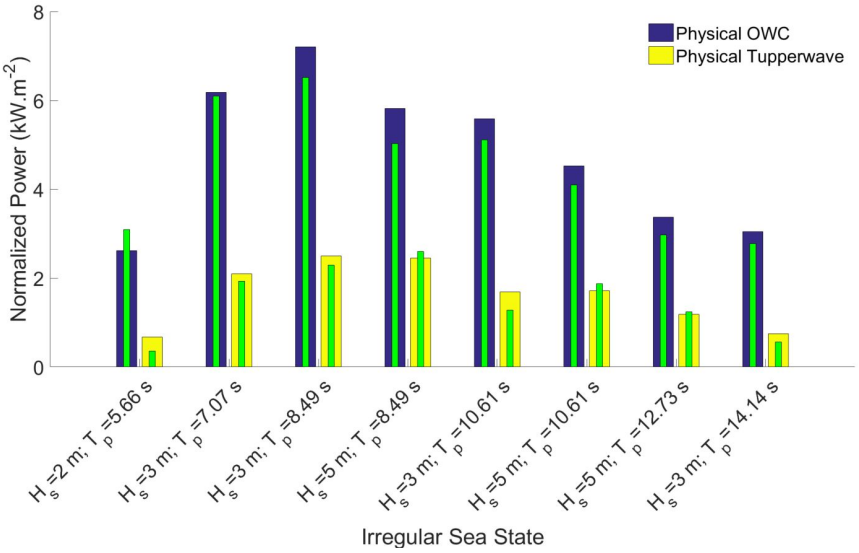


Figure C.16: Average pneumatic power normalized by the significant wave height squared for the conventional OWC and the Tupperwave device in irregular sea states

Good overall agreement is obtained between physical and numerical results. The errors of the numerical models on average power prediction in irregular wave tests in Figure C.16 were of 10.1% for the conventional OWC and 16.5% for the Tupperwave device. The passive valves in the Tupperwave model are an additional component to model and their fluctuating behaviour

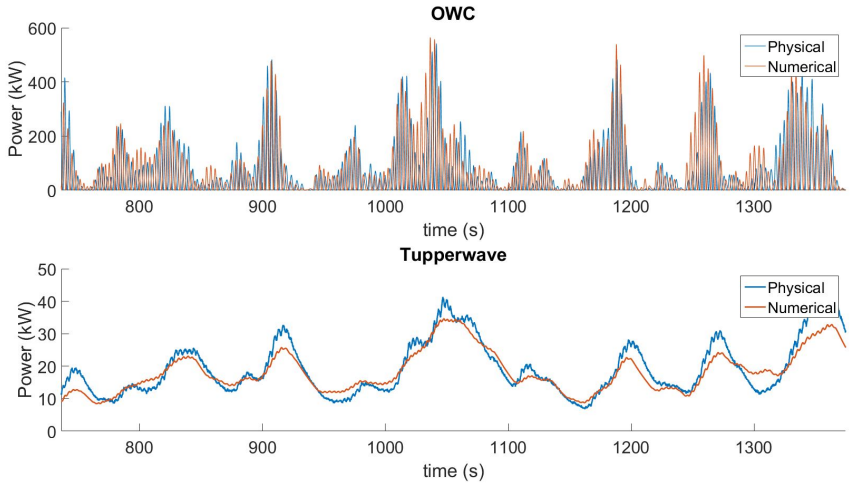


Figure C.17: Pneumatic power time series for the conventional OWC and the Tupperwave device in irregular sea state $\{H_s = 3 \text{ m}; T_p = 7.1 \text{ s}\}$

with the device excitation in irregular waves (see section C.3.1.3) is hence an additional source of error in numerical model fidelity.

Although moderate pitch and roll motions of the spar buoy were observed during the experiments, the satisfactory results of the numerical model prove, a posteriori, that considering heave only in the numerical model is a reasonable approach to assess the devices power conversion.

### C.4.3 Power performance comparison

Figure C.18 displays the average power absorbed by the device from the waves $\overline{P_{abs}}$ and the average pneumatic power $\overline{P_{avail}}$ available to the turbine in both devices in 2- and 4-meter high regular waves. In the case of the conventional OWC, the absorbed power is, in average, entirely made available to the turbine $\overline{P_{abs}} = \overline{P_{avail}}$ [67]. The Tupperwave device absorbs 4 to 20% less power from the waves than the conventional OWC for wave periods between 6 and 9.5 seconds. This is probably due to the stiffer coupling between the structure and the water column in the Tupperwave device which prevents optimal absorption. Moreover, unlike in the conventional OWC, only about 60% of the absorbed wave power is made available to the turbine and the rest is dissipated in the valves [122]. This reveals the poor efficiency of the valves used during the tests. In the end, the Tupperwave device produces in average only about 40% of the available pneumatic power produced by the conventional OWC device for wave periods between 6 and 9.5 seconds. This goes down to 33% in average in irregular waves, see Figure C.16. The efficiency of the Tupperwave device to convert the absorbed wave power into available power to the turbine is studied in greater detail in [126].

The poor performance of the Tupperwave physical model relative to the conventional OWC is largely due to the pneumatic power losses occurring

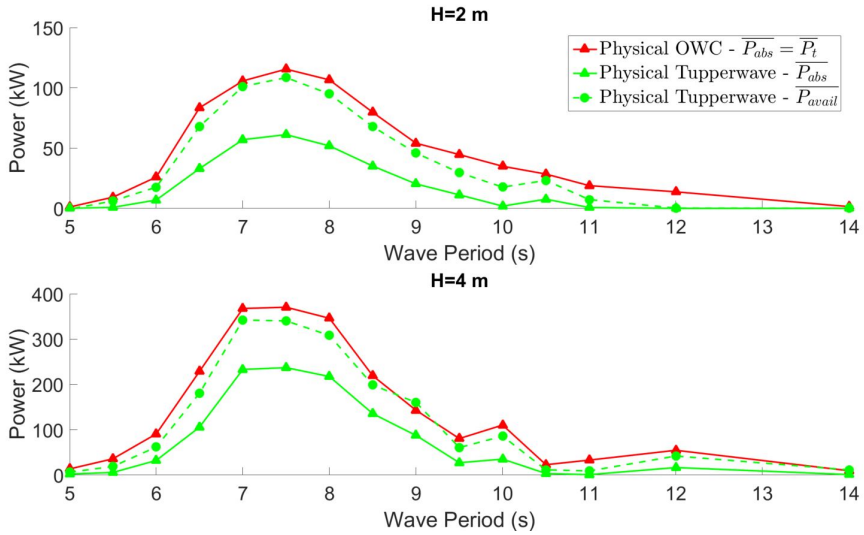


Figure C.18: Average power absorbed from the waves $P_{abs}$ and pneumatic power available to the turbine $P_{avail}$ by the conventional OWC and the Tupperwave device in two- and 4-meter high regular waves

in the valves used in this tests. The valves, described in section C.3.1.3, were bought off-the-shelf from the plumbing market and their poor performance is not representative of what could be obtained at full scale with purposely designed valves. It is likely that purposely designed valves would reach better performances. However, the available literature provides very little information on non-return valves for large OWC devices and no information on their achievable performances. This shortcoming of the available literature on OWC devices hinders definitive conclusions on the performance of flow-rectifying OWC devices like the Tupperwave device.

The valves used in these tests operated however sufficiently well to prove the capacity of the Tupperwave device to smoothen significantly the air flow across the turbine in comparison with the conventional OWC, see Figure C.17. In the latter, the air flow across the orifice stops every half wave period to change direction and the pneumatic power drops to zero. Between two flow directional change, the pneumatic power reaches a peak of 500kW in about 3-4 seconds in a relative low-energetic sea state. At full scale, the efficiency of an air turbine to convert pneumatic power into mechanical power is largely dependant on the pneumatic power fluctuations. Large fluctuations of pneumatic power prevent the turbine from working at maximum efficiency and the average efficiency of a self-rectifying turbine is lower in real flow condition than in constant flow condition as shown in [57]. It is however to be kept in mind that the inertia of the turbines acts as short-term energy storage. Hence, the final electrical power output of the conventional OWC and of the Tupperwave device would be smoother than the pneumatic power flowing across their turbines presented in Figure C.17.

The results show that the smoothing of the pneumatic power achieved by the Tupperwave device is significant but made at the expense of important pneumatic power losses in the valves resulting in lower power performance of the Tupperwave device. The smoothing of the pneumatic power will however play a role in the rest of the power conversion chain as it will simplify the pneumatic to mechanical power conversion by the turbine and may pay back in terms of overall electrical power performance and power quality.

## C.5 Conclusion

In this work, time-domain numerical models of a conventional OWC and of the Tupperwave device were developed. The models consider the conversion of wave power to pneumatic power; and were built using hydrodynamic and thermodynamic equations. A tank testing campaign was carried out for the two devices at 1/24th scale to prove the Tupperwave working principle and provide data for the numerical models validation.

Air compressibility is essential in the Tupperwave device working principle and it was attempted to model it physically by scaling down the HP and LP chambers by $\epsilon^2$. This was however not done correctly since the walls of the additional chambers used in the Tupperwave device were not perfectly rigid which invalidated the exact reproduction of the air compressibility in the HP and LP chambers. The chambers being very slightly deformable, it added a phenomenon of pneumatic power storing in the chambers under the form of strain energy and caused an additional unrealistic smoothing of pressure variations in the chambers. Nevertheless, the working principle of the Tupperwave device was validated and the device operated reasonably well. The numerical model of the Tupperwave device was corrected to take into account the chamber deformation by adding a linear model of the chamber volumetric deformation as a function of the excess pressure.
With this correction, the numerical models predicted correctly the influence of the orifice damping, wave period and wave height on the body motions, pressure and pneumatic power. In irregular waves, average pneumatic power productions were predicted by the numerical models with 10.1% and 16.5% error relatively to the physical results for the conventional OWC and the Tupperwave device respectively. The numerical model of the Tupperwave device showed less accuracy due to the fluctuating behaviour of the passive valves which revealed to be highly dependant on the device excitation.

Since the two devices are using the same Spar buoy, direct comparison in terms of pneumatic power performance was also possible. The physical model of the Tupperwave device produced in average only about one-third of the available pneumatic power produced by the conventional OWC device in irregular waves. The main reason for that is the large pneumatic power losses caused by the rectifying valves used in the tests which revealed to be of poor efficiency as only about 40% of the absorbed wave power is effectively

made available to the turbine. The poor performance of those valves is not representative of what could be achieved with purposely designed valves at full scale, but reveals the importance of the valve design in the Tupperwave device performance. However, the pneumatic power available to the turbine of the Tupperwave device is much smoother than in the conventional OWC. The pneumatic power smoothing of the Tupperwave device demonstrated in this paper is likely to have a positive influence on the turbine efficiency and on the overall electrical power production and quality.

The benefits of the pneumatic power smoothing on the Tupperwave device operation will be studied and quantified in future works, where a turbine and a generator will be added to the numerical model to build a complete wave-to-wire model.

## Acknowlegment

The authors would also like to thanks M. Tahar, T. Walsh and F. Thiebaut for their help in the physical tank testing campaign.

# Appendix D

# Paper D

# Modelling approaches of closed-circuit OWC wave energy converter

*Published in*

Journal of Marine Science and Engineering, MDPI

*Authors*

Pierre Benreguig[1], Jimmy Murphy[1]

[1]*MaREI Centre (ERI), University College Cork, Haulbowline Road, Ringaskiddy, Ireland*

# Abstract

The Tupperwave device is a wave energy converter based on the Oscillating Water Column (OWC) concept. Unlike conventional OWC devices, which are opened to the atmosphere, the Tupperwave device works in closed-circuit and uses non-return valves and accumulator chambers to create a smooth unidirectional flow across a unidirectional turbine. The EU-funded Ocean-EraNet project called Tupperwave was undertaken by a consortium of academic and industrial partners, aimed at designing and modelling the Tupperwave device. The device was numerically modelled using two different methods. It was also physically modelled at the laboratory scale. The various modelling methods are discussed and compared. An analysis of the dependence of the device efficiency on the valves and turbine aerodynamic damping is carried out, using both physical and numerical approaches.


## D.1 Introduction

Among the various types of wave energy converter technologies, Oscillating Water Column (OWC) devices are some of the most promising for extracting energy from the ocean. An OWC device consists of a partially-submerged fixed or floating hollow structure, open to the sea below the water surface, that traps air above the inner free-surface in the OWC chamber; wave action alternately compresses and decompresses the trapped air. In the most conventional sort of OWC devices, the OWC chamber is opened to the atmosphere through a self-rectifying turbine. The pressure variations in the OWC chamber create a bidirectional air flow across the turbine, which rotates in a single direction for both flow directions. This kind of turbine is therefore able to harness both directions of flow and does not require a system of non-return valves. The efficiency of self-rectifying turbines is however lower than conventional unidirectional turbines. Several types of self-rectifying turbines have been developed for OWCs with various working principles, benefits, and drawbacks. An extensive review of such turbines can be found in [9]. The best-performing self-rectifying turbines so far are the biradial and twin-rotor turbines, which reach about 75% efficiency [127, 128] in constant flow condition. In real ocean conditions, the flow across the turbine is however highly fluctuating and reverses at every half wave period. In these conditions, the average efficiency of self-rectifying turbines drops by 5–10% [57].

The Tupperwave device is a closed-circuit OWC using non-return valves and two accumulator chambers to create a smooth unidirectional flow across a unidirectional turbine. Figure E.2 describes schematically the working principle of the device under study. The motion of the water column alternatively pushes air into the High Pressure chamber (HP chamber) through the HP valves when rising and sucks air out from the Low Pressure chamber (LP

chamber) through LP valves when falling. Due to the flow restriction across the turbine, a pressure differential builds between the two chambers, and the air flows in a relatively steady manner from the HP chamber to the LP chamber across a unidirectional turbine. Therefore, the Tupperwave working principle does not only aim at using a unidirectional turbine, but also at smoothing the unidirectional air flow. The objective is to facilitate the conversion from pneumatic power to mechanical power by the unidirectional turbine and to reach a turbine efficiency close to the maximum efficiency obtained in the constant flow condition. The incentive of the Tupperwave principle is that unidirectional turbines can reach efficiencies close to 95% in such conditions. Ultimately, the Tupperwave principle aims at increasing both the electrical power output and quality, compared to a conventional OWC. Within

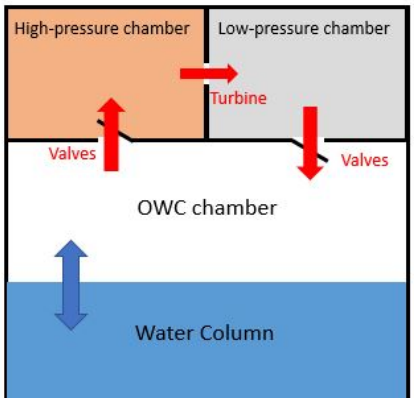


Figure D.1: Schematic diagram of the Tupperwave device concept.

the scope of the Tupperwave project, a parametric study was first carried out on the chambers' volume and turbine damping [95]. The results showed that larger chambers lead to better pneumatic power smoothing. Since it had been decided to apply the Tupperwave principle to a floating spar buoy, the entire buoyancy volume is used for the accumulator chambers. Figure G.1 displays the geometry of the full-scale Tupperwave device. The volumes of the HP and LP chambers have a constant value of 950 $m^3$ each.

In this paper, various methods to model the Tupperwave device are described, and the results are compared. In Section D.2, a numerical model of the device is developed based on the linear waves and potential flow theories using the Ordinary Differential Equations (ODEs), linking hydrodynamic and thermodynamic physical quantities. Hereinafter, this model is identified as Numerical Model 1. Section D.3 presents another model using the Computational Fluid Dynamics (CFD) software ANSYS CFX. In the scope of this document, this model will be designated as Numerical Model 2. The results of Numerical Model 2 are compared against the results of Numerical Model 1. Section D.4 presents the physical modelling of the device at $1/24^{th}$ scale tested in a wave tank. The physical results are compared against the

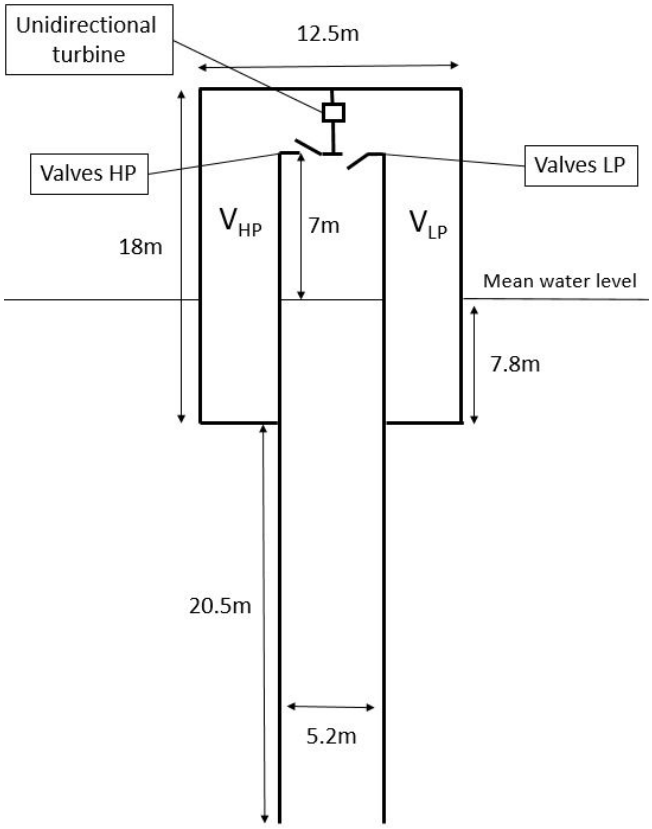


Figure D.2: 2D schematic of the full-scale Tupperwave device.

results of Numerical Model 1. The paper does not present results comparing the three models simultaneously. Although Numerical Model 1 is quite flexible, easily adapting its parameters, Numerical Model 2 and the physical model are subject to several constraints, which made it difficult to have a set of numerical simulations and physical tests with comparable parameters and conditions for the three approaches. Nevertheless, the comparisons presented are still of interest and useful to show the viability of the Tupperwave concept, as well as the relevance of the different methods. In Section D.5, the influence of valves and turbine damping on the device efficiency in converting the absorbed wave power into useful pneumatic power is studied using both physical observations and numerical simulations.

## D.2 Numerical Model 1

The numerical model of the Tupperwave device presented in this section uses ODEs coupling hydrodynamic and thermodynamic variables.

### D.2.1 Hydrodynamics

The spar buoy structure and the water column are considered as two rigid bodies moving only in heave in the waves relative to each other [80]. The model is based on linear waves and potential flow theories. Both bodies are subject to the Cummins equation, and their coupled heave motions (denoted as Index 1 for the buoy and 2 for the piston) can be written in time-domain as:

$$\begin{cases} [m_1 + a_{11}(\infty)]\ddot{x}_1(t) + \int_0^t K_{11}(t-\tau)\dot{x}_1(t)d\tau + a_{12}(\infty)\ddot{x}_2(t) \\ \quad + \int_0^t K_{12}(t-\tau)\dot{x}_2(t)d\tau + c_1 x_1(t) = f_1(t) + f_p(t) + f_{d1}(t) \quad (a) \\ a_{21}(\infty)\ddot{x}_1(t) + \int_0^t K_{21}(t-\tau)\dot{x}_1(t)d\tau + [m_2 + a_{22}(\infty)]\ddot{x}_2(t) \\ \quad + \int_0^t K_{22}(t-\tau)\dot{x}_2(t)d\tau + c_2 x_2(t) = f_2(t) - f_p(t) + f_{d2}(t) \quad (b) \end{cases} \tag{D.1}$$

where $m_i$ are the bodies' masses; $a_{ij}(\infty)$ are the bodies heave motion added masses at infinite frequency (proper and cross modes); $c_i$ are the restoring force coefficients; $K_{ij}$ are the radiation impulse functions for heave motions (proper and cross modes), which are functions of the radiation damping coefficients $b_{ij}(\omega)$; $f_i$ are the wave excitation forces. $f_p$ is the reciprocating force due to the pressure in the OWC chamber acting on both bodies and is calculated as: $f_p = S p_{owc}(t)$ where $S$ is the internal water free-surface in the water column and $p_{owc}$ is the excess pressure relative to the atmospheric pressure built in the OWC chamber. The viscous drag forces $f_{d1}$ and $f_{d2}$ are calculated as $f_{di} = -C_{di}|\dot{x}_i(t)|\dot{x}_i(t)$ where $C_{di}$ is the equivalent drag coefficient. This force incorporates the viscous drag effects, as well as all non-linear viscous effects [111].

The frequency domain coefficients $a_{ij}(\infty)$, $b_{ij}(\omega)$, and $c_i$ are calculated using the commercial BEM solver WAMIT [129]. The four convolution integrals $I_{ij}(t) = \int_0^t K_{ij}(t-\tau)\dot{x}_j(\tau)d\tau$ are called memory effect integrals. Their values depend on the history of the system, which implies their recalculation at each time step and is not practical for solving the system. By using the conventional Prony's methods [117], it is possible to calculate each of these functions as the sum of $N_p$ additional unknowns $\{I_{ij,k},\, k = 1 : N_p\}$, which are the solutions of $N_p$ additional first order equations that will be solved along with the system of Equations (G.1)a,b. For this research, $N_p = 4$ was taken, which adds 16 first order equations to the system.

The ODEs (G.1)a and (G.1)b in $x_1$ and $x_2$ are coupled together, but also with the thermodynamic variable $p_{owc}$.

### D.2.2 Thermodynamics

In the Tupperwave device, air is exchanged between three different air chambers. Unlike for the conventional OWC where the OWC chamber is open to the atmosphere, the air in the Tupperwave device is flowing in a closed-circuit. Figure E.2 displays the different thermodynamic variables in the

three chambers. The volume of the OWC chamber varies with the relative motion of the device structure and water column as:

$$V_{owc} = V_0 + S(x_2 - x_1) \tag{D.2}$$

where $V_0$ is the volume of the OWC chamber when both bodies are at rest and $S$ is the horizontal internal water surface area of the water column.

The compressibility of the air in the three chambers is modelled using the linearised isentropic relationship between pressure and density:

$$\rho = \rho_{atm}\left(1 + \frac{p}{\gamma p_{atm}}\right) \tag{D.3}$$

where $p$ is the excess pressure in the chamber relative to the atmospheric pressure $p_{atm}$. It was shown in [130] that the isentropic assumption provides a very satisfactory approximation of the air spring-like effect in the chambers.

In each chamber, the mass balance equation gives:

$$q = \rho_f q_{in} - \rho q_{out} \tag{D.4}$$

where $q_{in}$ and $q_{out}$ are the air volumetric flows rates flowing respectively in and out of the chamber and $\rho_f$ is the density of the incoming flow.

Moreover, the mass variation in a chamber can be written as:

$$q = \frac{d(\rho V)}{dt} = \rho \dot{V} + \dot{\rho} V \tag{D.5}$$

Equations (D.2)–(E.4) applied to the three chambers of the device lead to the three coupled thermodynamic ODEs, also coupled with the hydrodynamic ODEs (G.1)a and (G.1)b:

$$\begin{cases} \dot{p}_{owc} = \dfrac{\gamma p_{atm}}{\rho_{atm} V_{owc}}(\rho_{lp} q_{vl} - \rho_{owc} q_{vh} - \rho_{owc} S(\dot{x}_9 - \dot{x}_3)) & (a) \\ \dot{p}_{hp} = \dfrac{\gamma p_{atm}}{\rho_{atm} V_{hp}}(\rho_{owc} q_{vh} - \rho_{hp} q_t) & (b) \\ \dot{p}_{lp} = \dfrac{\gamma p_{atm}}{\rho_{atm} V_{lp}}(\rho_{hp} q_t - \rho_{lp} q_{vl}) & (c) \end{cases} \tag{D.6}$$

where $q_t$, $q_{vh}$, and $q_{vl}$ are the volumetric air flow rates across the turbine, the HP valve, and the LP valve. The sign convention for the volumetric flow rates is given by the arrow directions in Figure E.2.

The air flow rate across a real turbine is a function of the turbine diameter, rotational speed, and pressure head. In the following sections, the turbine will be modelled by an orifice, and the relationship between flow rate and pressure drop is considered as quadratic:

$$\Delta p_t = p_{hp} - p_{lp} = k_t q_t^2 \tag{D.7}$$

where $k_t$ is the damping coefficient of the orifice and is a function of its diameter.

The valves are non-return valves that close when the pressure head across the valves $\Delta p_v$ is under a certain positive opening pressure $p_o$. $\Delta P_v$ is defined as $\Delta p_v = p_{owc} - p_{hp}$ for the HP valve and as $\Delta p_v = p_{lp} - p_{owc}$ for the LP valve. When opened, the relation between flow rate and pressure drop is:

$$\Delta p_v = p_o + k_{v1} q_v + k_{v2} q_v^2 \qquad for \quad \Delta p_v > p_o \tag{D.8}$$

where $k_{v1}$ and $k_{v2}$ are the damping coefficients of the valve, a function of its opening area.

The system of ODEs is solved numerically via MATLAB using the first order ordinary differential equation solver ode45. Equations (G.1)a and (G.1)b are reduced to first order equations by introducing the variables $v_1 = \dot{x}_1$ and $v_2 = \dot{x}_2$.

## D.3 Numerical Model 2

This section presents the modelling of the Tupperwave device using Computational Fluid Dynamics (CFD), which is based on Reynolds Averaged Navier–Stokes (RANS) equations, which provides more advantages in overcoming the potential flow weaknesses in handling problems that involve strong nonlinearity, dispersion, wave breaking, complex viscosity, turbulence, and vortex shedding.

### D.3.1 Model Setup

The Tupperwave device was simulated in a 3D numerical wave tank with the software package ANSYS CFX V19.1. The geometry of the device was generated with the software Solidworks and brought to the air and water domain of the numerical wave tank.

The dimensions of the domain were set according to the guidelines given in [131]. The water depth at the device location was 100 m. The following boundary conditions were applied to the flow domain:

- Non-slip conditions prescribed at the wave energy device and the boundaries representing the tank walls;
- Non-slip wall conditions applied to the wave dissipation ramp and the tank bottom;
- Opening condition applied to the top wall. The mass and momentum transported through this boundary were constrained by an opening pressure and direction model, with 0 Pa relative pressure. The volume fraction of the opening for air was set to 1.0 and that of water to 0.0. The temperature was set to 17°C;

- The wavemaker end was specified as a no-slip wall with mesh displacement applied. This is a well-validated method for generating waves in a CFD model [131, 132]. The generated waves propagate along the x-axis in the negative direction.

The 3D wave tank and boundary conditions are displayed in Figure D.3.

Figure D.4a,b displays the three-dimensional drawings of the Tupperwave device used in the CFD model. The orifice representing the turbine is 22 cm in diameter. To maximise the opening area of the valves, there were two round HP valves of 1.8 m in diameter connecting the OWC chamber to the HP chamber and two round LP valves connecting the LP chamber to the OWC chamber. The valves were modelled as surface interfaces, with a logical expression that defined the condition of open or closed. The condition is based on the sign of the pressure difference on both sides of the valves. The open condition allowed air to flow through unimpeded, while the closed condition placed a barrier across the face of the valve. The pressures were measured as a volume average value in 5 cm-thick volumes immediately above and below the valves, over the whole area of the valves. The opening pressure of the valves was set to $p_o = 0$ Pa. This is an idealistic representation of the valves. In reality, the valve design is likely to be much more complex and the opening pressure to be a non-null value, but this representation indicates the upper limit of how good valves can be. The orifice and valves are displayed in Figure D.5.

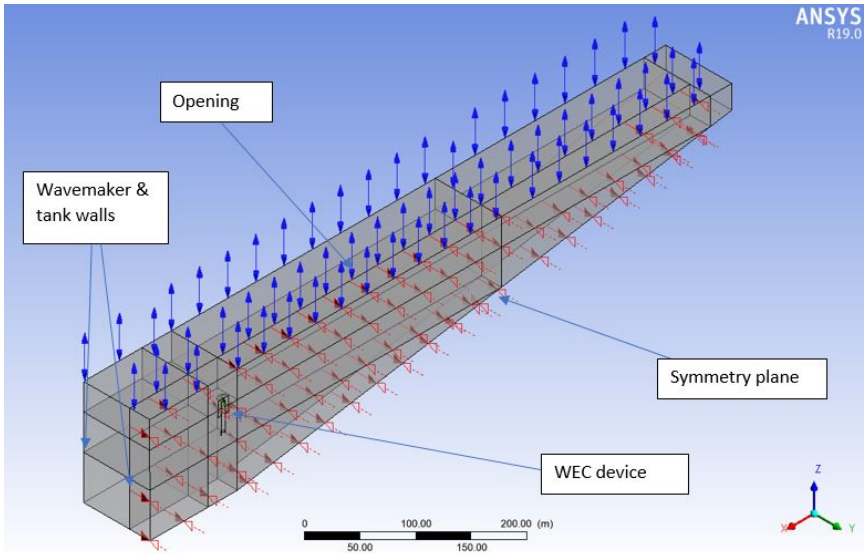


Figure D.3: 3D wave tank and boundary conditions.

A volumetric mesh was generated for the fluid and solid domains using ANSYS Workbench meshing v19.1. The mesh is a hybrid hexa/tetra/prism mesh. This meshing strategy was chosen since it is a flexible and inexpensive type of mesh. A finer resolution mesh was employed in the areas of interest,

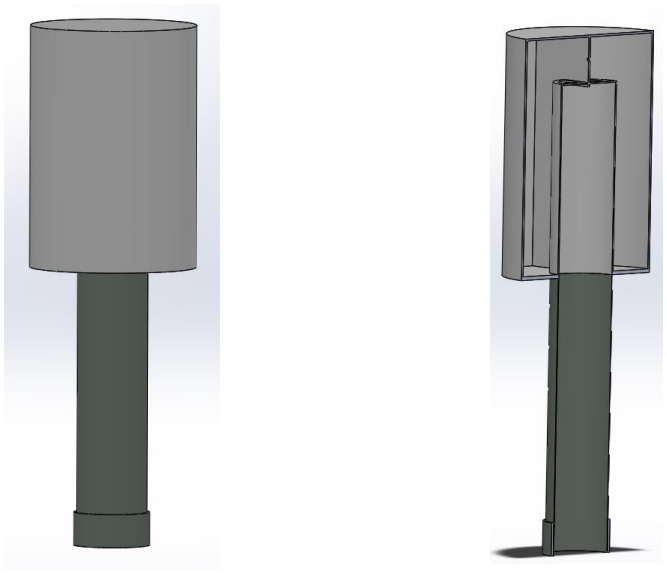

(a) Full device (b) Section

Figure D.4: 3D design of the full-scale Tupperwave device implemented in the CFD model.

and a boundary layer with appropriate thickness was used near the walls and in the turbine. At least four cells were present across the thickness of the device's solid walls. Between the wave source and the OWC device, the mesh was uniform along the x-axis and non-uniform along the y-axis, with a finer mesh region around the free-surface. This mesh contained 1,497,806 nodes and 4,066,389 elements in the fluid domain and 839,440 nodes and 1,983,223 elements in the solid domain. Figure D.6 displays the mesh in the vicinity of the device.

The analysis type was a transient, homogeneous, multiphase, thermal model analysis, with the standard free-surface model. The turbulence model employed to represent turbulent fluctuations was the k-wShear Stress Transport (SST) model. Interphase transfer was achieved with the free-surface model. The total simulation duration was 400 s with a time step interval of 0.06 s.

Difficulties in modelling the complete floating device were encountered when coupling the device motion with the compressible fluid model. This issue forced the authors to simplify the problem and give the device a fixed position, facilitating the computation.

Geometry preparation, meshing, and pre-processing were done on a Dell Z-book laptop with a four-core, Intel i7 processor, and 16 GB of RAM. The full model simulations were run on a 64-core, 157 GB RAM Amazon Web Services (AWS) EC2 virtual machine cluster over two compute nodes.

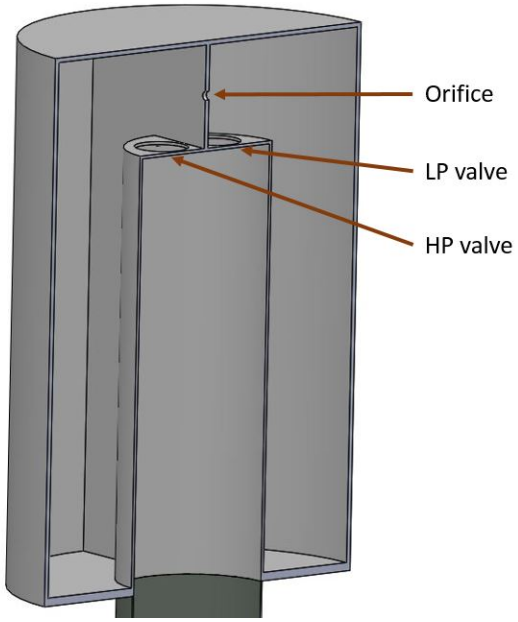


Figure D.5: Section view of the symmetry plane of the Tupperwave device.

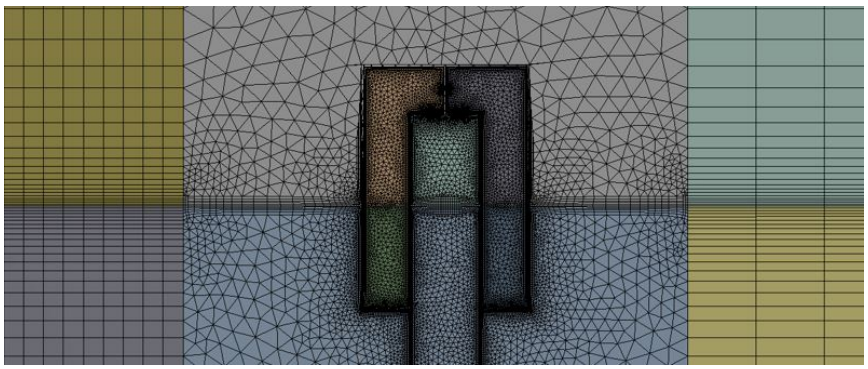

Figure D.6: Mesh in the vicinity of the device.

### D.3.2 CFD Results

Figure D.7 displays an image of a simulation run with a fixed buoy in two meter-high regular waves at 8-s periods. A video of the simulation has been added to the paper as a Supplementary File. It gives a good view of how the device works. The clear pressure difference all along the simulation was visible between the HP chamber on the left and the LP chamber on the right.

The damping coefficient $k_t$ of the orifice was determined by quadratic regression in Figure D.8. A coefficient of determination (or $R^2$ value) of 0.9996 was obtained. Being close to one, the coefficient indicated good regression fitting. For the valves, it was observed that the relationship between flow rate and pressure drop was not quadratic, but linear, as can be seen on Figure D.9. This is equivalent to $k_{v2} = 0$ in Equation (D.8). $k_{v1}$ was assessed by

linear regression with a coefficient of determination of 0.9828.

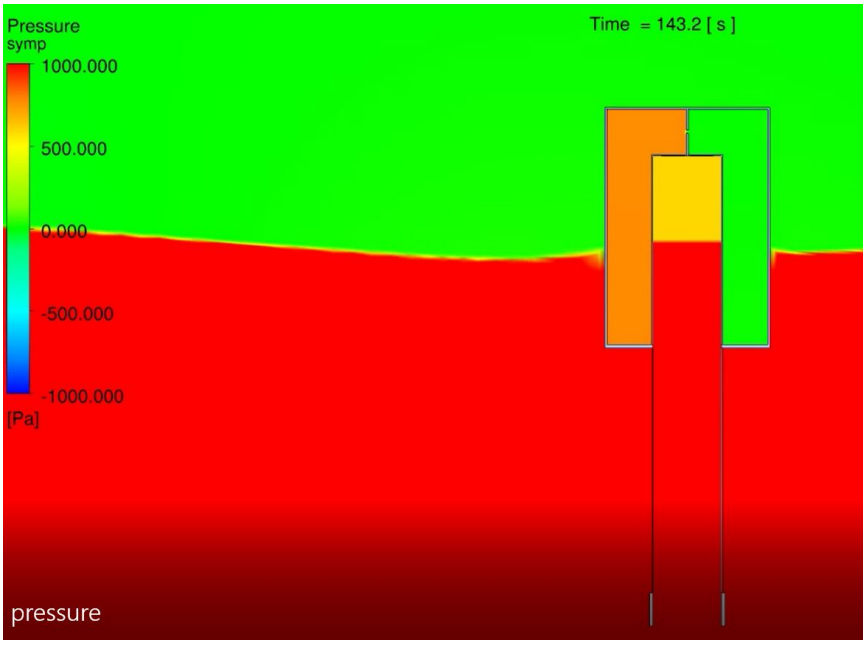


Figure D.7: 2D picture of the full-scale Tupperwave device in two-meter high regular waves of 8-s periods.

With the purpose of fairly comparing the numerical models, the damping coefficients of the orifice and valves obtained in the CFD simulations were used in the Numerical Model 1, and the floater was also considered to be fixed. Results from Numerical Models 1 and 2 are compared in Figure D.10. The Internal Water Surface (IWS) refers to the free-water surface elevation within the OWC chamber. Good agreement was obtained between the models, both on the relative motions of the bodies (IWS) and on the pressures in the different chambers. Small high-frequency fluctuations were observed in the pressures obtained by the CFD model due to fast unnecessary obstruction of the valves. Because the volumes used to measure the pressures on both sides of the valves were very small and close together, their average pressure values thus tended to equalize briefly every couple of time steps, closing the valves for one time step and creating a small pressure peak. The pressure fluctuations were especially visible in the OWC chamber, which was the smallest chamber. This did not happen in Numerical Model 1 because the pressures were assumed uniform in each chamber.

The power absorbed from the waves by the device is the mechanical power applied by the IWS on the air inside the OWC chamber and is calculated as:

$$P_{abs} = p_{owc} S (v_2 - v_1) \tag{D.9}$$

This power was converted into pneumatic power and distributed across the valves and the turbine. The pneumatic power available at the turbine $P_t$

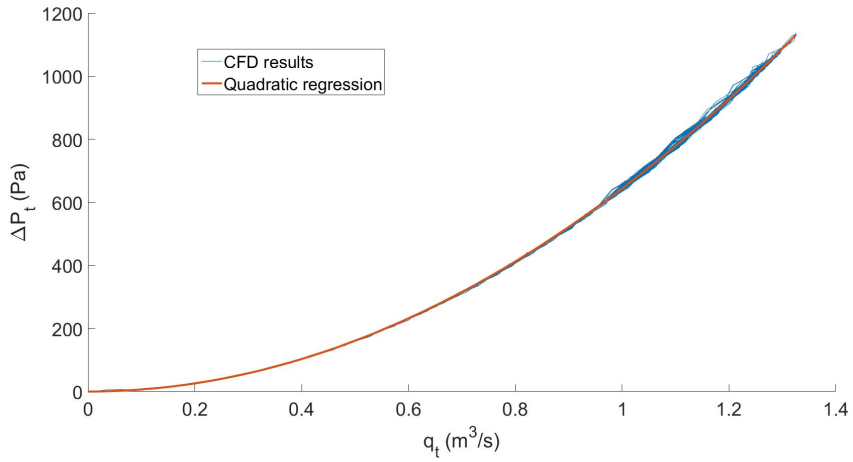


Figure D.8: Flow rate across the turbine-orifice as a function of the pressure drop with quadratic regression ($R^2$ = 0.9996).

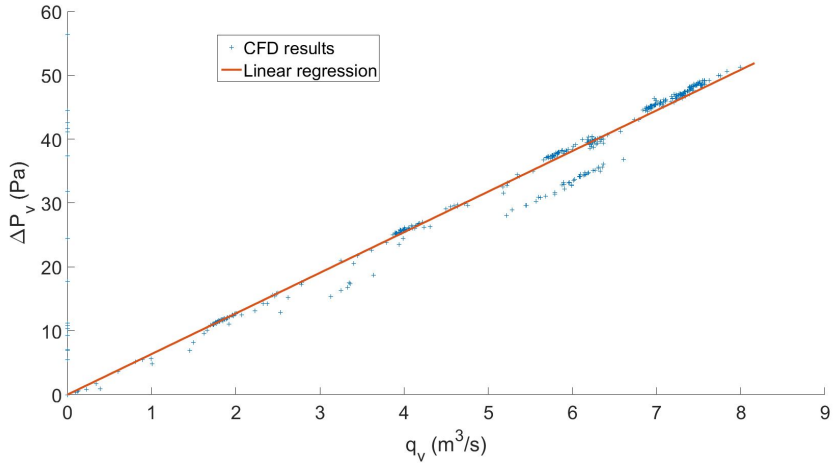


Figure D.9: Flow rate across the HP valves as a function of the pressure drop with linear regression ($R^2$ = 0.9828).

or across the valves $P_v$ was calculated as the product of the pressure drop times the volumetric flow rate:

$$P = \Delta p \, q \tag{D.10}$$

Only the power across the turbine is useful for electrical power production. The pneumatic power across the valves was dissipated under the form of heat due to viscous losses. The efficiency of the valves describes their capacity to let the air pass from one chamber to the next without dissipating energy. As a result of the valves' operation, the initial pneumatic power extracted from the waves was made available to the unidirectional turbine. The

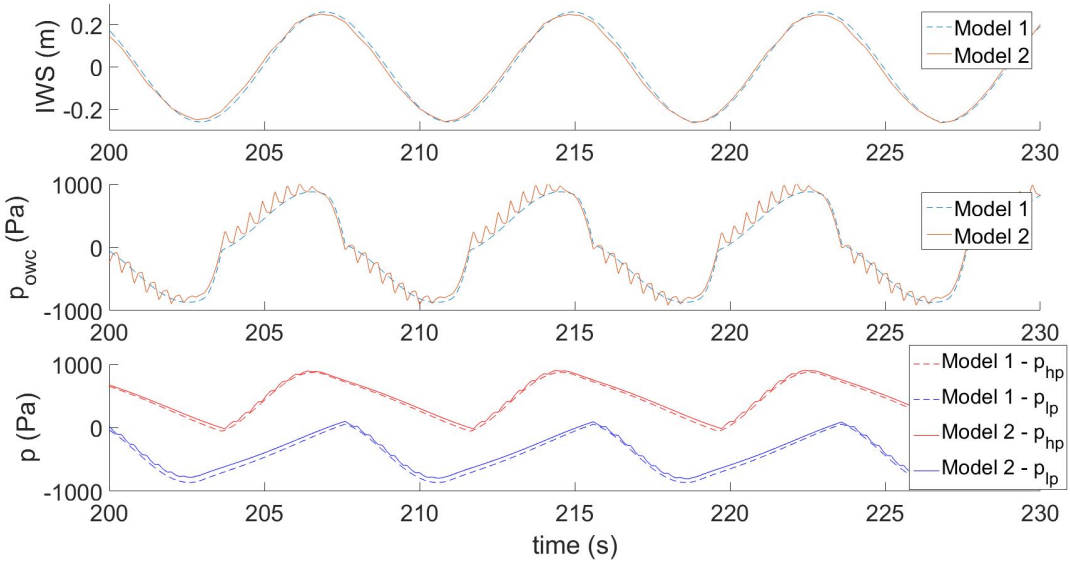


Figure D.10: Internal Water Surface (IWS) elevation and excess pressures obtained in OWC, HP and LP chambers obtained by Numerical Models 1 and 2 for 2 m-high and 8 s-period regular waves.

average efficiency of the valves was therefore defined as:

$$\eta_v = \frac{\overline{P_t}}{\overline{P_{abs}}} \tag{D.11}$$

It was shown in [133] that the Tupperwave device is competitive relatively to its corresponding conventional OWC when the valves' efficiency is higher than 80%. With the valves implemented in this CFD model, the valves' efficiency reached 95%. Since the valves were assumed to be ideal, 95% valve efficiency is probably the upper limit achievable.

# D.4 Physical Modelling

## D.4.1 Experimental Setup

A tank testing campaign of the Tupperwave device at the model scale was carried out in the Deep Ocean Basin of the Lir-National Ocean Test Facility at the MaREICentre, Ireland. The device was built at the model scale and equipped with all necessary instrumentation to monitor its behaviour fully. For the underwater part of the device, a Froude scaling factor $\varepsilon = 0.0415$, which was close to $1/24^{\text{th}}$ scale, was applied. However, the Tupperwave working principle relies on the air compressibility in the HP and LP chambers, which is not scalable with Froude similarity law. The Froude scaling similarity law requires to scale down the 950 $m^3$ chambers by $\epsilon^3$, which gives

0.068 $m^3$. With such small volumes and in the pressure conditions of the experiment, the air in the chambers would act as incompressible. According to a method suggested in [74], the volumes of the HP and LP chambers were scaled by $\epsilon^2$ to properly scale down the compressibility effect of the air, which gave 1.64 $m^3$ per chamber. This scaling law for the chambers size requires much larger size chamber than the Froude similarity would indicate. Unlike for the full scale, it was impossible to fit both chambers on the laboratory scale device as their volume largely exceeded the overall volume of the device. The alternative at a small scale was to locate the main volume of the HP and LP chambers outside of the device and to connect them to two smaller chambers on the device with flexible pipes. The reservoirs were located on the pedestrian bridge above the water. The flexible pipes were chosen as lightweight and flexible as possible to reduce their influence on the floating device motion. Part of the pipes' weight was supported by bungee ropes. Figure E.4 displays a schematic of the Tupperwave model-scale device, and Figure E.5 shows a picture of the Tupperwave physical model in the water.

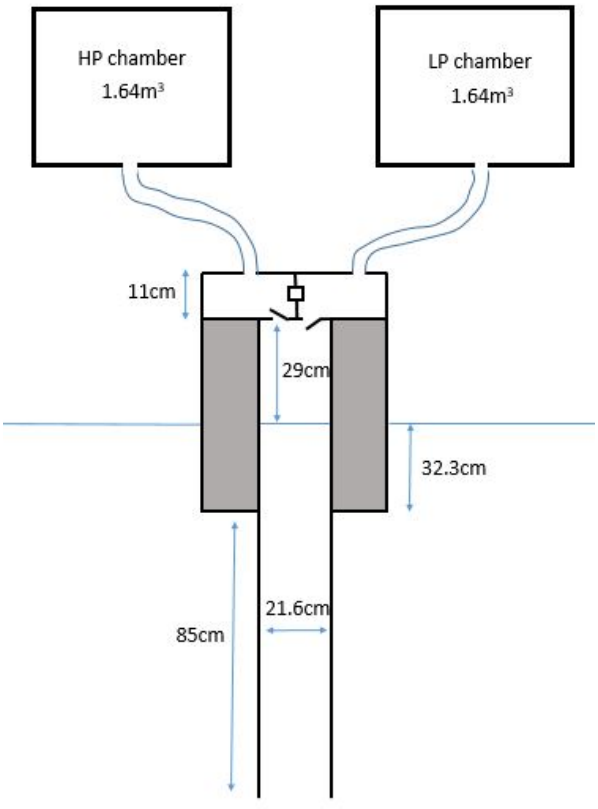


Figure D.11: Schematic of the model-scale conventional OWC and Tupperwave devices.

Ideally, the same scaling method applied to the HP and LP chambers should be used for the OWC chamber, adding a third flexible pipe connecting the OWC chamber to another reservoir outside the device. However, air

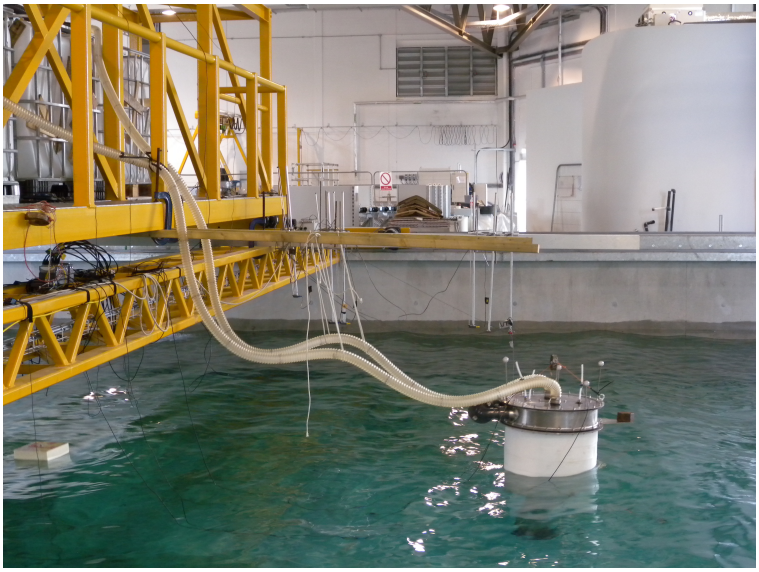

Figure D.12: Physical model of the Tupperwave device.

compressibility in the OWC chamber is not essential for the device working principle, and the OWC chamber was therefore scaled down using Froude scaling for simplicity.

The most appropriate valves found on the market were the Capricorn MiniHab HypAirBalance; see Figure D.13a,b. They are passive normally

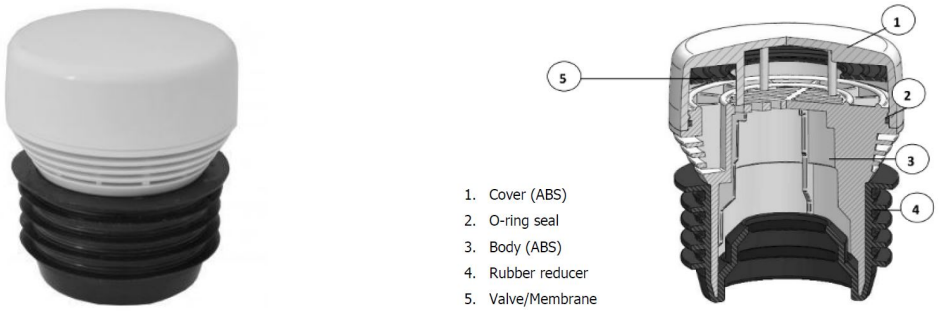


(a) Full device

(b) Section

Figure D.13: MiniHab HypAirBalance from Capricorn used in the Tupperwave small-scale model.

closed air admittance valves from the plumbing market. A rubber membrane contained in the valve obstructs its opening by gravity. When sufficient pressure is applied, the rubber membrane is lifted up, and the valve opens. Their light weight allowed their use in the small-scale Tupperwave physical model.

A large number of tests were undertaken. For the regular waves, two wave heights (2 m and 4 m) were tested with periods ranging from 5–14 s. Note that these are the full-scale equivalent dimensions. Eight irregular sea

states of various significant wave heights and peak periods were also tested. In each wave condition, the device was tested with three different orifices numbered from 1–3 with increasing damping (decreasing orifice diameter).

### D.4.2 Experimental Results

It was observed experimentally that the relationship between pressure drop and flow rate across the valves was quadratic. This relationship is characteristic for turbulent flows. The Reynolds number across the valves was assessed, and was in the order of $10^4$, which demonstrates that the regime was turbulent [134]. This is equivalent to $k_{v1} = 0$ in Equation (D.8), and the relationship between pressure drop and flow rate across the valves becomes:

$$\Delta P_v = p_o + k_{v2} q_v^2 \qquad for \quad \Delta P_v > 70Pa \tag{D.12}$$

The valves opening pressure $p_o$ was found close to 70 Pa (equivalent to 1686 Pa at full scale).

The damping coefficient $k_{v2}$ of the passive valves was assessed in every test. It was found that its value changed significantly depending on the wave conditions and device excitation. This phenomenon is particularly obvious in regular waves. Figure D.14 displays the damping coefficient $k_{v2}$ of the HP valves in regular waves for the two wave heights tested. It was observed that when the device was close to resonance (for 6.5 s $< T <$ 8.5 s, near its resonance), large pressure drops across the valves were created. The valves were thus open fully, and their damping coefficient was small. On the contrary, when the device was poorly excited by the waves (for $T <$ 6.5 s and $T >$ 8.5 s), the valves did not open fully and created large damping (i.e., large losses). The variation of damping coefficient led to a variation in the valves' efficiency to rectify the flow through the turbine. This is a major difference compared to the ideal valves used in the CFD model that are open instantaneously with a given opening area and therefore with a given damping and given efficiency. The dependence of the valves' efficiency on the damping is addressed in the next section.

The tank testing campaign of the Tupperwave device proved that the Tupperwave principle was viable and that it actually built a steady pressure differential between the HP and LP chambers, hence creating a very smooth unidirectional flow across the turbine. To illustrate this feature, Figure D.15 displays the time series of the pressures in the chambers and flows across the valves and turbine for a 2 m-high regular wave of a 9-s period (full-scale equivalent). More details on the physical tank testing of the Tupperwave model can be found in [122].

The results of the physical tank testing were used to validate the first numerical model of the device. Very good agreement was obtained between numerical and physical models. Details on the numerical model validation

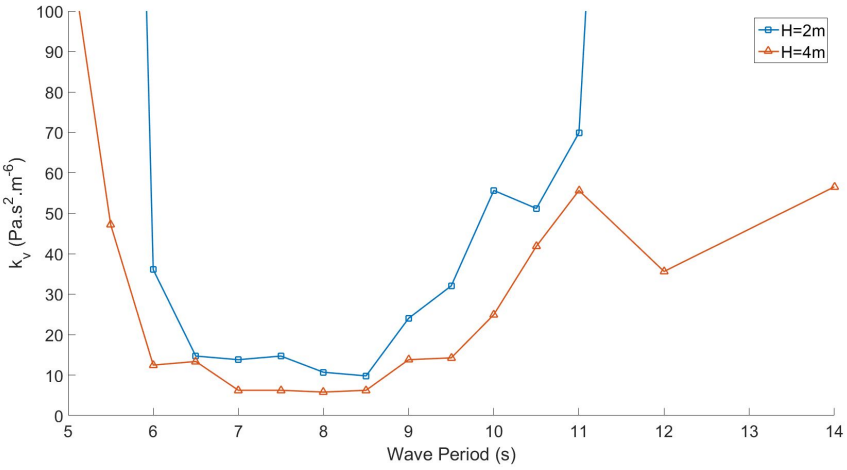


Figure D.14: HP valve damping coefficient in regular waves (full-scale equivalent).

using the tank testing results can be found in [135]. Moreover, the tank testing provided physical observations on the real behaviour of the device and especially of the valves.

## D.5 Device Conversion Efficiency

In this section, the ability of the device to convert the absorbed wave power into available power to the turbine is analysed in regular waves using both physical and numerical approaches.

This analysis was initially driven by physical observations made during the tank testing. Figure D.16 compares the average absorbed power on regular waves to the sum of the dissipated pneumatic power in the valves and orifice, for the case of Orifice 2, and shows that the absorbed power was entirely dissipated in the valves and the turbine.

The average valves' efficiency can therefore be rewritten as:

$$\eta_v = \frac{\overline{P_t}}{\overline{P_{abs}}} = \frac{\overline{P_t}}{\overline{P_t} + \overline{P_{v_{hp}}} + \overline{P_{v_{lp}}}} = \frac{1}{1 + \dfrac{\overline{P_{v_{hp}}} + \overline{P_{v_{lp}}}}{\overline{P_t}}} \tag{D.13}$$

At model scale, the variation of air density in the device chamber was small compared to the atmospheric density, and therefore, it was assumed that $\rho = \rho_{atm}$ in all chambers. The average pneumatic power across the turbine can be calculated using the damping coefficient and the average mass flow across the turbine:

$$\overline{P}_t = \overline{q_t \Delta p_t} = \overline{k_t q_t^3} = k_t \overline{q_t^3} \tag{D.14}$$

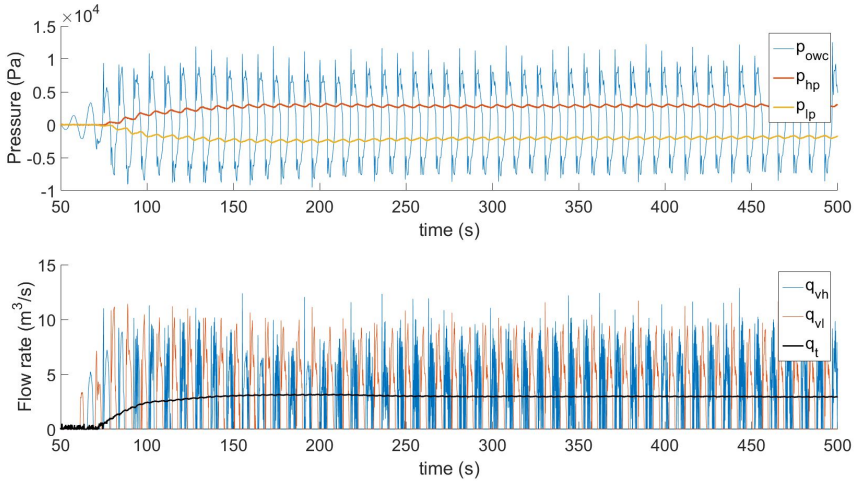


Figure D.15: Time series of pressures in the chambers and flows across the valves and turbine for a 2 m-high regular wave of a nine-second period (full-scale equivalent) obtained in tank testing.

Since the mass flow across the turbine was almost constant, it is a reasonable approximation to write:

$$\overline{q_t^3} \simeq \overline{q_t}^3 \tag{D.15}$$

The total power dissipated in the turbine can be approximated by:

$$\bar{P}_t \simeq k_t \overline{q_t}^3 \tag{D.16}$$

Using Equation (D.12), the instantaneous power dissipated in the LP and HP valves can be expressed as:

$$\begin{aligned} P_{v_{total}} &= P_{v_{hp}} + P_{v_{lp}} \\ &= k_{v_{hp}} q_{v_{hp}}^3 + k_{v_{lp}} q_{v_{lp}}^3 + p_o(q_{v_{hp}} + q_{v_{lp}}) \end{aligned} \tag{D.17}$$

As the HP and LP valves were identical, their damping was the same, $k_v = k_{v_{hp}} = k_{v_{lp}}$. Furthermore, since the HP and LP valves were never open at the same time, we have:

$$q_{v_{hp}}^3 + q_{v_{lp}}^3 = (q_{v_{hp}} + q_{v_{hp}})^3 \tag{D.18}$$

Hence, Equation (D.17) becomes:

$$P_{v_{total}} = k_v(q_{v_{hp}} + q_{v_{hp}})^3 + p_o(q_{v_{hp}} + q_{v_{lp}}) \tag{D.19}$$

Moreover, since the circuit was closed, the valves were crossed by the same amount of air as the turbine in the overall simulation. The air was constantly flowing across the turbine, while the air was only flowing alternatively across each valve less than half of the time. The average value of

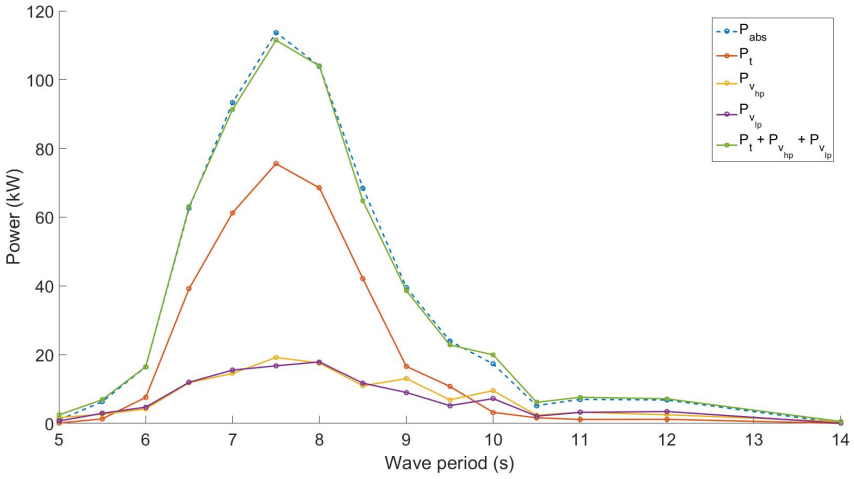


Figure D.16: Average absorbed power from the waves and dissipated powers across valves and orifice (full-scale equivalent).

the sum of the mass flow rate across the valves $q_{v_{hp}} + q_{v_{hp}}$ can be roughly approximated as a constant flow of value $2q_t$. Figure D.15 illustrates this fact, and it can be written as:

$$q_{v_{hp}} + q_{v_{lp}} \simeq 2q_t \tag{D.20}$$

The average pneumatic power dissipated across the valves was obtained by averaging Equation (D.19) and using Equations (D.15) and (D.20):

$$\overline{P_{v_{tot}}} \simeq 2^3 k_v \overline{q_t}^3 + 2p_o\overline{q_t} \tag{D.21}$$

Using Equations (D.16) and (D.21) in Equation (D.13) results in:

$$\eta_v \simeq \frac{1}{1 + 2^3\dfrac{k_v}{k_t} + 2\dfrac{p_o}{k_t\overline{q_t}^2}} \tag{D.22}$$

Finally, the average pressure head across the turbine can be written as:

$$\overline{\Delta p_t} = \overline{k_t q_t^2} = k_t\overline{q_t}^2 \tag{D.23}$$

Eventually, the average valve efficiency can be approximated from the turbine and valve damping characteristics using the equation:

$$\eta_v \simeq \frac{1}{1 + 2^3\dfrac{k_v}{k_t} + 2\dfrac{p_o}{\overline{\Delta p_t}}} \tag{D.24}$$

The valves' efficiency was not only dependent on the valves' damping coefficient (i.e., opening area), but it was a function of the ratios $\dfrac{k_v}{k_t}$ and $\dfrac{p_o}{\overline{\Delta p_t}}$.

Results obtained from Equation (D.24) were tested against the actual efficiency of the valve obtained in tank testing. Figure D.17 compares the measured efficiency to the estimation for H = 2 m and H = 4 m and for the three tested orifices. Equation (D.24) yields a good approximation of the measured valves' efficiency. Despite the approximations used in its derivation, the formula shows that, in order to maximise the Tupperwave valves efficiency, the opening pressure of the valves needs to be small compared to the average pressure drop across the valves, and the damping coefficient of the valves needs to be small compared to the damping coefficient of the turbine.

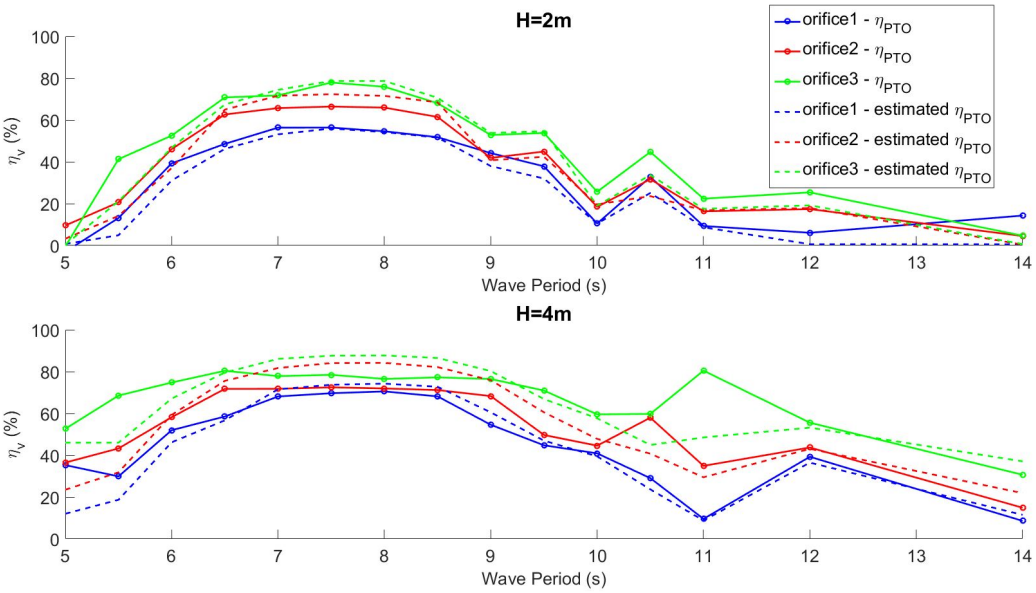


Figure D.17: Valve efficiency obtained in regular waves compared to the efficiency estimated via Formula (D.24).

Figure D.17 also shows that the maximum valve efficiency reached during the tank testing was between 50% and 80%, depending on the orifice. The maximum efficiencies were reached for wave periods 6.5 s $< T <$ 8.5 s, where the valves' damping coefficient $k_v$ was the smallest (see Figure D.14). In accordance with Formula (D.24), the best efficiencies were reached with Orifice 3, which had the largest damping $k_t$. This was due to the fact that $\frac{k_v}{k_t}$ became smaller, thus increasing $\eta_v$.

Moreover, orifices with larger damping created greater average pressure difference between the HP and LP chamber $\Delta p_t$, decreasing the ratio $\frac{p_o}{\Delta p_t}$ and, consequently, increasing $\eta_v$. Physically, one can explain this phenomenon with the following reasoning: higher $k_t$ represents more difficulty for the passage of air through the turbine, thus increasing the pressure drop between the HP and LP chambers and reducing the flow across the turbine; since the circuit of air was closed, the flow across the valves was also reduced, which

implies a lower velocity of the air through the valves; in turn, lower velocity represents less friction losses, and ultimately led to higher efficiency of the valves for a smaller orifice.

Therefore, for a given valve damping coefficient, the efficiency of the valves to not dissipate the absorbed power from the waves became higher for larger values of the turbine damping coefficient, $k_t$. However, similarly to a conventional OWC device, the absorbed wave power was also largely dependent on $k_t$.

Figure D.18 displays the results of a parametric study carried out with Numerical Model 1 on the full-scale device to find the optimal $k_t$ coefficient maximising the power production of the device in 2 m-high regular waves of eight-second periods. The damping coefficient of the valves was set to $k_v$ = 5 Pa s$^2$ m$^{-6}$ and the opening pressure $p_o$ = 150 Pa. On the one hand, and similarly to conventional OWC devices, the power absorbed by the device (dashed line) was largely dependent on $k_t$ and reached a maximum for a certain value of $k_t$. On the other hand, and as discussed in the previous paragraph, the valves' efficiency to convert the absorbed power into useful pneumatic power (dotted line) became higher for larger values of $k_t$. In the end, finding the optimal damping coefficient maximising the power made available to the turbine (solid line) was a trade-off between maximising the wave power absorption by the device and maximising the valves' efficiency.

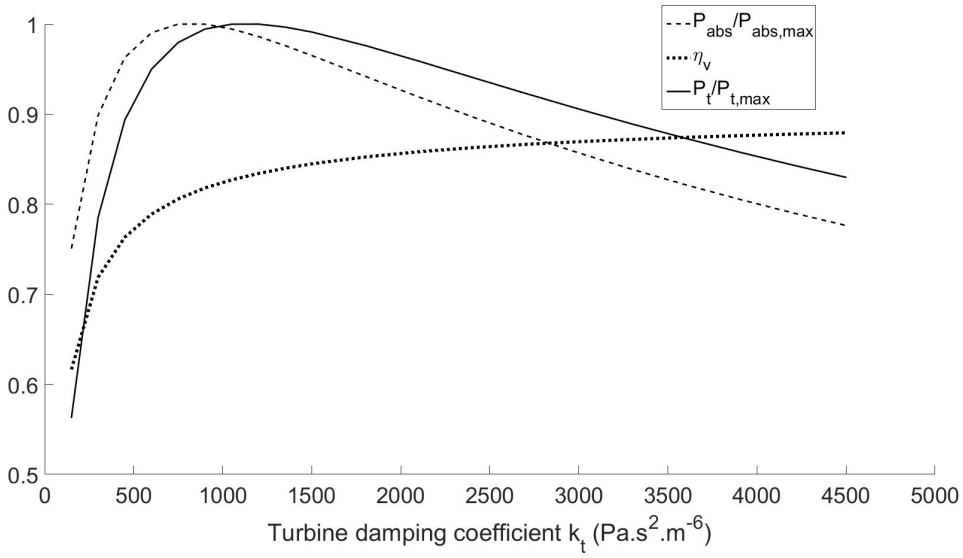


Figure D.18: Parametric study of the turbine damping coefficient to maximise pneumatic power made available to the turbine.

## D.6 Conclusions

In this paper, the modelling of the Tupperwave device was approached with three different methods, which all enabled various observations of the device behaviour.

The first approach, using potential flow theory and hydrodynamic and thermodynamic ordinary differential equations, was revealed to be the most efficient and quickest method to model the Tupperwave device in various conditions and was the most appropriate to carry out parametric optimisation. The second approach, using three-dimensional CFD with the software Ansys CFX, was the longest to implement, and the results within the duration of the Tupperwave project were limited due to the slow computational time. The third approach, using physical tank testing at $1/24^{\text{th}}$ scale, provided real-life observations of the device and especially of the valves.

Ideal active valves were tested in the CFD model with zero opening pressure and a large opening area. With those valves, 95% of the absorbed wave power was converted into pneumatic power available to the turbine. Real passive off-the-shelf valves from the plumbing market were tested in the physical model. Being passive, the valves only opened well when the device was close to resonance, leading to a varying efficiency depending on the wave conditions, but also on the tested orifice-turbine. Their maximum efficiency ranged from 50%–80%. The CFD model and in particular the physical models both provided a validation of the first model.

From observations made numerically and physically, it was shown that the valves' efficiency was a function of the ratio between the valve and turbine dampings $\frac{k_v}{k_t}$. While larger turbine damping increased the valve efficiency, lower values of $k_t$ allowed larger wave power absorption by the device. Finding the optimal $k_t$ value is therefore a trade-off between maximising wave power absorption and maximising the valve efficiency.

## Acknowledgement

The authors would like to acknowledge funding received through OCEANERA-NET European Network (OCN/00028).

# Appendix E

# Paper E

# Modelling air compressibility in OWC devices with deformable air chambers

*Published in*

Journal of Marine Science and Engineering, MDPI

*Authors*

Pierre Benreguig[1], Jimmy Murphy[1]

[1]*MaREI Centre (ERI), University College Cork, Haulbowline Road, Ringaskiddy, Ireland*

# Abstract

Air compressibility effects play an important role in large scale Oscillating Water Column (OWC) wave energy converters. Air compressibility is however not scalable with Froude similarity law. An existing scaling method allows to correctly reproduce the air compressibility at model scale but its implementation is effortful and becomes cumbersome for floating devices and tests at relatively large scales (1/15th to 1/2th). Air compressibility is therefore commonly ignored in model scale tank testing of conventional OWC devices, which can lead to substantially unrealistic results on the device performance relatively to the full scale device. In the case of the Tupperwave device, which is a closed circuit OWC device, correctly modelling air compressibility during tank testing is however essential because the device relies on air compressibility to work. In this paper, a new method for modelling air compressibility at model scale is presented. The method uses variable volume chambers which mimic air compressibility by storing energy under the form of strain energy. This method, reduces the difficulties of implementation and enhances the application of the existing method to larger scales. Various applications to this method are identified and described, including the presentation of a novel OWC concept.


## E.1 Introduction

Model scale physical testing is essential in the development of wave energy converters and especially for the advancement through the Technology Readiness Levels (TRLs) [15]. Oscillating water column (OWC) devices are a major class of wave energy converters that have been object of extensive research and development effort over many years, including the deployment of prototypes at sea [9]. The OWC converter consists of a hollow (fixed or floating) structure, open to the sea below the water surface. Wave action alternately compresses and decompresses the air trapped above the inner water free-surface in the OWC chamber, converting wave energy into pneumatic energy. Different types of OWC devices can be distinguished on the basis of their working principle for harnessing the pneumatic energy. The most commonly studied type of OWC device, which will be referred to as conventional type in the rest of the paper, is equipped with a self-rectifying turbine located on top of the OWC chamber and connecting it with the atmosphere. The compression and decompression of the air in the OWC chamber forces air in and out of the chamber through the turbine which is coupled to a generator. Self-rectifying turbines are able to harness both directions of air flow, but there efficiency is lower than a unidirectional turbine. Conventional OWC devices have been installed on the shoreline, standing near shore on the sea floor, incorporated into breakwaters or deployed offshore

as floating structures. Other types of OWC devices use non-return valves to rectify the air flow across a unidirectional turbine. Various flow-rectifying OWC devices have been studied, such as the Masuda's navigation buoy [9], the Kaimei [104], the Leancon [53], the vented OWC from Wave Swell Energy [49] and the Tupperwave device [95], all using different air flow rectification methods for rectifying the air flow.

In a full scale conventional OWC device, the compressibility of the air in the OWC chamber acts as a brief storage of energy and introduces a phase shift between the air flow rate displaced by the water column and the flow rate across the turbine. This effect is called spring-like effect and plays an important role in large scale OWC devices [67] and especially on the dynamic motion of the water column relatively to the device structure. For accurate modelling of a OWC device, either numerically or physically, the spring-like effect of air needs to be taken into account.

Numerically, the modelling of air compressibility is easily achievable by using the linearised isentropic relationship between air density and pressure ([68, 130]). Physically, modelling air compressibility in model scale OWC devices can be demanding. Hydrodynamic similarity at model scale is commonly achieved using Froude scaling which respects geometrical similarity of the underwater part of the device by multiplying all geometrical dimensions by the Froude scaling factor $\epsilon < 1$. Air compressibility in an air chamber is however not scalable with Froude similarity law. It was recognized in [74] that, to scale adequately air compressibility in an air chamber, the ratio between the air chamber volume of the model and full-scale device has to be equal to $\epsilon^2$ and not to $\epsilon^3$ as the Froude similarity would suggest. The required volume for the chamber is therefore a lot bigger than the volume suggested by Froude similarity. The solution to implement this method, without changing the geometry of the device on the water, is to connect the device chamber to an external reservoir of the required volume with a pipe, as was done in [74, 136] on a small bottom fixed conventional OWC devices. Figure E.1 displays a picture of the testing setup for a fixed-structure conventional OWC device.

Implementing this method on a floating OWC devices is particularly difficult because the connection of a stationary air volume with the floating OWC may introduced elastic, damping and inertia forces associated with the motion and deformation of the flexible pipes. The difficulty of implementing this method increases with the scale of the tested device because the volume of the additional reservoirs increase with the square of the scaling factor. And the method quickly become unpractical.

Moreover, this method introduces another dissimilarity between the full scale device and the physical model: The relative volume change of the OWC chamber due to the elevation of the internal water column becomes much

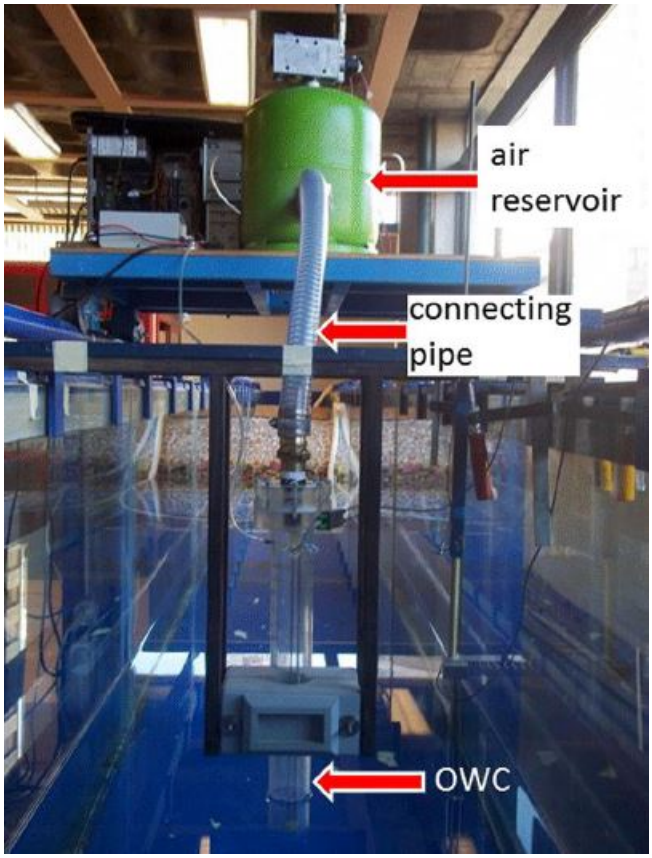


Figure E.1: Model testing of a cylindrical fixed-structure OWC in a wave flume using an external reservoir connected to the OWC chamber to reproduce air compressibility effects (Instituto Superior Tcnico, Lisbon, 2013) [74]

smaller in the physical model than in the full scale device, thus omitting non-linearities due to significant volume changes in the full scale device [137].

Since the spring-like effect of the air in conventional OWC chambers is not fundamental to the working principle, it is often neglected in tank testing. Certain types of OWC devices do however rely on air compressibility to work and the correct modelling of air compressibility at model scale is therefore important. It is the case for the Tupperwave device which was physically tested at 1/24th scale ([122, 135]). The Tupperwave device is a floating OWC device and more than three cubic meters of additional air reservoirs were connected to the floating device, making the testing particularly challenging.

The practical implementation difficulty of modelling air compressibility at model scale using additional fixed volume air reservoirs, motivates the search for other approaches. In the present paper, a method for modelling air compressibility in OWC devices using deformable volume chambers is presented. The chamber deformation mimics the air compression or decompression by storing energy under the form of strain energy. A similar idea was already mentioned in [138]. Section E.2 of this paper mathematically

demonstrates the possibility of modelling air compressibility happening in a large air chamber using a smaller chamber with slightly deformable walls. Section E.3 describes the effect of deformable air chambers observed during the model scale testing of the Tupperwave device. Section E.4 finally identifies practical applications to the new method presented.

## E.2 Deformable volume air chamber

Considering the following open thermodynamic system: an air chamber containing a mass $m$ of air at the density $\rho = \rho_{atm} + \Delta\rho$ and at pressure $p_{atm} + p_1$. The air mass flow rates $w_{in}$ and $w_{out}$ flow respectively in and out of the chamber. They are functions of the air excess pressure $p_1$. It is assumed that the transformations are slow enough for the thermodynamic state of air in the chamber to be uniform. The volume $V_1$ of the chamber is elastically deformable and the chamber walls have no inertia. Hence, $V_1$ evolves linearly with the excess pressure such that:

$$V_1(p) = V_{1,0} + C.p_1 \tag{E.1}$$

where $V_{1,0}$ is the initial volume of the chamber when the inner pressure equals atmospheric pressure and C is the chamber stiffness in $m^3.Pa^{-1}$. We note that the excess pressure $p_1$ can either be positive or negative.

It is assumed that in the pressure conditions considered, the volume variation of the chamber remains small compared to the initial volume:

$$C.p_1 << V_{1,0} \tag{E.2}$$

and the air density variation remain small compared to atmospheric density:

$$\Delta\rho << \rho_{atm} \tag{E.3}$$

Neglecting second order terms, the mass conservation equation in the system is:

$$\dot{m} = \rho_{atm}\dot{V}_1 + \dot{\rho}V_{1,0} \tag{E.4}$$

Equation E.4 informs that the variation of mass in the chamber is the sum of two phenomena: air density variations (compressibility) and chamber volume variations.
The mass balance equation gives:

$$\dot{m} = w_{in} - w_{out} \tag{E.5}$$

If the system is considered adiabatic and the transformations slow enough to be reversible, the transformations become isentropic and consequently we may write:

$$\rho = \rho_{atm}\left(\frac{p_{atm} + p_1}{p_{atm}}\right)^{\frac{1}{\gamma}} \tag{E.6}$$

where $\gamma$ is the air heat capacity ratio. Moreover, in the case where the excess pressure remains small compared to the atmospheric pressure, it is possible to linearise the isentropic relationship between density and pressure. Once linearised, equation G.11 leads to:

$$\rho = \rho_{atm}\left(1 + \frac{p_1}{\gamma p_{atm}}\right) \tag{E.7}$$

and to:

$$\dot{\rho} = \frac{\rho_{atm}}{\gamma p_{atm}}\dot{p}_1 \tag{E.8}$$

Using equations E.4, G.9 and E.8, the pressure variation in the deformable chamber can be written as:

$$\dot{p}_1 = \frac{\gamma p_{atm}}{\rho_{atm} V_{1,0}}(w_{in} - w_{out} - \rho \dot{V}_1) \tag{E.9}$$

Finally, using the derivative of equation E.1 into equation G.16, we can write:

$$\dot{p}_1 = \frac{\gamma p_{atm}}{\rho_{atm}(V_{1,0} + \gamma p_{atm} C)}(w_{in} - w_{out}) \tag{E.10}$$

We now consider a larger air chamber of fixed volume $V_2$, subjected to the same incoming and outcoming mass flow rates $w_{in}$ and $w_{out}$. $p_2$ is the air pressure in this chamber. $V_2$ being a fixed volume, the mass variation of air in the chamber is only made possible by the compressibility of the air:

$$\dot{m} = \dot{\rho} V_2 \tag{E.11}$$

In a like manner as equation G.16, the pressure variation in the fixed volume chamber is:

$$\dot{p}_2 = \frac{\gamma p_{atm}}{\rho_{atm} V_2}(w_{in} - w_{out}) \tag{E.12}$$

By analogy between equations E.10 and E.12, it is clear that the pressures $p_1$ in the elastically deformable chamber, and $p_2$ in the fixed volume chamber, will evolve the same way if:

$$V_2 = V_{1,0} + \gamma p_{atm} C \tag{E.13}$$

It is thus possible to mimic air compressibility effects happening in a large fixed volume chamber of volume $V_2$ while using a smaller chamber of volume $V_{1,0} = V_2 - \gamma p_{atm} C$ which is slightly elastically deformable with a stiffness $C$. It is however important to keep in mind that the conditions given by equation E.2 and E.3 need to be respected. The possibility of using variable volume air chambers to model air compressibility effects in larger fixed volume chambers finds an application in model scale testing of OWC devices. In the next section, the effect of air chamber volume variation is observed on a practical case.

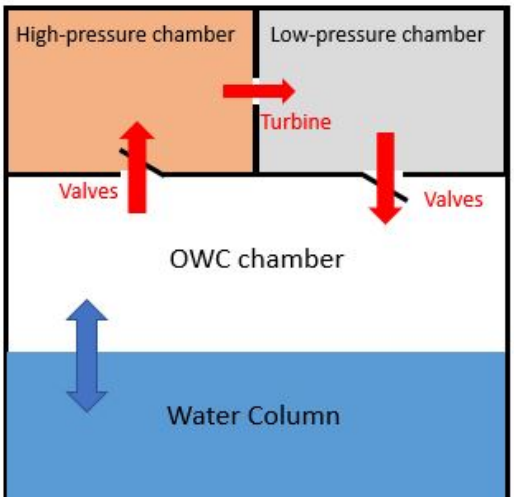


Figure E.2: Schematic diagram of the Tupperwave device concept

## E.3 Tank testing of the Tupperwave device

The Tupperwave concept is a flow-rectifying OWC working in closed-circuit which uses non-return valves and two large fixed volume chambers acting as accumulators. Figure E.2 displays a schematic of the Tupperwave working principle: when the water column rises, air is compressed in the high-pressure (HP) chamber and when the water falls, the air is sucked from the LP (low-pressure) chamber. The continuous oscillatory motion of the water column creates a pressure differential between the HP and LP chambers which creates a smooth unidirectional flow across the unidirectional turbine located in between. The Tupperwave working principle was studied in [95, 135, 133, 130] when applied to a floating spar buoy. Figure G.1 displays the geometry of the full scale Tupperwave device. The volume of the HP and LP chambers have a constant value of $950m^3$ each, providing also buoyancy volume. The Tupperwave working principle is entirely relying on air compressibility in the HP and LP chambers. For this reason, it is essential to correctly reproduce air compressibility in the two chambers at model scale. The device was physically modelled and tested in [122] with a Froude scaling ratio of $\epsilon = 0.0415$. To reproduce air compressibility, the volumes of the chambers on the model were scaled by $\epsilon^2$ and were $1.64m^3$ each. Unlike for the full scale, it is impossible to fit both chambers on the device as their volume largely exceed the overall volume of the device. The alternative at small scale is to locate the main volume of the HP and LP chambers outside of the device and connect them to two smaller chambers on the device with flexible pipes. Large reservoirs were used for the HP and LP chambers and located on the pedestrian bridge above the tank. Figure E.4 displays the schematic of the device with the external reservoirs. The flexible pipes were chosen as lightweight and flexible as possible to reduce their influence on the floating

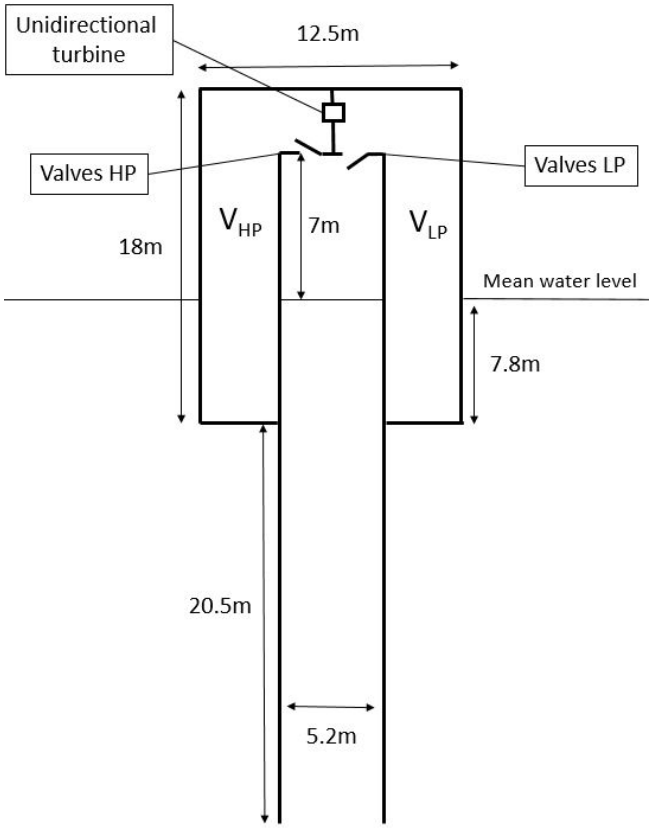


Figure E.3: 2D schematic of the full scale Tupperwave device

device motion. Part of the pipes weight was supported by bungee ropes, see figure E.5.

It is important to note that the modelling of the air compressibility effects in the OWC chamber was omitted during the experiment since it is not essential in the device working principle. In the case of conventional OWC devices, it is well-established that failure to model air compressibility effects results in an over-estimation of the device performance ([67, 139, 140]). In the case of the Tupperwave device, similar consequences are expected. But modelling the air compressibility in the OWC chamber of the Tupperwave device would have increased the difficulty of the testing, as it would have required one more additional chamber on the bridge and one more flexible pipe linking the device to the chamber. Such level of complexity to model the spring-like effect in the OWC chamber were not required at this scale of development.

A numerical model of the device was developed and validated using the physical model results [135]. The numerical model does not take into account the presence of the flexible pipes (mass, inertia, elasticity,...) but provided very good prediction of the physical model hydrodynamic behaviour. This showed that such effects due to the presence of the pipes were negligible.

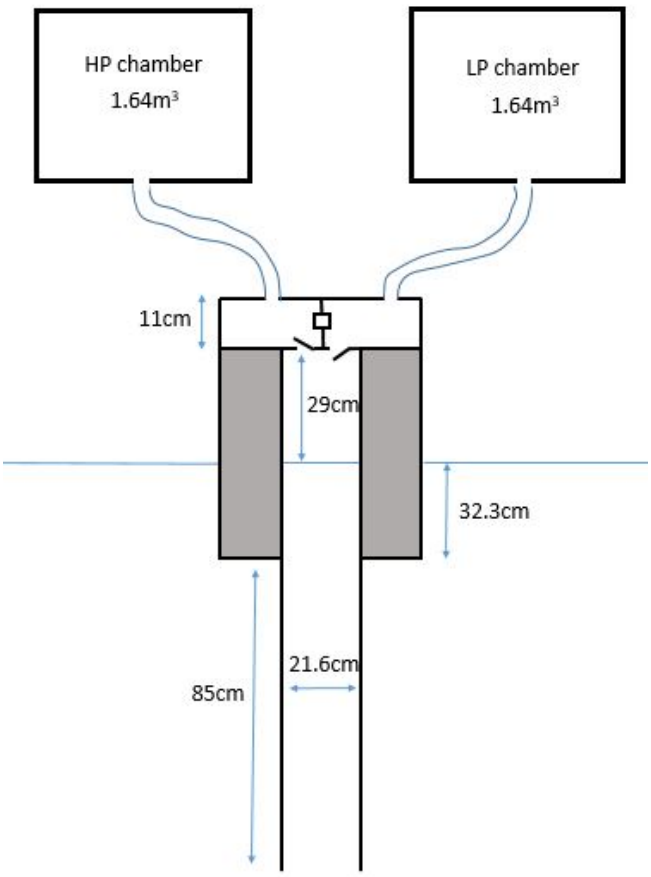


Figure E.4: Schematic of the model scale conventional OWC and Tupperwave devices

The results of the initial version of the numerical model, assuming fixed volumes for the HP and LP chambers, did however not predict the pressure evolution in the chambers correctly. The reason for this was that the reservoirs used for the HP and LP chambers of the Tupperwave physical model did not have perfectly rigid walls. During the tests, it was observed that the reservoir walls moved by a few millimetres proportionally to the pressure building inside the chambers. The HP chamber was observed to inflate with the build-up of a positive excess pressure inside and the LP chamber was observed to deflate due to the negative excess pressure inside. This required a correction in the numerical model to take into account the slight volumetric change of the HP and LP chambers. An elastic deformation of the chambers, function of the excess pressure, was added to the numerical model such that:

$$\begin{cases} V_{hp,1} = V_0 + C.p_{hp} \\ V_{lp,1} = V_0 + C.p_{lp} \end{cases} \tag{E.14}$$

where $V_0 = 1.64m^3$ is the initial volume of the chambers and $C = 8.34.10^{-5}m^3.Pa^{-1}$ is the chambers stiffness assessed empirically.

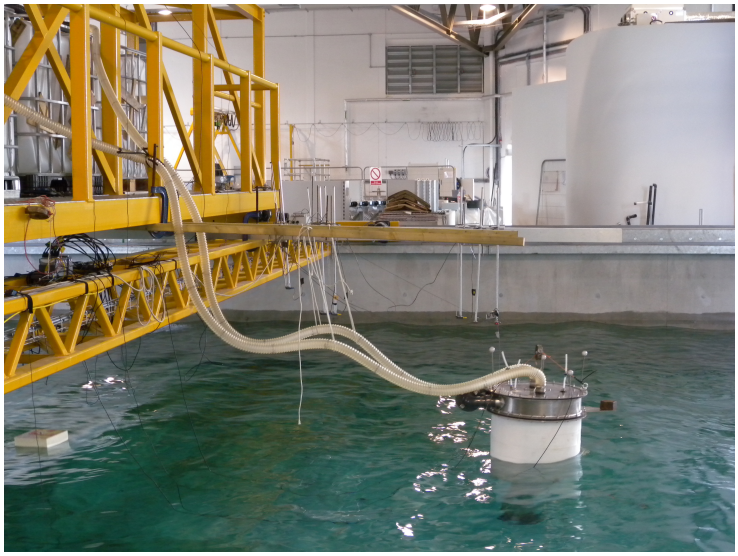

Figure E.5: Physical model of the Tupperwave device

Figure E.6 compares the time series of the pressure drop $\Delta P_t = p_{hp} - p_{lp}$ across orifice of the Tupperwave device in the irregular sea state {Hs=3m; Tp=8.485s} obtained by the physical model, the initial numerical model, and the corrected model. Results are given at full scale equivalence to give the reader perspective. The pressures in the rigid-wall chambers from the initial numerical model vary quicker with the wave groups than in the chambers used in the physical tests. As a result of the chambers deformation, an extra smoothing effect of the pressure variations between the wave groups was observed in irregular waves. Accounting for the small volume variations of the HP and LP chambers in the numerical model very clearly enhance the fidelity with the physical model.

From an energy transfer perspective, the pneumatic energy stored in the HP and LP chamber is not only stored in the form of pressure but also in the form of strain energy. This explains the lower pressure variations between wave groups. The strain energy stored by the elastic chamber deformation is recoverable. This is why the average value of the pressure drop across the orifice is not impacted.

According to equation E.13, the $1.64m^3$ HP and LP deformable chambers of the physical model were actually behaving as if they were fixed volume chambers of volume:

$$V_{hp,2} = V_{lp,2} = V_0 + \gamma p_{atm} C = 13.5\ m^3 \tag{E.15}$$

and therefore modelling full scale fixed volume HP and LP chambers of volume:

$$V_{hp}^{full} = V_{lp}^{full} = V_{hp,2}/\epsilon^2 = 7839\ m^3 \tag{E.16}$$

which is not what was intended in the first place, but explains the smoother

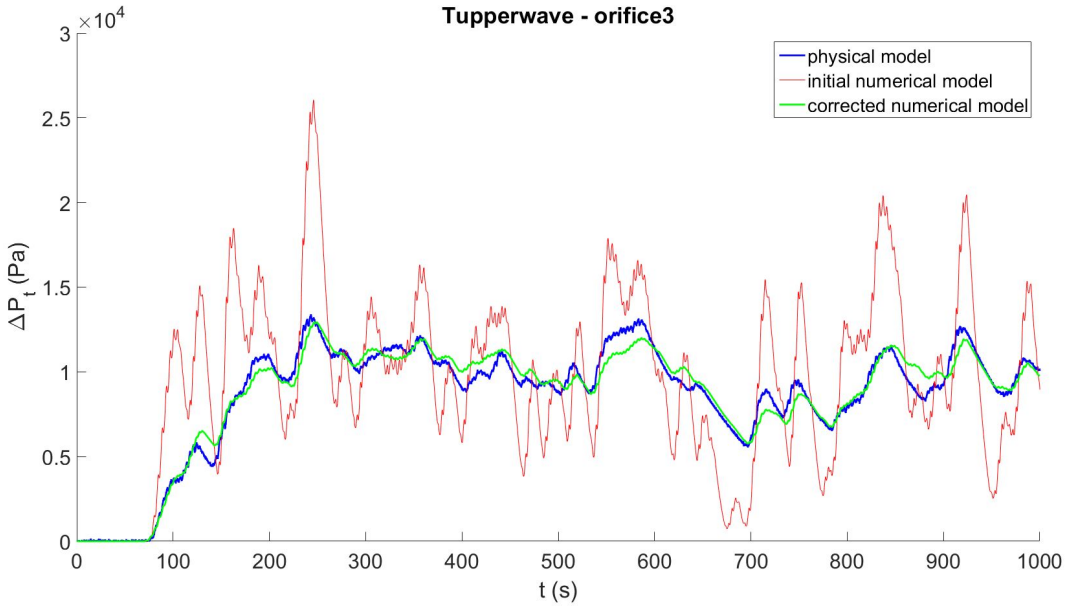


Figure E.6: Pressure drop time series (given at full scale equivalence) across orifice 3 of the Tupperwave device obtained by the physical model, the initial numerical model, and the corrected model in the scaled irregular sea state equivalent to {Hs=3m; Tp=8.5s}

evolution of the pressures in the chambers.

This experience constitute the first (involuntary) physical implementation of the method suggested in section E.1 to model large fixed volume air chambers using smaller deformable air chamber. The device modelled was therefore not exactly the intended one, but the cause was understood and the numerical model validated [135].

In the next section, applications for deformable air chambers are identified.

## E.4 Possible applications

Deformable air chambers in OWC devices can either be used for air compressibility modelling purposes in scaled physical modelling of OWC prototypes, or directly integrated in the working principle of full scale OWC device.

## E.4.1 Modelling of air compressibility

### E.4.1.1 Deformable chamber on the scaled device

The main advantage of using deformable volume chambers over fixed volume chambers for the modelling of air compressibility is their substantially smaller volume. If well designed and sufficiently small, the deformable chamber can directly be used on the device, respecting geometrical similarity with the full scale device and hence the relative volume change due to the motion of the water column. This is of particular interest for floating devices because it avoids the use of additional external chambers and flexible pipes. It is however obvious that the design and calibration of a custom deformable air chamber to the device geometry requires considerable efforts and is therefore only relevant in relatively large scale testing.

A practical example would be for the testing of the IST Spar buoy at 1/16th scale ($\epsilon = 1/16$) which was tested in [141]. The full scale OWC chamber has a volume $V^{full} = 515m^3$ which is equivalent to $V_{0,1} = 515\epsilon^3 = 0.126m^3$ when scaled geometrically. The full scale air chamber should however be modelled by a fixed volume $V_2 = 515\epsilon^2 = 2.0m^3$ in order to scale air compressibility correctly. This volume is too large to fit on the device and the use of an additional external air chamber located outside of the device and connected to the device by flexible pipe is unpractical at this scale. Hence, the physical modelling in [141] omitted the reproduction of air compressibility in the OWC chamber. Figure 7.a displays a schematic of the device as tested. The construction of the upper part of the cylindrical OWC chamber with a deformable walls, as presented in figure E.7, is a potential solution to model the spring-like effect of the air. Obviously, the deformable chamber can be designed in different ways, using either deformable material (polymer membrane, plastic or a flexible bellows) or a mechanical piston combined with a spring. The stiffness of the chamber is easily assessed using equation E.13:

$$C = \frac{V_2 - V_{0,1}}{\gamma p_{atm}} = 1.32.10^{-5}\ m^3.Pa^{-1} \tag{E.17}$$

Assuming that the maximum excess pressures achieved in the OWC chamber during the tests are $\pm 1250Pa$ (equivalent to $20000Pa$ at full scale), the diameter of deformable cylindrical part of the OWC chamber would change by $\pm 5cm$.


(a) Picture of the 1/16th scale IST Spar buoy tested in [141]

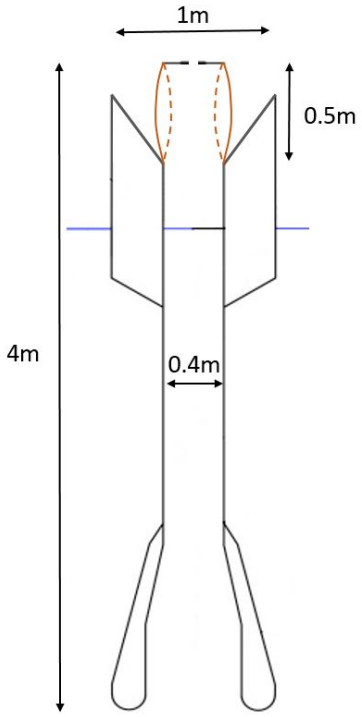


(b) OWC chamber with deformable walls: solid lines corresponds to exhalation and dash line to inhalation

Figure E.7: Suggestion for pratical application of deformable air chamber to model air compressibility on the IST Spar buoy

#### E.4.1.2 Tunable external deformable chamber

For smaller scale devices, the use of additional fixed volume external chambers connected with flexible pipes is achievable, as seen in section E.3. The volume of a given fixed volume chamber is tunable by filling the chamber with water, but the tuning remains limited and the volume of the additional chamber may become quite large for large models. The use of deformable chamber can considerably reduce the volume. Moreover, if the stiffness of the deformable chamber is tunable (with the help of mechanical springs for example), the same chamber can be used to model a wide scope of fixed volume chambers.

Figure E.8 displays the schematic of a 50*50*50cm chamber that deforms elastically as one of the walls moves along the x-axis. The stiffness of the chamber is adjustable with mechanical springs. We note that the inertia of the moving wall needs to be small enough to react quickly to a sudden change of pressure in the chamber. This deformable chamber can be used to model the HP and LP chambers of the Tupperwave device at various scales. The HP and LP chambers of the full scale Tupperwave device are $950m^3$ each and its is considered that the maximum excess pressure achieved in the chambers

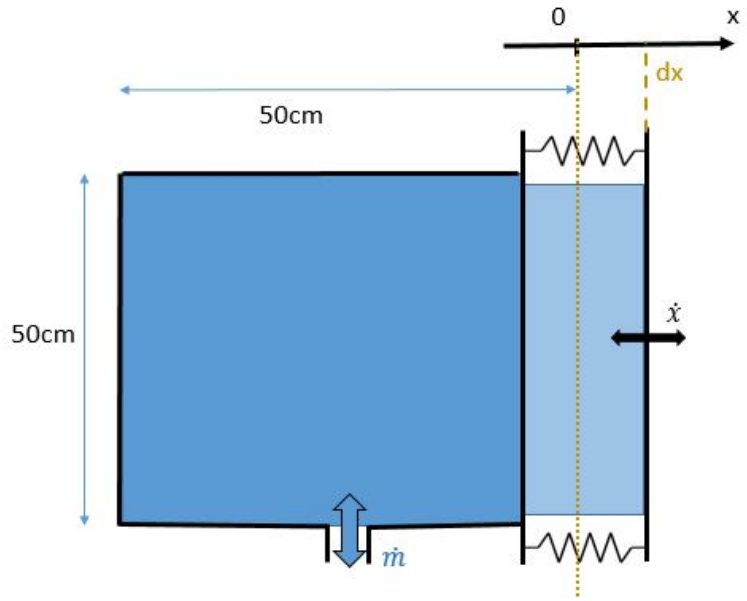


Figure E.8: Example of variable volume chamber with adjustable stiffness

is $\pm 10^4 Pa$. Table E.1 gives, for various scaling factors, the required chamber stiffness $C$ and maximum deformation $dx_{max}$ achieved under maximum pressure. The table also gives the necessary volume if fixed volume chambers were to be used.

| | Fixed volume chamber | Variable volume chamber (figure E.8) | | |
|---|---|---|---|---|
| Scale | Volume ($m^3$) | Initial volume ($m^3$) | Chamber stiffness ($m^3.Pa^{-1}$) | $dx_{max}$ (cm) |
| 1/50th | 0.38 | 0.125 | $2.63 \times 10^6$ | 0.2 |
| 1/25th | 1.52 | 0.125 | $1.03 \times 10^5$ | 1.6 |
| 1/15th | 4.22 | 0.125 | $2.78 \times 10^5$ | 7.4 |

Table E.1: Physical modelling requirements for the modelling of air compressibility effects in a $950m^3$ chamber of the Tupperwave full scale device

Hence, the same deformable chamber can be used in different experiments for various scales and is relevant in a centre likely to carry out many experiments.

Figure E.9: Full set of of the Irish national bagpipes: The Uilleann pipes [142]

### E.4.2 The Uilleann WEC

Variable volume air chambers find also an application in full scale OWC wave energy converter (WEC) giving birth to a new concept of OWC device, named by the authors as the Uilleann WEC. The working principle of the Uilleann WEC is similar to that of the Tupperwave device but uses variable volume air chambers for the HP and LP chambers instead of fixed volume chambers.

The Uilleann pipes are the characteristic national bagpipes of Ireland. The player uses a bellow strapped around the left elbow and the waist to inflate the main bag, held under the right elbow. In the same time, the player gently presses the main bag with his right elbow and slowly empties the main bag through the pipes providing a smooth and continuous air flow. A picture of a set of Uilleann pipes is displayed in figure E.9. The alternative pneumatic power generated by the below under the right elbow is accumulated in the main bag and smoothly released in the pipes. The Uilleann WEC uses the same principle, hence its name.

The working principle of the Uilleann WEC is displayed in figure E.10 where the HP and LP chambers are represented as piston-type variable volume chambers. The OWC chamber is equivalent to the bellows under the left elbow of the pipes player. The HP chamber is the exact equivalent of the Uilleann pipes' main bag: The upward motion of the water column inflates the HP chamber, which is constantly forced to empty through the turbine due a restoring force $F_1$, symbolised as a weight. Inversely, the downward motion of the water column sucks air from the LP chamber, which is constantly forced to fill up through the turbine due to a restoring force $F_2$ symbolised as a spring. The alternative pneumatic power created from the motion of the water column is therefore not only stored under the form of pressure (com-

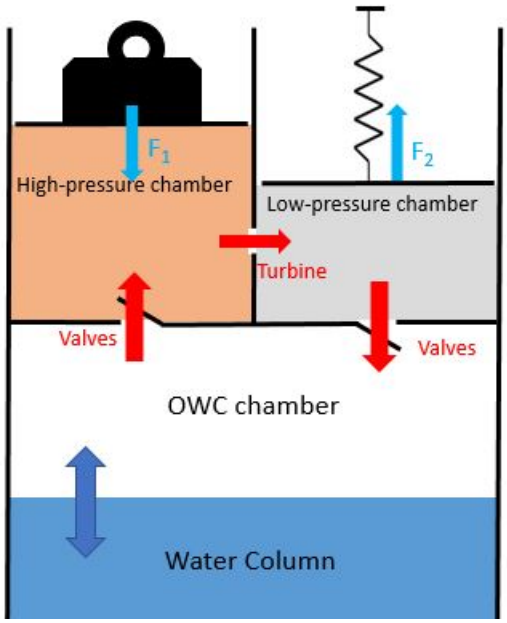


Figure E.10: Schematic diagram of the Uilleann WEC concept

pressibility) in the chambers, like it is the case in the Tupperwave device, but also under the form of strain, elastic or gravitational potential energy, depending on the deformation mechanism of the chambers.

As observed at model scale in section E.3, the additional energy storing mechanism due to the deformation of the chambers results in a better smoothing of the pneumatic power flowing across the turbine, which will eventually enhance the electrical power quality delivered by the device. The Uilleann concept can therefore be applied to the full scale spar buoy in figure G.1, and a slight deformation of the chambers would enhance considerably the power quality. But further assessment of the concept is required to determine its technical and economic feasability at full scale and the gain in electrical power quality compared to the fixed volume chambers of the Tupperwave device.

Very large HP and LP chamber volumes are necessary to allow power accumulation and create decent pneumatic power smoothing [95]. The Tupperwave concept is therefore particularly suited to large floating OWC structure which benefit from large buoyancy volume where the HP and LP chambers can be located, see figure G.1. The application of the Tupperwave concept to onshore OWC devices is however limited due to the cost of the large HP and LP chambers construction and of the onshore space required. The Tupperwave concept is also not suitable for self-powered sensor buoys due to their small size. Due to the much smaller size of the deformable chambers, the Uilleann concept opens the possibilities for the extension of closed-circuit systems to onshore OWCs and small self-powered sensor buoys, where the Tupperwave concept is not applicable. Another advantage of the closed-

circuit OWC system against the conventional OWC is the reduction of noise because no atmospheric discharge, which is very relevant for onshore OWC structures.

## E.5 Conclusion

In the present paper, a method to reproduce air compressibility effects occurring in a large fixed volume air chamber, using a smaller but slightly elastically deformable chamber is presented and mathematically analysed. A formula to assess the deformable chamber stiffness was found.

The use of deformable air chamber had its first application in the scaled physical modelling of OWC wave energy devices. It was implemented involuntary during the testing of the Tupperwave device at 1/24th scale. This provided a first experience of the method and revealed its potential.

The combination of the Tupperwave concept with deformable air chamber also resulted in a novel closed-circuit OWC device concept called the Uilleann WEC concept. The deformable accumulator chambers of the Uilleann WEC are much smaller than the fixed volume accumulator chambers of the Tupperwave device. For that reason, the Uillean WEC extends the application of the closed-cicuit OWC system to onshore OWC structures and self-powered buoys.

In further works, the suggested method for modelling air compressibility will be (voluntarily) experimented and validated for model scale testing. Specific applications of the Uilleann WEC concept will also be investigated and its power performance and smoothing capacities will be studied.

## Acknowledgment

The authors would like to acknowledge funding received through OCEANERA-NET European Network (OCN/00028).

# Appendix F

# Paper F

# Wave-to-Wire model development and validation for two OWC type wave energy converters

*Published in*

Energies, MDPI

*Authors*

Pierre Benreguig[1], James Kelly[1], Vikram Pakrashi[2], Jimmy Murphy[1]

[1]*MaREI Centre (ERI), University College Cork, Haulbowline Road, Ringaskiddy, Ireland*
[2]*Department of Civil, Structural and Environmental Engineering, Trinity College, Dublin, Ireland*

# Abstract

The Tupperwave device is a closed-circuit oscillating water column (OWC) wave energy converter that uses non-return valves and two large fixed-volume accumulator chambers to create a smooth unidirectional air flow, harnessed by a unidirectional turbine. In this paper, the relevance of the Tupperwave concept against the conventional OWC concept, that uses a self-rectifying turbine, is investigated. For this purpose, wave-to-wire numerical models of the Tupperwave device and a corresponding conventional OWC device are developed and validated against experimental tests. Both devices have the same floating spar buoy structure and a similar turbine technology. The models include wave-structure hydrodynamic interaction, air turbines and generators, along with their control laws in order to encompass all power conversion stages from wave to electrical power. Hardware-in-the-loop is used to physically emulate the last power conversion stage from mechanic to electrical power and hence validate the control law and the generator numerical model. The dimensioning methodology for turbines and generators for power optimisation is explained. Eventually, the validated wave-to-wire numerical models of the conventional OWC and the Tupperwave device are used to assess and compare the performances of these two OWC type wave energy device concepts in the same wave climate. The benefits of pneumatic power smoothing by the Tupperwave device are discussed and the required efficiency of the non-return valves is investigated.


## F.1 Introduction

Harnessing wave energy to produce electrical energy in an economically sustainable way requires the development of efficient and reliable wave energy converters. Despite significant research and development, the concepts for converting wave energy into electricity still have not converged to any favoured solution [143]. The oscillating water column (OWC) concept is among the most promising types of devices due to its simplicity and robustness and is therefore the most extensively studied [9]. An OWC consists of a partially submerged fixed or floating hollow structure, open to the sea below the water surface, that traps air between the inner free-surface and the top of the structure; under the wave excitation, the internal water column oscillates in the structure and alternately compresses and decompresses the trapped air which is forced in and out of the structure through a turbine coupled to a generator.

In the most common form of OWC, the compression and decompression of the air in the chamber directly creates a bidirectional flow across a self-rectifying turbine opened to the atmosphere. Such a turbine can harness both in-coming and out-coming flows. Their rotational direction remains un-

changed regardless of the direction of the air flow. Several types of such special turbines have been developed: Wells and impulse turbines are the two main types of self-rectifying turbines [9]. Their maximum total-to-static efficiency in constant flow condition varies between 30% and 72% depending on their level of complexity and cost [57]. To date, the biradial and twin-rotor turbines are the best performing self-rectifying turbines and reach, respectively, about 79% and 74% efficiency in steady flow conditions [144, 60]. In real ocean conditions, the flow across the turbine is, however, highly fluctuant and stops at every half-wave period to change direction. In these conditions, the average efficiency of self-rectifying turbines drops by 5 to 10% [57].

Other forms of OWC devices use non-return valves to rectify the flow across a unidirectional turbine. The incentive is that unidirectional turbines are more efficient than self-rectifying turbines with efficiencies higher than 85% [128, 99]. Various OWC devices using a unidirectional turbine have been studied and different methods for rectifying the air flow have been considered: The Masuda's navigation buoy [9], the Kaimei [104], the Leancon [53] and the vented OWC from wave swell energy [49] all use a different air flow rectification method. Rectifying valves, however, induce pneumatic power losses [122] and can also be unpractical at full scale [104].

The Tupperwave concept, described in [126], is equipped with two non-return valves, two large air chambers that act as accumulators and a unidirectional turbine. The vertical motion of the internal water surface (IWS) alternatively compresses the air into the high-pressure chamber (HP chamber) and decompresses the air in the low-pressure chamber (LP chamber). This creates a differential of pressure between the HP and LP chambers which are connected via the unidirectional turbine. The air flows in a closed-circuit in the device.

In order to study the relevance of the Tupperwave principle against the conventional OWC principle, two devices using each principle and the same floating spar buoy structure are compared in this article. The chosen floating structure is an axisymmetric spar buoy which suits both working principles. The volume of the Tupperwave HP and LP chambers is maximized according to an optimization study [95] and hence the whole buoyancy volume is used. Each chamber is 950 $m^3$. The electrical power performance of each device in terms of electrical energy production and power quality are to be assessed and compared. For this purpose, complete wave-to-wire numerical models of the two devices presented in Figure F.1 are required.

The power conversion chain of an OWC type device is split in four main stages. Part of the wave power $P_w$ reaching the device is absorbed by the floating device. The absorbed power $P_{abs}$ is the power applied by IWS on the air contained in the OWC chamber. It is then converted into pneumatic power $P_{avail}$ available across the turbine. The pneumatic power is converted into mechanical power $P_m$ by the turbine and further converted into electrical power $P_e$ by the generator. Accurate wave-to-wire modelling requires the mod-

elling of each power conversion stage and a validation against physical results. Such modelling and validation has already been achieved for OWC devices. This was done, for example, in [105], where the model is verified using experimental data from open sea device deployment. The model can then be used to test control strategies in specific conditions. However, if the device is at an earlier development stage, as is the case in this paper, no large scale prototype data are yet available. The wave-to-wire model validation therefore has to be done step-by-step across the power conversion stages using scaled lab tests. The power performances of the device can then be predicted using the validated model before the building and deployment of a large scale prototype.

In [133], numerical models from wave power to pneumatic power of the Tupperwave device and corresponding conventional OWC were developed and the results were validated against physical tank testing at 1/24th scale. The results also demonstrated the capacity of the Tupperwave concept to produce a smoother pneumatic power made available to the turbine. In this paper, the models from [133] are extended to build complete wave-to-wire models which are validated step-by-step as illustrated in Figure F.2. The models are then used to compare the power performance of both devices and conclude on the relevance of the innovative Tupperwave concept.

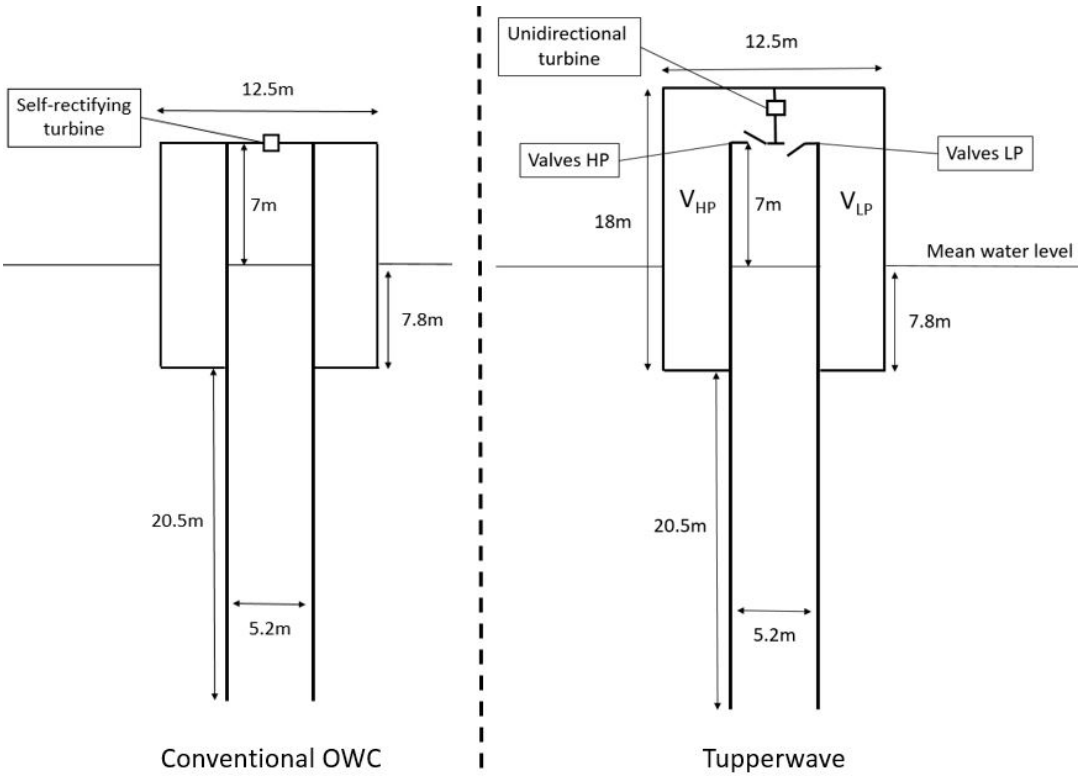


Figure F.1: Two-dimensional schematic of the full scale conventional oscillating water column (OWC) and Tupperwave devices.

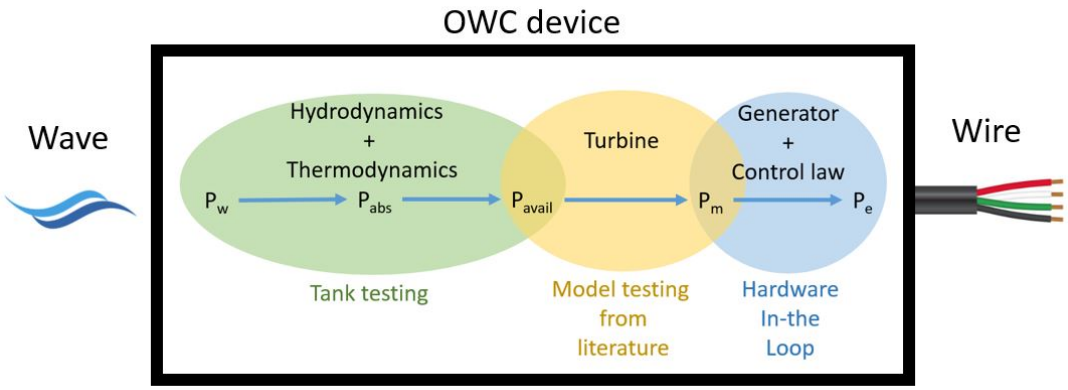


Figure F.2: Schematic of power conversion chain of OWC device from wave to wire and step-by-step validation methods achieved in [133, 128] and the present paper.

In Section F.2 of this paper, the rest of the power conversion chain is considered and added to the existing models by the addition of a turbine and generator model to obtain the complete wave-to-wire models of the two devices. Section F.3 explains the dimensioning methodology used on the turbine-generator systems for the devices' power performance optimisation in the wave climate of the EMEC test site located in Orkney, Scotland. Hardware-in-the-loop experiments were carried out to provide physical validation for the last power conversion stage and are described in Section F.4. Eventually, the complete wave-to-wire models are used in Section F.5 to assess and compare the power performances of the Tupperwave device and conventional OWC equipped with state of the art turbines in the EMEC wave climate. The impacts of the pneumatic power smoothing capacity of the Tupperwave working principle are identified.

## F.2 Wave-to-Wire Models

The wave-to-wire models are based on several considerations. Hydrodynamic and thermodynamic equations were used in [133] for the development of wave-to-pneumatic power models and are first summarized for the two full scale devices. The rest of the power conversion chain is then described. State-of-the-art turbines are chosen and modelled using physical testing results from the literature. Finally the generator model and its control are presented.

### F.2.1 Hydrodynamics

The Tupperwave device and the conventional OWC use the same floating spar structure. Therefore, the hydrodynamic wave-structure interactions for

both devices can be described by the same set of equations within the linear wave theory. The structure and the water column are considered as two rigid bodies moving in heave only in the waves relatively to each other. The coupled heave motions of the two bodies (noted with indices 1 and 2) can be written in time-domain as [133, 80]:

$$\begin{cases} [m_1 + A_{11}(\infty)]\ddot{x}_1(t) + \int_0^t K_{11}(t-\tau)\dot{x}_1(t)d\tau + A_{12}(\infty)\ddot{x}_2(t) \\ \quad + \int_0^t K_{12}(t-\tau)\dot{x}_2(t)d\tau + c_1 x_1(t) = f_1(t) + f_p(t) + f_{d1}(t) \quad (a) \\ A_{21}(\infty)\ddot{x}_1(t) + \int_0^t K_{21}(t-\tau)\dot{x}_1(t)d\tau + [m_2 + A_{22}(\infty)]\ddot{x}_2(t) \\ \quad + \int_0^t K_{22}(t-\tau)\dot{x}_2(t)d\tau + c_2 x_2(t) = f_2(t) - f_p(t) + f_{d2}(t) \quad (b) \end{cases} \tag{F.1}$$

where $m_i$ are the bodies' masses; $A_{ij}(\infty)$ are the bodies' heave motion added masses at infinite frequency; $c_i$ are the restoring force coefficients; $K_{ij}$ are the impulse response functions for heave motions and their interactions; $f_i$ are the wave excitation forces. $f_p$ is the reciprocating pressure force acting on both bodies and is calculated as: $f_p = S p_{owc}(t)$ where $S$ is the internal water free surface in the water column and $p_{owc}$ is the excess pressure relatively to atmospheric pressure built in the OWC chamber. The viscous drag forces $f_{d1}$ and $f_{d2}$ are calculated as $f_{di} = -C_{di}|\dot{x}_i(t)|\dot{x}_i(t)$ where $C_{di}$ is the equivalent drag coefficient. This force includes the viscous drag effects and all non-linear viscous effects [111]. The equivalent drag coefficients at full scale are unknown. The values of $C_{d1} = 150$ N·s$^2$·m$^{-2}$ and $C_{d2} = 40$ N·s$^2$·m$^{-2}$ were established using the experimental results from the tank testing at 1/24th scale [133]. It is, however, to be noted that possible differences on these coefficients between model scale and full scale may arise from different flow characteristics between the two scales. The scaled-up coefficients provide reference values that were used for the numerical models at full scale.

### F.2.2 Thermodynamics

The general thermodynamic differential equation relating the excess pressure $p$ and volume $V$ of air considered as a perfect gas in a chamber during isentropic transformations was derived in [133]:

$$\dot{p} = \frac{\gamma p_{atm}}{\rho_{atm} V}(w_{in} - w_{out} - \rho \dot{V}) \tag{F.2}$$

where $p_{atm}$ and $\rho_{atm}$ are the pressure and air density in atmospheric conditions; $w_{in}$ and $w_{out}$ are the mass flow rates of air flowing, respectively, in and out of the system.

If the system is considered adiabatic and the transformations slow enough to be reversible, the isentropic density-pressure relation is applicable:

$$\rho = \rho_{atm}\left(1 + \frac{p}{p_{atm}}\right)^{\frac{1}{\gamma}} \tag{F.3}$$

where $\gamma$ is the isentropic expansion factor.

If the excess pressure $p$ remains small compared to the atmospheric pressure $p_{atm}$, Equation (G.11) can be linearised:

$$\rho = \rho_{atm}\left(1 + \frac{p}{\gamma p_{atm}}\right) \tag{F.4}$$

At full scale, the turbine and the generator need to be protected from possible overloading happening in high energy sea-states. Bypass valves are commonly used as security system in OWC devices for this purpose [68]. The valve is normally closed and located in parallel to the turbine. When it opens, the flow splits between the turbine and the bypass valve, reducing the flow through the turbine and alleviate the load on this latter. The control of the bypass valve is described in Section G.2.3.

Figure G.7 displays a schematic of the OWC thermodynamic system. The value of mass flow rate $w_t$ and $w_{bypass}$ crossing the turbine and the bypass valves are considered positive whatever the flow direction. Equation (G.16) applied on the OWC chamber becomes:

$$\dot{p}_{owc} = \begin{cases} \dfrac{\gamma p_{atm}}{\rho_{atm} V_{owc}}\Big( -(w_t + w_{bypass}) - \rho_{owc}\dot{V}_{owc}\Big) & \text{for} \quad p_{owc} > 0 \\ \dfrac{\gamma p_{atm}}{\rho_{atm} V_{owc}}\Big( +(w_t + w_{bypass}) - \rho_{owc}\dot{V}_{owc}\Big) & \text{for} \quad p_{owc} < 0 \end{cases} \tag{F.5}$$

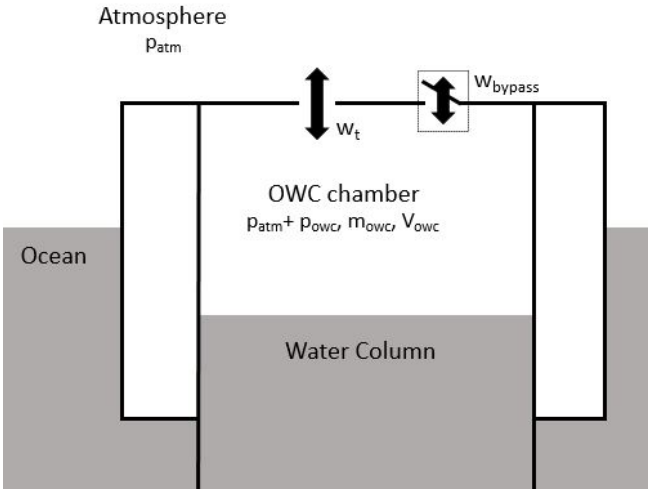


Figure F.3: Conventional OWC schematic with thermodynamic variables.

Figure F.4 displays a schematic of the three chambers of the Tupperwave device which constitute three interconnected thermodynamic systems. Unlike in the conventional OWC, in which the air is partly renovated during the inhalation part of the cycle, the air in the Tupperwave device is exchanged between the chambers in closed-circuit with no exchange with the atmosphere. This brings into question the possible air temperature increase in

the device due to energy dissipation by viscous effects across the turbine and the valves. The study of such irreversible processes is not in the scope of this research and it is assumed that the heat transfer through the device walls into the environment is sufficient to prevent the temperature in the device to rise significantly above atmospheric conditions. Moreover, the pressure conditions in the Tupperwave device being of similar order to the ones in the conventional OWC, the linearised isentropic assumption is also adopted for the Tupperwave device and Equation (G.16) is directly applied to the three chambers:

$$\begin{cases} \dot{p}_{owc} = \dfrac{\gamma p_{atm}}{\rho_{atm} V_{owc}} \left( w_{vl} - w_{vh} - \rho_{owc} \dot{V}_{owc} \right) & (a) \\ \dot{p}_{hp} = \dfrac{\gamma p_{atm}}{\rho_{atm} V_{hp}} \left( w_{vh} - (w_t + w_{bypass}) \right) & (b) \\ \dot{p}_{lp} = \dfrac{\gamma p_{atm}}{\rho_{atm} V_{lp}} \left( (w_t + w_{bypass}) - w_{vl} \right) & (c) \end{cases} \tag{F.6}$$

where $w_t$, $w_{bypass}$, $w_{vh}$ and $w_{vl}$ are the air mass flow rates across the turbine, the HP valve and the LP valve. The expression of these flows as functions of the pressure are established using the turbine and valve models.

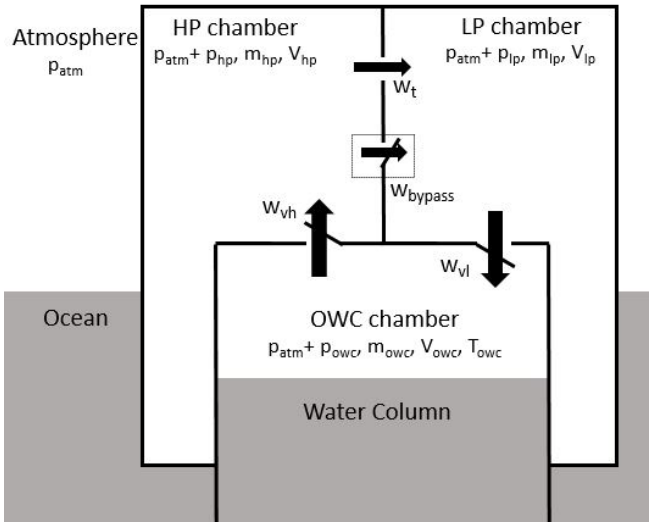


Figure F.4: Tupperwave device schematic with thermodynamic variables.

### F.2.3 Tupperwave Non-Return Valves

The valves are a key components in the Tupperwave device efficiency because they cause pneumatic power losses. The effective area of the valves and the opening pressure are the key parameters for the device efficiency [122]. Passive valves do not require to be electrically activated and are therefore very easy to implement. The use of passive valves in the full-scale Tupperwave device is justified to reduce the device mechanical and electrical complexity and hence to reduce its price. In this paper, the same passive valve

model as in [133] is used. The valves only allow air flow in one direction when the pressure head $\Delta p_v = p_{in} - p_{out}$ is larger than their opening pressure $p_o$. In high energy sea states, the Mach number of the flow across the valves rises above 0.3. Hence, the flow is considered as compressible and a steady-state subsonic compressible flow model is adopted to calculate the air mass flow rates across the valves [145]:

$$w_{v,in\to out} = \begin{cases} 0 & \text{if} \quad p_{in} - p_{out} < p_0 \\ \alpha A_v \sqrt{\dfrac{2\gamma}{\gamma - 1} \rho_{in} (p_{in} - p_0) \left( r^{\frac{2}{\gamma}} - r^{\frac{\gamma+1}{\gamma}} \right)} & \text{if} \quad p_{in} - p_{out} > p_0 \end{cases} \tag{F.7}$$

where $r = \dfrac{p_{out}}{p_{in} - p_0}$ is the pressure ratio over the valve when open; $\alpha A_v$ is the effective opening area of the valves when fully opened [68]. To maximise the efficiency of the valves, the effective area should be maximised while the opening pressure should be minimised. No valves were designed and studied for the full scale device. Moreover, hardly any information on non-return valves for large OWC devices is available in the literature. Therefore, it is hard to know what effective area and opening pressure are practically achievable at full scale. During physical model testing carried out at model scale in [122, 133], the valves caused very important pneumatic power losses, dissipating up to 60% of the absorbed wave power. They operated at best with a effective area of $0.286\,\mathrm{m}^2$ at full scale equivalent. The area available for the valve connecting the OWC chamber to the HP chamber (resp. LP chamber) is about $10\,\mathrm{m}^2$. With such a large available area, it is very likely that properly designed full scale valves could reach larger effective opening area than $0.286\,\mathrm{m}^2 = 53 \times 53\,\mathrm{cm}$. Nevertheless, this value will be used in the wave-to-wire model as a reference value. Regarding the opening pressure, a pressure differential of 150 Pa between both sides of the valve is equivalent to a force of $43\,\mathrm{N} = 4.4\,\mathrm{kgf}$ acting on the valve. Considering the small dimensions of the valve, such force should be sufficient to open it. The value of $p_0 = 150\,\mathrm{Pa}$ was therefore chosen as a reasonable pressure value to activate the opening of the valves. The influence of the values of $\alpha A_v$ and $p_0$ are investigated in Section F.5.

### F.2.4 Turbine Model

The conventional OWC and the Tupperwave device are equipped with two different turbines, which will be described in Section F.3.1. However, the numerical modelling remains the same for both turbines. The mechanical power $P_{mech}$ extracted by a turbine from an air flow is a function of its diameter D, its rotational speed $\Omega$, its pressure head $\Delta p_t = p_{in} - p_{out}$ between inlet and outlet, and of the volumetric air flow rate $q_t$ flowing across a turbine. These relationships are usually presented in dimensionless form, assuming incompressible flow and using the dimensionless flow coefficient $\Phi$, dimensionless

pressure head $\Psi$ and dimensionless turbine power output $\Pi$ which are defined as [9]:

$$\Phi = \frac{q_t}{\Omega D^3}; \quad \Psi = \frac{\Delta p_t}{\rho_{in}\Omega^2 D^2}; \quad \Pi = \frac{P_{mech}}{\rho_{in}\Omega^3 D^5} \tag{F.8}$$

The dimensionless coefficients can be related by the polynomial functions $f_\Psi$ and $f_\Pi$, established at model scale during laboratory tests:

$$\Psi = f_\Psi(\Phi)\,; \quad \Pi = f_\Pi(\Phi) \tag{F.9}$$

Neglecting the influence of the Reynolds and Mach numbers, the dimensionless turbine representation enables to describe any geometrically similar scaled-up version of the turbine.

From Equations (G.31) and (G.32), the mass flow rate crossing the turbine can be expressed as a function of pressure head and its expression can be used in Equations (F.5) and (F.6):

$$w_t = \rho_{in} q_t = \rho_{in}\Omega D^3 f_\Psi^{-1}\left(\frac{p_{in} - p_{out}}{\rho_{in}\Omega^2 D^2}\right) \tag{F.10}$$

The total-to-static turbine efficiency $\eta_t$ is obtained by the ratio of the mechanical power of the turbine $P_m$ and the pneumatic power available to the turbine $P_{avail}$:

$$\eta_t = \frac{P_m}{P_{avail}} = \frac{P_m}{q_t \times \Delta p_t} = \frac{\Pi}{\Phi \times \Psi} = f_\eta(\Phi) \tag{F.11}$$

The turbine reaches a maximum of efficiency for an optimal dimensionless flow coefficient $\Phi_{opt}$.

### F.2.5 Generator Model, Bypass Valve and Control Law

The mechanical power from the turbine is finally converted into electrical power by the generator. Newton's law applied on the generator rotor gives:

$$I\dot{\Omega} = T_{turb} - T_{gen} - T_{wind} \tag{F.12}$$

where $I$ is the inertia of the turbine-generator system; $T_{gen}$ is the electromagnetic braking torque applied by the generator; $T_{wind}$ is the aerodynamic friction torque due to windage losses of the twin-rotor turbine (only relevant for the conventional OWC, see Section F.3.1); $T_{turb}$ is the mechanical torque applied by the turbine obtained from Equations (G.31) and (G.32) by:

$$T_{turb} = \frac{P_{mech}}{\Omega} = \rho_{hp}\Omega^2 D^5 f_\Pi(\Phi) \tag{F.13}$$

The control of the turbine-generator system is achieved via the generator torque. In this paper, the control strategy implemented is a maximum power

point tracking (MPPT) based on optimal torque control. It is sought to optimise the instantaneous turbine efficiency by matching the generator braking torque to the torque expected to be produced by the turbine at maximum efficiency. According to Equation (G.31), the value of $T_{gen}$ is obtained by:

$$T_{gen} = T_{turb}(\Phi_{opt}) = \frac{P_m(\Phi_{opt})}{\Omega} = \rho_{in}\Omega^2 D^5 f_{\Pi}(\Phi_{opt}) \tag{F.14}$$

We note that with this control law, the generator torque only depends on the rotational speed such that $T_{gen} = a\Omega^2$ with $a = \rho_{in}D^5 f_{\Pi}(\Phi_{opt})$. It is a fast, robust, simple and well-established control law to implement since it does not require any additional sensor [70]. Moreover, no power is required from the grid and energy only flows in one direction. For example, a nearly identical strategy to the MPPT control was used as a base case control strategy for comparing more complex control algorithms during sea trials of a OWC device in [146].

Care must, however, be taken so that the generator rotational speed remains within its operational range $[\Omega_{min}; \Omega_{max}]$. In low energy sea states, the generator braking torque is dropped to zero for $\Omega < \Omega_{min}$ and no electrical power is produced. In high energy sea states, the generator is at risk to be over spun. The generator and the power electronics are limited by their rating power, the maximum braking torque $T_{gen,max} = P_{rated}/\Omega_{max}$ is reached when $\Omega > \Omega_{max}$. The normally closed bypass valve, located in parallel to the turbine, is electrically activated and opens fully when the generator is overloaded to reduce the flow across the turbine until the condition $\Omega < \Omega_{max}$ is satisfied again. This security system dissipates the excess energy and prevents the over spinning of the generator. The same valve model as in Equation F.7 is used to calculate the mass flow rate $w_{v,bypass}$ across the bypass valve. For quick relief of the turbine pressure head, the opening area of the bypass valve $\alpha A_{v,bypass}$ was chosen of $0.15\,\mathrm{m}^2$.

Then, the electromagnetic power $P_{em} = \Omega T_{gen}$ is converted into electricity by the generator with the efficiency $\eta_{gen}$. The efficiency of a generator is largely dependant on its load $\Lambda = \dfrac{P_{em}}{P_{rated}}$ where $P_{rated}$ is the generator rated power. The efficiency drops very sharply for partial loads. $\eta_{gen}$ was taken from [71] and is displayed in Figure G.6 as a function of the load. The dimensioning of the generator is discussed in Section F.3.

Finally, the electrical power produced by the generator is conditioned by power electronics before being delivered to the grid. The influence of the conditioning stage on the device efficiency is neglected here. As shown in [27], this assumption is reasonable in applications such as control parameters optimisation and power production assessment. The electrical power produced by the generator is therefore simply calculated as:

$$P_{elec} = \eta_{gen} P_{em} \tag{F.15}$$

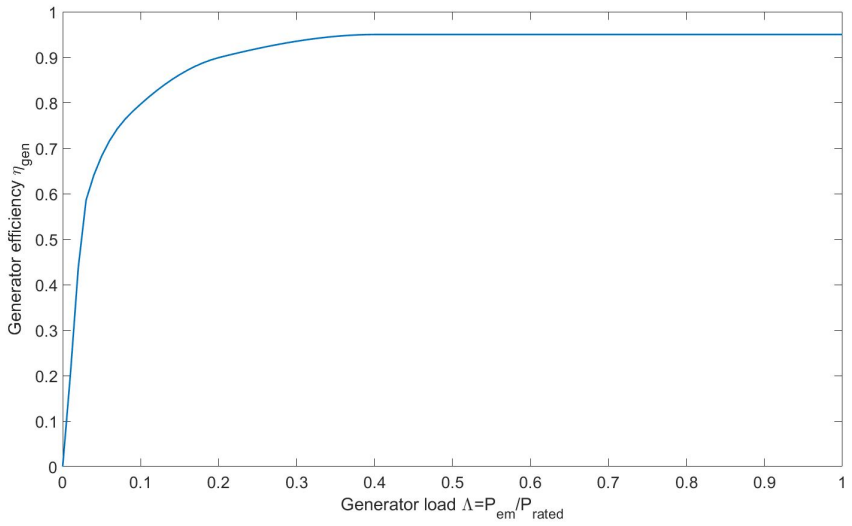


Figure F.5: Generator efficiency curve as a function of the load based on [71].

### F.2.6 Numerical Integration

Equations (G.1), (F.6) and (F.12) form the system of differential equations governing the behaviour of the Tupperwave device. The conventional OWC is governed by Equations (G.1), (F.5) and (F.12). Each of the four convolution integrals in Equation (G.1) are approximated using the Prony's decomposition method at order four. Details of the method can be found in [117, 116]. The numerical integration of these equations is achieved using the ordinary differential equation solver ode45 from the mathematical software MATLAB [118].

## F.3 Turbine-Generator Systems Dimensioning

### F.3.1 Turbines

The objective of the paper being to assess and compare the power performances of the Tupperwave device against a conventional OWC, both devices are equipped with the state-of-the-art turbines.

The twin-rotor turbine, displayed in Figure F.6a, is among the most efficient self-rectifying turbines [57]. It uses the idea that a bidirectional flow can be harnessed by two conventional air turbines in parallel: It consists on a pair of conventional radial-inflow rotors mounted on the same shaft in opposite direction, complemented by the corresponding guide vane rows and by a two-position cylindrical valve which, according to the flow direction, orientates the flow through one rotor or the other [96]. At all times, one rotor is driven by the air flow, while the other spins in no flow. The latter creates windage losses due to aerodynamic drag. Due to its symmetry,

half of the turbine was built at model scale in [60] in order to assess its performance experimentally (Figure F.6b). The resulting unidirectional single-rotor radial inflow unidirectional turbine was tested and the polynomial functions $f_\Psi$ and $f_\Pi$ relating the dimensionless coefficients were established. The experimental assessment of the windage losses allowed the establishment of the twin-rotor turbine dimensionless coefficients.

In this paper, the conventional OWC and the Tupperwave device are, respectively, equipped with the twin-rotor turbine and the corresponding single-rotor unidirectional turbine. Both turbines are therefore very similar and based on the same aerodynamic design. The unidirectional turbine is, however, less mechanically complex with no need for the fast-acting and electrically activated two-position valve. Moreover, due to the windage losses, the twin-rotor turbine is less efficient than the unidirectional turbine: It reaches 72.7% while the unidirectional turbine reaches 83.9%. Their total-to-static efficiencies in constant flow condition are compared in Figure F.7.

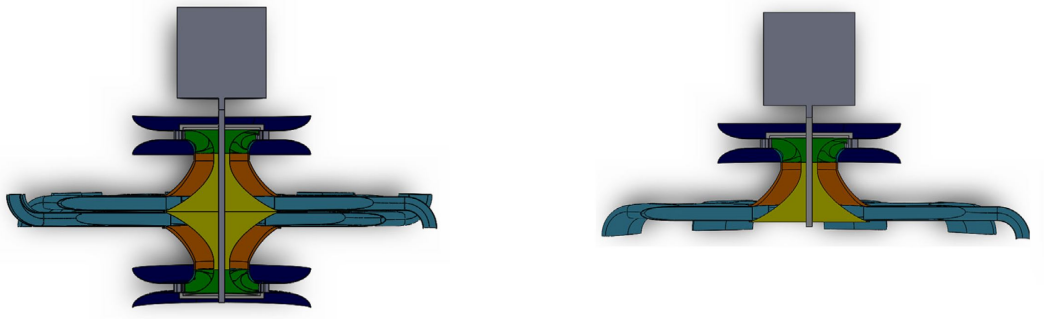

(a) (b)

Figure F.6: Schematics of the radial-inflow twin-rotor turbine modelled in the conventional OWC device and corresponding unidirectional radial-inflow turbine modelled in the Tupperwave device [60]. (**a**) Twin-rotor turbine. (**b**) Single rotor turbine.

In [133], the devices absorbed most power out of the waves for wave periods from 6 to 9 s. They are therefore well adapted for the EMEC wave energy test site located off the coast of Scotland where such wave periods prevail. The scatter diagram of the EMEC wave climate is given in Figure F.8.

For a fair comparison between the two devices, the turbines were optimised using the same methodology described below. The method described has no pretension of the being the best optimisation method. The turbine parameters to optimise are the diameter and the rotational speed. Their optimisation aims at maximising the device power output in the wave climate in which they are tested.

The optimisation of the turbines to maximise electrical power production in the EMEC wave climate was made in four steps:

1. Identification of the sea states for which the devices are the most productive over the year.

2. Assessment of optimal damping coefficients for the most productive sea states.

3. Assessment of turbine diameter and rotational speed to achieve optimal damping.

4. Verification that the damping achieved by the chosen turbine is close to optimal.

Basic turbine models were first used. A quadratic relationship was assumed between flow rate and pressure drop across the turbine such that:

$$\Delta P_t = k_t q_t^2 \tag{F.16}$$

where $k_t$ is the damping coefficient of the turbine. The damping of the turbine is fundamental for the efficiency an OWC device in absorbing the wave energy. As a starting point, the turbine damping coefficients obtained by parametric optimisation in [95] carried out in regular waves were first tried over the whole EMEC wave climate and showed that the sea states of significant wave height $H_s = 2$–$3\,\mathrm{m}$ and peak period $T_p = 8$–$9\,\mathrm{s}$ are the most productive sea states over the year. Due to the large discrepancy of the sea states energy density, the most productive sea states are not the one that occur most often.

The turbine characteristics were then optimised for the most productive sea states. The damping coefficients maximising the devices' available power in the turbine $P_{avail}$ for those sea states were investigated in detail. Figures F.9 and F.10 show the evolution of the average pneumatic power flowing across the turbine $P_{avail}$ over the turbine damping coefficient in sea state $\{H_s = 2\,\mathrm{m}\,;\, T_p = 8\,\mathrm{s}\}$ and $(H_s = 3\,\mathrm{m}\,;\, T_p = 9\,\mathrm{s})$ for the two devices, respectively.

It is observed that the ranges of damping coefficients maximising the power absorption from the waves are $k_t = 35$–$75\,\mathrm{Pa}\cdot\mathrm{s}^2\cdot\mathrm{m}^{-6}$ for the conventional OWC and $k_t = 1000$–$2500\,\mathrm{Pa}\cdot\mathrm{s}^2\cdot\mathrm{m}^{-6}$ for the Tupperwave device. The average flow rates achieved across the turbines in those conditions are denoted as $\overline{q_t}$.

It is fundamental that the turbines work close to their design flow coefficients $\Phi_{opt}$ (highlighted in Figure F.7) which maximise their efficiencies. Therefore, for each turbine, a design rotational speed $\Omega_d$ is first chosen arbitrarily and its diameter is calculated from Equation (G.31) by:

$$D = \sqrt[3]{\frac{\overline{q_t}}{\Omega_d \Phi_{opt}}} \tag{F.17}$$

The obtained turbine characteristics are given in Table F.1.

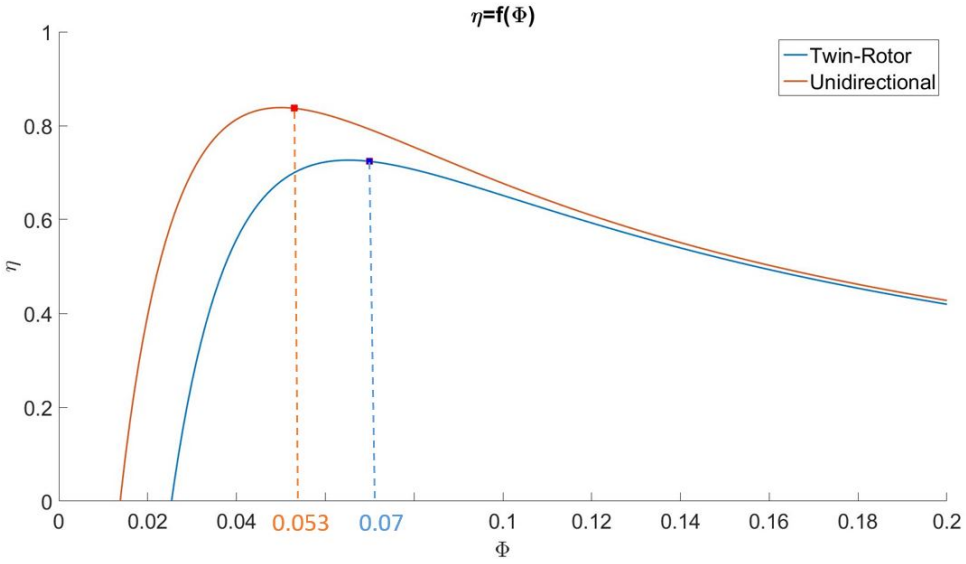


Figure F.7: Total-to-static efficiencies for the twin-rotor and unidirectional turbines as functions of the flow coefficient.

Table F.1: Chosen turbine characteristics.

| | **Unidirectional** | **Twin-Rotor** |
|---|---|---|
| $\Phi_{opt}$ | 0.053 | 0.07 |
| $\Omega_d$ (rpm) | 4000 | 1000 |
| $\overline{q_t}$ $(\mathrm{m}^3 \cdot \mathrm{s}^{-1})$ | 2.8 | 9.8 |
| D (m) | 0.5 | 1.10 |

It is then necessary to verify if the diameter and rotational speed selected induce a damping close to optimal for different turbine speeds. Figures F.11 and F.12 display the relationships between flow rates and pressure drops of the turbine models with the chosen parameters for different rotational speeds at which the turbines are likely to spin. They are compared with the simplified laws of optimised constant damping $k_t$. The damping achieved by the turbines for the different rotational speeds falls right in the range of optimum damping maximising wave absorption for sea states between $\{H_s = 2\,\mathrm{m}\,;\, T_p = 8\,\mathrm{s}\}$ and $(H_s = 3\,\mathrm{m}\,;\, T_p = 9\,\mathrm{s})$. This confirms that the diameters and rotational speeds of the turbine are well established. If it was not the case, the rotational speed of the turbines should be reconsidered until good agreement is obtained.

It is observed in Figures F.11 and F.12 that the damping of the turbines increases slightly with the rotational speed. It is, however, interesting to note

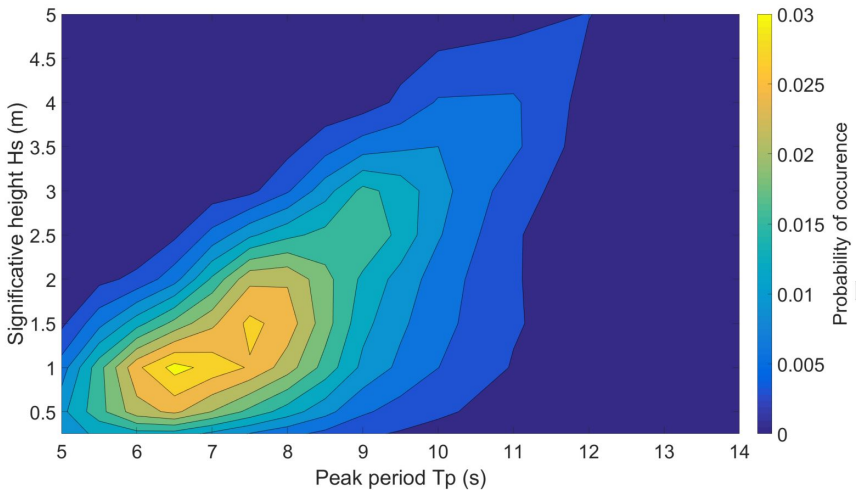


Figure F.8: Scatter diagram of wave data statistic for the EMEC wave energy test site.

that, according to Figures F.9 and F.10, the optimal turbine damping becomes smaller for larger sea states where the turbine is likely to be spun faster. This shows that speed control of the turbines depending on the wave condition would theoretically enable the turbine damping to be matched with the optimal damping and hence maximise the absorbed power and the real delivered power production. In the case of the conventional OWC, the flow across the turbine very quickly varies and stops every 3–5 s to change direction. In this flow condition, a fixed-speed generator would experience severe shock loads on the generator shaft, whereas if the speed were allowed to increase, the inertia of the system would absorb some of the extra power input. This consideration led to the adoption of the more simple variable speed control law described in Section G.2.3. With such a control law, the turbines gain to be designed so that their damping stays relatively constant with various rotational speeds.

The adaptation of the unidirectional turbine tested in [128] for the pneumatic damping needs of the Tupperwave turbine and the conventional OWC led to very different results on what concerns the size (diameter D) and the rotational speed. This is due to the different working conditions of the turbines in the two devices. The turbine in the Tupperwave device has a small diameter of 0.5 m but a very high design rotational speed of 4000 rpm. In addition of being less mechanically complex because of the absence of valve and of a single rotor, the chosen Tupperwave turbine is half the size of the conventional OWC turbine, it is therefore likely to be much cheaper. Unfortunately, a gearbox is necessary to bring down its high design speed to a commonly used generator design speed (1000 rpm) and the investment cost and maintenance issues associated with a gearbox are undesirable.

The Cordier diagram, see [147], is an empirical diagram commonly used

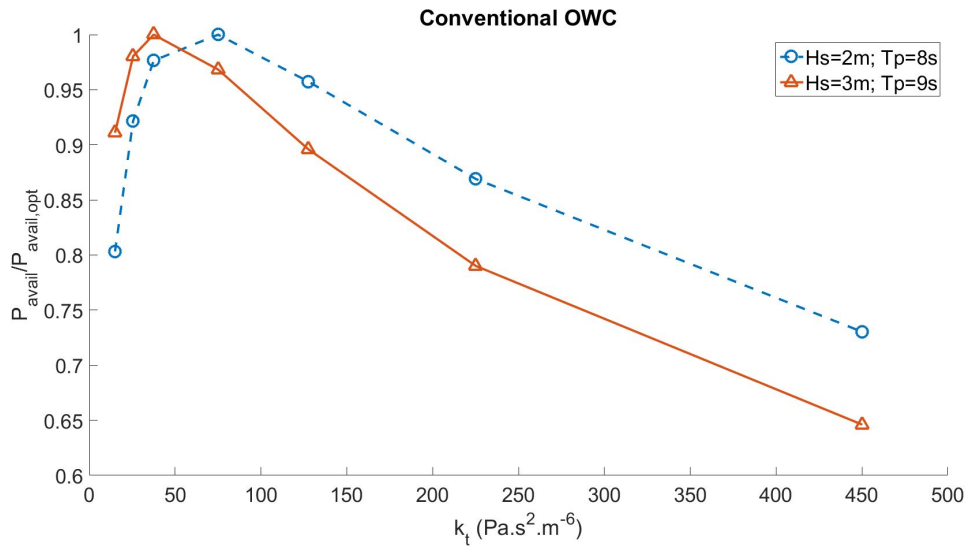


Figure F.9: Evolution of pneumatic power available to the turbine with turbine damping coefficient for the conventional OWC.

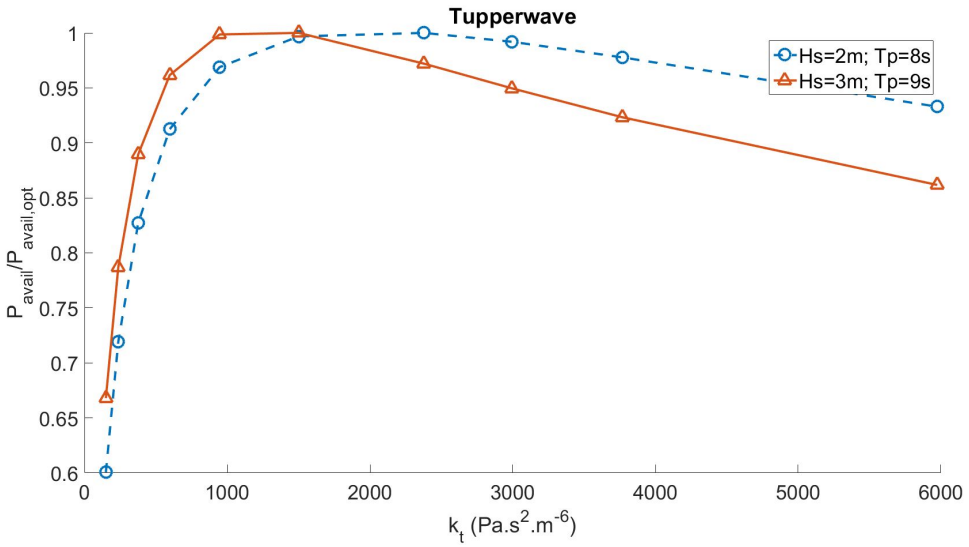


Figure F.10: Evolution of pneumatic power available to the turbine with turbine damping coefficient for the Tupperwave device.

as a tool by turbine designers. It indicates that if the optimum operating conditions are kept constant and if the design speed of the turbine is lowered, then the diameter of the turbine increases. This shows that the use of a gearbox could be avoided if a different turbine design with larger diameter was adopted. The Cordier diagram does not, however, provide any information on the blade shape (i.e., angles and blade width) and such designing exercise is out of the scope of the present research.

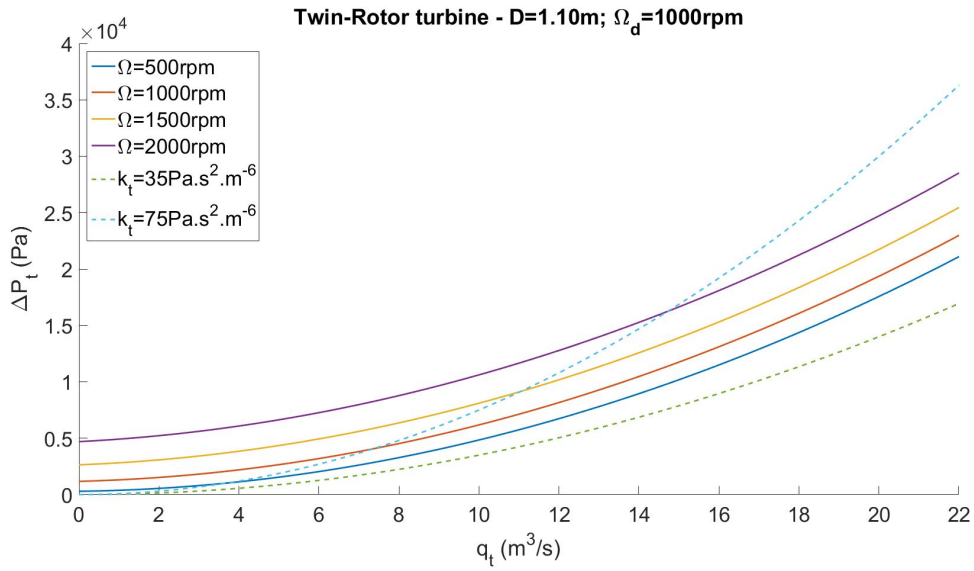


Figure F.11: Relationship between pressure head $\Delta P_t$ and volumetric flow rate $q_t$ for the twin-rotor turbine at various rotational speeds $\Omega$ compared to the optimal fixed damping relationships.

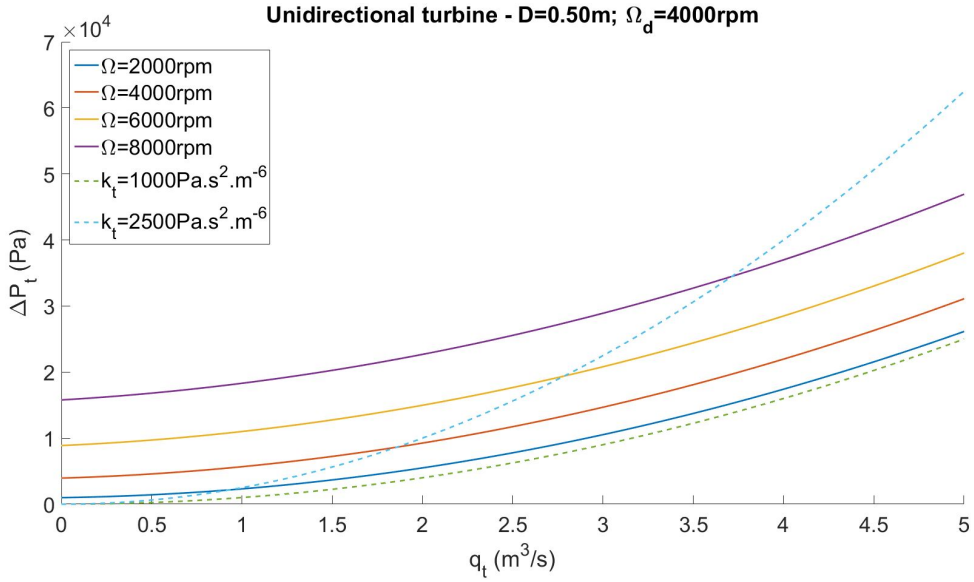


Figure F.12: Relationship between pressure head $\Delta P_t$ and volumetric flow rate $q_t$ for the unidirectional turbine at various rotational speeds $\Omega$ compared to the optimal fixed damping relationships.

### F.3.2 Generator

As described in Section G.2.3, the efficiency of conventional electrical generators decays markedly for loads less than one-third of the rated power. During operation the electrical equipment, especially the power electronics,

cannot be subjected to overloads. It is the purpose of the bypass valve to protect the electrical equipment from overloads. This security system should be used the least possible to reduce the risk of failure and increase the reliability of the device. For these reasons, the generator rated power needs to be carefully chosen. Similarly to the turbine, the generator should be sized according to the sea states of the site's wave climate for which the device extract the most wave power over the year. In those sea states, the generator should work at maximum efficiency but its rated power should be such that it is able to withstand the power peaks when high energy is available.

The most productive sea states of the EMEC wave climate for the devices studied in this paper are sea states of significant wave height $H_s = 2$–$3\,\mathrm{m}$ and peak period $T_p = 8$–$9\,\mathrm{s}$. According to Figure G.6, the generator works at maximum efficiency for loads from $\Lambda = 0.35$ onwards. The rated power of the generator is therefore chosen so that the average load of the generator in these sea states is close to 0.35. It will be seen in Section F.5 that the conventional OWC and the Tupperwave device produce similar amount of electrical power and a generator of 100 kW rated power was chosen for both devices. Its inertia was estimated from an exiting generator of similar rated power.

Table G.1 displays the optimised turbine and generator characteristics for the two devices studied. The turbines were assumed to be built in aluminium and their inertia were approximated based on their diameter.

Table F.2: Turbine and generator parameters used in the wave-to-wire models.

| | | **Tupperwave** | **Conventional OWC** |
|---|---|---|---|
| **Turbine** | Type | Unidirectional radial inflow turbine | Self-rectifying radial inflow twin-rotor turbine |
| | Diameter (m) | 0.50 | 1.10 |
| | Inertia (kg·m$^2$) | 1.7 | 38 |
| | Max. efficiency (%) | 86.6 | 73.9 |
| **Gearbox** | Gearing Ratio | 4 | 1 |
| **Generator** | Rated power (kW) | 100 | |
| | Inertia (kg · m$^2$) | 3.6 | |
| | Design speed (rpm) | 1000 | |
| | Max. speed (rpm) | 2000 | |
| | Min. speed (rpm) | 400 | |

## F.4 Numerical Model Validation

The wave-to-wire models are validated in different power conversion steps. In [133], the models from wave to useful pneumatic power available to the turbine were validated. The turbine models added in this paper were established by the experimental tests carried out in [128] providing accurate modelling of the pneumatic to mechanical power conversion. The last power conversion step from mechanical to electrical power achieved by the generator is validated experimentally in this paper.

### F.4.1 Objective and Method

The objective is to emulate the mechanical to electrical power conversion happening at full scale in the two devices studied and compare the results with the numerical models. This is achieved using Hardware-in-the-Loop (HIL) to simulate physically and in real time the turbine action on a real generator. The hardware is the rotary test rig of the Lir National Ocean Test Facilities (Lir-NOTF), MaREI Center, Ireland. The rig is basically composed of two 22 kW coupled electrical machines. One is used as a motor and acts as the prime mover (turbine). The other acts as the electrical generator and is connected to the local electrical grid using an off-the-shelf back-to-back converter. A picture of the rig is shown in Figure F.13. Detailed descriptions of the rig, its capabilities and its limitations are described in [148, 149]. The generator of the rotary test rig in the Lir NOTF includes several different configurations. For the HIL tests performed for validation, the selected generator configuration was the squirrel cage induction generator (SCIG) as suggested in [150].

The generator control law presented in Section G.2.3 is directly applied on the real generator. This type of simulation is generally undertaken in the development of full scale devices. The controlled environment enables to simulate the equipment and control system in offshore-like conditions at a significantly lower cost prior to offshore tests.

The HIL system includes a Matlab–Simulink numerical model of the wave energy device from wave to mechanical power. The torque $T_{turb}$ created by the turbine on the shaft is solved based on the measured rotational speed of the rig. This torque is then applied in real time by the motor on the shaft. The connected generator converts the mechanical power into electrical power which is sent onto the grid. Since the numerical model depends on the turbine state, the measured rotational speed of the system is fed back into the numerical model at each time step.

The numerical model from wave to mechanical power is run at full scale while the hardware is run at model scale. The model scaling is determined by the hardware installation limits in power and speed. The scaling is executed through a two-step process. Since surface waves are gravity driven,

Figure F.13: Rotary test rig of the Lir National Ocean Test Facilities (Lir-NOTF), used to emulate the turbine-generator systems of the devices.

the Froude similarity law of coefficient $\lambda$ is first used to scale down the turbine output power to fit on the rig installation which is limited to 22 kW. For that, the Froude similarity law is applied on the turbine output torque $T_{turb}$ and on the turbine speed $\Omega$. As a result, the torque is reduced, but the speed is increased. To adapt the rotational speed of the model in line with the limitations of the rig (2200 rpm), the second step of the scaling process is the implementation of a virtual gearbox to the system with a virtual gearbox coefficient $G$, where a decrease in speed is exchanged for an increase in torque. The flow chart presenting the HIL system and the scaling method is displayed in Figure F.14. As explained in Section F.1, all parts of the device model (hydrodynamic, thermodynamic, turbine, generator) are strongly coupled and this is represented by the bidirectional arrows.

### F.4.2 Hardware-in-the-Loop Results

HIL tests were carried out for three common sea states of the EMEC wave climate and compared to the fully numerical results. The Pearson correlation coefficient for the electrical power $P_e$ and generator rotational speed $\Omega_{gen}$ were calculated and are displayed in Table F.3. The coefficients are close to 1 and indicate good agreement between the fully numerical model and the tests with HIL.

For a more illustrative comparison, time series are displayed in Figures F.15 and F.16. The results in Table F.3 and very good visual agreement are obtained; Figures F.15 and F.16 validated the last power conversion step of the fully numerical wave-to-wire models. It is noticeable for the conventional

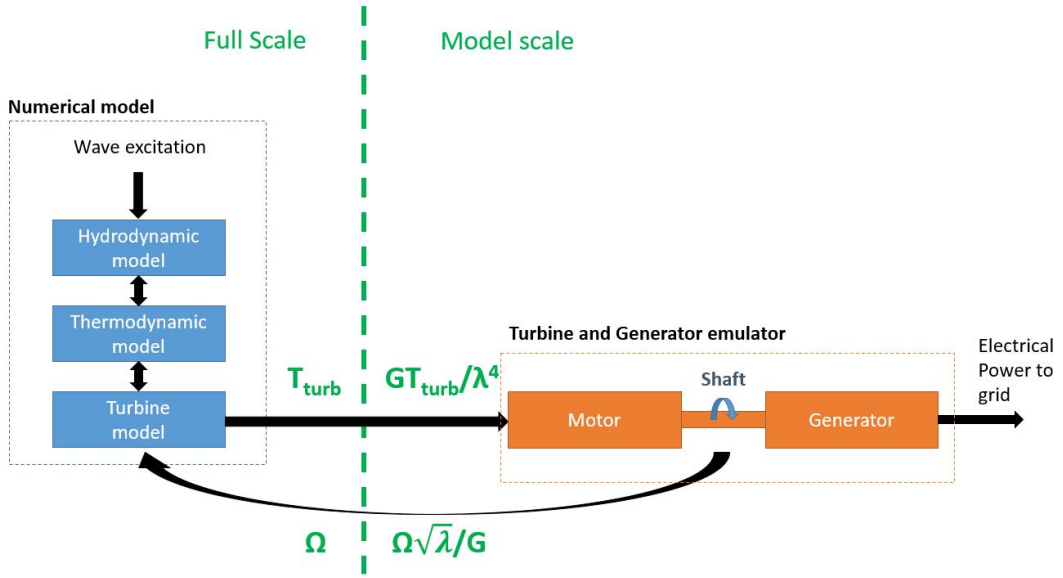


Figure F.14: Hardware-in-the-Loop flow chart with scaling laws applied to the turbine speed $\Omega$ and output torque $T_{turb}$.

Table F.3: Pearson correlation coefficients between Hardware-in-the-Loop (HIL) and fully numerical results for the time series of electrical power $P_e$ and generator rotational speed $\Omega_{gen}$ in three common sea states of the EMEC wave climate.

| | **Tupperwave** | | **Conventional OWC** | |
|---|---|---|---|---|
| | $P_e$ | $\Omega_{gen}$ | $P_e$ | $\Omega_{gen}$ |
| $H_s$ = 1.5 m; $T_p$ = 7.5 s | 0.954 | 0.956 | 0.953 | 0.990 |
| $H_s$ = 2 m; $T_p$ = 8 s | 0.978 | 0.958 | 0.959 | 0.990 |
| $H_s$ = 3 m; $T_p$ = 9 s | 0.974 | 0.961 | 0.944 | 0.985 |

OWC that the high power peaks are reduced by the HIL due to limitations in the power output of the prime-mover motor of the rotary rig and the low power are increased by the HIL due to a baseline power output that the Regen drive needs for output to the grid. These effects are caused by intrinsic limitations of the rotary rig and are more noticeable for the conventional OWC than for the Tupperwave device because of the larger power fluctuations.

For the two devices, the generator control law gives satisfactory results since it allows the generator to spin close its design speed of 1000 rpm.

This validates the last power conversion stage and concludes the validation by experimental testing of the entire power conversion chain, as illus-

trated in Figure F.2.

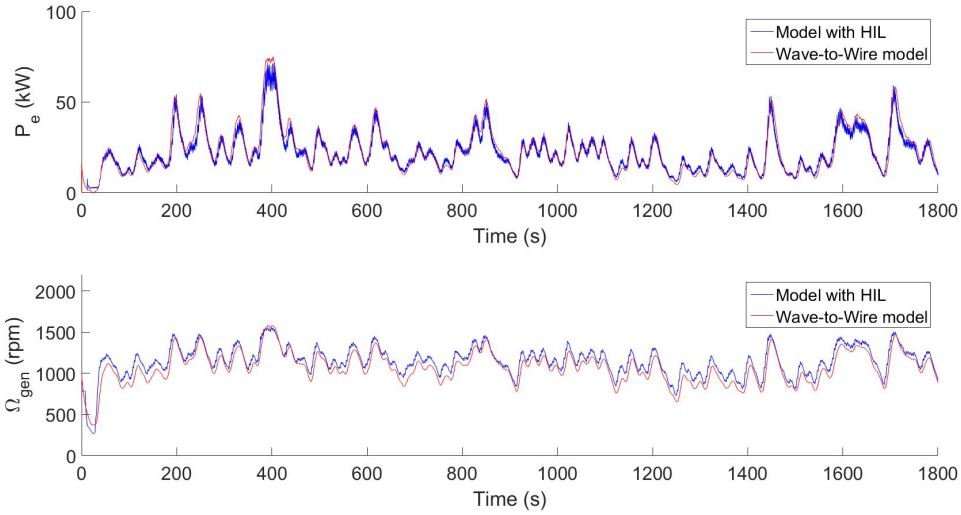


Figure F.15: Time series of electrical power $P_e$ and generator rotational speed $\Omega_{gen}$ obtained for the Tupperwave device with HIL and fully numerical model in sea state $\{H_s = 2\,\mathrm{m}\,;\, T_p = 8\,\mathrm{s}\}$.

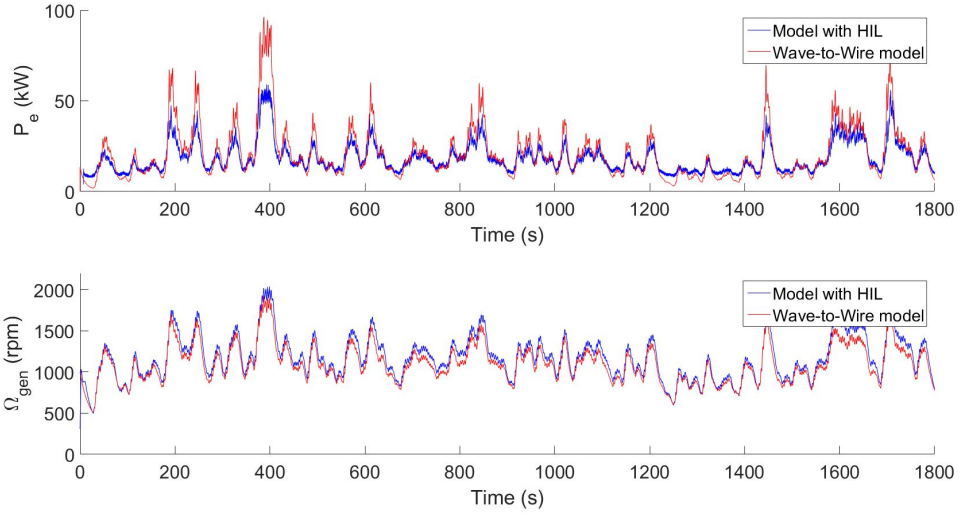


Figure F.16: Time series of electrical power $P_e$ and generator rotational speed $\Omega_{gen}$ obtained for the conventional OWC with HIL and fully numerical model in sea state $\{H_s = 2\,\mathrm{m}\,;\, T_p = 8\,\mathrm{s}\}$.

## F.5 Wave-to-Wire Models Results

Once, the Tupperwave and conventional OWC wave-to-wire models were validated against physical testing for all power conversion stages, their re-

sults are used to compare the device performances. The different power conversion processes are first compared for a single sea state. The devices' yearly performance in the EMEC test site are then compared both in terms of average electrical power output and power quality. Since both devices have the same floating structure, the same turbine aerodynamic geometry, the same generator and the same control law, this comparison aims at comparing the two devices' working principles.

The performances of the Tupperwave device are largely dependant on the non-return valves characteristics. Since the available literature provides no information on the achievable performances of non-return valves, three cases of valve characteristics were considered and detailed in Table F.4.

Table F.4: Non-return valve characteristics considered in the Tupperwave device.

| **Tupperwave Valves** | $p_0$ **(Pa)** | $\alpha A_v$ **(m²)** |
|---|---|---|
| Case 1 | 1700 | 0.286 |
| Case 2 | 150 | 0.286 |
| Case 3 | 150 | 1.3 |

The experience on non-return valves gained from the tank testing campaign of the Tupperwave device carried out in [133] is valuable. Even though their performances were poor, the characteristics of the valves used in [133] can be used as a starting point. In case 1, the valves opening pressure $p_0$ and effective opening area $\alpha A_v$ corresponds to the ones obtained, at best, during the tank testing campaign. The values obtained at model scale were simply scaled up with Froude similarity law. In case 2, the opening area is kept unchanged and the opening pressure is set to 150 Pa. This pressure applied on the area of the valve correspond to an opening force of 5 kgf which seems reasonable for such a small valve. This case was used for the turbine-generator dimensioning described in Section F.3. In the third case, the effective opening area of the valves is increased to 1.3 $m^2$. We recall that the wall surface available between the OWC chamber and the HP (resp. LP) chamber is 10.6 $m^2$. An effective opening area of 1.3 $m^2$ therefore seems easily achievable.

### F.5.1 Along the Power Conversion Chain

It will be seen in Section F.5.2 that both devices produce annually the most in the sea state $\{H_s = 3\,\text{m}\,;\, T_p = 9\,\text{s}\}$. This sea state is considered in this section and the powers along the conversion chain are observed.

The amount of incident wave power reaching the devices is the same and only about 11% is effectively absorbed from the motion of the IWS in

the devices. This absorbed power $P_{abs}$ is the product of the volumetric flow rate $q_{IWS}$ displaced by the motion of the IWS (counted positive for upward motion) by the pressure in the OWC chamber and is the rate of work applied by the IWS on the air in the OWC chamber:

$$P_{abs} = p_{owc} q_{IWS} = -p_{owc} \dot{V}_{owc} \tag{F.18}$$

Figure F.17 displays the absorbed power by the two devices. The power mainly flows from the IWS to the air in the chamber but it is alternatively positive and negative, meaning that energy is exchanged back and forth between the IWS and the air in the OWC chamber. At each stroke of IWS, a slight part of the power is stored by the air under the form internal energy. This power is then released back in the IWS at the next stroke in the opposite direction. This is caused by the spring-like air compressibility effect in the OWC chamber. This phenomenon is clearly described in [67]. Larger compressibility effect is observed in the OWC chamber of the Tupperwave device. The average power absorbed by the Tupperwave device is 5% lower than the power absorbed by the conventional OWC.

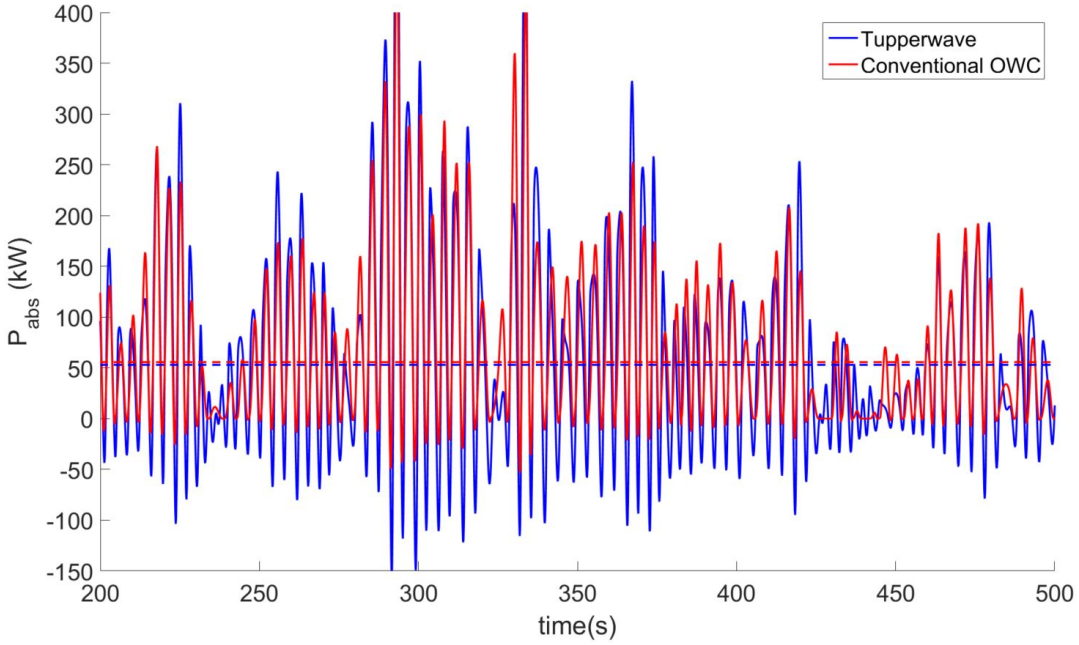


Figure F.17: Power applied by the internal water surface (IWS) on the air in the OWC chamber (or absorbed wave power) in a conventional OWC and Tupperwave device (case 2) in sea state ($H_s = 3\,\mathrm{m}$; $T_p = 9\,\mathrm{s}$). Solid lines: Time series; dash lines: Average values.

The absorbed power is then converted into useful pneumatic power or power available at the turbine $P_{avail}$ which, in compressible flow, is the rate of enthalpy drop of the air across the turbine:

$$P_{avail} = w_t (h_{in} - h_{out,s}) \tag{F.19}$$

where $h_{in}$ is the specific enthalpy of the air at the entrance of the turbine, and $h_{out,s}$ is the specific enthalpy at the exit of the turbine for an isentropic expansion. Since the process is assumed adiabatic and isentropic without any dissipative losses, the absorbed power is, on average, entirely converted into power available at the turbine in the case of the conventional OWC: $\overline{P_{avail}} = \overline{P_{abs}}$. For the Tupperwave device, the air flow is rectified by the non-return valves to build a pressure differential between two accumulator chambers. This provides a smoothing of the pneumatic power across the turbine at the expense of pneumatic power losses across the valves. We define the valves efficiency as:

$$\eta_v = \frac{\overline{P_{avail}}}{\overline{P_{abs}}} \tag{F.20}$$

In the case presented in Figure F.17, for the Tupperwave device, 80.5% of the absorbed power is actually converted into power available at the turbine and the rest is dissipated in the valves. The valves are thus 80.5% efficient. Figure F.18 displays the resulting pneumatic powers available to the turbines in the Tupperwave device (case 2) and in the conventional OWC in sea state $H_s$ = 3 m and $T_p$ = 9 s.

The power available at the turbines is then converted into mechanical power by the turbine. The smooth pneumatic power available at the turbine of the Tupperwave device is easier to harness and the turbine works very close to maximum efficiency while the turbine of the conventional OWC works on average 10% away from its maximum efficiency. Figure F.19 illustrates this fact by showing the density of the working points along the turbines efficiency curves during the sea state. The unidirectional turbine of the Tupperwave device works 84% of the time within 1% of its maximum efficiency while the twin-rotor turbine only works in this state for 17% of the time.

Finally the smoothed mechanical power available to the generator is converted into electrical power with an efficiency close to 94% for both devices. The time-series of the devices' electrical power production are displayed in Figure F.20.

The significant electrical power fluctuations, delivered by wave energy converters in general, may have a negative impact on the power quality of the local grid to which the wave farms is connected [151]. They are an issue of concern for grid operators as they can introduce undesirable effects on the grid such as voltage and frequency variations and flickers [26]. Regarding Figure F.20, the power fluctuations can be split in two groups: The wave-by-wave fluctuations or the wave-group by wave-group. Wave-by-wave power fluctuations cause the small peaks at every half wave-period visible for the conventional OWC and are due the high pneumatic power fluctuation between waves. These peaks are smoothed for the Tupperwave device. The Tupperwave accumulator system also smoothen the power between wave groups: Part of the energy of a wave group is stored under the form of pressure differ-

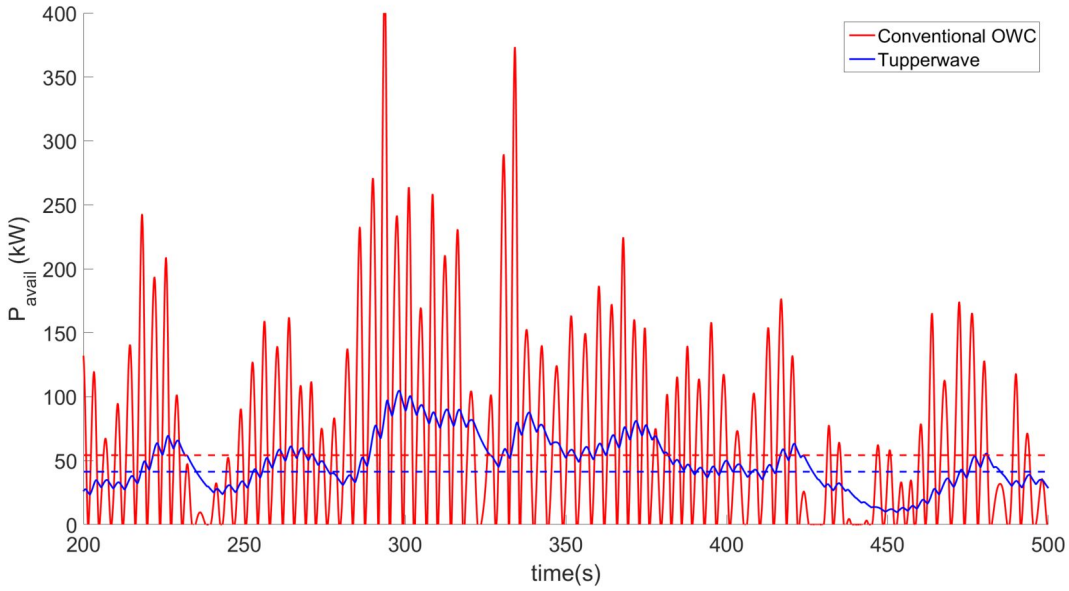


Figure F.18: Pneumatic power available to the turbines in a conventional OWC and Tupperwave device (case 2) in sea state ($H_s = 3\,\text{m}$; $T_p = 9\,\text{s}$). Solid lines: Time series; dash lines: Average values.

ential between the accumulators and is slowly released through the turbine until the next wave group. This also introduces a phase shift between the two curves. As a result the electrical power delivered by the Tupperwave device is smoother than for the conventional OWC. For the smoothing of the power, the conventional OWC relies only on the inertia of its turbine. The larger inertia of the twin-rotor turbine due to its larger diameter is an asset and the turbine is able to absorb temporarily the pneumatic power under the form of kinetic energy and alleviate the load variations on the generator. The inertia of the unidirectional turbine being smaller, the Tupperwave device relies almost only on the pneumatic power storing capacity to smoothen the turbine mechanical output power. The pneumatic power smoothing achieved by the Tupperwave device leads to smoother electrical power than the mechanical power smoothing achieved by the conventional OWC's turbine inertia.

By adding a flywheel of inertia $150\,\text{N}\cdot\text{m}^2$ to the twin-rotor turbine, it is possible to obtain the same level of smoothness with the conventional OWC. Such inertia can be obtained with a 1.2 m diameter and 0.1 m thick iron wheel which weighs approximately 820 kg. This naturally adds to the initial cost of the turbine and the added mass could lead to additional maintenance costs due to larger stresses on the bearings. It also causes a 3% reduction in power production.

A smaller flywheel of inertia $36.3\,\text{N}\cdot\text{m}^2$ can be added to the Tupperwave power-take off (PTO) system so that the resulting PTO inertia is the same as in the conventional OWC (see Table G.1). This represents a 0.85 m diame-

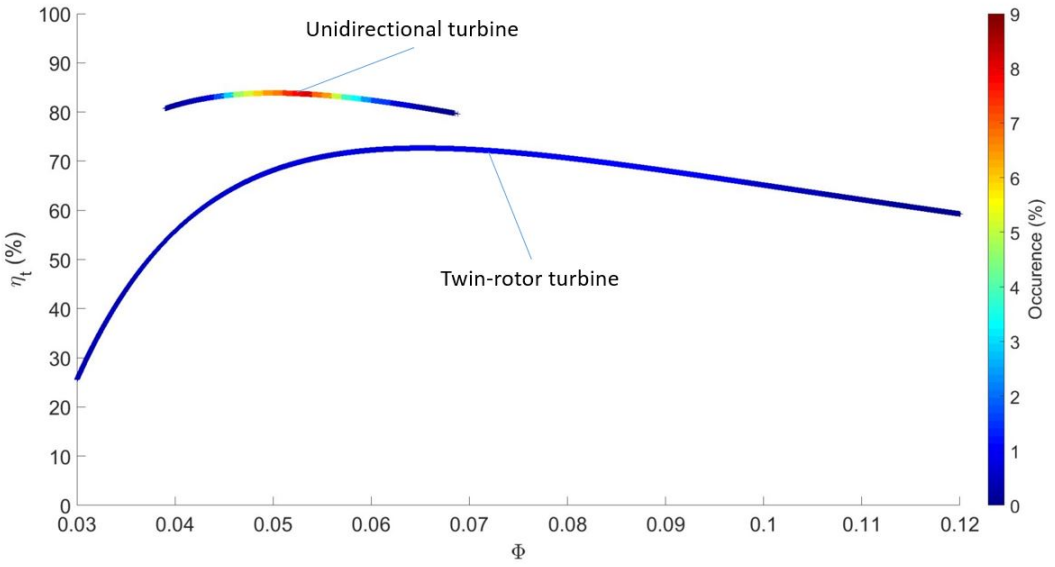


Figure F.19: Percentage of occurrence of turbine working points in sea state ($H_s = 3\,\mathrm{m}$ ; $T_p = 9\,\mathrm{s}$).

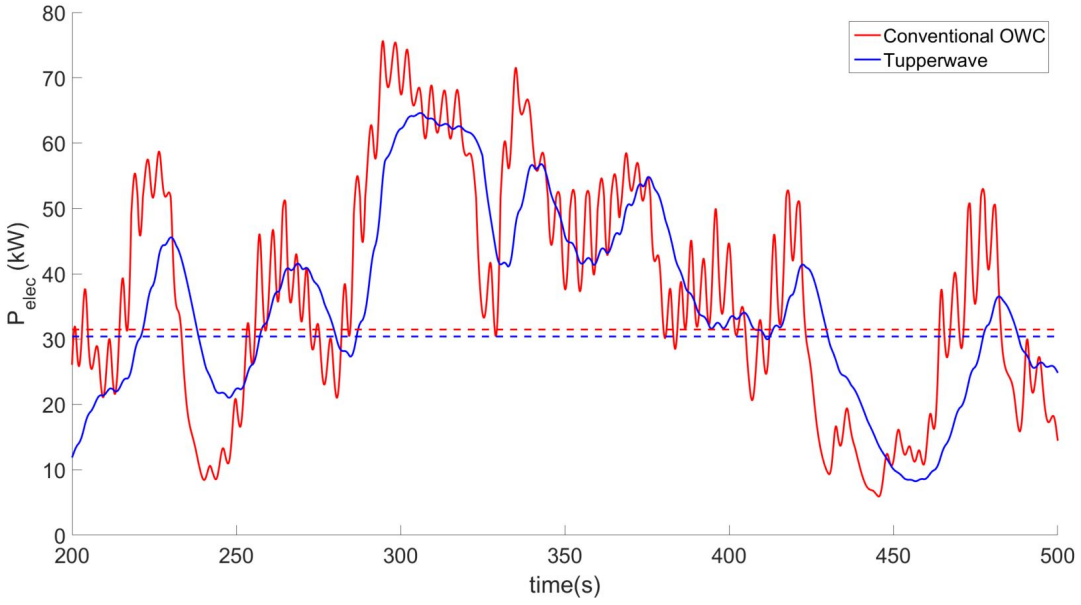


Figure F.20: Electrical power produced by the conventional OWC and Tupperwave device (case 2) in sea state ($H_s = 3\,\mathrm{m}$ ; $T_p = 9\,\mathrm{s}$). Solid lines: Time series; dash lines: Average values.

ter and 0.1 m thick iron wheel of about 400 kg. The time-series of the devices' electrical power production are displayed in Figure F.21. The pneumatic power smoothing of the accumulator chambers is combined with the mechanical power smoothing of the inertial PTO and the resulting electrical power is remarkably smooth. The addition of the flywheel only causes a 0.3%

reduction in average electrical power production for this sea state.

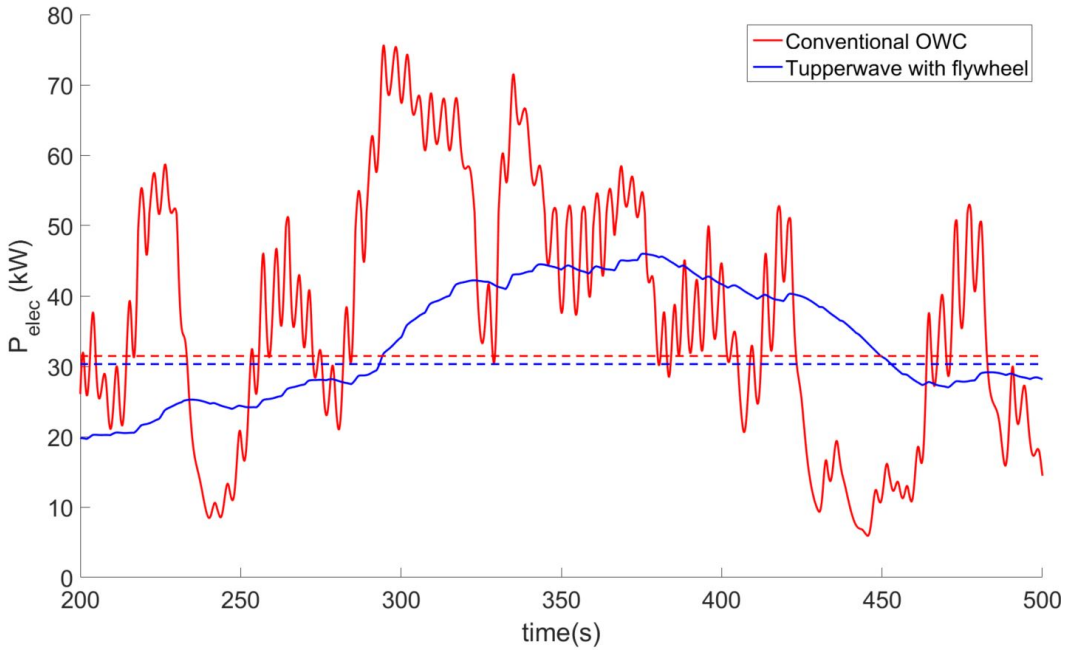


Figure F.21: Electrical power produced by the conventional OWC and Tupperwave device (case 2) in sea state ($H_s = 3\,\mathrm{m}$; $T_p = 9\,\mathrm{s}$). A flywheel of inertia 36.3 N·m$^2$ was added to the Tupperwave power-take off (PTO) so that the resulting PTO inertia is the same as in the conventional OWC. Solid lines: Time series; dash lines: Average values.

Finally, Figure F.22 displays the average power available at the different stages of the power conversion chain and for the three Tupperwave valves cases displayed in Table F.4. It is clear that the efficiency of the Tupperwave device depends on the efficiency of its non-return valves in the conversion from absorbed power to available power at the turbine. The valve efficiencies are of 63.7%, 77.9% and 96.9% for cases 1–3, respectively. The Tupperwave device outperforms the conventional OWC in terms of electrical power production only if the non-return valves efficiency is greater than 80%. Case 3 corresponds to the best possible case tested with valve efficiencies close to 100%. In that case, the Tupperwave device produces 18% more electrical power than the conventional OWC.

### F.5.2 Yearly Power Performance Comparison

A large number of simulations were run to assess and compare the device power performances on the EMEC wave energy test site in a one year time period. The comparison is based on several criteria listed below:

- Annual electrical power production.

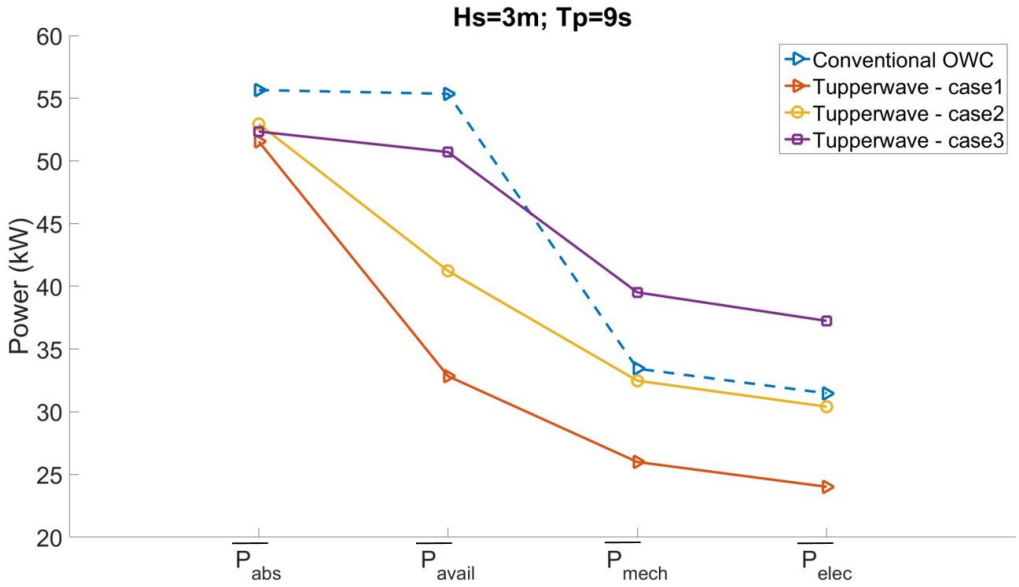


Figure F.22: Average power along the power conversion chain of the conventional OWC and Tupperwave device in sea state ($H_s = 3\,\text{m}$ ; $T_p = 9\,\text{s}$).

- Electrical power fluctuation.
- Use of the security system (bypass valve).

The level of electrical power fluctuation f around its average value is calculated as the standard deviation normalised by the average value:

$$f = \frac{1}{\overline{P}} \sqrt{\frac{1}{t_f} \int_0^{t_f} \left(P(t) - \overline{P}\right)^2 dt} \tag{F.21}$$

Table F.5 compares the devices' performances over a year in the EMEC test site. The performances of the Tupperwave device were assessed with the three different valve characteristics (see Table F.4) and also when equipped with a flywheel providing the Tupperwave PTO the same inertia as the conventional OWC PTO.

Table F.5: Devices performances over a year in the EMEC test site.

| | **Tupperwave** | | | | **Conventional OWC** |
|---|---|---|---|---|---|
| Valve characteristics | case 1 | case 2 | case 3 | case 2 | - |
| Flywheel inertia (N·m$^2$) | - | - | - | 36.3 | - |
| Annual electrical production (MWh) | 70.6 | 97.6 | 119.5 | 99.3 | 99.9 |
| Average power fluctuation (%) | 64.9 | 55.0 | 55.1 | 23.2 | 70.2 |
| Annual pneumatic energy dissipated in bypass valves (MWh) | 0.009 | 0.051 | 0.619 | 0.012 | 0.582 |
| Bypass valve opening per year | 44 | 287 | 3209 | 65 | 8537 |

The results show that the Tupperwave device in case 2 produces very similar electrical power on all sea states to the conventional OWC. Figure F.23 displays the amount of electrical energy produced by the Tupperwave device (case 2) in each sea state over a year. The results obtained for the conventional OWC being very similar, it is not represented here. As mentioned for the dimensioning of turbine-generator system in Section F.3, the most producting sea states over the year are $H_s = 2$–$3\,\text{m}$ and $T_p = 8$–$9\,\text{s}$.

The values of average power fluctuations displayed in Table F.5 are obtained for the most productive sea states. As illustrated in Figure F.20, the result indicates that the electrical power delivered by the Tupperwave device is smoother than the conventional OWC in all cases. In addition to enabling the turbine to work close to maximum efficiency, the short term pneumatic power storage mechanism using air compressibility in the HP and LP chambers of the Tupperwave device contributes to the enhancement of power quality by mitigating the power fluctuations.

As a result of the smoother electrical power output, the Tupperwave device requires less use of the security system to protect its generator. At equal power production, the bypass valve opens 30 times less often over a year in in the Tupperwave device (case 2) than in the conventional OWC. This naturally leads to greater generator and power electronics longevity and reduces the risks of failure of the security system. Smoother operation of the turbine and generator also result in less fatigue and hence higher reliability of the system. Figure F.24 shows on which sea states the use of the bypass valve is required by displaying the amount of pneumatic power dissipated in the bypass valve per year in each sea state for Tupperwave (case 2) and the conventional OWC. To reduce the use of the bypass valve by the conventional OWC, the generator rated power can be increased but this would reduce its efficiency in most sea states, see Figure G.6. The total amount of pneumatic power dissipated through the bypass valve is, however, small compared to the yearly production.

The addition of a flywheel to the Tupperwave PTO so that its inertia equals the inertia of the conventional OWC PTO (case 2 with flywheel) is very

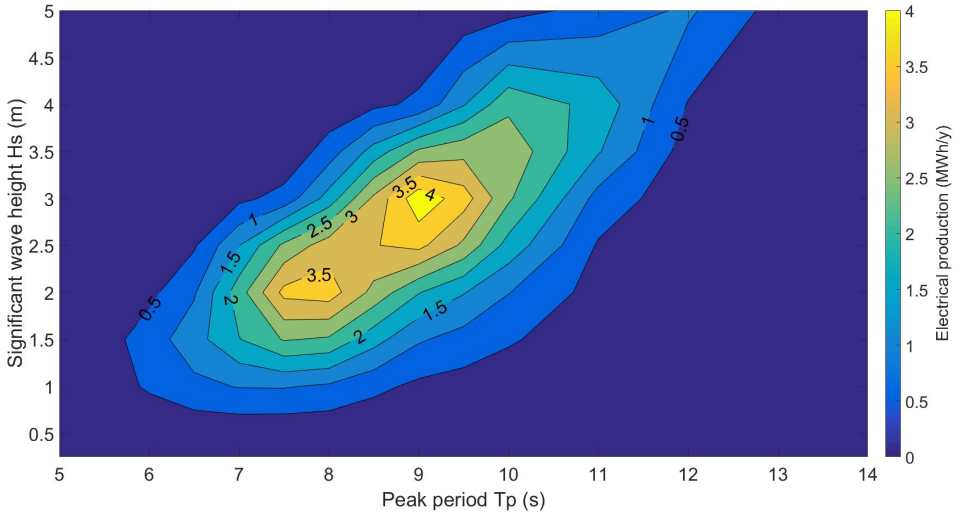


Figure F.23: Electrical energy production on all sea states of the EMEC wave energy test site over a year by the Tupperwave (case 2). Quasi-identical figure is obtained for the conventional OWC device.

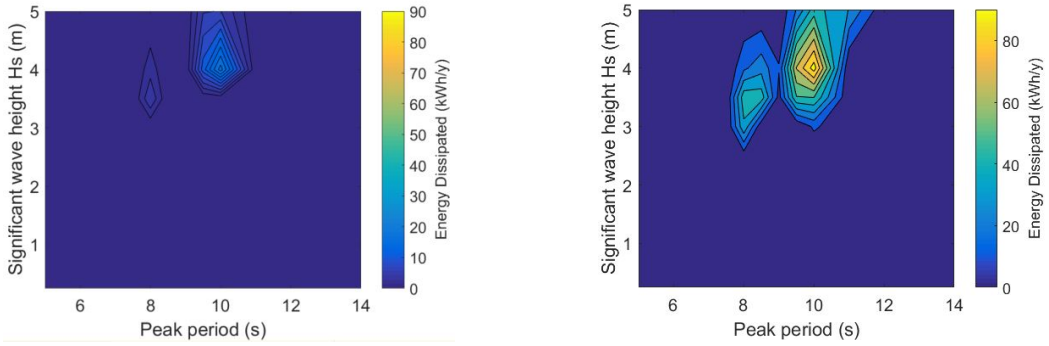


(a) Tupperwave: Case 2

(b) Conventional OWC

Figure F.24: Pneumatic power dissipated in the bypass valve in each sea state per year.

profitable in terms of electrical power quality: The average electrical power fluctuations are considerably reduced and thus, the use of the bypass valve is also reduced. A slight increase in annual electrical production is also observed. This increase is due to the larger production in low energy sea states ($H_s = 1$–$2$ m) where the device benefits from having a more inertial PTO.

The results show that the Tupperwave device can compete with the conventional OWC provided that the non-return valves are correctly designed to be sufficiently efficient. Low opening pressure and large effective opening area are required. The physical feasibility and practicability of such non-return valves with adequate efficiency, however, remains to be proven.

## F.6 Conclusions

In this research, the time-domain wave-to-wire models of the innovative Tupperwave device and corresponding conventional OWC were built. The two devices use the same floating spar buoy structure. The hydrodynamic equations are based on the linear wave theory and the thermodynamic processes are assumed isentropic. The two devices are equipped with the same floating structure geometry, turbine rotor geometry, generator and control law.

In a previous publication [133], the numerical models from wave to pneumatic power had been validated against tank testing experiments. In this paper, the conversion from pneumatic to electrical power was studied and validated against Hardware-in-the-Loop experiments, completing the validation of the entire power conversion chain. Their power performances in the EMEC wave energy test site were assessed using the validated wave-to-wire models after optimisation of their turbine-generator systems.

The methodology for dimensioning the turbine-generator systems to the wave climate of the test site was detailed and can be applied to similar design problems. The turbine used in the Tupperwave device is half the size of the turbine used in the conventional OWC and is also less mechanically complex. It is therefore likely to be cheaper. However, its high rotational speed requires the use of a mechanical gearbox which is associated with undesirable reliability and maintenance issues. The use of the gearbox could be avoided with a different turbine design.

The comparison of the device power performances allowed the assessment of the Tupperwave device concept against the conventional OWC. Due to its working principle, the Tupperwave device produces smooth pneumatic power across its turbine, allowing this latter to work close to maximum efficiency at all times. In the end, and despite its small PTO inertia, the Tupperwave device produces a smoother electrical power than the conventional OWC, enhancing power quality. This reduces the peak-to-average power ratio and hence requires less use of the security system that protects the generator from power peaks. The smoother operation is likely to have a positive impact on the system reliability. The power quality enhancement becomes particularly remarkable if the Tupperwave PTO inertia is increased to the same level as the conventional OWC PTO inertia. In terms of power production, if the non-return valves dissipate less than 20% of the absorbed wave power, the Tupperwave device can outperform the conventional OWC by up to 20%. Such performance is achievable with sufficiently low opening pressure and a sufficiently large effective opening area of the valves. Further research on the Tupperwave concept should focus on the physical feasibility and reliability of such non-return valves in order to enable definitive conclusions on the relevance of the concept.

The use of the isentropic relationship between air density and pressure for the modelling of the Tupperwave device, in spite of the irreversible thermo-

dynamic processes, represents a limit to the present study. A non-isentropic study of the Tupperwave device will be undertaken in future works to accurately model these processes.

## Acknowledgement

The authors would like to thanks Bàrbara S. Lopes for kindly sharing the results of her experimental work on the twin-rotor turbine.

# Appendix G

# Paper G

# Non-isentropic study of a closed-circuit oscillating-water-column wave energy converter

*Published in*

Ocean Engineering, Elsevier

*Authors*

Pierre Benreguig[1], Miguel Vicente[2], Sarah Crowley[2], Jimmy Murphy[1]

[1]*MaREI Centre (ERI), University College Cork, Haulbowline Road, Ringaskiddy, Ireland*
[2]*WavEC - Offshore Renewables, Rua Dom Jerónimo Osório, nº. 11, 1º, 1400-119 Lisboa, Portugal*

# Abstract

The thermodynamics of the air inside a conventional Oscillating Water Column (OWC) is commonly modelled using the isentropic relationship between pressure and density. The innovative Tupperwave device is based on the OWC concept but uses non-return valves and two extra reservoirs to rectify the flow into a smooth unidirectional air flow harnessed by a unidirectional turbine. The air, flowing in closed-circuit, experiences a temperature increase due to viscous losses across the valves and turbine along the repetitive cycles of the device's operation. In order to study this temperature increase which represents a potential issue for the device operation, a non-isentropic wave-to-wire model of the Tupperwave device is developed taking into account the irreversible thermodynamic processes. The model is based on the First Law of Thermodynamics, and accounts for viscous losses at the valves and turbine as well as solar radiation and heat transfer across the device walls and inner free-surface. The results reveal that the temperature increase in the device remains harmless for its operation. The difference between the power performance of the Tupperwave device based on the non-isentropic and isentropic models is found to be relatively small. Its performance are also compared to the corresponding conventional OWC device.


## G.1 Introduction

Oscillating Water Column (OWC) devices are amongst the most promising types of wave energy converters because of their relative simplicity. In the most conventional sort of OWC devices, the OWC chamber is open to the atmosphere through a self-rectifying turbine. The pressure variations in the OWC chamber create a bidirectional air flow across the turbine which is able to convert energy regardless the direction of the flow. Several types of self-rectifying turbines have been developed for OWCs with various working principles, advantages and drawbacks. An extensive review of such turbines can be found in [9]. The best performing self-rectifying turbines are the bi-radial and twin-rotor turbines which reach respectively about 79% and 74% efficiency [144, 60] in steady flow conditions. Self-rectifying turbines are not as efficient as conventional unidirectional air turbines which may attain peak efficiencies close to 90% in steady flow conditions. The use of a unidirectional turbine in an OWC device is possible using non-return valves to create a unidirectional flow driven by the motion of the OWC. Various OWC devices using a unidirectional turbine have been studied and different methods for rectifying the air flow were considered. Among those devices, there are for example the Masuda's navigation buoy [9] and the vented OWC from Wave Swell Energy [49]. These devices are opened to the atmosphere like in a conventional OWC, whereas other devices such as the Tupperwave device work

in closed-circuit.

In the Tupperwave device, a pressure differential is built between two accumulator chambers using the motion of the water column and non-return valves, in a similar way to a hydraulic circuit. Air compressibility in the large fixed volume accumulator chambers is used to store pneumatic energy which is then released smoothly across a unidirectional turbine located between the two chambers. Wave-to-wire numerical models of the Tupperwave device and of the corresponding conventional OWC device, displayed in figure G.1, were developed in [135] and [133] to assess and compare their performances. The results showed that the performance of the non-return valves is of critical importance for the Tupperwave device to compete with the conventional OWC. The thermodynamics in the devices was modelled using the linearized isentropic relationship between pressure and density in the different chambers of the device and the results were validated against model scale experimental tests.

In a conventional OWC converter the air is partly renovated once in a wave cycle (a few seconds). This prevents the averaged inner air temperature from differing significantly from the outer air temperature. As it was shown in [68], despite non-reversible processes such as viscous losses across the turbine, the use of the linearised isentropic relationship between pressure and density provides a satisfactory approximation and simplifies the numerical modelling of conventional OWC devices. This simplifying assumption is therefore commonly used in the numerical modelling of conventional OWC devices [113, 152]. The situation is different in the Tupperwave device where the air flows in closed-circuit. The energy dissipation at the non-return valves and at the imperfectly efficient turbine is likely to increase the entropy and temperature of the inner air. The validity of the isentropic assumption for the modelling of the Tupperwave device at full scale is therefore questionable. Moreover, the increase of air temperature in the device potentially represents a risk for the device operation. This potential issue, common to all closed-circuit OWC devices, and associated with others issues related to the use of non-return valves (such as cost and reliability), discouraged many developers from taking this technology further. The present study develops for the first time a non-isentropic numerical model for a closed-circuit OWC and investigates the air temperature increase in the Tupperwave device.

In section G.2 and G.3, the non-isentropic models of the Tupperwave device and corresponding OWC device (figure G.1) are developed, taking into account irreversible thermodynamic processes such as the energy dissipation in the turbine and the valves, the heat exchanges between the inner air and the environment, and the solar radiations. In section G.4, the air temperature evolution in the different chambers and the energy flows in the Tupperwave device are analysed. Finally, isentropic and non-isentropic model results are compared in order to conclude on the reliability of the isentropic simplification.

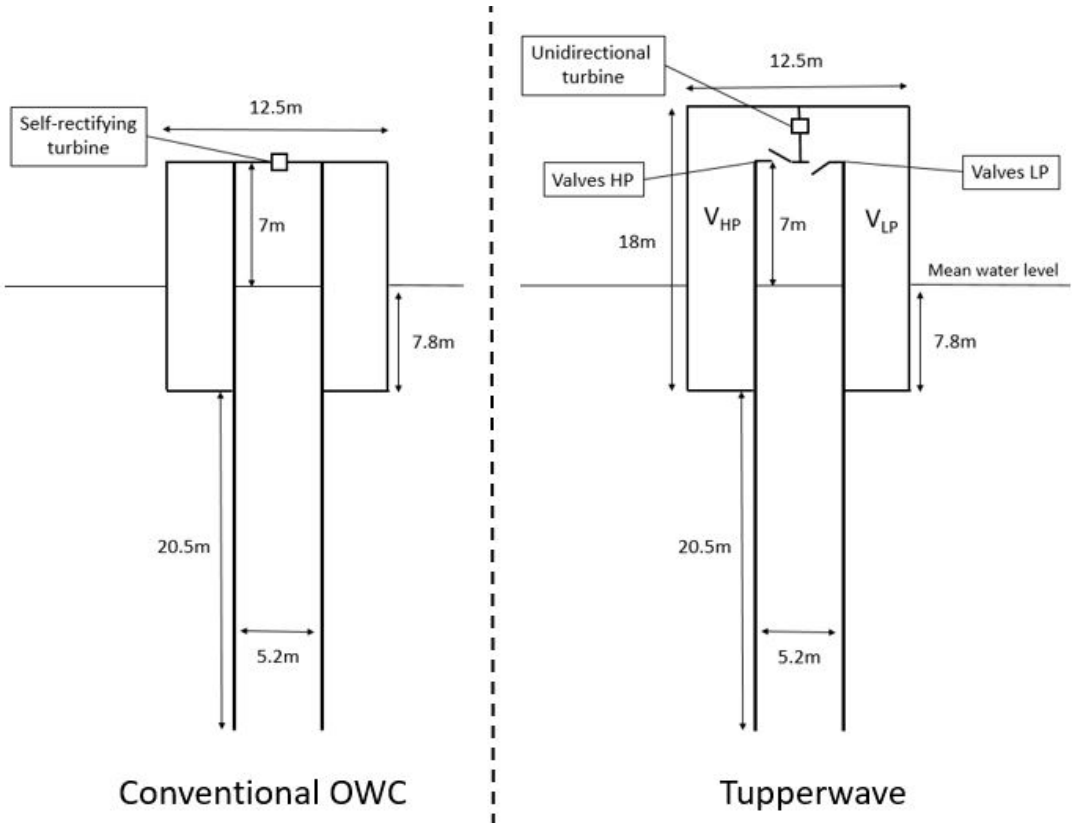


Figure G.1: 2D schematic of the full scale conventional OWC and Tupperwave devices

## G.2 Tupperwave non-isentropic model

In this section, a non-isentropic model of the Tupperwave device is developed based on the wave-to-wire model built in [133]. The thermodynamic component of the model is largely revised to account for the irreversible thermodynamic processes. The other components of the model, although quasi-identical, are also briefly described to allow this publication to be read independently from the previous one.

### G.2.1 Hydrodynamics

For the hydrodynamic modelling of the device, the two-body approach described in [80] is adopted: the first rigid body is the spar buoy structure and the second rigid body is an imaginary thin piston at the internal free surface. Both bodies are considered as rigid bodies moving only in heave due to the action of the waves. The model is based on linear wave theory. The motion of both bodies in a wave field may be modelled in the time domain applying the Cummins equation, with subscript 1 for the buoy and subscript 2 for the

piston:

$$\begin{cases} [m_1 + A_{11}(\infty)]\ddot{x}_1(t) + A_{12}(\infty)\ddot{x}_2(t) + I_{11} + I_{12} + c_1 x_1(t) = f_1(t) + f_p(t) + f_{d1}(t) \\ A_{21}(\infty)\ddot{x}_1(t) + [m_2 + A_{22}(\infty)]\ddot{x}_2(t) + I_{21} + I_{22} + c_2 x_2(t) = f_2(t) - f_p(t) + f_{d2}(t) \end{cases} \tag{G.1}$$

where $m_i$ are the bodies masses; $c_i$ are the hydrostatic stiffness terms and are calculated as $c_1 = \rho_w g S_1$ and $c_2 = \rho_w g S_2$, where $\rho_w$ is the water density, $g$ is the acceleration of gravity, $S_1$ is the cross sectional area of body 1 defined by the undisturbed sea surface and $S_2$ is the area of the OWC free surface; $A_{ij}(\infty)$ are the bodies heaving added masses at infinite frequency (including the proper and crossed modes); $f_p$ is the reciprocating pressure force acting on both bodies and is calculated as $f_p = S_2 p_{owc}(t)$ where $p_{owc}$ is the excess pressure relatively to atmospheric pressure built in the OWC chamber. The terms $I_{ij}$ are called memory effect terms and are convolution integrals:

$$I_{ij} = \int_0^t K_{ij}(t-\tau)\dot{x}_j(t)d\tau \tag{G.2}$$

where $K_{ij}$ are the impulse functions for heave motions and their interactions. $f_i$ are the wave excitation forces acting on the two bodies and are calculated as:

$$f_i(t) = \int_0^t K_{ex,i}(t-\tau)\eta(t)dt \tag{G.3}$$

where $\eta$ is the external wave elevation and $K_{ex,i}$ is the excitation force impulse response function for body $i$.

The viscous drag forces $f_{d1}$ and $f_{d2}$ are calculated as $f_{di} = -C_{di}|\dot{x}_i(t)|\dot{x}_i(t)$, where $C_{di}$ is the equivalent drag coefficient. The coefficients $C_{d1} = 150$ N.s$^2$.m$^{-2}$ and $C_{d2} = 40$ N.s$^2$.m$^{-2}$ were found in [135] to provide the best fit between the vertical displacement of the bodies predicted numerically and the ones obtained physically. For the present study, this values are converted to full scale using the Froude scaling similarity. All the hydrodynamic coefficients $A_{ij}(\infty)$, $K_{ij}$, $K_{ex,i}$ were computed in the frequency domain using WAMIT [129], a commercial Boundary-Element-Method software.

The volume of the OWC chamber is calculated as: $V_{owc} = V_0 + S_2(x_1 - x_2)$. The variations of $V_{owc}$ are related to variations in $p_{owc}$. System of equations G.1 needs to be completed by thermodynamic considerations.

### G.2.2 Thermodynamics

In this section, the general thermodynamic equations ruling an open air chamber are derived assuming consecutively non-isentropic and isentropic assumptions. The non-isentropic model is then applied to the modelling of the Tupperwave device.

#### G.2.2.1 General equations

We consider the following open thermodynamic system: an air chamber of volume $V$ containing a mass $m$ of air with density $\rho = \frac{m}{V}$, at the temperature $T$ and at pressure $p_{atm} + p$. $w_{in}$ and $w_{out}$ are the air mass flow rates, respectively, in and out of the chamber and are functions of the air excess pressure $p$. It is assumed that the transformations are slow enough for the thermodynamic state of air in the chamber to be uniform. The air is assumed as a perfect and dry gas of constant specific heat capacities $c_v$ and $c_p$.

##### G.2.2.1.1 Non-isentropic equations

The first thermodynamic principle applied to the open system gives [152]:

$$\dot{E} = \dot{U} + \dot{E}_c + \dot{E}_p = \dot{W} + \dot{Q} + \dot{H}_{in} - \dot{H}_{out} \tag{G.4}$$

where $E$ is the energy of the system; $U$ is the internal energy; $E_c$ and $E_p$ are the kinetic and potential energy; $\dot{W}$ is the mechanical power provided to the system by the motion of the walls; $\dot{Q}$ is the rate of heat transfer provided to the system; $\dot{H}_{in}$ and $\dot{H}_{out}$ are the enthalpy flow rates due to exchange of matter coming in and out of the system.

The variations of the system kinetic and potential energy are neglected. Equation G.4 therefore becomes:

$$\frac{d}{dt}\left(c_v m T\right) = -\left(p_{atm} + p\right)\dot{V} + \dot{Q} + c_p w_{in} T_f - c_p w_{out} T \tag{G.5}$$

where $\rho_f$ and $T_f$ are the density and temperature of the incoming air.

The Mayer's equations are:

$$\begin{cases} c_p - c_v = R & (a) \\ \frac{c_p}{c_v} = \gamma & (b) \end{cases} \tag{G.6}$$

where $R$ is the specific ideal gas constant. The ideal gas law is:

$$p_{atm} + p = \rho R T \tag{G.7}$$

and its derivative gives:

$$\dot{p} = \dot{\rho} R T + \rho R \dot{T} \tag{G.8}$$

The mass balance equation gives:

$$\dot{m} = \rho \dot{V} + \dot{\rho} V = w_{in} - w_{out} \tag{G.9}$$

Finally, equations G.5, G.6.a,b, G.7, G.8 and G.9 lead to the non-isentropic model of the system:

$$\begin{cases} \dot{m} = w_{in} - w_{out} & (a) \\ \dot{p} = \dfrac{\gamma(p_{atm} + p)}{m}\left(\dfrac{\dot{Q}}{c_p T} + w_{in}\dfrac{T_f}{T} - w_{out} - \rho\dot{V}\right) & (b) \end{cases} \tag{G.10}$$

System of equations G.10.a,b was obtained from the 1st Thermodynamic principle and displays the general equations relating mass, density, pressure and volume of the air considered as a perfect gas in an open system during non-isentropic transformations. In this model, the specific entropy of the system is likely to change due to the irreversible processes across the valves and turbine and to the heat transferred across the boundaries of the system.

#### G.2.2.1.2 Isentropic equations

If the system is considered adiabatic and the transformations are slow enough to be reversible, the transformations become isentropic and consequently we may write:

$$\rho = \rho_{atm} \left( \frac{p_{atm} + p}{p_{atm}} \right)^{\frac{1}{\gamma}} \tag{G.11}$$

Equation G.11 once derivated gives:

$$\dot{\rho} = \frac{\rho_{atm} \dot{p}}{\gamma p_{atm}} \left( \frac{p_{atm} + p}{p_{atm}} \right)^{\frac{1}{\gamma} - 1} \tag{G.12}$$

Equation G.12 combined with equation G.9 and G.11 leads to the isentropic model of the system:

$$\dot{p} = \frac{\gamma (p_{atm} + p)}{m} (w_{in} - w_{out} - \rho \dot{V}) \tag{G.13}$$

Equation G.13 displays the equations relating mass, density, pressure and volume of the air considered as a perfect gas in an open system during isentropic transformations. Unlike in the non-isentropic system G.10, the mass of air in the chamber $m = \rho V$ and the excess pressure $p$ are directly related by the equation G.11. Hence a single differential equation is necessary. We note that equation G.13 can be obtained from G.10.b by adding the adiabatic assumption ($\dot{Q} = 0$) and further assume no temperature difference between inner and outside air ($T_f = T$).

#### G.2.2.1.3 Linearised isentropic equations

Moreover, in the case where the excess pressure remains small compared to the atmospheric pressure, it is possible to linearise the isentropic relationship between density and pressure. Once linearised, equation G.11 leads to:

$$\rho = \rho_{atm} \left( 1 + \frac{p}{\gamma p_{atm}} \right) \tag{G.14}$$

and to:

$$\dot{\rho} = \frac{\rho_{atm}}{\gamma p_{atm}} \dot{p} \tag{G.15}$$

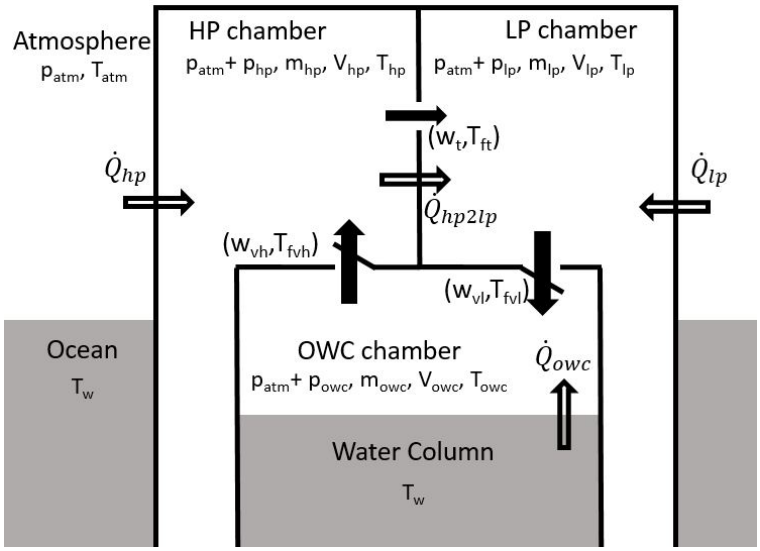


Figure G.2: Tupperwave device schematic with thermodynamic variables

Finally, the linearised isentropic system of equations relating mass, density, pressure and volume of the system is:

$$\dot{p} = \frac{\gamma p_{atm}}{\rho_{atm} V}(w_{in} - w_{out} - \rho \dot{V}) \tag{G.16}$$

Depending on the feasible assumptions and on the level of accuracy desired, equations G.10.a,b, or G.13 or G.16 can be directly applied for the modelling of the thermodynamic happening in OWC type wave energy devices air chambers. In this paper, the non-isentropic model (system of equations G.10) will be used to model the thermodynamic happening in the Tupperwave device.

### G.2.2.2 Tupperwave thermodynamics

Figure G.2 displays a schematic of the 3 chambers of the Tupperwave device and their thermodynamic variables. Solid arrows represent mass flow of air and hollow arrows represent heat exchanges through the walls. Exchanges are counted positive in the direction of the arrows. Each chamber of the device is modelled as an open thermodynamic system. The non-isentropic system of equations G.10.a,b is therefore applied to each of the three chambers.

In the following paragraphs, the heat transfer rates, mass flow rates and flow temperatures at the exit of the turbine and valves are mathematically expressed as functions of the temperatures and pressures in the different chambers.

#### G.2.2.2.1 Heat exchanges

In the event of air temperature increase in the device, thermal exchanges through the walls of the device need to be considered. Due to the large surface area of the walls, exchanges between the HP and LP chambers and the exterior (atmosphere and water) are considered. HP and LP chambers also exchange heat across the separation wall. Heat transfers through the walls between the OWC chamber and the two other chambers are neglected because of the smaller common wall surface. Heat is also exchanged between the air contained in the OWC chamber and the water.

The device's walls are considered homogeneous and separate either air and water, or air and air at different temperatures. The heat transfer from a fluid 1 to a fluid 2 across a wall results of a combination in series of convection mechanisms from the fluids to the wall surfaces and conduction mechanism across the wall. To evaluate the heat transfer rate, a steady one-dimensional heat exchange model in the normal direction to the wall's surface is adopted, as displayed in figure G.3. The precise study of the transient state requires to solve the unsteady heat conduction equation across the wall which would increase the mathematical complexity of the problem and was not considered by the authors. The steady state assumption will be verified in section G.4 depending on the wall's material. The overall heat transfer coefficient between fluid 1 and 2 is therefore defined as [145]:

$$K_{1-2} = \frac{1}{\frac{1}{h_1} + \frac{l}{k} + \frac{1}{h_2}} \tag{G.17}$$

where $h_1$ and $h_2$ are the fluids convective heat transfer coefficients, $l$ and $k$ are the thickness and heat conductivity of the wall. The heat transfer rate resulting from conduction and convection through the wall of area $A$, between fluid 1 at temperature $T_1$ and fluid 2 at temperature $T_2$ takes the form:

$$\dot{Q}_{1\to 2} = K_{1-2} A \left(T_1 - T_2\right) \tag{G.18}$$

Radiative heat transfer from the sun may play an important role in sunny days. To account for solar radiation on the device, the equivalent sol-air temperature method is used. $T_{sol-air}$ is the outside air temperature for which, in the absence of heat radiation, the external environment delivers the same heat flux to the wall surface. If the wall surface in contact with fluid 1 is exposed to sun radiation, $T_{1,sol-air}$ can be calculated as [153]:

$$T_{1,sol-air} = T_1 + \frac{\alpha I_t}{h_1} \tag{G.19}$$

where $\alpha$ the material absorptivity and $I_t$ is the total solar irradiation. Hence, the total heat transfer rate across the wall is simply calculated as:

$$\dot{Q}_{1\to 2} = K_{1-2} A \left(T_{1,sol-air} - T_2\right) \tag{G.20}$$

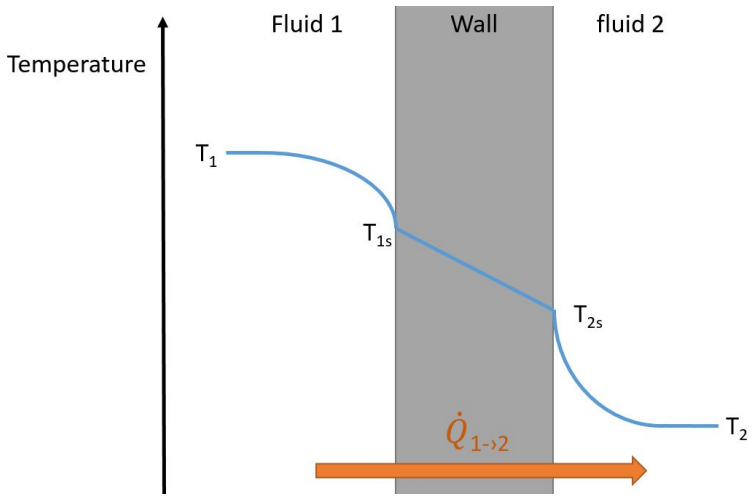


Figure G.3: One-dimensional temperature evolution across a wall separating two fluids at different temperatures

The outside wall surface area of the HP chamber and LP chamber are approximately $A_{hp} = A_{lp} = 400\,\mathrm{m}^2$. For each chamber, about half of their outside wall surface area is in contact with water, and the other half is in contact with air. The wall surface area of the device exposed to solar radiation is a function of the sun position and device orientation. For simplicity it is assumed that only the outside wall surface of the HP chamber in contact with air is exposed to the solar irradiation $I_t$. Thus, we write:

$$\dot{Q}_{hp} = K_{a-a}\frac{A_{hp}}{2}\left(T_a + \frac{\alpha I_t}{h_a} - T_{hp}\right) + K_{w-a}\frac{A_{hp}}{2}\left(T_w - T_{hp}\right) \tag{G.21}$$

$$\dot{Q}_{lp} = K_{a-a}\frac{A_{lp}}{2}\left(T_a - T_{lp}\right) + K_{w-a}\frac{A_{lp}}{2}\left(T_w - T_{lp}\right) \tag{G.22}$$

$$\dot{Q}_{hp2lp} = K_{a-a}A_{hp2lp}\left(T_{hp} - T_{lp}\right) \tag{G.23}$$

where the subscribes $a$ and $w$ respectively refer to the atmospheric air and the ocean water. Atmospheric and ocean temperatures $T_a$ and $T_w$ are assumed constant. $A_{hp2lp} = 135\,\mathrm{m}^2$ is the surface area of the wall separating the HP chamber from the LP chamber.

The convective heat transfer between the air in the OWC chamber and the internal water surface is calculated as:

$$\dot{Q}_{owc} = h_{aw}S\left(T_w - T_{owc}\right) \tag{G.24}$$

where $h_{aw}$ is the convective heat transfer coefficient between air and water and $S$ is the internal water surface area.

#### G.2.2.2.2 Turbine

To assess the temperature of the flow at the exit of the turbine, we consider the real expansion process happening across the turbine from the stagnation

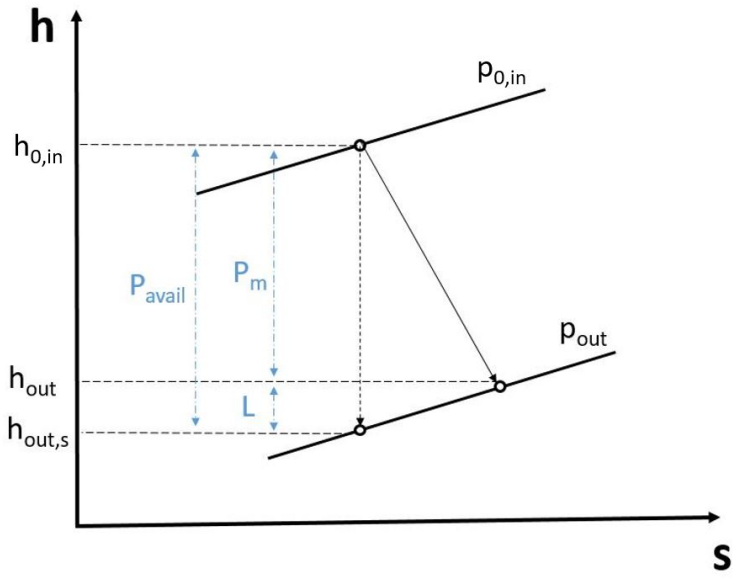


Figure G.4: Specific entropy-enthalpy diagram for the turbine

pressure $p_{0,in}$ at the inlet to the static pressure $p_{out}$ at the outlet. The entropy-enthalpy diagram is shown in figure G.4 where perfect (dashed-arrow) and real (full arrow) expansions are represented between the two isobaric lines. The kinetic energy at the entrance of the turbine is neglected and the kinetic energy in the exhaust gases is not contributing to the total useful energy at the turbine. The total-to-static efficiency of the turbine is therefore defined as:

$$\eta_t = \frac{P_m}{P_{avail}} = \frac{h_{0,in} - h_{out}}{h_{0,in} - h_{out,s}} \tag{G.25}$$

where $P_{avail}$ is the available power to the turbine (defined as the power output of a perfectly efficient turbine), $P_m$ is the power converted by the actual turbine into mechanical power, $h_{0,in}$ is the stagnation specific enthalpy at the entrance of the turbine, $h_{out}$ is the specific enthalpy at the exit of the turbine, and $h_{out,s}$ is the specific enthalpy at the exit of the turbine if the expansion were perfect (i.e. isentropic). The turbine losses are dissipated into heat and are calculated as:

$$L_t = P_{avail} - P_m = P_{avail}(1 - \eta_t) = w_{in}(h_{out} - h_{out,s}) \tag{G.26}$$

The air is considered as a perfect gas and so $dh = c_p dT$. Equation G.26 can be written as:

$$L_t = w_{in} c_p (T_{out} - T_{out,s}) \tag{G.27}$$

i.e.

$$T_{out} = T_{out,s} + \frac{L_t}{c_p w_{in}} \tag{G.28}$$

The temperature of the flow at the exit of the isentropic expansion is calculated using the well-known isentropic relationship:

$$T_{out,s} = T_{in}\left(\frac{p_{out}}{p_{0,in}}\right)^{\frac{\gamma-1}{\gamma}} \tag{G.29}$$

Applying equations G.28 and G.29 to the expansion from the HP to the LP chamber across the turbine leads to the expression of the air temperature at the exit of the turbine and entering the LP chamber:

$$T_{ft} = T_{hp}\left(\frac{p_{atm}+p_{lp}}{p_{atm}+p_{hp}}\right)^{\frac{\gamma-1}{\gamma}} + \frac{L_t}{c_p w_t} \tag{G.30}$$

The mass flow rate across the turbine now needs to be expressed. The model of the radial-inflow turbine used in this paper is taken from the literature and was obtained with a rotor of 500mm at rotational speeds between 700 and 1300rpm. The Reynolds number ranged between $9.2 \times 10^5$ and $2.1 \times 10^6$ and the Mach number did not exceed 0.1 [60]. In this conditions, the flow can be considered as incompressible. In this paper, the Tupperwave device is equipped with same turbine diameter (see table G.1 in section G.4) but the rotational speeds considered are 4 times higher. Changes in Reynolds and Mach number can modify the turbine performances: a higher Reynolds number may modify the turbulent behaviour of the flow and compressibility effects may be introduced if the Mach number rises above 0.3. In what follows, Mach and Reynolds number effects are ignored and the flow through the turbine is considered as approximately incompressible. Thus, the performance of the turbine can be presented non-dimensionally and the results can be applied to a geometrically similar turbine of different size, rotating at different speed and with a fluid of different density [69].

If the flow is assumed incompressible, the turbine power output $P_m$ depends on the turbine geometry, on the turbine size (rotor diameter), on the rotational speed $\Omega$, and on the pressure head $\Delta p_t = p_{0,in} - p_{out}$ between inlet and outlet (or on the air flow rate $w_t$). The corresponding dimensionless variables are the dimensionless flow coefficient $\Phi$, dimensionless pressure head $\Psi$ and dimensionless turbine power output $\Pi$ which are defined as [9]:

$$\Phi = \frac{w_t}{\rho_{in}\Omega D^3}; \quad \Psi = \frac{\Delta p_t}{\rho_{in}\Omega^2 D^2}; \quad \Pi = \frac{P_m}{\rho_{in}\Omega^3 D^5} \tag{G.31}$$

Neglecting the influence of the Reynolds and Mach numbers, we may write:

$$\Psi = f_\Psi(\Phi)\,; \quad \Pi = f_\Pi(\Phi) \tag{G.32}$$

where the functions $f_\Psi$ and $f_\Pi$ depend only on the turbine geometry but not on size, rotational speed or fluid density. From equations G.31 and G.32, the

mass flow rate through the turbine $w_t$ and the turbine torque $T_{turb}$ can be expressed as a functions of the pressure head and the rotational speed:

$$w_t = \rho_{hp}\Omega D^3 f_\Psi^{-1}\left(\frac{p_{0,in} - p_{out}}{\rho_{in}\Omega^2 D^2}\right) \tag{G.33}$$

$$T_{turb} = \frac{P_m}{\Omega} = \rho_{hp}\Omega^2 D^5 f_\Pi\left(\frac{w_t}{\rho_{in}\Omega D^3}\right) \tag{G.34}$$

For low Mach numbers ($M < 0.3$ as during the experimental assessment of the turbine performances [60]), the flow can be considered as incompressible and the dimensionless power available to the turbine is the product of the volumetric flow rate and the pressure head. Hence, the total-to-static turbine efficiency $\eta_t$ is obtained by:

$$\eta_t = \frac{P_m}{P_{avail}} = \frac{\Pi}{\Phi\Psi} = f_\eta(\Phi) \tag{G.35}$$

The turbine works at maximum efficiency for the optimal dimensionless flow coefficient $\Phi_{opt}$.

The turbine functions $f_\Psi$ and $f_\Pi$ of the unidirectional turbine used in the Tupperwave model were established at model scale during laboratory tests described in [60, 128]. This unidirectional turbine was tested in the framework of the twin-rotor turbine development which is among the most efficient self-rectifying turbine. Being symmetrical, only half of the turbine (designated single-rotor turbine) was designed, constructed and tested in unidirectional flow at Instituto Superior Tecnico (IST), Lisbon. This single-rotor turbine is used here in the Tupperwave device. It reaches 84% maximum efficiency in constant flow condition.

#### G.2.2.2.3 Valves

The non-return valves are essential for the successful performance of the Tupperwave device [135, 122]. Valves can either be passive (check valves) or active (on/off valves). The valves considered in this paper are passive valves that require a pressure head $\Delta p_v = p_{in} - p_{out}$ larger than their opening pressure $p_{v0}$ to open. We note that each valve (HP or LP) is open only about half of the time. Therefore, the average flow rate across them when they are open is about twice as high as the average flow across the turbine. In the conditions in which the model is simulated in this paper, the Mach number of the flow across the valves sometimes rises above 0.3. Hence, the flow needs to be considered as compressible. The mass flow rates of air across the valves are calculated from their pressure head using a steady-state subsonic compress-

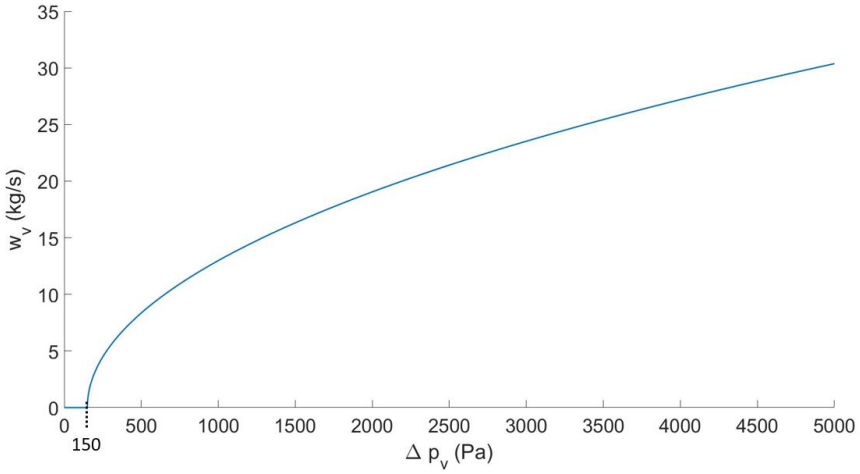


Figure G.5: Mass flow rate across the valves as function of the pressure head with an opening pressure $p_{v0} = 150Pa$. For the illustration, $\rho_{in}$ is set to atmospheric value.

ible flow model [145]:

$$w_{v,in\to out} = \begin{cases} 0 & if \quad p_{in} - p_{out} < p_{v0} \\ \alpha_d A_v \sqrt{\dfrac{2\gamma}{\gamma - 1}\rho_{in}(p_{in} - p_{v0})\left(r^{\frac{2}{\gamma}} - r^{\frac{\gamma+1}{\gamma}}\right)} & if \quad p_{in} - p_{out} > p_{v0} \end{cases} \tag{G.36}$$

where $r = \dfrac{p_{out}}{p_{in} - p_{v0}}$ is the pressure ratio over the valve when open; $A_v$ is the opening area of the valve; $\alpha_d$ is a correction coefficient called discharge coefficient, accounting for the further contraction of the flow cross-sectional area downstream of the valve opening (also called vena-contracta). As illustration, figure G.5 displays the mass flow rate across the valves as function of the pressure head, for $\rho_{in} = \rho_{atm}$. In the present work, the equivalent opening area of the valves was set to $\alpha_d A_v = 0.286\,\mathrm{m}^2$ and the opening pressure set to $p_{v0} = 150\,\mathrm{Pa}$. Further considerations on the valves characteristics, although critical for the Tupperwave performances, are not in the scope of this paper.

The expansion across the valves corresponds to a throttling process and is fundamentally irreversible as the exit kinetic energy is dissipated. No work is done on or by the air and the expansion therefore happens at constant enthalpy [154]: $h_{in} = h_{out}$, i.e. for a perfect gas $T_{in} = T_{out}$. Thus, using the ideal gas law, we have:

$$T_{fvh} = T_{owc} = \frac{(p_{atm} + p_{owc})V_{owc}}{m_{owc}R} \quad \text{and} \quad T_{fvl} = T_{lp} = \frac{(p_{atm} + p_{lp})V_{lp}}{m_{lp}R} \tag{G.37}$$

Finally, we have obtained the mathematical expressions of the heat trans-

fers across the walls, the mass flow rates across the turbines and valves and their exit temperatures as functions of the pressures, volumes and masses of air in each chamber. Equations from system G.10 can be directly applied to each of the three chambers of the Tupperwave device, thus obtaining the non-isentropic thermodynamic model of the device:

$$\begin{cases} \dot{m}_{owc} = w_{lp} - w_{hp} \\ \dot{m}_{hp} = w_{hp} - w_t \\ \dot{m}_{lp} = w_t - w_{lp} \\ \dot{p}_{owc} = \dfrac{\gamma(p_{atm} + p_{owc})}{m_{owc}} \left( \dfrac{\dot{Q}_{owc}}{c_p T_{owc}} + w_{vl} \dfrac{T_{lp}}{T_{owc}} - w_{vh} - \rho_{owc} \dot{V}_{owc} \right) \\ \dot{p}_{hp} = \dfrac{\gamma(p_{atm} + p_{hp})}{m_{hp}} \left( \dfrac{\dot{Q}_{hp} - \dot{Q}_{hp2lp}}{c_p T_{hp}} + w_{vh} \dfrac{T_{owc}}{T_{hp}} - w_t \right) \\ \dot{p}_{lp} = \dfrac{\gamma(p_{atm} + p_{lp})}{m_{lp}} \left( \dfrac{\dot{Q}_{lp} + \dot{Q}_{hp2lp}}{c_p T_{lp}} + w_t \dfrac{T_{ft}}{T_{lp}} - w_{vl} \right) \end{cases} \tag{G.38}$$

### G.2.3 Generator model and control law

The last differential equation of the model is given by the Newton's law applied on the generator rotor:

$$I\dot{\Omega} = T_{turb} - T_{gen} \tag{G.39}$$

where $I$ is the inertia of the turbine-generator system; $T_{gen}$ is the electromagnetic braking torque of the generator and $T_{turb}$ is given in equation G.34.

A Maximum Power Point Tracking (MPPT) control strategy is applied to control the generator braking torque and optimise the instantaneous turbine efficiency. This control strategy was physically implemented in [133] on a rotary test rig to simulate the turbine-generator interaction.

The electromagnetic power $P_{em} = \Omega T_{gen}$ is finally converted into electricity by the generator with the efficiency $\eta_{gen}$ which depends on its load $\Lambda = \dfrac{P_{em}}{P_{rated}}$, where $P_{rated}$ is the generator rated power. The realistic generator efficiency is displayed in figure G.6 and drops very sharply for partial loads.

### G.2.4 Global numerical model and numerical integration method

The systems of differential equations G.1, G.38 and G.39 constitute the model of the Tupperwave device. Computing the solution of these equations to find the nine unknown variable $(x_1, x_2, m_{owc}, m_{hp}, m_{lp}, p_{owc}, p_{hp}, p_{lp}, \Omega)$ is made difficult by the fact that equations from the system G.1 are second-order differential equations and by the presence of the memory effect convolution integrals $I_{ij}$.

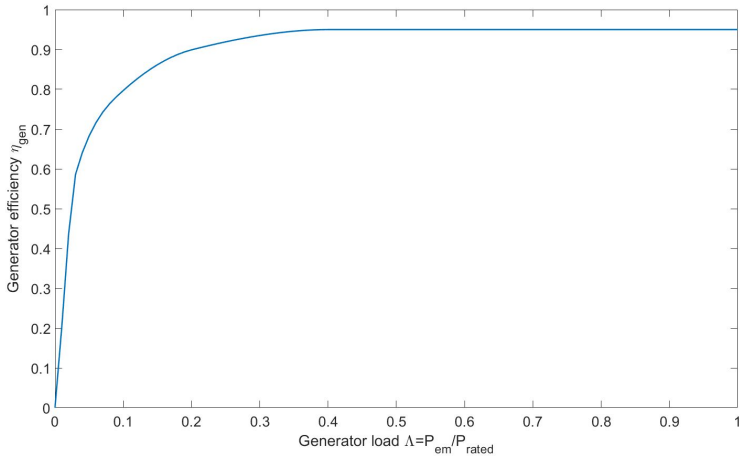


Figure G.6: Generator efficiency curve as a function of the load [71]

In the present work, the memory effect terms are approximated using a state-space representation. Each of the four convolution integrals $I_{ij}$ can be approximated by the sum of n additional state variables $I_{ij,k}$, using the Prony's method [117, 116]:

$$I_{ij} \simeq \sum_{1}^{n} I_{ij,k} \tag{G.40}$$

Each $I_{ij,k}$ is governed by an additional first order differential equation of the form:

$$\dot{I}_{ij,k} = \beta_{ij,k} I_{ij,k} + \alpha_{ij,k} \dot{x}_j \tag{G.41}$$

Moreover the two second order differential equations of the system G.1 can be reduced to first order differential equations by introducing the matrix variables $U = \begin{bmatrix} x_1 \\ x_2 \end{bmatrix}$ and $V = \begin{bmatrix} \dot{x}_1 \\ \dot{x}_2 \end{bmatrix}$.

Finally, the system of equations governing the non-isentropic wave-to-

wire model of the Tupperwave device can be expressed as:

$$\begin{cases} \dot{U} = V \\ \dot{V} = M^{-1}\left( \begin{bmatrix} f_1 \\ f_2 \end{bmatrix} + \begin{bmatrix} 1 \\ -1 \end{bmatrix} Sp_{owc} - \begin{bmatrix} \sum_1^n I_{11,k} + \sum_1^n I_{12,k} \\ \sum_1^n I_{21,k} + \sum_1^n I_{22,k} \end{bmatrix} - \begin{bmatrix} C_{d1} \\ C_{d2} \end{bmatrix} .V.|V| - \begin{bmatrix} c_1 \\ c_2 \end{bmatrix} .U \right) \\ \dot{I}_{11,k} = \beta_{11,k} I_{11,k} + \alpha_{11,k} \dot{x}_1, \qquad k = 1:n \\ \dot{I}_{12,k} = \beta_{12,k} I_{12,k} + \alpha_{12,k} \dot{x}_2, \qquad k = 1:n \\ \dot{I}_{21,k} = \beta_{21,k} I_{21,k} + \alpha_{21,k} \dot{x}_1, \qquad k = 1:n \\ \dot{I}_{22,k} = \beta_{22,k} I_{22,k} + \alpha_{22,k} \dot{x}_2, \qquad k = 1:n \\ \dot{m}_{owc} = w_{lp} - w_{hp} \\ \dot{m}_{hp} = w_{hp} - w_t \\ \dot{m}_{lp} = w_t - w_{lp} \\ \dot{p}_{owc} = \dfrac{\gamma(p_{atm} + p_{owc})}{m_{owc}} \left( \dfrac{\dot{Q}_{owc}}{c_p T_{owc}} + w_{vl} \dfrac{T_{lp}}{T_{owc}} - w_{vh} - \rho_{owc} \dot{V}_{owc} \right) \\ \dot{p}_{hp} = \dfrac{\gamma(p_{atm} + p_{hp})}{m_{hp}} \left( \dfrac{\dot{Q}_{hp} - \dot{Q}_{hp2lp}}{c_p T_{hp}} + w_{vh} \dfrac{T_{owc}}{T_{hp}} - w_t \right) \\ \dot{p}_{lp} = \dfrac{\gamma(p_{atm} + p_{lp})}{m_{lp}} \left( \dfrac{\dot{Q}_{lp} + \dot{Q}_{hp2lp}}{c_p T_{lp}} + w_t \dfrac{T_{ft}}{T_{lp}} - w_{vl} \right) \\ I\dot{\Omega} = T_{turb} - T_{gen} \end{cases} \tag{G.42}$$

This system is composed of 9+4n first order differential equations which can be solved using a numerical first-order differential equation solver. In the present work, the order of the Prony's function is $n = 4$. The system is solved with the variable step ordinary differential equation solver ode45 from the software MATLAB.

## G.3 Conventional OWC non-isentropic model

The wave-to-wire model of the corresponding OWC device is relatively similar to the Tupperwave device. Since both devices use the same floating spar structure, the hydrodynamic set of equations is the same. Figure G.7 displays a schematic of the OWC thermodynamic system. The air in the chamber is thermally isolated from the atmosphere by the buoyancy volume around the chamber. Heat exchange however occurs by convection between the air and the water column. To separate inhalation and exhalation processes, we define the two positive quantities $w_{t,in}$ and $w_{t,out}$ as the absolute values of the air flow rates respectively entering and exiting the turbine such that:

$$\text{for} \quad p_{owc} < 0 \; : \begin{cases} w_{t,in} = |w_t| \\ w_{t,out} = 0 \end{cases} \quad \text{and for} \quad p_{owc} > 0 \; : \begin{cases} w_{t,in} = 0 \\ w_{t,out} = |w_t| \end{cases} \tag{G.43}$$

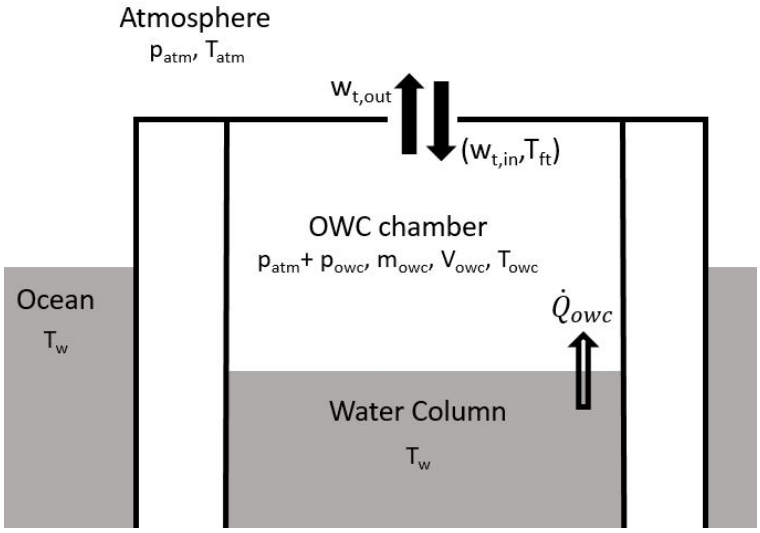


Figure G.7: Conventional OWC schematic with thermodynamic variables

The system of equations G.10 applied on the OWC chamber gives:

$$\begin{cases} \dot{m}_{owc} = w_{t,in} - w_{t,out} \\ \dot{p}_{owc} = \dfrac{\gamma(p_{atm} + p_{owc})}{m} \left( \dfrac{\dot{Q}_{owc}}{c_p T_{owc}} + w_{t,in} \dfrac{T_f}{T_{owc}} - w_{t,out} - \rho_{owc} \dot{V}_{owc} \right) \end{cases} \tag{G.44}$$

with:

$$T_{ft} = T_{atm} \left( \frac{p_{atm} + p_{owc}}{p_{atm}} \right)^{\frac{\gamma-1}{\gamma}} + \frac{L}{c_p w_t} \tag{G.45}$$

The turbine used in the OWC model is the twin-rotor turbine. The turbine is based on a pair of conventional radial-inflow rotors mounted on the same shaft, complemented by the corresponding guide vane rows, and by a two-position cylindrical valve which orientates the air across one rotor or the other depending on the flow direction (inhalation or exhalation). The rotor spinning in no flow generates a braking torque and causes windage losses [60]. The turbine's characteristic functions $f_\Psi$ and $f_\Pi$ were established by physical testing in [128], as well as an expression of the windage torque as a function of the rotational speed. The maximum efficiency of the twin-rotor turbine is 74% in constant flow condition.

The generator and its control law are the same as in the Tupperwave model. The only difference is that the aerodynamic friction torque $T_{wind}$ created by the passive rotor (the one with no flow) is added in the shaft rotational speed's differential equation:

$$I\dot{\Omega} = T_{turb} - T_{gen} - T_{wind} \tag{G.46}$$

Using the same method as in section G.2.4, the system of equations governing the non-isentropic wave-to-wire model of the conventional OWC de-

vice is expressed as 5+4n first-order differential equations:

$$\begin{cases} \dot{U} = V \\ \dot{V} = M^{-1}\left( \begin{bmatrix} f_1 \\ f_2 \end{bmatrix} + \begin{bmatrix} 1 \\ -1 \end{bmatrix} Sp_{owc} - \begin{bmatrix} \sum_1^n I_{11,k} + \sum_1^n I_{12,k} \\ \sum_1^n I_{21,k} + \sum_1^n I_{22,k} \end{bmatrix} - \begin{bmatrix} C_{d1} \\ C_{d2} \end{bmatrix} .V.|V| - \begin{bmatrix} c_1 \\ c_2 \end{bmatrix} .U \right) \\ \dot{I}_{11,k} = \beta_{11,k} I_{11,k} + \alpha_{11,k} \dot{x}_1, \qquad k = 1:n \\ \dot{I}_{12,k} = \beta_{12,k} I_{12,k} + \alpha_{ij,k} \dot{x}_2, \qquad k = 1:n \\ \dot{I}_{21,k} = \beta_{21,k} I_{21,k} + \alpha_{ij,k} \dot{x}_1, \qquad k = 1:n \\ \dot{I}_{22,k} = \beta_{22,k} I_{22,k} + \alpha_{ij,k} \dot{x}_2, \qquad k = 1:n \\ \dot{m}_{owc} = w_{t,in} - w_{t,out} \\ \dot{p}_{owc} = \dfrac{\gamma(p_{atm} + p_{owc})}{m} \left( \dfrac{\dot{Q}_{owc}}{c_p T_{owc}} + w_{t,in} \dfrac{T_f}{T_{owc}} - w_{t,out} - \rho_{owc} \dot{V}_{owc} \right) \\ I\dot{\Omega} = T_{turb} - T_{gen} - T_{wind} \end{cases} \tag{G.47}$$

## G.4 Numerical results

In this section, the numerical results are obtained assuming an atmosphere and ocean temperature of 15°C. At the beginning of each simulation, the device is idle and the air in the device is at atmospheric condition.

The same turbine blade geometry as the one tested in [60] was used in both device. The diameters and rotational speeds were optimised in [133] to maximise the electrical power output from both devices in the wave climate of the EMEC test site, located in the north of Scotland. Information on the turbine and generator parameters used in the Tupperwave and the conventional OWC model are given in table G.1.

As shown in table G.1, the optimisation results were very different on what concerns the size (diameter D) and the rotational speed. This is due to the very different working conditions of the turbines in the two devices as can be seen in figure G.8 which displays the pressure head and the flow rate to which both turbines are subjected in the same sea state. The pressure head across the Tupperwave turbine is larger with a lower flow rate. This is confirmed by the very different sizes of the orifices used to simulate the turbines in model testing of Tupperwave and conventional OWC in [135]. The higher rotational speed of the Tupperwave turbine unfortunately requires the use of a gearbox, associated with undesirable cost and maintenance issues. It can be found from the well-known Cordier diagram [147], that the use of different turbine design with a larger diameter could avoid the use of a gearbox and enable the direct driving the generator.

Table G.1: Turbine and generator parameters used in the models

| | | **Tupperwave** | **Conventional OWC** |
|---|---|---|---|
| **Turbine** | Type | Unidirectional radial inflow turbine | Self-rectifying radial inflow twin-rotor turbine |
| | Diameter (m) | 0.50 | 1.10 |
| | Design speed (rpm) | 4000 | 1000 |
| | Inertia (kg.m2) | 1.7 | 38 |
| | Max. efficiency (%) | 86.6 | 73.9 |
| **Gearbox** | Gearing Ratio | 4 | 1 |
| **Generator** | Rated power (kW) | 100 | |
| | Inertia (kg.m$^2$) | 3.6 | |
| | Design speed (rpm) | 1000 | |
| | Max. speed (rpm) | 2000 | |
| | Min. speed (rpm) | 400 | |

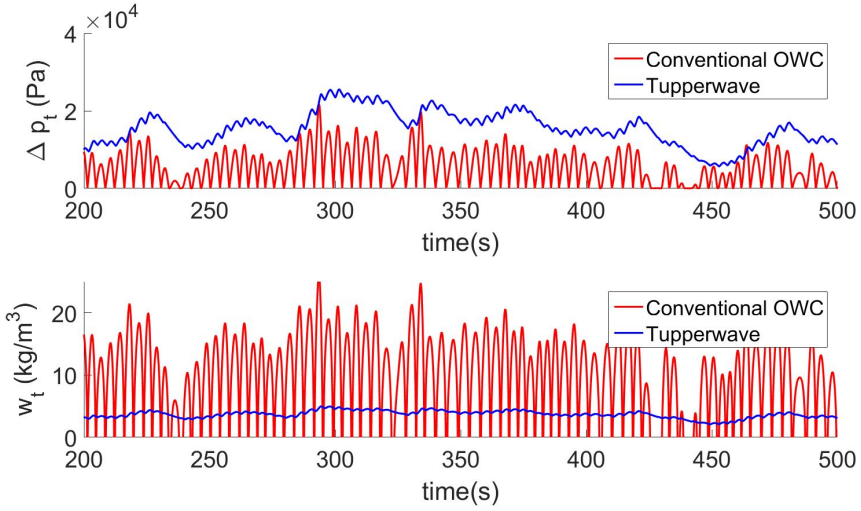


Figure G.8: Pressure head and mass flow rate across the turbines in the Tupperwave device and the conventional OWC in sea state $\{H_s = 3\,\mathrm{m}\,;\, T_p = 9\,\mathrm{s}\}$

## G.4.1 Temperature analysis

### G.4.1.1 In the Tupperwave device

#### G.4.1.1.1 Adiabatic case

Figure G.9 displays the temperature of the air in the HP and LP chambers in the case where the device does not receive any radiation from the sun and no heat exchange is allowed across the walls or with the water (adiabatic):

$$\dot{Q}_{owc} = \dot{Q}_{hp} = \dot{Q}_{lp} = \dot{Q}_{hp2lp} = 0$$

The simulation is 30-minute long in the irregular sea state $\{H_s = 3\,\mathrm{m}\,;\, T_p = 9\,\mathrm{s}\}$, which represents a relatively common sea state of moderate energy in offshore ocean conditions. The black line represents the average air temperature of the system at the end of the simulation.

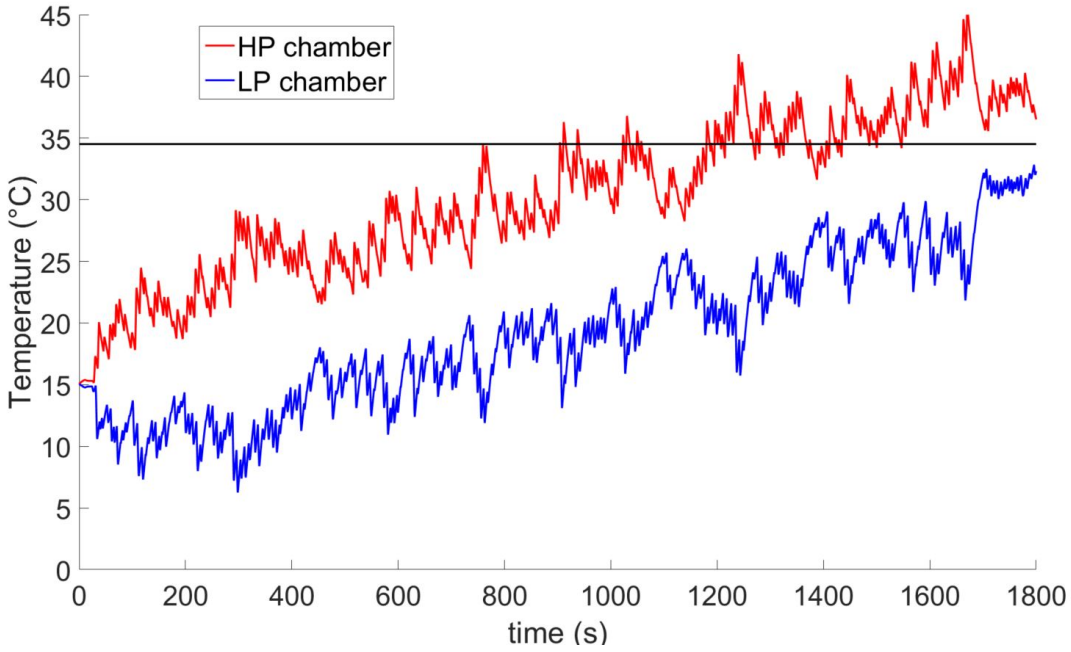


Figure G.9: Air temperature in HP and LP chambers in adiabatic scenario for sea state $\{H_s = 3\,\mathrm{m}\,;\, T_p = 9\,\mathrm{s}\}$

Given the pressure difference between the two chambers, the HP chamber is naturally hotter than the LP chamber. The temperature in the OWC chamber oscillates successively between the temperatures of the HP and LP chambers and was not represented in the figure for clarity. Significant temperature elevation occurs in the chambers due to the viscous losses. The air temperature in both chambers increases steadily by approximately 20°C in 30 minutes and would keep rising to infinity in this theoretical case. As a result, the air expands and the average pressure in the device increases. This

pushes the water column down and the buoy up and would eventually modify the hydrostatic equilibrium and the hydrodynamics of the device. High temperatures are also undesirable because they could damage on-board instrumentation or the buoy structure itself.

#### G.4.1.1.2 Diathermal case

In reality, heat transfers need to be considered due to the large outer wall's surface area of the Tupperwave device and the contact between air and water in the OWC chamber. The total solar irradiation at sea level $I_t = 1000\,\mathrm{W/m^2}$, corresponding to a clear summer day in Europe, is adopted. This value is generally used as standard test conditions for photovoltaic devices. The absorptivity $\alpha$ of the solar radiation by a surface is complex to assess and can vary from 0 to 1 depending on the material, the colour and the roughness of the surface. In general it is higher for dark colours and rough surface. The value $\alpha = 0.7$ is adopted for this study and corresponds to the absorptivity of concrete according to [155]. Values for the convective heat transfer coefficients between the fluids (air or water) and device walls strongly depends on the fluid properties, the roughness of the surface and on the flow velocity in the vicinity of the wall. In the present case, the fluid flows around the device depend on the wind and water current, as well as on the motion of the device due to the wave excitation. The overall air flow velocity around the device is taken of $v_1 = 5\,\mathrm{m/s}$ and the empirical law suggested in [155] leads to a convective heat transfer coefficient $h_a = 4 + 4v_1 = 24\,\mathrm{W/(m^2.K)}$. Assuming a turbulent flow of water outside the device with 1 m/s average overall speed, the convective heat transfer coefficient of the water is estimated using the Dittus-Boelter equation to $h_w = 1000\,\mathrm{W/(m^2.K)}$ [156]. Considering the motion of the IWS in the OWC chamber of approximately $v_2 = 1\,\mathrm{m/s}$, the forced convection model adopted in [157] leads to convective heat transfer coefficient between air and water $h_{aw} = 2.8 + 3v_2 = 5.8\,\mathrm{W/(m^2.K)}$. We note that the values of the thermal parameters given in this paragraph can vary largely depending on the adopted assumptions relative to the weather conditions, the device construction and the sea state. Choosing realistic values is made even more difficult by the large variability of information found in the literature. The chosen values are meant to represent the heat exchanges in light wind, current and wave conditions on a very sunny day around noon in order to avoid the underestimation of the temperature rise in the device.

The walls are first considered to be made of concrete with a thickness $l = 20\,\mathrm{cm}$. The thermal conductivity of concrete is greatly affected by mix proportioning, aggregate types and sources, as well as moisture status. Complex considerations on concrete are beyond the scope of this paper. Measurements made in [158] give an average value of $k_{th,concrete} = 2\,\mathrm{W/(m.K)}$. Figure

G.10 displays the temperature of the air in the HP and LP chambers in the case of a concrete buoy structure in sea state $\{H_s = 3\,\text{m}\,;\, T_p = 9\,\text{s}\}$. The black line represents the average air temperature in the chambers at the end of the simulation. After a transient state of about 10 minutes where the temperature increases slowly, the system reaches a steady state and the average air temperature settles 10°C higher than the initial temperature. In 5 meter high waves, the same phenomenon is observed and the increase in temperature is found to be of about 16°C.

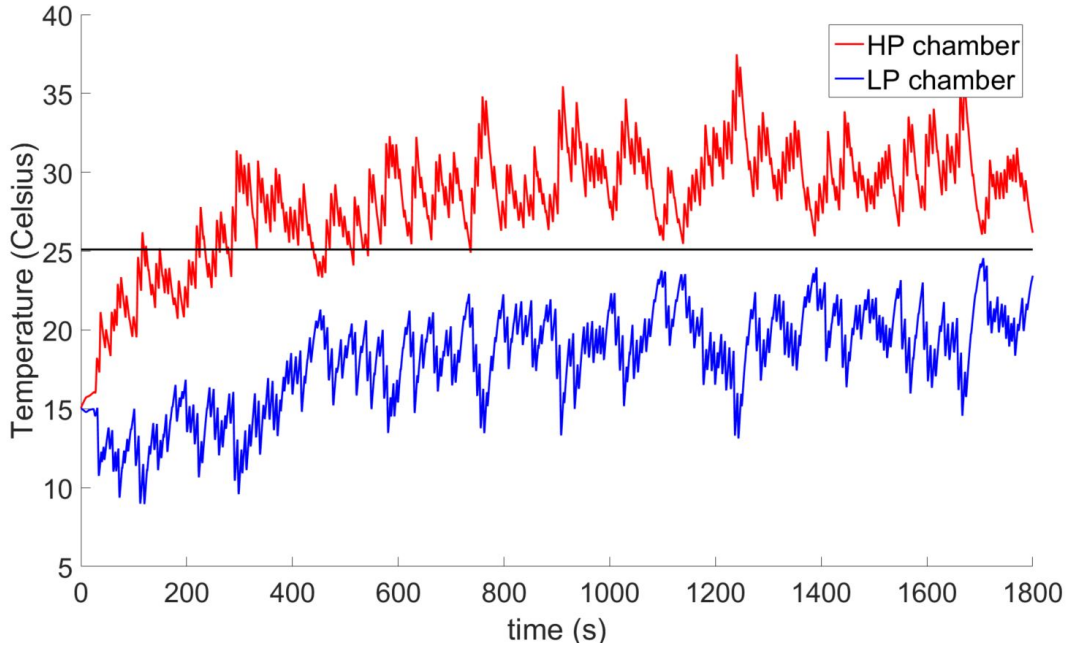


Figure G.10: Air temperature in HP and LP chambers assuming heat transfers across the concrete buoy structure and with the water column for sea state $\{H_s = 3\,\text{m}\,;\, T_p = 9\,\text{s}\}$

Another wall material is considered, with a higher heat conductivity than that of concrete. The walls are assumed made of steel sheets of thickness $l = 15\,\text{mm}$, and with heat conductivity $k_{th,steel} = 30\,\text{W.m}^{-1}\text{.K}^{-1}$ [145]. Assuming similar walls surface colour and roughness as for the concrete walls, the same convective heat transfer and absorptivity coefficients are adopted. Figure G.11 displays the temperature of the air in the HP and LP chambers in the case of a concrete buoy structure in sea state $\{H_s = 3\,\text{m}\,;\, T_p = 9\,\text{s}\}$. In that case, the steady state is reached in about 5 minutes. The average air temperature increase in the device is of 6.3°C and reaches 8.5°C in extreme sea states. Simulations were also carried out in the absence of solar radiation (night conditions). The results obtained on temperature increase in the Tupperwave device under the assumption of steady state heat transfer across the walls are summarized in Table G.2.

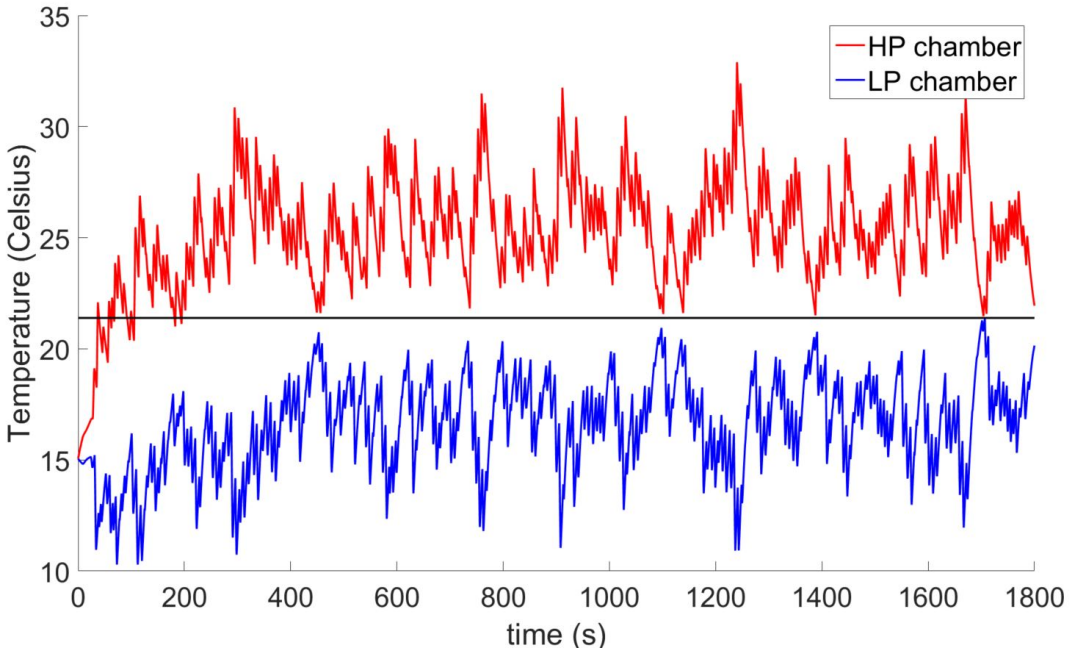


Figure G.11: Air temperature in HP and LP chambers assuming heat transfers across the steel buoy structure and with the water column for sea state $\{H_s = 3\,\text{m}\,;\, T_p = 9\,\text{s}\}$

Table G.2: Average air temperature increase from atmospheric conditions in the Tupperwave device depending the wall structure and solar irradiation and assuming steady state conductive heat transfer across the walls

| **Sea state** | **Solar irradiation** | **Wall structure** | |
|---|---|---|---|
| | | **Concrete** | **Steel** |
| | | $k_{th} = 2\,\text{W/(m.K)}$ | $k_{th} = 30\,\text{W/(m.K)}$ |
| | | $l = 20\,\text{cm}$ | $l = 15\,\text{mm}$ |
| $H_s = 3\,\text{m}\,;\, T_p = 9\,\text{s}$ | $I_t = 1000\,\text{W/m}^2$ | 10.0°C | 6.3°C |
| | $I_t = 0\,\text{W/m}^2$ | 4.0°C | 1.5°C |
| $H_s = 5\,\text{m}\,;\, T_p = 9\,\text{s}$ | $I_t = 1000\,\text{W/m}^2$ | 15.8°C | 8.5°C |
| | $I_t = 0\,\text{W/m}^2$ | 9.8°C | 3.7°C |

The assumption of steady state conductive heat transfer across the device walls adopted in section G.2.2.2.1 can be checked by the calculation of the characteristic diffusion time $\tau$ across the thickness $l$ of the wall [159]:

$$\tau = \frac{l^2}{D_{th}} = \frac{l^2 \rho c_v}{k_{th}} \tag{G.48}$$

where $D_{th}$, $\rho$, $c_v$ and $k_{th}$ are respectively the thermal diffusivity, density, heat capacity and heat conductivity of the wall material. For the steel wall, the characteristic diffusion time is about 30 seconds. In that case, the conductive heat transfer across the wall is quickly established and the assumption of steady state conductive heat transfer enabling a resistive thermal model of the walls is reasonable at all times. For the concrete wall, the characteristic time of diffusion is close to 10 hours. This means that, after the sudden change of excitation force or solar radiation, the conduction heat transfer requires a 10-hour long transient state to settle back to a steady state. Hence, the resistive thermal model of the concrete wall is not valid during such transient state. The results displayed in figure G.10 are therefore likely to underestimate the duration of the transient state, and higher temperature levels are likely to be reached during this period before the steady state is settled. The installation of steel heat exchangers across the concrete walls could be a solution to prevent high temperature increase caused by the sudden increase of the wave excitation force or solar radiation on the device. The temperature increase displayed in Table G.2 are however still valid under the assumption that the conductive heat transfer across the walls has had sufficient time to settle. Such low air temperature increase does not represent any danger for the device operation.

The isentropic model does not predict this increase in temperature, as it can be seen in figure G.12. The average air temperature in the device remains equal to the initial temperature.

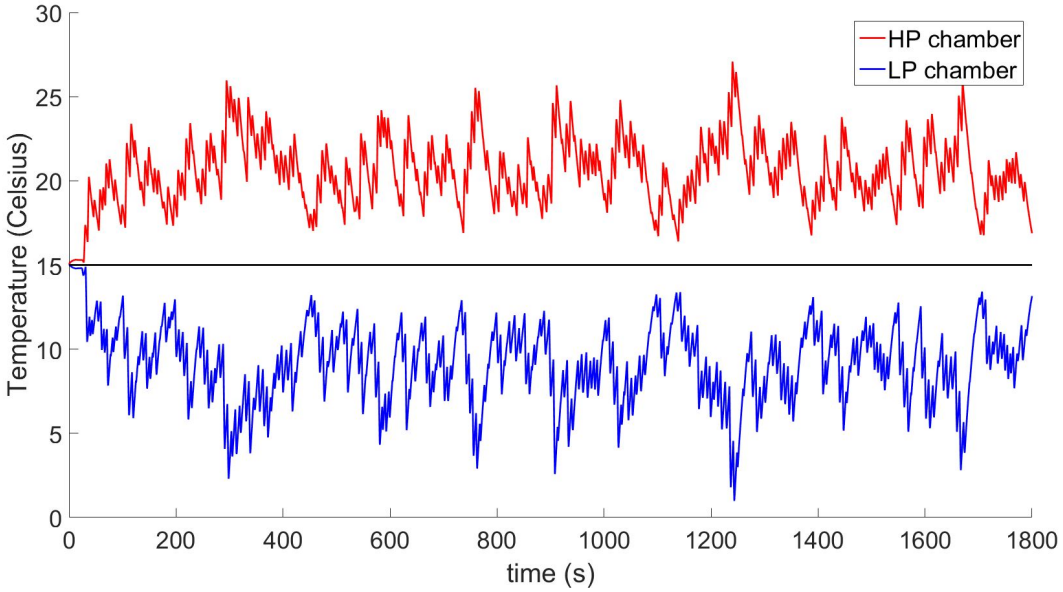


Figure G.12: Air temperature in HP and LP chambers with isentropic model for sea state $\{H_s = 3\,\mathrm{m}\,;\, T_p = 9\,\mathrm{s}\}$

#### G.4.1.2 In the conventional OWC

In the case of the conventional OWC, a slight temperature increase in the OWC chamber is also observed. During the inhalation process, the viscous losses at the turbine result in an increase of specific internal energy in the OWC chamber. But unlike the Tupperwave device, the OWC chamber is open to the atmosphere whose temperature remains constant. This prevents large increase in temperatures. Figure G.13 displays the temperature of the OWC chamber in the conventional OWC device in sea state $\{H_s = 3\,\mathrm{m}\,;\, T_p = 9\,\mathrm{s}\}$. The average temperature of the chamber towards the end of the simulation (represented by the black line) is 1.5°C higher than the initial temperature. In 5m high waves, the increase in temperature is of 3°C.

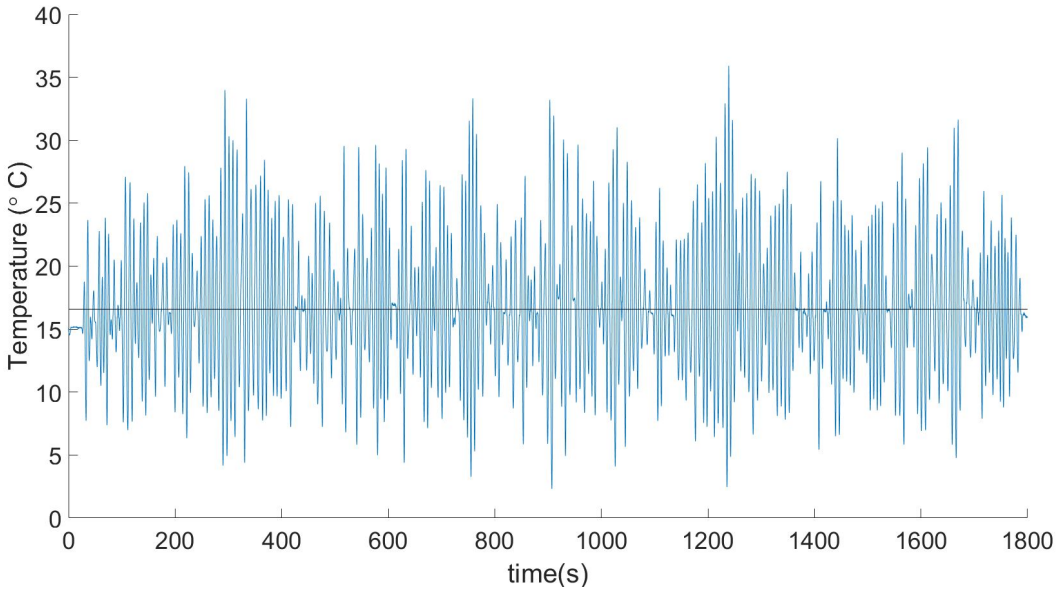


Figure G.13: Air temperature of the OWC chamber of conventional OWC device for sea state $\{H_s = 3\,\mathrm{m}\,;\, T_p = 9\,\mathrm{s}\}$

## G.4.2 Energy balance analysis

The review on wave-to-wire models of wave energy converters [23] distinguishes four main stages in the power conversion process of a wave energy converter: Absorption, transmission, generation and conditioning. In a conventional OWC, the power effectively absorbed from the waves $P_{abs}$ is the power applied by internal water surface on the air contained in the OWC chamber (absorption stage). This energy is briefly stored by the air contained in the OWC chamber under the form of internal energy and released, for the most part and with a delay, as power available to the turbine $P_{avail}$. This is the spring-like compressibility effect of the air [67]. We note that, if the process is assumed adiabatic and isentropic without any dissipative losses, the averaged values of the absorbed power and power available to the turbine over a sufficiently long time interval, must be equal $\overline{P_{avail}} = \overline{P_{abs}}$. This is not the case in the non-isentropic model of the conventional OWC developed in this study where the internal energy of the air is likely to change due to the heat transfer with the water column. Besides, in the case of the Tupperwave device, some energy is dissipated in the valves and the power available to the turbine is eventually lower than the power absorbed from the waves: $\overline{P_{avail}} < \overline{P_{abs}}$. Part of the power available to the turbine is then effectively converted by the turbine into mechanical power (transmission stage). The mechanical power is further converted into electrical power by the generator (generation stage). Finally, the raw electrical power created by the generator is adapted to be delivered into the grid by a power electronic converter (conditioning stage). In the present paper, the wave-to-wire models presented

neglect the influence of the conditioning stage on the device efficiency. This simplification was shown in [27] to be perfectly reasonable in applications such as control parameters optimisation and power production assessment. Figure G.14 displays a bar diagram of the average powers along the power conversion chain for the Tupperwave device. In the end, 57% of the absorbed power is converted in electrical power and the rest is disspated in the turbine, the valves and the generator.

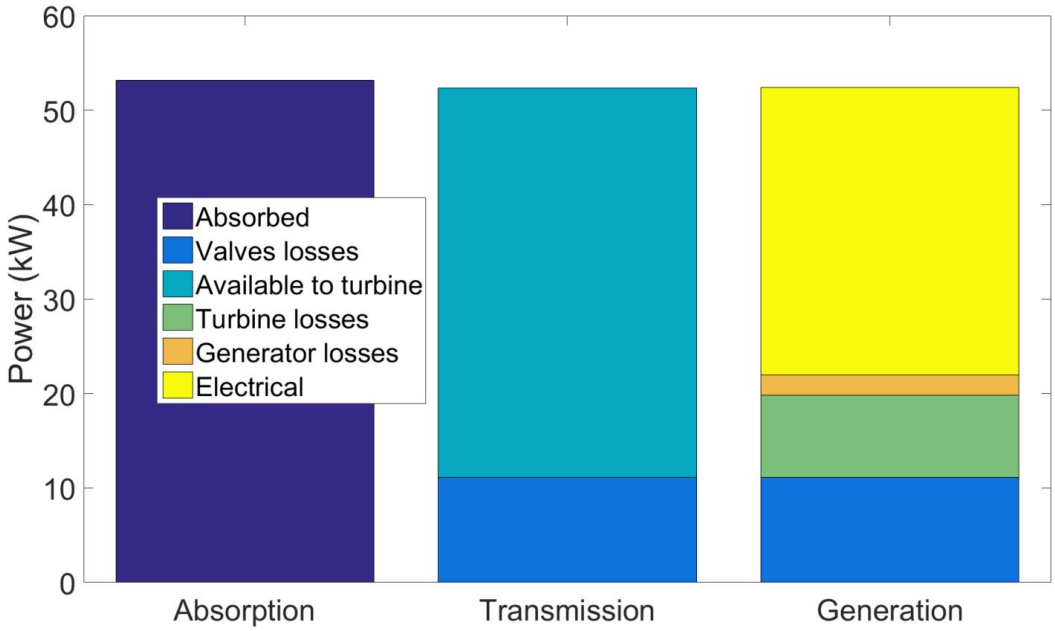


Figure G.14: Diagram of average power along the conversion stages for sea state $\{H_s = 3\,\mathrm{m}\,;\, T_p = 9\,\mathrm{s}\}$ for the Tupperwave device with steel structure

In section G.2.2.1, a general open thermodynamic system has been defined to derive the general equations relating mass, density, pressure and volume. These equations were then applied to each chamber of the Tupperwave device to build the numerical model. We now consider the thermodynamic system which refers to the total air contained in the Tupperwave device which is a closed system. According to the first law of thermodynamics, the change in the internal energy $\Delta U$ of a closed system is equal to the amount of heat supplied to the system, plus the amount of mechanical work $W$ received by the system. The work received by the considered system is the work $W_{abs}$ done by the internal water surface acting as a piston. The system also absorbs the heat $Q_{rad}$ from the solar radiation. Within the system, part of the absorbed energy is dissipated in the turbine and valves $W_{losses}$. The mechanical work done by the system is the work provided to the turbine $W_{turb}$. Finally, the heat $Q_{out}$ is transferred to the environment via conduction and convection through the control surface. Figure G.15 displays a schematic of the energy balance of the system. Exchanges are counted positive in the

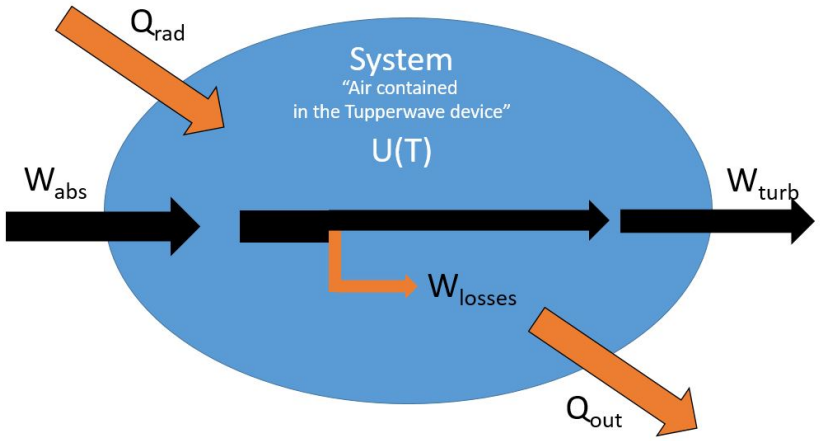


Figure G.15: Energy balance schematic of the air contained in the Tupperwave device

direction of the arrows. The energy balance is written as:

$$W_{abs} + Q_{rad} = \Delta U + W_{turb} + Q_{out} \tag{G.49}$$

Figure G.16 and G.17 displays the bar diagram illustrating the energy balance of the system after 30 minutes of simulation in sea state $\{H_s = 3\,\text{m}\,;\, T_p = 9\,\text{s}\}$ respectively with and without solar radiation. This verifies the conservation of energy in the numerical model. The solar radiation on the device has little impact on the output power since the average turbine output power is 2.2% higher with the high solar radiation than without solar radiation.

Once the air temperature in the device reaches a steady state, the average internal energy of the system does not vary any more over a time period in the order of 10 minutes. The heat $Q_{out}$ transferred through the control surface is equal to the sum of the heat absorbed from the solar radiations $Q_{rad}$ and the turbine and valves losses $W_{losses}$. Hence, the steady state conditions, over a time period of about 10 minutes, are:

$$\begin{cases} \Delta U = 0 \\ Q_{rad} + W_{losses} = Q_{out} \end{cases} \tag{G.50}$$

We note that the turbine and valve losses do not depend on the material of the device walls. Thus, for the same solar radiation absorption, the heat transfer across the walls in steady state is independent from the wall material. Therefore, the steel device does not transfer more heat to the environment than the concrete device in steady state and their power output can be expected to be similar. This will be confirmed in the next section.

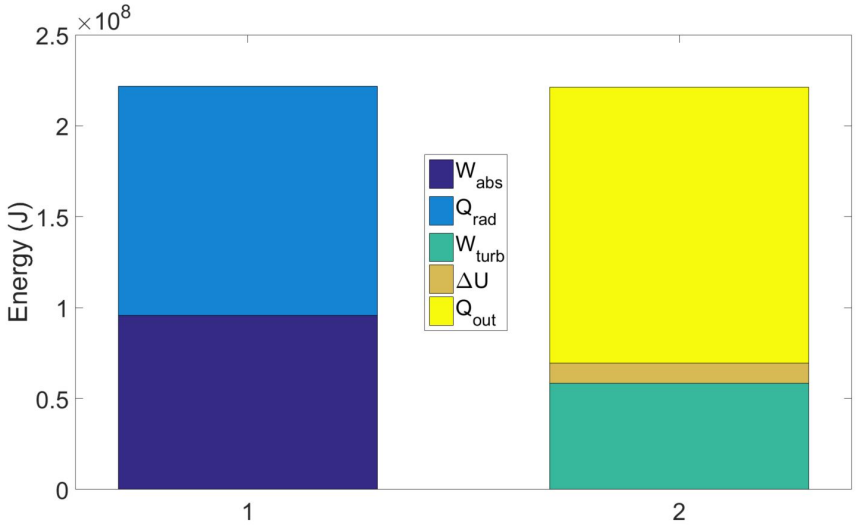


Figure G.16: Energetic balance diagram of the air contained in the Tupperwave device with steel walls for sea state $\{H_s = 3\,\mathrm{m}; T_p = 9\,\mathrm{s}\}$ for a 30 minute simulation with solar irradiation $I_t = 1000\,\mathrm{W/m^2}$

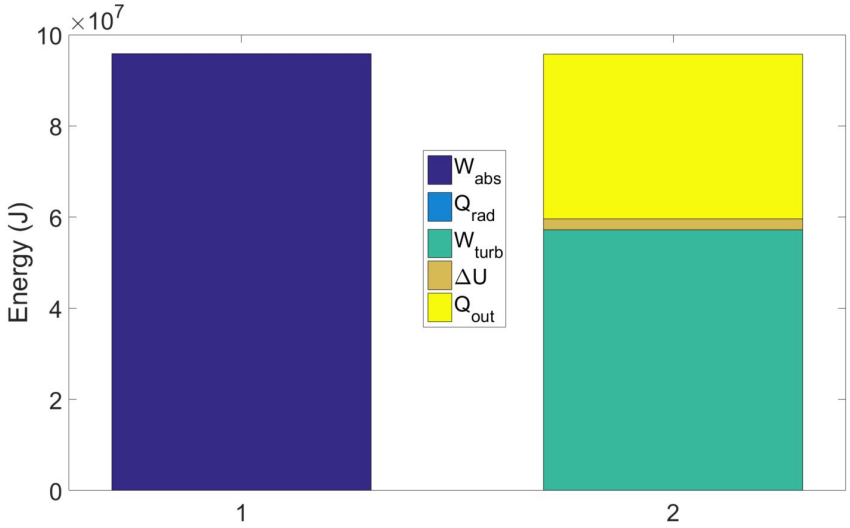


Figure G.17: Energetic balance diagram of the air contained in the Tupperwave device with steel walls for sea state $\{H_s = 3\,\mathrm{m}; T_p = 9\,\mathrm{s}\}$ for a 30 minute simulation without solar irradiation

### G.4.3 Isentropic / Non-isentropic comparison

In this section, the non-isentropic model results of the Tupperwave and corresponding conventional OWC devices presented in this paper, are compared to the model results using the linearised isentropic thermodynamic assumption, given in equation G.14.

The devices were simulated in the wave climate of the EMEC wave energy test site. For the non-isentropic model, the yearly average global solar

irradiance in the north of Scotland is $I_t = 115\,\mathrm{W/m^2}$ [160]. Table G.3 displays the annual electrical power production of both devices in the EMEC wave climate, assessed with both non-isentropic model and linearised isentropic model.

Table G.3: Annual electrical power production assessement with non-isentropic and isentropic models of the Tupperwave and conventional OWC devices

| **Annual production (MWh)** | **Tupperwave** | | **Conventional OWC** |
|---|---|---|---|
| | **Concrete** | **Steel** | |
| Non-isentropic | 97.5 | 96.3 | 98.9 |
| Isentropic linearised | 97.6 | | 99.9 |

The non-return valves are key components in the power conversion efficiency of the Tupperwave device. Depending on their characteristics (opening area and opening pressure), the Tupperwave device can either be more or less efficient than the conventional OWC. The influence of the valves characteristics was discussed in [133] and is not in the scope of this present paper. With the valves characteristics (opening area and pressure) used in this study, the Tupperwave device produces a similar amount of electrical energy as the conventional OWC.

The easier heat transfer to the environment through the walls of the steel device only reduces the electrical power output by 1-2% relative to the concrete device over a whole year on the EMEC test site.

Non-isentropic and isentropic models give very similar results as can be seen in figure G.18 which displays the electrical power output time-series in a sea state. Over the whole year on the EMEC test site, the electrical power generation prediction obtained with both models differ by less than 1%. This shows that the isentropic linearized assumption provides satisfactory results for power production assessment in the case of the conventional OWC, as it was already shown in [68], and also in the case of the Tupperwave device.

## G.5 Conclusion

In this paper, non-isentropic models of the Tupperwave device and corresponding conventional OWC were developed. The models account for the energy dissipation across the turbine and the valves, the heat transfers between the inner air and the environment, and the solar radiations on the device.

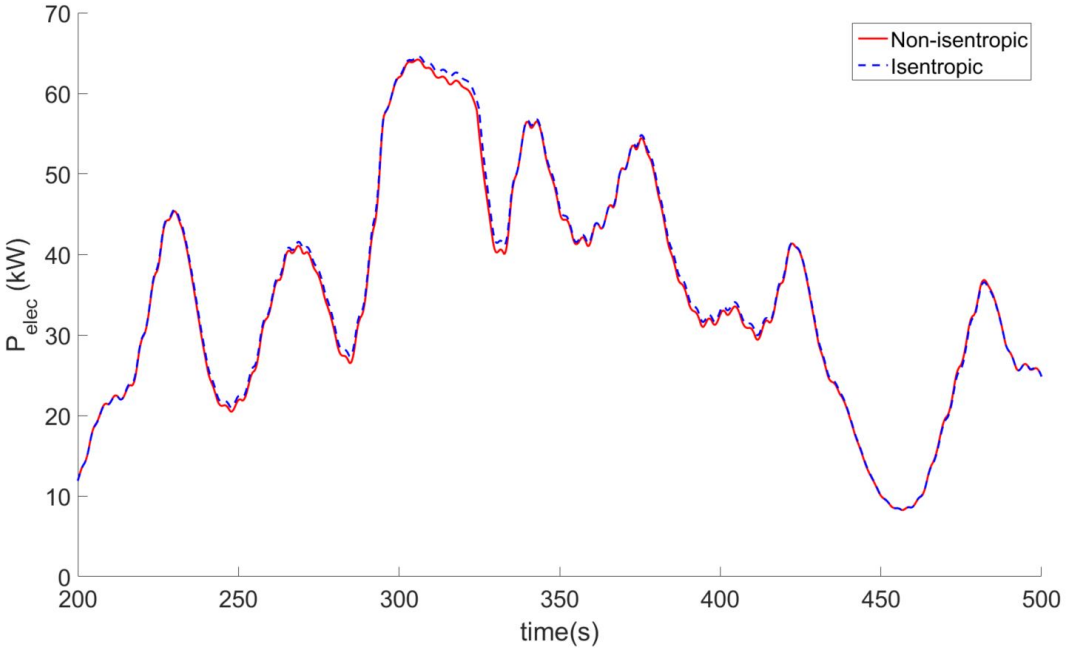


Figure G.18: Time series of electrical output power of the Tupperwave device in sea state $\{H_s = 3\,\mathrm{m}\,;\, T_p = 9\,\mathrm{s}\}$ obtained with the non-isentropic model and isentropic model.

The results showed that the energy dissipation by viscous losses and the heat absorbed by the walls from solar radiations results in an increase in inner air temperature. The large surface area of the device outside walls allows sufficient heat transfer to the environment to limit the temperature increase to a certain threshold depending on the sea state, on the walls thermal conductivity, and on the level of solar irradiance. Eventually the internal air temperature does not reach any problematic value for the operation of the closed-circuit OWC device. This result demonstrate that the air temperature increase in a closed-circuit OWC device such as the Tupperwave device should not be considered as a barrier for the further development of this technology.

Whether steel or concrete walls are considered, the average temperature increase in the Tupperwave device does not exceed 16°C in very energetic sea states, even in very sunny days. For low thermal conductivity material such as concrete, the heat transfer by convection and conduction through the walls is much longer to settle and the resistive heat transfer model used in this manuscript is not adapted to predict the temperatures increase caused by sudden increase of wave excitation force or solar radiation on the device. A more sophisticated heat transfer model would be necessary to correctly assess the transient state.

Similar temperature increase phenomenon was also observed in the corresponding conventional OWC device due to the viscous losses occurring

in the turbine during the inhalation process. The temperature increase in the conventional OWC was however lower than in the Tupperwave device, since the air inhaled in every cycle is always at atmospheric temperature; the average temperature increase in the OWC chamber was limited to 3°C in very energetic sea states.

The results also showed that the solar radiation and the heat conductivity of the wall material have relatively small impact on the device electrical power output. The difference observed between high and low solar radiations, or between high and low heat conductivity of the walls, are in the order of 2%.

The more realistic non-isentropic models of the Tupperwave and conventional OWC devices were finally compared to the simpler models using linearised isentropic relationship between pressure and density within the chambers. The isentropic assumption was found to provide a satisfactory approximation of the power output for both open- and closed-circuit OWC devices. Realistic prediction of the temperatures in the devices can however only be achieved with the non-isentropic models.

## Acknowledgement

The authors would like to acknowledge funding received through OCEANERA-NET European Network (OCN/00028).

# Appendix H

# Linear wave theory

## H.1 Wave-structure interaction

A number of phenomenon are involved in the wave-structure interaction and the wave theory is based on the decomposition of those phenomenon in the equation of motion:

- **Buoyancy:** In the absence of waves, the body floats on the surface due to the buoyancy force which acts against gravity and is equal to the weight of the fluid displaced by the body. This force therefore varies with the displacement of the body in the water. Generally, the difference between buoyancy and gravity force is called the hydrostatic force $F_H$:

$$F_H = \rho g V(X) - mg = \rho g(V(X) - V_0) \tag{H.1}$$

  where $\rho$ is the water density; $V$ is the immersed volume of the body; $V_0$ is the immersed volume of the body when at rest; $m$ the mass of the body; $g$ the standard acceleration due to gravity.

- **Wave excitation:** In the presence of waves and in absence of body displacement, the unsteady pressure field generated by the propagating waves induces excitation forces $F_{ex}$ on the immersed body surface. Generally the excitation forces are decomposed into the sum of the Froude-Krylov forces $F_{KV}$ associated with the pressure field from the undisturbed incident waves $p_I$ and the diffraction forces $F_D$ associated with the pressure field from the waves diffracted by the idle body $p_D$:

$$F_{ex} = F_{KV} + F_D = \int_S (p_I + p_D) dS \tag{H.2}$$

  where $S$ is the immersed surface of the body.

- **Radiation:** In the absence of incident waves, the unsteady motion of the body in the water generates waves on the surface of the water. This

results in a radiation force applying on the body, associated with the radiated pressure field $p_R$:

$$F_R = \int_S p_R dS \tag{H.3}$$

- **Drag:** The motion of the body in the water generates vortices in the flow which result in a dissipative (or damping) force applied on the body. Another component of drag force is the friction force due to the fluid viscosity (shear stresses in the boundary layer). The drag depends on the properties of the fluid and on the size, shape and speed of the body and on the Reynolds number. Its impact on WEC dynamics can be significant in some cases [161]. A model for the drag force commonly used in wave energy application is proportional and opposite to the square of the velocity:

$$F_{Drag} = -C_d|\dot{X}|\dot{X} \tag{H.4}$$

where $C_d$ is the drag coefficient. The significance of the drag depends on the drag coefficient $C_d$, which needs to be estimated using experimental tests or CFD simulations [162].

The equation of motion of a floating body with 6 degrees of freedom, in cartesien coordinates (x,y,z) is:

$$M\ddot{X} = F_H + F_{ex} + F_R + F_{Drag} + F_{PTO} \tag{H.5}$$

where:

- $M = \begin{bmatrix} m & & & & & \\ & m & & & & \\ & & m & & & \\ & & & I_{xx} & I_{xy} & I_{xz} \\ & & & I_{xy} & I_{yy} & I_{yz} \\ & & & I_{xz} & I_{yz} & I_{zz} \end{bmatrix}$ is the mass matrix of the structure with $m$ being the mass and $I_{ij}$ the moments and products of inertia of the device solid structure;

– $X = \begin{bmatrix} x_G \\ y_G \\ z_G \\ \phi \\ \theta \\ \psi \end{bmatrix}$ is the displacement vector of the solid structure for the three translations along the axis and three rotations around the axis;

– $F_{PTO}$ is an externally applied force and moment applied by the power take-off mechanisms in a wavepower context.

## H.2 Linear potential theory and frequency analysis

Within the potential theory, the water is assumed as an inviscid and incompressible fluid, and the flow is irrotational. These assumptions enable the description of the flow by a velocity potential function $\Phi$, such that the velocity field is the gradient of the potential:

$$v(x,y,z,t) = \nabla\Phi = \begin{bmatrix} \partial\Phi/\partial x \\ \partial\Phi/\partial y \\ \partial\Phi/\partial z \end{bmatrix} \tag{H.6}$$

The flow being incompressible, the divergence of the velocity field is zero and thus the flow velocity potential verify the Laplace equation:

$$\Delta\Phi = \nabla.\nabla\Phi = \nabla.v = \frac{\partial^2\Phi}{\partial x^2} + \frac{\partial^2\Phi}{\partial y^2} + \frac{\partial^2\Phi}{\partial z^2} = 0 \tag{H.7}$$

The solutions of the Laplace equation are known and are the harmonic functions. The solution must however respect specific boundary conditions on the free surface, on the sea bottom and on the body surface. Significant simplification through linearisation of the boundary conditions can be obtained when further assumptions are made:

– the wave steepness is supposed to be small, i.e. the wave height a lot larger than the wave length;

– the displacement of the body around its mean position is supposed to be small relatively to its size.

Finding a solution to the velocity potential is necessary to obtain the pressure field around the body, which is given by the linearised Bernoulli equation:

$$p(x,y,z,t) = -\rho g z - \rho \frac{\partial \Phi}{\partial t} \tag{H.8}$$

and hence, enables the calculation of the forces applied on the body.

In pratice, the velocity potential flow is solved numerically. This requires industrial strength codes and are based upon the Boundary Element Method (BEM). The computational domain is discretized into numerous cells or boundary elements and then the velocity potentials are calculated for each element. The diffracted potential $\Phi_{diffraction}$ and radiated potential $\Phi_{radiation}$ are solved separately and form the perturbed wave field. Because of the linearisation, the total velocity potential is the sum of the known incident wave field and the pertubed wave field:

$$\Phi = \Phi_{incident} + \Phi_{diffraction} + \Phi_{radiation} \tag{H.9}$$

All BEM solvers based on potential flow theory solve the perturbed velocity potential as a 3D solution in the frequency domain from the linear wave-body interaction boundary value problem.

In frequency domain, all variables (causes and effects) are sinusoidal of the form $Z(t) = \Re\big(\widetilde{Z}(\omega)e^{-i\omega t}\big)$. The results of the numerical resolution by the BEM solver are given in the form of three frequency dependant matrix coefficients $\widetilde{F}_{ex}(\omega) = (F_{ex_{i,j}}(t))_{6\times 1}$, $A(\omega) = (A_{i,j}(\omega))_{6\times 6}$, $B(\omega) = (B_{i,j}(\omega))_{6\times 6}$ with which the wave-structure forces can be expressed in the frequency domain as:

$$F_{ex}(t) = \Re\big(\widetilde{F}_{ex}(\omega)e^{-i\omega t}\big) \tag{H.10}$$

$$F_R(t) = -A(\omega)\ddot{X}(t) - B(\omega)\dot{X}(t) \tag{H.11}$$

where $\widetilde{F}_{ex}(\omega)$ is the complex force transfert function, $A(\omega)$ is the real added mass matrix and $B(\omega)$ is the real radiation damping matrix.

The assumption of small body displacement around its mean position made earlier also allows to write the hydrostatic force as:

$$F_H(t) = -K_H X(t) \tag{H.12}$$

where $K_H = (K_{H_{i,j}})_{6\times 6}$ is the hydrostatic stiffness matrix.

The equation of motion in frequency domain therefore becomes:

$$(M + A(\omega))\ddot{X} + B(\omega)\dot{X} + K_H X = \Re\big(\widetilde{F}_{ex}(\omega)e^{-i\omega t}\big) + F_{Drag} + F_{PTO} \tag{H.13}$$

The form of the PTO and drag forces is crucial to progress further. In the case of a linear damper $F_{PTO} = -B_{PTO}\dot{X} - K_{PTO}X$, and no or linear drag $F_{Drag} = -C\dot{X}$, the equation of motion in the frequency domain can be solved.

## H.3 Time domain analysis

In reality, most converters are equipped with strongly nonlinear PTO mechanisms. Moreover, other non-linear effects are involved such as non-linear drag forces, moorings, ... In that case, the frequency domain analysis is no longer suitable, hence a time domain analysis must be employed. For a time-domain analysis, the Cummin-Olgivie hybrid frequency-time domain method is commonly used: The hydrodynamic coefficients $\widetilde{F}_{ex}$, $A$, and $B$ are first analysed in the frequency domain and transferred into time-domain using the Olgivie's relations based on Fourier transfrom techniques [83, 163]. This hybrid frequency-time domain approach has been a popular choice in the development of wave energy conversions since it allows to implement the non-linear effects from PTO or any other sources. This method is however more computationally demanding than the frequency domain analysis.

The equation of motion in time domain is:

$$[m + a(\infty)]\ddot{X}(t) = F_{ex}(t) - \int_0^t K_R(t-\tau)\dot{X}(t)d\tau - K_H X(t) + F_{PTO} + F_{Drag} \tag{H.14}$$

where $a(\infty)$ is added mass at infinite frequency and $K_R$ is the impulse response functions of the structure.

The impulse function, also called retardation, can be obtained by the following formula:

$$K_R(t) = \frac{2}{\pi}\int_0^\infty B(\omega)cos(\omega t)d\omega \tag{H.15}$$

where $b_{ij}$ is the radiation damping coefficient in the frequency domain.
The added mass at infinite frequency is obtained by:

$$a(\infty) = A(\omega) + \frac{1}{\omega}\int_0^\infty K_R(\tau)sin(\omega\tau)d\tau \tag{H.16}$$

The excitation force is calculated as:

$$F_{ex}(t) = \int_0^t K_{ex}(t-\tau)\eta(t)dt \tag{H.17}$$

where $\eta$ is the external wave elevation and $K_{ex}$ is the excitation force impulse response function calculated as:

$$K_{ex}(t) = \frac{1}{\pi}\int_0^\infty \Re(\tilde{F}_{ex}(\omega)e^{-i\omega t})d\omega \tag{H.18}$$

## H.4 Time-domain resolution

The time-domain equation of motion is a second-order Ordinary Differential Equation (ODE) in X. Its resolution is possible using first-order numerical solvers. To reduce the ODE order, we introduce two new variables (U,V) such that:

$$\begin{cases} U = X \\ V = \dot{X} \end{cases} \tag{H.19}$$

The presence of the convolution product $I = \int_0^t K_R(t-\tau)V(t)d\tau$ is however an issue for the step-by-step integration of the solver. A solution is to approximate the convolution product by the sum of n additional variables $I_k$, using the Prony's method:

$$I \simeq \sum_1^n I_k \tag{H.20}$$

Each $I_k$ being governed by additional first order equations ODEs of the form:

$$\dot{I}_k = f_k(I_k, V) \tag{H.21}$$

More on Prony's method can be found in Appendix.

The equation of motion finally becomes a system of 2+n coupled first-order ODEs in $U$, $V$ and $\{I_{ij,k}, k = 1:n\}$:

$$\begin{cases} \dot{U} = V \\ \dot{V} = \dfrac{1}{m + a(\infty)}\left(F_{ex}(t) - \sum_1^n I_k - K_H U(t) + F_{PTO} + F_{Drag}\right) \\ \dot{I}_k = f_k(I_k, V), \qquad k = 1:n \end{cases} \tag{H.22}$$

This system can be solve directly using a first-order numerical solvers.

Alternatives to the Prony's method exist such as the direct calculation of the momery effect at each time step or iterative methods such as the one suggested in [117].

# Appendix I

# Prony's method

The Prony's method allows the estimation of the impulse response function K as the sum of $N_p$ damped complex exponentials:

$$K(t) \simeq \sum_{k=1}^{N_p} \alpha_k e^{\beta_k t} \tag{I.1}$$

where $\alpha_k$ and $\beta_k$ are complex coefficient and $N_p$ is the order of the Prony function.

The memory effect integral I can then therefore be calculated as the sum of $N_p$ functions $I_k$:

$$I(t) = \int_0^t K(t-\tau)\dot{x}(\tau)d\tau \simeq \sum_{k=1}^{N_p} I_k(t) \tag{I.2}$$

where:

$$I_k(t) = \alpha_k e^{\beta_k t} \int_0^t e^{-\beta_k \tau}\dot{x}(\tau)d\tau \tag{I.3}$$

Differentiating equation I.3 leads to the differential equation:

$$\dot{I}_k(t) = \beta_k I_k(t) + \alpha_k \dot{x}(t) \tag{I.4}$$

The memory effect integral is therefore calculated as the sum of $N_p$ additional function $\{I_k, k = 1 : N_p\}$ which are the solutions of $N_p$ additional first order equations.